

# **Cellular Logistics of Glycosylation Disorders**

Peter Theodorus Alexander Linders

The research presented in this thesis was performed at the Department of Tumor Immunology at the Radboud Institute for Molecular Life Sciences, Radboud University Medical Center, Nijmegen, The Netherlands. The research presented in this thesis was financially supported by an NWO Vidi grant.

**ISBN**

1234567890123

**Design**

P.T.A. Linders

**Print**

Gildeprint

**©2021 — Peter Theodorus Alexander Linders**

All rights reserved. No part of this book may be reproduced, distributed, stored in a retrieval system or transmitted in any form or by any means, without prior written permission by the author.

# Cellular Logistics of Glycosylation Disorders

## Proefschrift

ter verkrijging van de graad van doctor  
aan de Radboud Universiteit Nijmegen  
op gezag van de rector magnificus prof. dr. J.H.J.M. van Krieken,  
volgens besluit van het college van decanen  
in het openbaar te verdedigen op vrijdag 24 december 2021  
om 12.30 uur precies

door

**Peter Theodorus Alexander Linders**

geboren op 28 april 1993  
te Oss

**Promotoren**

Prof. dr. Geert van den Bogaart (Rijksuniversiteit Groningen)

Prof. dr. Dirk J. Lefeber

**Copromotor**

Dr. Martin ter Beest

**Manuscriptcommissie**

Harry van den Boekel

# Contents

1	General Introduction	9
1.1	The Golgi Apparatus . . . . .	10
1.2	The Secretory Pathway . . . . .	10
1.3	Glycosylation . . . . .	13
1.4	Membrane Fusion . . . . .	15
1.5	Scope of this Thesis . . . . .	18
2	Sugary Logistics Gone Wrong: Membrane Trafficking and Congenital Disorders of Glycosylation	21
2.1	Abstract . . . . .	22
2.2	Introduction . . . . .	23
2.3	Membrane Trafficking Components in CDG . . . . .	26
2.4	Discussion and Conclusions . . . . .	38
2.5	Supplementary Information . . . . .	40
3	Fluorescence lifetime imaging of pH along the secretory pathway	47
3.1	Abstract . . . . .	48
3.2	Introduction . . . . .	49
3.3	Results . . . . .	50
3.4	Discussion . . . . .	57
3.5	Methods . . . . .	59
3.6	Supplementary Information . . . . .	62
4	N-glycosylation is dependent on TMEM199-mediated V-ATPase assembly	65
4.1	Abstract . . . . .	66
4.2	Introduction . . . . .	67
4.3	Results . . . . .	67
4.4	Discussion . . . . .	76
4.5	Methods . . . . .	78
4.6	Supplementary Information . . . . .	81
5	Stx5-Mediated ER-Golgi Transport in Mammals and Yeast	91
5.1	Abstract . . . . .	92
5.2	Introduction . . . . .	93
5.3	SNARE Proteins in ER-Golgi and Intra-Golgi Transport . . . . .	94
5.4	Subcellular Localization of Stx5 Isoforms . . . . .	98
5.5	Posttranslational Modifications . . . . .	103
5.6	Scfd1/Sly1p . . . . .	103
5.7	Tethering Complexes . . . . .	104
5.8	Infections and Neurodegenerative Disease . . . . .	106
5.9	Discussion . . . . .	107
6	Congenital disorder of glycosylation caused by starting site-specific variant in syntaxin-5	111

6.1	Abstract . . . . .	112
6.2	Introduction . . . . .	113
6.3	Results . . . . .	114
6.4	Discussion . . . . .	131
6.5	Methods . . . . .	134
6.6	Supplementary Information . . . . .	141
7	Discussion & Future Perspectives	173
7.1	The Clinical Foundation of this Thesis . . . . .	174
7.2	On Tissue-Specific Glycosylation . . . . .	175
7.3	The Use of Primary Human Material in Cell Biological Studies . . . . .	176
7.4	How Advancements in Microscopy Advance Golgi and Glycosylation Research . . . . .	178
7.5	Intersecting Membrane Trafficking and Glycosylation . . . . .	180
7.6	Concluding Remarks . . . . .	181
	References	182





# 1

## General Introduction

## 1.1 The Golgi Apparatus

The human body is one of the most complicated systems in nature. On the larger scale, each organ has its separate function but it also works in concert with the other organs. Descending a level, organs and tissues are built up from cells. To function normally, cells need to communicate with each other, through physical contact with one another but also via the secretion of soluble molecules such as cytokines, growth factors and hormones. Cells can be considered *bona fide* specialized 'factories' within the human body, with distinct tasks: for instance, neurons produce and secrete neurotransmitters for optimal brain function, while immune cells produce and secrete cytokines and antibodies to protect the body from threats from outside.

As with man-built factories, the cellular 'factory' needs 'machines' to process the raw materials and prepare the products for secretion. In cells, the main responsible 'machine' (organelle), is the Golgi apparatus, also known as the Golgi. Central to secretion, the Golgi is part of the endomembrane system in the cytoplasm and can be observed by light and electron microscopy as a compact, but large, network-like structure. In 1898, the Italian physician Camillo Golgi discovered the Golgi while investigating the nervous system, initially calling the structure *apparato reticolare interno* (internal reticular apparatus)<sup>1,2</sup>. At first, Golgi's observation was believed to be an artifact caused by the staining he used, but with the invention of the electron microscope in the twentieth century, the existence of the Golgi was confirmed<sup>3</sup>. For their work on the structure of the nervous system, Camillo Golgi and Santiago Ramón y Cajal were jointly awarded the Nobel Prize in Physiology or Medicine in 1906<sup>4</sup>.

The Golgi acts as a distribution center, relaying newly synthesized proteins to their correct destination both within and outside the cell. Proteins synthesized in the endoplasmic reticulum (ER) often require post-translational modifications such as the addition of sugar molecules (glycosylation) or sulfation; these processes require the Golgi<sup>5</sup>. Glycosylation is of particular significance as most secreted proteins are glycosylated, which is of utmost importance for their structure, stability, function, transit, and selective targeting<sup>6–13</sup>.

The mammalian Golgi exists as a single large perinuclear organelle, organized in separate compartments also known as cisternae<sup>14–16</sup>. These compartments are named based on their layout relative to the cell nucleus: the compartment closest to the nucleus is named *cis*-Golgi while the compartments furthest from the nucleus are the *trans*-Golgi and *trans*-Golgi network (TGN). The medial-Golgi resides in-between the *cis*- and *trans*-Golgi. Each Golgi compartment has its distinct environment composed of not only enzymes necessary for glycosylation<sup>17–20</sup> but also various trafficking proteins<sup>13,21</sup> and ions<sup>13,22,23</sup>.

## 1.2 The Secretory Pathway

In a broader, intracellular context, the Golgi forms the heart of the secretory pathway. The secretory pathway, together with the endocytic pathway, constitutes the endomembrane system<sup>24,25</sup> (Figure 1.1a). The secretory pathway comprises all organelles responsible for the synthesis and secretion of proteins destined for the extracellular space: the ER, Golgi apparatus, and

secretory vesicles. In principle, the secretory pathway enables cells to work together and not just on their own, as the secretion of signaling molecules and production of surface exposed receptors enables the communication between cells. Thus, the secretory pathway is responsible for the correct production and delivery of molecules outside the cell, such as cytokines, extracellular matrix proteins, and hormones.

In human cells, new proteins are translated from DNA-derived mRNA and co-translationally inserted into the rough ER. Within the lumen of the ER, proteins are folded and an initial quality control step is performed. This ensures that only properly folded proteins can exit the ER and continue their journey through the secretory pathway<sup>26</sup>. Newly synthesized proteins are then packaged and transported in vesicles to the Golgi where they can be further modified and sorted to their correct destination (Figure 1.1b). One driver in this sorting process is the decrease of pH (acidification) of the Golgi lumen from *cis* (pH 6.7) to *trans* (pH 6.0). pH differences are important for the acceptance and release of cargo from cargo adapters due to conformational changes and pH-dependent binding affinity<sup>27–30</sup>. Therefore, pH is of critical importance for the correct maintenance of Golgi cisterna identity<sup>13,31–33</sup>, as well as for the optimal function of glycosylation enzymes<sup>34</sup>.

After the newly synthesized proteins have sufficiently been modified, they are ready to be sorted at the TGN and exit the Golgi<sup>35</sup>. This final sorting step sends the newly synthesized proteins to their final location, including endosomes, lysosomes, the plasma membrane, and the extracellular space.

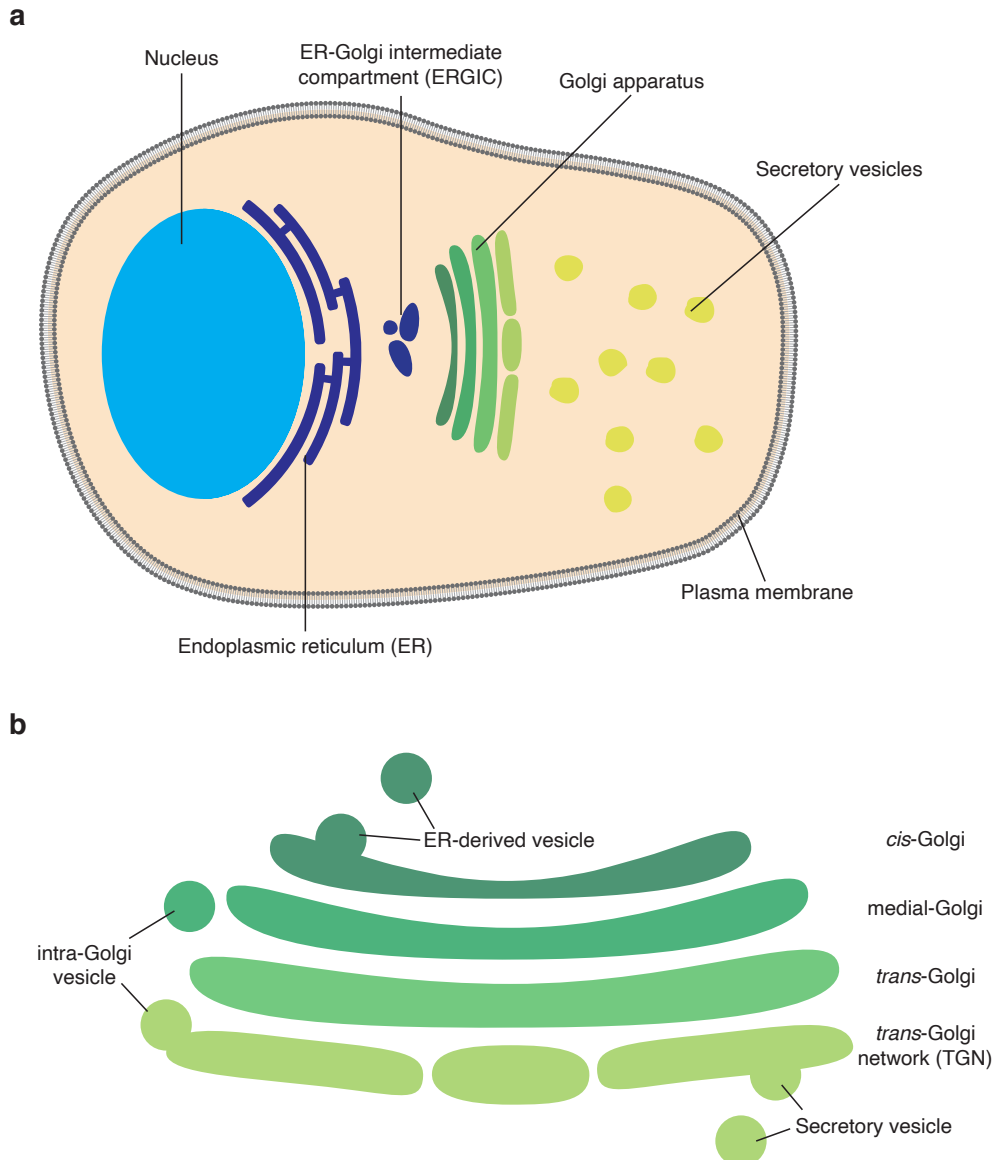


**Figure 1.1:** (a) Schematic overview of the mammalian secretory pathway. (b) Closer view of the mammalian Golgi apparatus. ER-derived vesicles arrive at the *cis*-face of the Golgi, while secretory vesicles depart from the *trans*-face. Cargo is exchanged between cisternae via intra-Golgi transport vesicles.

## 1.3 Glycosylation

One of the most important functions of the Golgi apparatus is to ensure the correct glycosylation of newly synthesized proteins. In vertebrates, glycosylation is a sequential process involving both the addition and trimming of glycan structures by glycosyltransferases and glycosidases<sup>36</sup>. In contrast to other essential protein synthesis processes such as translation and transcription, glycosylation is not template-based (cf., DNA serves as a template for transcription and mRNA as a template for translation)<sup>37</sup>. Around 700 proteins are responsible for the full spectrum of around 7,000 unique glycan structures. Only ten different monosaccharides, fucose (Fuc), galactose (Gal), glucose (Glc), N-acetylgalactosamine (GalNAc), N-acetylglucosamine (GlcNAc), glucuronic acid (GlcA), mannose (Man), sialic acid (SA, also known as neuraminic acid), xylose (Xyl), and recently identified ribitol, are the necessary building blocks for glycans of mammalian cells<sup>38–43</sup>. Based on which amino acid residue of the protein the glycan is attached, O- and N-linked glycosylation can be distinguished. O-linked glycosylation occurs on the side chain hydroxyl oxygen of either serine or threonine residues, while N-linked glycosylation occurs on asparagine residues. As the work in this thesis is mainly focused on N-linked glycosylation, below I will shortly summarize the basic mechanism of N-linked glycosylation.

N-linked glycosylation begins in the ER where a precursor glycan consisting of 14 monosaccharides is transferred from the carrier lipid dolichol to the newly synthesized protein. Concurrent with translation, the precursor glycan is removed from dolichol and placed on N-linked glycosylation acceptor peptide sequons (Asn – X – (Ser/Thr)) of nascent polypeptides by oligosaccharyltransferase (OST)<sup>44–50</sup>. Before Golgi entry of the newly synthesized glycoproteins, distal glucose moieties are trimmed as an important step in the control of misfolded glycoproteins in the ER<sup>10,51,52</sup>. Once quality control is complete, the newly synthesized glycoproteins are transported to the Golgi, where the glycan structures are further trimmed, extended, and branched until the final form of the glycan is reached (Figure 1.2, adapted from Figure 9.4 of *Essentials of Glycobiology*<sup>53</sup>).

The non-template-driven characteristics of glycosylation imply that stringent regulation of all glycosylation machinery is required to maintain physiological glycosylation. As such, small abnormalities can have a large effect on the final glycan product<sup>54</sup> and currently already over 100 monogenic diseases have been found that are characterized by incorrect glycosylation. Collectively, these diseases are known as congenital disorders of glycosylation (CDG)<sup>13,31,55,56</sup>. Therefore, the proper localization of all glycosylation machinery and other required factors is paramount.

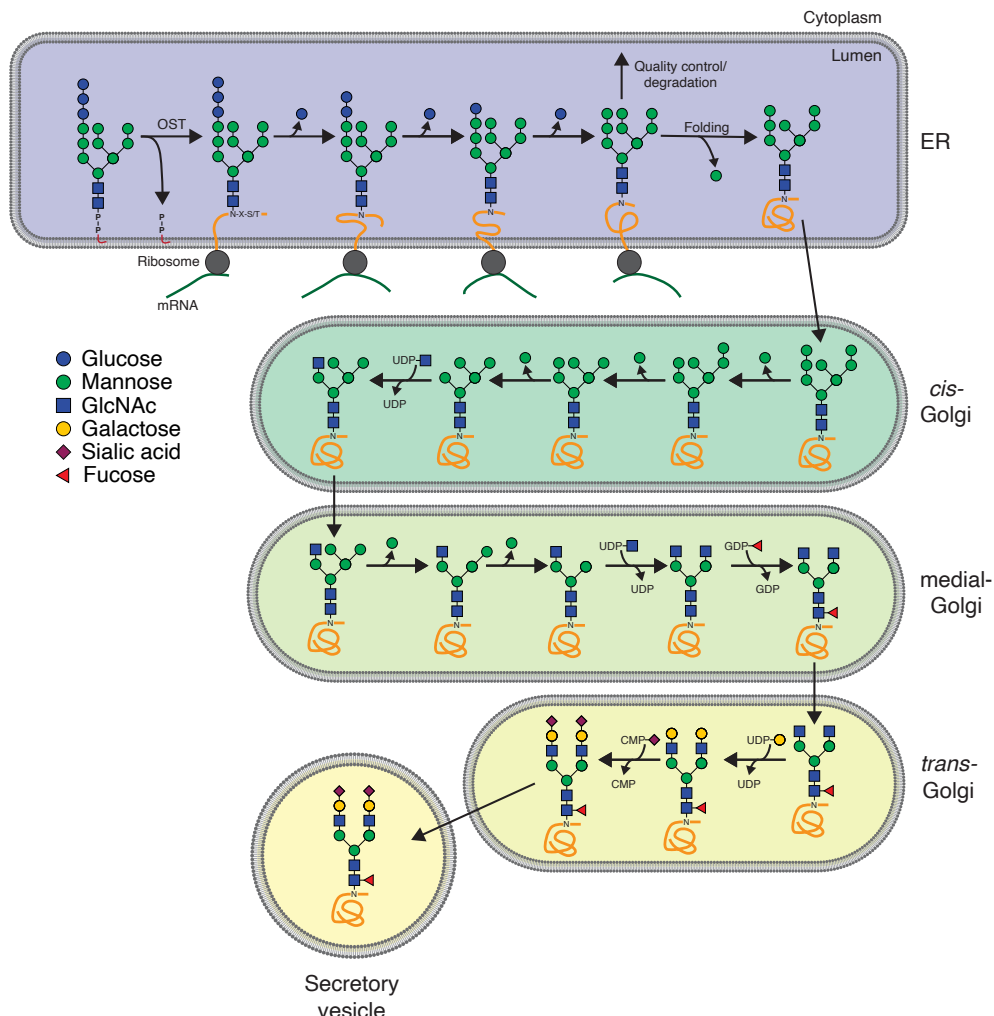


**Figure 1.2: The processing and maturation of a biantennary, fucosylated N-glycan.** The immature glycan structure is transferred from dolichol phosphate to the nascent polypeptide in the ER. Following quality control, the folded glycoprotein is then exported to the Golgi where the final glycan structure is produced.

## 1.4 Membrane Fusion

Crucial to all transport steps in mammalian cells is the delivery of (cargo) proteins from one organelle, or organellar sub-compartment, to the next. Considering the compartmentalization of the secretory pathway, the prevailing theory of protein transport in mammalian cells is via membrane vesicles. Once a vesicle has been released and is destined for an organelle, such as the Golgi apparatus, the vesicle must fuse its membrane with the membrane of the accepting compartment to transfer the cargo to the intraorganellar lumen. This step is mediated by SNARE proteins.

SNAREs (soluble *N*-ethylmaleimide-sensitive factor attachment protein (SNAP) receptors) mediate all fusion events in eukaryotic cells, except for mitochondrial fusion<sup>57,58</sup>. The human SNARE family consists of 36 members, which all carry one or two SNARE motifs, domains of approximately 60-70 amino acid residues arranged in heptad repeats<sup>59</sup>. Most SNAREs are anchored to the membrane and most SNAREs contain a transmembrane domain, while others can be anchored through lipid modifications such as palmitoylation or prenylation.

Mammalian SNAREs can be roughly classified into two groups based on their membrane location: the vesicular SNAREs (v-SNARE) present on cargo vesicles and target SNAREs (t-SNARE) on the acceptor membrane. In some cases, this classification can be inconsistent, for instance when SNAREs are involved in bidirectional (anterograde and retrograde) transport of molecules or homotypic vesicle fusion without defined donor or acceptor compartments. SNAREs can also be classified by the central functional residue in the SNARE motif: R-SNAREs contain an arginine residue while Q-SNAREs (these can be subdivided in Qa, Qb, Qc or, Qbc depending on their location in the SNARE bundle) contain a glutamine residue<sup>55</sup>. For successful membrane fusion, four SNARE motifs, one R-SNARE and 3 Q-SNAREs, interact together to form a tight coiled-coil bundle that brings the vesicular and acceptor membranes together (Figure 1.3). This mechanism overcomes the energy barrier of membrane fusion.

Considering the Golgi as the central hub of the mammalian cell, it is an important location where many membrane fusion events occur. Vesicles containing newly synthesized proteins from the ER, vesicles going to and from the plasma membrane, and vesicles involved in intra-Golgi trafficking all need to fuse with Golgi membranes. Two main models of Golgi apparatus transport exist. The first model is the vesicular trafficking model, where each cisterna is a static sub-compartment and cargo molecules are transported by vesicles between the cisternae<sup>14</sup>. The second, more widely-accepted model is cisternal maturation in which vesicles with newly synthesized proteins from the ER fuse with each other to form the *cis*-Golgi. Each cisterna is highly dynamic and gradually matures into *trans*-Golgi through accepting lipids and glycosylation enzymes from later Golgi cisternae<sup>14</sup>. At the ER – Golgi trafficking interface in the cisternal maturation model, four distinct trafficking steps can be identified: anterograde transport from ER to the ER – Golgi intermediate compartment (ERGIC), from ERGIC to *cis*-Golgi, intra-Golgi transport between cisternae and retrograde trafficking from *cis*-Golgi to the ER. In these four different trafficking steps, syntaxin-5 (Stx5) is the most important Qa-SNARE, participating in three out of the four different SNARE complexes<sup>21</sup> (Figure 1.4). The formation of different SNARE complexes with unique cognate SNAREs is beneficial to the specificity of membrane trafficking, ensuring

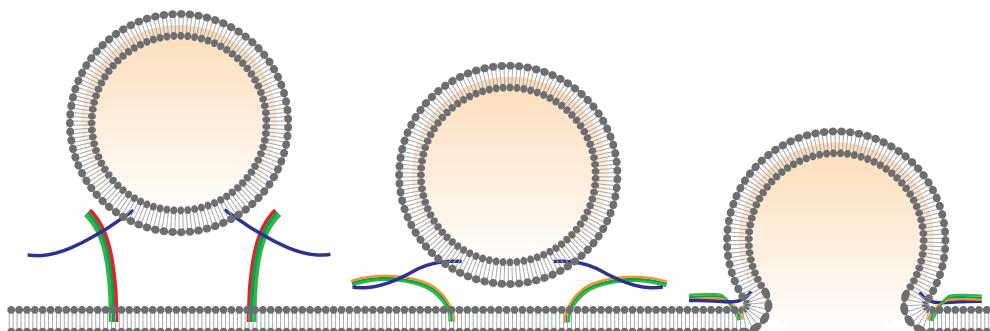


**Figure 1.3: SNARE-mediated membrane fusion at the ER - Golgi interface.** The t-SNARE complex on the acceptor membrane (red: Qa-SNARE, green: Qb/R-SNARE) and the v-SNARE (blue: Qc-SNARE) on the vesicular membrane come into close proximity and form a *trans*-SNARE complex. As this complex tightens, the two membranes are forced closer to each other and the lipid bilayers fuse.

that the right cargo is transported to the right destination.

Taken together, the secretory pathway is the veritable heart of the eukaryotic cell, by ensuring that newly synthesized proteins are delivered in the correct composition and at the correct location. Each transport step is finely tuned for optimal performance and maximum fidelity of the respective cargo. Unfortunately, only small abnormalities in this trafficking system can cause large problems on both the cellular and organism level, but the molecular mechanisms are often poorly understood. In this thesis, I addressed the molecular mechanisms behind CDGs of components involved in protein transport from ER to Golgi.

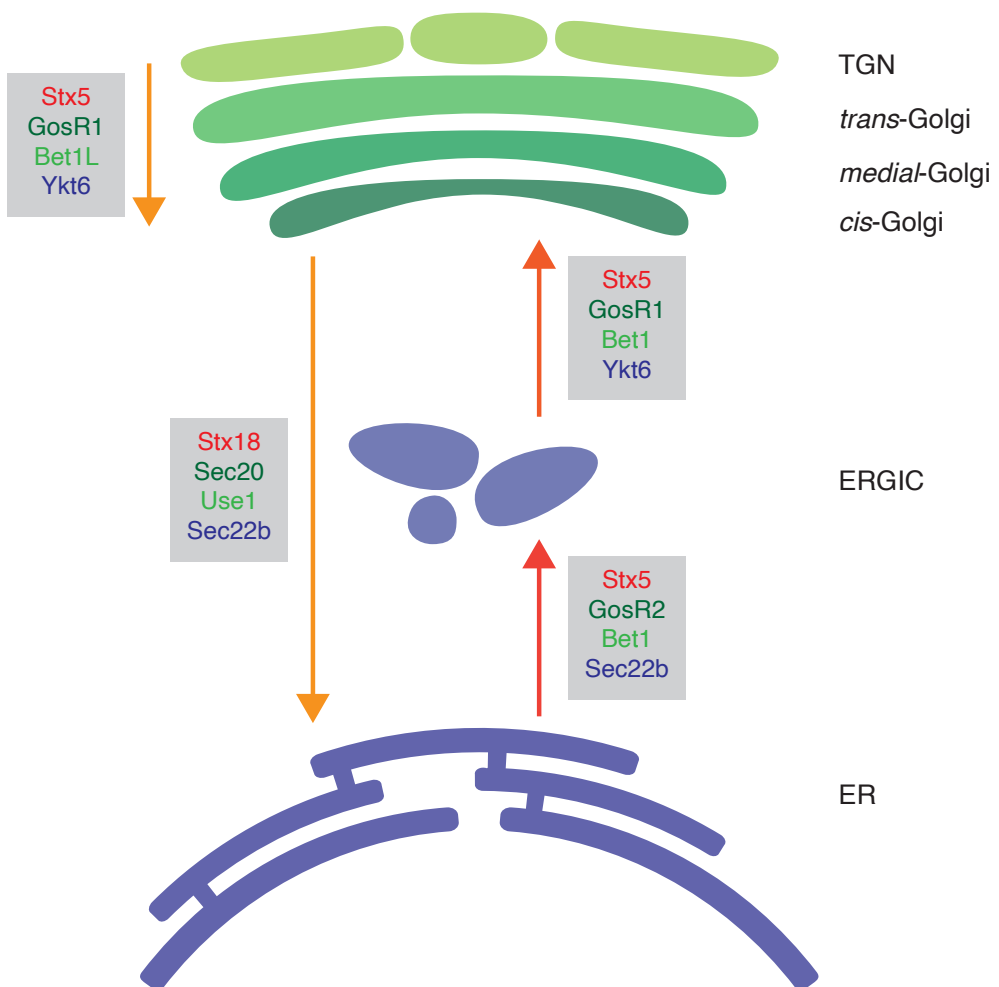


Figure 1.4: Schematic overview of SNARE complexes at the ER-Golgi interface in mammalian cells. Adapted from Chapter 5, Figure 5.1.

## 1.5 Scope of this Thesis

The principal aim of this thesis is to obtain a better understanding of the involvement of intracellular trafficking proteins in ER-Golgi transport and glycosylation. To achieve this, I performed cell biological and biochemical experiments to uncover the molecular mechanism of patients with novel CDGs.

**Chapter 2** provides an overview of all CDGs that are related to intracellular trafficking proteins. Recent developments in diagnostic methods for CDG have enabled the discovery of new genetic variants in trafficking proteins that result in glycosylation disorders. I discuss these developments and how they help understand ER-Golgi trafficking better. In **chapter 3**, I demonstrate a newly developed technique based on fluorescence lifetime imaging microscopy (FLIM) to measure intraorganellar pH with high accuracy. I apply the technique on both static organelle markers and dynamic cargo proteins. This improved imaging technique is subsequently applied in **chapter 4** to determine the role of V-ATPase assembly factor TMEM199 in ER-Golgi transport and luminal acidification.

An integral component of ER-Golgi transport, syntaxin-5, is the focus of the second part of this thesis. **Chapter 5** provides a comprehensive examination of all published literature on syntaxin-5 and disseminates the differences and similarities of syntaxin-5 and ER-Golgi trafficking in both mammals and yeast. This forms the preface to **chapter 6**, where I present the discovery of a new genetic variant in syntaxin-5 resulting in a CDG with a severe phenotype. I demonstrate the molecular mechanism behind this CDG and thereby improve our understanding of the role of syntaxin-5 in mammalian intracellular trafficking and glycosylation.





P.T.A. Linders, E. Peters, M. ter Beest, D.J. Lefever and G. van den Boogaart

*International Journal of Molecular Sciences* 2020, 21(13), 4654

# 2

## Sugary Logistics Gone Wrong: Membrane Trafficking and Congenital Disorders of Glycosylation

## 2.1 Abstract

Glycosylation is an important post-translational modification for both intracellular and secreted proteins. For glycosylation to occur, cargo must be transported after synthesis through the different compartments of the Golgi apparatus where distinct monosaccharides are sequentially bound and trimmed, resulting in increasingly complex branched glycan structures. Of utmost importance for this process is the intraorganellar environment of the Golgi. Each Golgi compartment has a distinct pH, which is maintained by the vacuolar H<sup>+</sup>-ATPase (V-ATPase). Moreover, tethering factors such as Golgins and the conserved oligomeric Golgi (COG) complex, in concert with coatomer (COPI) and soluble N-ethylmaleimide-sensitive factor attachment protein receptor (SNARE)-mediated membrane fusion, efficiently deliver glycosylation enzymes to the right Golgi compartment. Together, these factors maintain intra-Golgi trafficking of proteins involved in glycosylation and thereby enable proper glycosylation. However, pathogenic mutations in these factors can cause defective glycosylation and lead to diseases with a wide variety of symptoms such as liver dysfunction and skin and bone disorders. Collectively, this group of disorders is known as congenital disorders of glycosylation (CDG). Recent technological advances have enabled the robust identification of novel CDGs related to membrane trafficking components. In this review, we highlight differences and similarities between membrane trafficking-related CDGs.

## 2.2 Introduction

The conjugation of oligosaccharide structures to proteins, glycosylation, is a ubiquitous and fundamental post-translational modification found in all domains of life. Glycosylation is not only important for the structure and function of proteins, but also for their transit and selective targeting through the secretory pathway<sup>6–12</sup>. In mammals, approximately 700 proteins are necessary for generating the full diversity of over 7000 glycan structures<sup>38–42</sup>. The addition of glycan structures in vertebrates is a sequential process and involves both the addition of monosaccharides via glycosyltransferases and the trimming of glycans by glycosidases<sup>36</sup>. Only ten different monosaccharides are required to build the full glycan spectrum: fucose (Fuc), galactose (Gal), glucose (Glc), N-acetylgalactosamine (GalNAc), N-acetylgalactosamine (GlcNAc), glucuronic acid (GlcA), mannose (Man), sialic acid (SA, also known as neuraminic acid), xylose (Xyl), and recently identified ribitol<sup>38,40,41,43</sup>.

In vertebrates, N-glycan synthesis is initiated in the ER as a 14 monosaccharide precursor on the carrier lipid dolichol. During translation, this glycan is transferred by oligosaccharyltransferase (OST)<sup>44–46</sup> from dolichol to the nascent polypeptide at acceptor peptide sequons, generally consisting of an Asn-X-(Ser/Thr) motif<sup>47–50</sup>. Distal glucose moieties of these immature, high glucose and mannose containing, glycan structures are subsequently trimmed before Golgi entry; an important step in the control of misfolded glycoproteins in the ER<sup>10,51,52</sup>. Glycoproteins then exit the ER via, for instance, cargo receptor ERGIC-53<sup>60–62</sup> and are transported to the Golgi apparatus for further processing. In the Golgi, glycoproteins are trimmed, extended, and branched until they reach their final glycan form. The mammalian Golgi apparatus is a single large perinuclear organelle, organized into discrete compartments or cisternae<sup>14–16</sup>. The Golgi can be subdivided into *cis*-Golgi, closest to the ER, medial-Golgi, *trans*-Golgi, and the *trans*-Golgi network (TGN), furthest away from the nucleus. Furthermore, mammals have a pre-Golgi compartment known as the ER-Golgi intermediate compartment (ERGIC, previously known as the vesicular-tubular cluster (VTC))<sup>63,64</sup>. Newly synthesized glycoproteins emanating from the ER enter the Golgi apparatus at the *cis*-Golgi, sequentially pass through medial- and *trans*-Golgi, and finally, exit the Golgi at the TGN. The compartmentalization of the Golgi allows for distinct environments containing subsets of glycosylation enzymes<sup>17–20</sup>, enabling sequential modifications for the formation of completely mature glycoproteins. The organization of Golgi-resident enzymes and the Golgi apparatus itself differs between cell types, contributing to glycoprotein diversity<sup>15,65–68</sup>. Two examples are the distribution of  $\alpha$ -mannosidases I and II, which primarily localize to the *trans*-Golgi in intestinal goblet cells, but are distributed over all Golgi cisternae in hepatocytes, the functional consequences of which are currently unknown<sup>68</sup>.

Efficient glycosylation fully relies on the correct localization of glycosylation enzymes, as well as on the delivery of other glycosylation machinery, such as nucleotide sugar transporters, and cargo proteins to be glycosylated to the correct Golgi compartment. An important factor involved in the correct trafficking of glycosylation enzymes is the maintenance of pH within the Golgi apparatus. In eukaryotic cells, the principal proton pump for the regulation of intraorganellar pH is the vacuolar H<sup>+</sup>-ATPase (V-ATPase). The membrane V<sub>0</sub> domain anchors this complex in the membrane, and the V<sub>1</sub> domain is cytosolic<sup>69</sup>. The V<sub>0</sub> domain contains six dif-

ferent subunits (a, d, e, c, c', and c''). This domain functions as a proton translocator across the membrane, which not only results in a pH gradient, but also in a change in membrane potential, which is neutralized by counter ions such as K<sup>+</sup> and Cl<sup>-</sup>. The cytosolic V<sub>1</sub> domain contains eight subunits (A-H), and its main function is ATP hydrolysis<sup>69</sup> to provide the energy needed for the pH gradient. In mammals, the specificity of V-ATPase localization is encoded in the V<sub>0</sub>a subunit, as four unique isoforms exist (V<sub>0</sub>a1-4). This is in contrast to *Saccharomyces cerevisiae*, which has only two unique isoforms (Vph1p and Stv1p)<sup>69–73</sup>. The diversity in V<sub>0</sub>a subunits is likely important for specific cell type-dependent functions and differential regulation of the pH in different organelles. Isoform V<sub>0</sub>a1 is targeted to secretory vesicles and V<sub>0</sub>a2 to the Golgi and endosomes, and V<sub>0</sub>a3, highly expressed in macrophages and osteoclasts<sup>74,75</sup>, is enriched in late endosomes and lysosomes, while V<sub>0</sub>a4 is mainly expressed in the kidney, inner ear, and ocular ciliary body<sup>76–79</sup>. The V-ATPase ensures a constant pH in the various Golgi compartments, which ranges from 6.7 for the *cis*-Golgi to 6.0 for the *trans*-Golgi<sup>22</sup>. Given the pH optima of glycosylation enzymes, this pH gradient could restrict the activity of glycosylation enzymes to their target Golgi compartment<sup>34</sup>. However, this might not be the complete explanation considering the broad distribution of pH optima and the small differences in absolute pH between the cisternae. Instead, or additionally, the pH-sensitive binding and release to cargo adapters might ensure correct enzyme localization to the target Golgi compartment<sup>31–33</sup>.

Several models for the trafficking routes in the Golgi exist, but the most favorable model of membrane traffic within the Golgi is the cisternal maturation model (Figure 2.1)<sup>80</sup>. Cisternal maturation is the gradual conversion of a Golgi compartment by the delivery of proteins and lipids from more mature Golgi compartments concomitant with the removal of Golgi proteins and lipids from previous Golgi compartments by coatomer (coat protein complex I; COPI)-mediated retrograde membrane trafficking<sup>14,80</sup>. Before membrane fusion of these COPI vesicles, a set of molecular instruments orchestrates correct vesicle targeting to and within the Golgi. An important group of such trafficking factors is the Golgin family, which consist of large coiled-coil proteins that associate with the Golgi membrane. Golgins form a tentacular web in the cytosol that efficiently and selectively tethers cargo vesicles<sup>81,82</sup>. Concurrently, Golgins can act as scaffolding proteins for small Rab or Arf GTPases<sup>83–85</sup>. At the Golgi, Rab6 and Rab30 can recruit effectors, such as the cytoskeletal motor protein myosin II, for vesicle trafficking<sup>86–90</sup>. Completing the ensemble is the conserved oligomeric Golgi (COG) tethering complex, a heterooctameric protein complex bridging the Golgi membrane and COPI vesicles<sup>91,92</sup>. Finally, when the Golgi membrane and the uncoated COPI vesicle are in close enough proximity, membrane fusion occurs. Membrane fusion is performed by soluble N-ethylmaleimide-sensitive factor attachment protein receptor (SNARE) proteins.

As glycosylation is such an extensive process with a multitude of different factors that operate together for sequential remodeling of glycan moieties, only slight disturbances can have major implications on glycosylation. As such, over 100 monogenic diseases have been identified characterized by dysfunctional glycosylation, which form a group collectively known as congenital disorders of glycosylation (CDG)<sup>31,55,56</sup>. A large subset of these includes genetic variants in the prior mentioned trafficking proteins, but also in subunits of the vacuolar H<sup>+</sup>-ATPase and its assembly factors. Recent technological advances in CDG diagnostics have enabled more com-

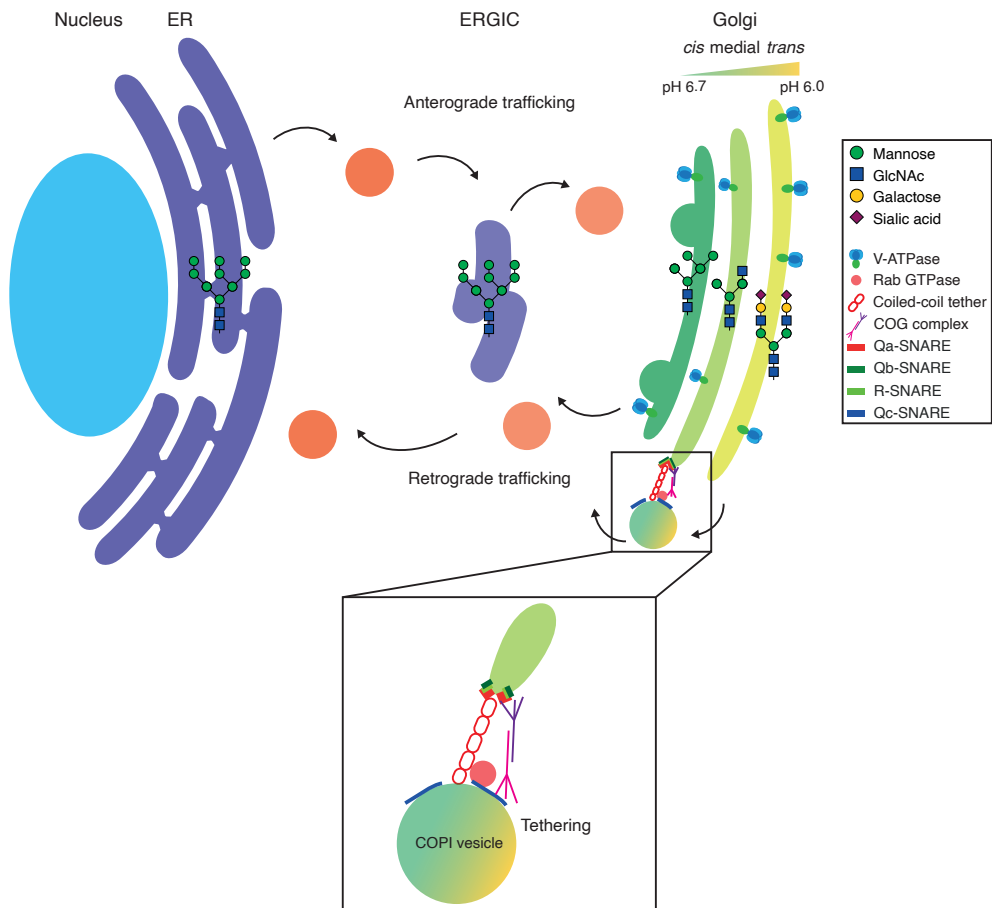


**Figure 2.1: Schematic overview of the early secretory pathway in mammalian cells.** Abbreviations: ER, endoplasmic reticulum; ERGIC, endoplasmic reticulum-Golgi intermediate compartment; COG complex, conserved oligomeric Golgi complex; COPI, coat protein complex I.

prehensive analysis of glycosylation disorders. Novel mass spectrometric methods to detect changes in glycosylation<sup>93</sup> together with next-generation sequencing to detect novel genomic mutations<sup>94,95</sup> are a powerful combination for the interrogation of membrane trafficking components in CDGs. This review serves to provide a comprehensive overview of trafficking-related CDGs and to form a detailed understanding of how Golgi trafficking influences glycosylation.

## 2.3 Membrane Trafficking Components in CDG

Efficient membrane trafficking is of utmost importance for the entire secretory pathway. In this review, we focus on disorders directly affecting Golgi function. Therefore, other disorders affecting for instance ER to ERGIC transport will not be discussed.

### 2.3.1 Vacuolar H<sup>+</sup>-ATPase

For efficient delivery of glycosylation enzymes to Golgi cisternae to occur, the intraorganellar pH must allow the association of the glycosylation enzyme with a trafficking cargo receptor at the donor compartment and release from the receptor at the receiving compartment. Given the role of pH in intracellular trafficking and how stringent cisternal pH is regulated in the Golgi apparatus (Figure 2.2)<sup>22</sup>, alterations in pH maintenance might be expected to lead to mislocalization of glycosylation enzymes, which in turn cause glycosylation disorders. Indeed, genetic variants in *ATP6VOA2*, the gene encoding the membrane-bound V<sub>o</sub>a2 subunit of the V-ATPase localized to endosomes and TGN<sup>78,79</sup>, lead to glycosylation defects<sup>77</sup>. Patients with pathogenic variants, loss-of-function mutations leading to a truncated protein, in *ATP6VOA2* present with wrinkly skin syndrome and autosomal recessive cutis laxa type II, both connective tissue disorders related to the secretion of elastin to the extracellular matrix, and neurological involvement. Moreover, experiments in patient fibroblasts with the fungal metabolite Brefeldin A (BFA), which inhibits the formation of COPI vesicles<sup>96</sup>, demonstrate that retrograde intra-Golgi trafficking is impaired in pathogenic *ATP6VOA2* variants, likely causing the mislocalization of glycosyltransferases. Supporting this, neutralization of the Golgi pH with the weak base ammonium chloride or proton pump inhibitor Bafilomycin A1 also mislocalizes glycosyltransferases<sup>97</sup>. Furthermore, the misregulation of Golgi pH could influence the delivery of glycosylated cargo via the cargo receptor ERGIC53, which binds high mannose glycans in the ER in a pH-dependent manner and transports them to the Golgi apparatus<sup>60–62,98</sup>. Thus, in addition to the deviation of the pH values away from those optimal for glycosyltransferase activity, mutations in subunits of the V-ATPase could result in mislocalization of both glycosyltransferases and their substrates, and this likely contributes to the CDG pathology. General pH maintenance in the Golgi is imperative for physiological glycosylation.

Aside from variants in the V-ATPase itself, assembly factors and accessory proteins have also been implicated in CDGs. One accessory protein of the V-ATPase, Ac45 (Figure 2; also known as ATP6AP1, the ortholog of yeast Voa1p), is ubiquitously expressed<sup>104–107</sup> and mainly guides the V-ATPase into cell type-specific subcellular compartments such as neuroendocrine secretory vesicles<sup>108,109</sup> or the ruffled border of osteoclasts<sup>104,110,111</sup>. Missense mutations at sites coding for

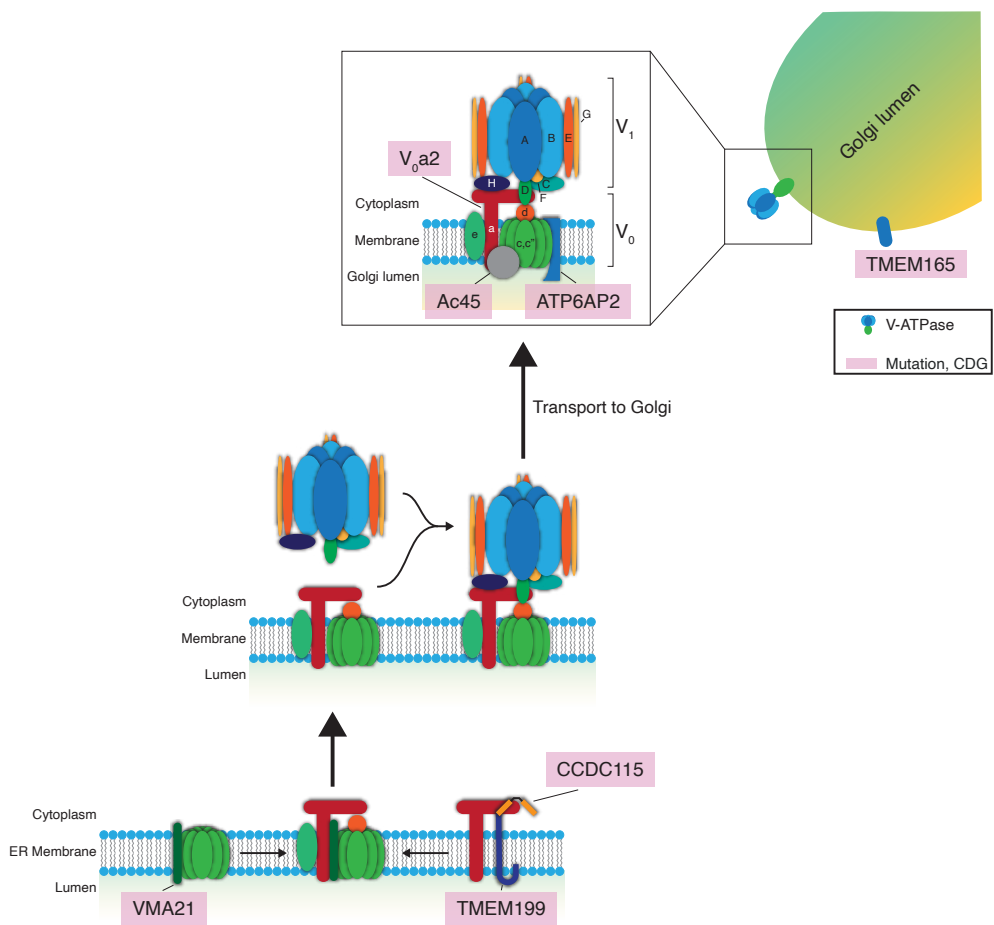


**Figure 2.2: Schematic overview of the mammalian V-ATPase and the putative model of its assembly.** Lower-case letters denote the various subunits of the  $V_0$ -domain; uppercase letters denote the subunits of the  $V_1$ -domain. The assembly factors VMA21, TMEM199, and CCDC115 might assemble the membrane-associated  $V_0$ -domain of the V-ATPase. VMA21 interacts with  $V_{0c}$ ' and  $V_{0a}$ <sup>99–102</sup>, TMEM199 and CCDC115 interact with  $V_{0a}$ <sup>103</sup>. Abbreviations: V-ATPase, vacuolar H<sup>+</sup>-ATPase; CDG, congenital disorder of glycosylation.

highly conserved residues in Ac45 have been identified<sup>112</sup> with patients suffering from immunodeficiencies, hepatopathy, neurocognitive abnormalities, and abnormal protein glycosylation. This not only demonstrates that Ac45 is an important factor in (tissue-specific) trafficking of the V-ATPase, but also strengthens the notion that the trafficking of the V-ATPase is imperative for functional protein glycosylation.

Another accessory protein, ATP6AP2 (Figure 2.2), has also been implicated recently in CDG<sup>113</sup>. While its precise mechanistic role in V-ATPase assembly has not been determined, loss of ATP6AP2 in murine cardiomyocytes, hepatocytes, or podocytes causes a decrease in V<sub>0</sub>a1-3 protein levels, as well as defects in autophagy<sup>114–116</sup>. Patients with missense mutations in ATP6AP2 present protein glycosylation abnormalities with hypogalactosylation and hyposialylation and autophagic defects relating to aberrant lysosomal acidification<sup>113</sup>. This phenotype demonstrates the importance of a functional V-ATPase for both glycosylation and lysosomal function.

Similarly, recently, a novel CDG involving the putative V-ATPase assembly factor VMA21 (ortholog of yeast Vma21p) was discovered, with patients presenting with a hepatic phenotype with steatosis and hypercholesterolemia<sup>117</sup>. Two mutations causing a premature stop codon and one missense mutation in VMA21 were discovered. Mechanistically, the symptoms of VMA21-CDG patients are the result of impaired lipophagy due to reduced lysosomal acidification, and patients present with a loss of sialic acid and galactose on glycoproteins<sup>117</sup>. In yeast, Vma21p interacts with V<sub>0</sub> subunit c' and thus promotes the assembly of the V<sub>0</sub> proteolipid subunits into a ring (Figure 2.2)<sup>99,100</sup>. In mammals, VMA21 can also directly interact with subunit a of the V<sub>0</sub> domain, and this interaction is dependent on glycosylation of subunit a (Figure 2.2)<sup>101,102</sup>. This observation has a two-pronged implication: efficient glycosylation is reliant on the proper assembly of the V-ATPase, and the proper assembly of the V-ATPase is reliant on efficient glycosylation. This could function as a quality control mechanism to abrogate the assembly of a faulty V-ATPase. Most interestingly, in yeast strains lacking Vma21p, the ER-Golgi SNARE Bos1p (ortholog of mammalian GosR2<sup>21,118</sup>) was completely absent from COPII vesicles<sup>119</sup>, strengthening the importance of pH homeostasis for functional ER-Golgi trafficking.

Furthermore, missense mutations in the gene coding for putative V-ATPase assembly factors uncharacterized transmembrane protein 199 (TMEM199, the ortholog of yeast Vma12p) and coiled-coil-domain containing protein 115 (CCDC115, the ortholog of yeast Vma22p) have also been found in novel CDGs<sup>120,121</sup>. CCDC115 and TMEM199 are hypothesized to assemble the membrane-integral V<sub>0</sub> domain of the V-ATPase through interactions with subunit a (Figure 2.2)<sup>103</sup>. In *S. cerevisiae*, assembly of the V<sub>0</sub> domain mediated by Vma21p, Vma12p, and Vma22p occurs at the ER membrane<sup>122–124</sup>, after which the V<sub>0</sub> domain is transported to the Golgi and associates with the V<sub>1</sub> domain to form the fully functional V-ATPase complex<sup>69</sup>. In mammals, the exact mechanism of V-ATPase assembly is still unclear, but as TMEM199 and CCDC115 localize to the ER, it is suggested that mammalian V-ATPase assembly is analogous to that in yeast<sup>125</sup>. Pathogenic variants in either protein mainly have a hepatic phenotype similar to VMA21-CDG, although a neurological phenotype is observed for CCDC115-CDG patients. Abnormal glycosylation, mainly the truncation of glycans through the loss of sialylation and galactosylation, is seen for both CDGs. This observation corresponds to the mislocalization of especially *trans*-Golgi-resident galactosyltransferases, which is consistent with the concomitant acidification of

## 2.3. Membrane Trafficking Components in CDG

the Golgi apparatus. In contrast to VMA21-CDG<sup>117</sup>, but in line with ATP6VOA2-CDG<sup>77</sup>, no disorders in autophagy were described for TMEM199-CDG and CCDC115-CDG<sup>120,121</sup>. One explanation is that a potential lysosomal defect was not investigated. Another plausible explanation for this phenomenon is that TMEM199 and CCDC115 participate in the assembly of a specific V-ATPase for the Golgi apparatus, while the lysosomal V-ATPase is still assembled regularly in TMEM199-CDG and CCDC115-CDG. This raises the possibility that TMEM199 and CCDC115 primarily interact with a certain  $V_0$ a subunit, likely  $V_0$ a2 concerning the glycosylation phenotypes in TMEM199-CDG and CCDC115-CDG, to facilitate the assembly of a Golgi-specific V-ATPase<sup>126–128</sup>. The severity of the symptoms of ATP6AP1-CDG, ATP6AP2-CDG, and VMA21-CDG patients could stem from a more general role of these factors in V-ATPase assembly. Incomplete assembly of the V-ATPase might also result in mislocalization of the  $V_0$  domain, as the trafficking of the  $V_0$  domain might be pH dependent itself, thereby amplifying the phenotypes. Aside from their role in CDG, TMEM199 and CCDC115 have also been implicated in iron metabolism<sup>125</sup> and influenza A virus infection, most probably via a pH-dependent mechanism<sup>129</sup>. These observations underpin how V-ATPase assembly, glycosylation, ER-to-Golgi, and intra-Golgi trafficking are intertwined.

Finally, pathogenic variants in the uncharacterized transmembrane protein 165 (TMEM165, also known as TPRL) leading to CDG have been identified<sup>130</sup>, one intronic mutation in the gene coding for TMEM165 leading to the production of a truncated protein and two missense mutations at sites coding for highly conserved residues. Patients with TMEM165-CDG mainly present with skeletal and hepatic abnormalities and an N-glycosylation defect consisting of hyposialylation and hypogalactosylation. No O-glycosylation abnormalities were observed in these patients. TMEM165 is a putative proton pump, based on protein sequence homology<sup>130</sup>, primarily localizing to the late Golgi apparatus and potentially maintaining the pH in this compartment (Figure 2.2). This theory is corroborated by the similar glycosylation defects observed with TMEM165-CDG and V-ATPase-related CDGs discussed above. Additionally, depletion of TMEM165 using RNA interference in HEK293 cells revealed a defect in Golgi galactosylation, which could be rescued by supplementation with manganese<sup>23</sup>. As manganese is required for the proper functioning of some glycosylation enzymes<sup>131,132</sup>, TMEM165 may also be required for manganese homeostasis, perhaps by functioning as a manganese transporter.

### 2.3.2 Golgins, GRASPs, GORAB, and Rabs

Vesicle fusion with the Golgi apparatus is initiated by specific capture of vesicles by long coiled-coil proteins decorating the Golgi membrane: Golgins<sup>81,82,133,134</sup>. Next to this, Golgins also act as structural proteins to maintain Golgi architecture<sup>135</sup>. To date, genetic variants in several Golgins have been identified that affect both retrograde intra-Golgi trafficking and glycosylation. For instance, a nonsense mutation in the gene coding for GMAP-210 (Figure 2.3, also known as TRIP11) causes neonatal lethal skeletal dysplasia in both mice and humans<sup>136</sup>. Similar to GORAB (see below), the phenotypes in patients carrying loss-of-function mutations in *TRIP11* are caused by defective glycosylation of extracellular matrix proteins. GMAP-210 normally functions as a tether for both ER-to-Golgi and intra-Golgi vesicles<sup>137,138</sup>. *TRIP11* mutant chondrocytes and osteoblasts isolated from mice carrying this nonsense mutation showed swollen ER and

a disrupted Golgi architecture. Patient fibroblasts with either a heterozygous or homozygous nonsense variant of GMAP-210 showed incomplete glycosylation of the model secretory protein vesicular stomatitis virus G protein (VSVG) fused to GFP, suggesting a function of GMAP-210 in trafficking. These mutant cells also showed increased lectin GS-II binding along cell surfaces, indicating a defect in glycosylation due to GMAP-210 loss-of-function, as lectin GS-II binds to terminal non-reducing N-acetyl-D-glucosamine, which is normally not present in fully processed glycoproteins<sup>136</sup>. Hypomorphic mutations, or partial loss-of-function mutations, in *TRIP11* cause a different genetic disorder called odontochondrodysplasia (ODCD)<sup>139</sup>, affecting skeletal and dental development. In contrast to the loss-of-function mutations in *TRIP11*, secretion is not affected in ODCD. Glycans on the lysosomal glycoprotein LAMP2 and the extracellular matrix protein decorin were both abnormal, and synthesis of extracellular matrix proteins was strongly reduced, leading to disease<sup>139</sup>.

Other Golgins also regulate glycosylation, but have not been associated with CDGs. An intronic splice donor site mutation in the gene coding for Golgin giantin (Figure 2.3, also known as GOLGB1) produces a truncated protein, which causes cleft palate in mice, with murine embryos showing an increase in GS-II lectin binding to terminal GlcNAc moieties within the palatal regions, which is indicative of incomplete protein glycosylation. In parallel, frontal sections of developing palatal shelves of giantin loss-of-function mutant mice show increased binding of PNA lectin after desialylation with neuraminidase, showing an increase in galactosylated O-type mucins on the cell surface<sup>140</sup>. In addition to giantin, certain membrane tethering proteins, such as giantin, GRASP55, and GRASP65 (Figure 2.3), are thought to regulate the rate of retrograde trafficking, likely to assure efficient recycling of glycosylation enzymes to their target Golgi compartment. RNA interference-mediated depletion of giantin in HeLa cells revealed that this causes aberrant fusion of Golgi cisternae<sup>141</sup>. This, in turn, caused a two-fold increase in the mobility of the glycosylation enzyme ManII as measured by fluorescence recovery after photobleaching and accelerated the trafficking of VSVG to the plasma membrane<sup>142</sup>. Furthermore, siRNA depletion of giantin caused overexpression of sialylated glycoproteins at the cell surface<sup>142</sup>. Moreover, depletion by RNA interference of GRASP55/65 accelerated the anterograde trafficking of VSVG, independent of ER stress and unconventional protein secretion, and concurrently decreased the complete glycosylation of VSVG<sup>143</sup>.

More recently, several missense and nonsense mutations in *GORAB* have been identified in patients (Figure 2.3). Although *GORAB* was previously described to be a Golgin, it is now understood that it is a COPI vesicle coat scaffolding protein that likely engages in vesicle formation and has been associated with the development of the skin and bone disorder geroderma osteodysplastica (GO)<sup>144–147</sup>. GO presents with osteoporosis and has a similar elastin deficiency as cutis laxa<sup>148,149</sup>. Importantly, patients have deficient glycosylation of proteoglycans including decorin and biglycan, leading to their pathologies. *GORAB* is primarily functional at late stages of intra-Golgi trafficking. *GORAB* promotes COPI recruitment to the *trans*-Golgi through the formation of stable membrane domains. *GORAB* also scaffolds the catalytically inactive protein kinase Scyl1<sup>144</sup>. Scyl1 localizes to the ERGIC and *cis*-Golgi budding sites and binds to COPI coats using a C-terminal RKLD sequence, similar to the KKXX COPI-binding motif present in ER transmembrane proteins. The depletion of Scyl1 in HeLa cells by RNA interference dis-

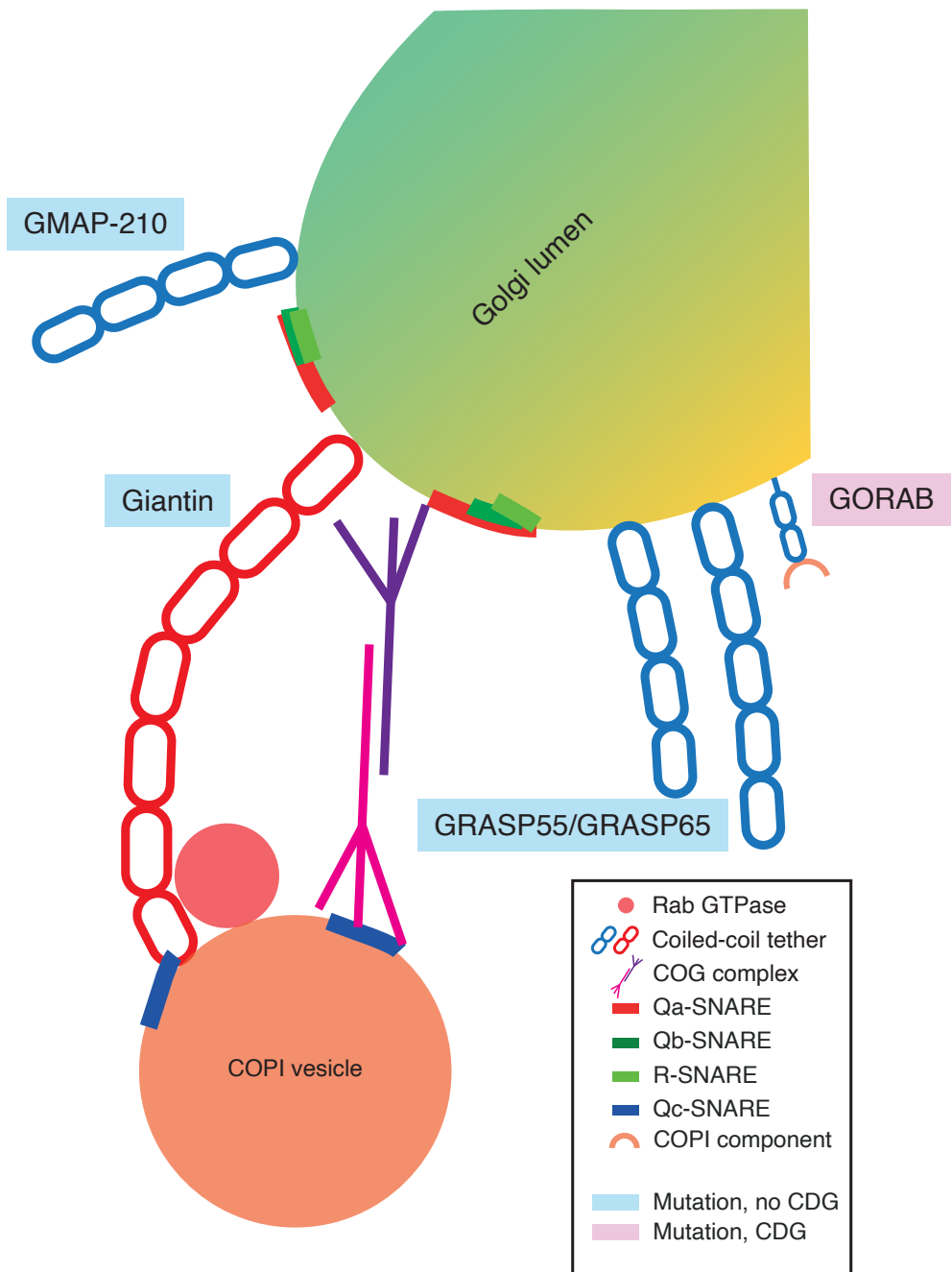


**Figure 2.3: Schematic overview of COPI vesicle capture by coiled-coil tethering proteins at the Golgi.** Tentacular coiled-coil proteins attached to the Golgi membrane can capture COPI vesicles to direct them to the Golgi. Abbreviations: CDG, congenital disorder of glycosylation; COG complex, conserved oligomeric Golgi complex; COPI, coat protein complex I; SNARE, soluble N-ethylmaleimide-sensitive factor attachment protein receptor.

rupts COPI-mediated retrograde trafficking of the KDEL receptor towards the ER<sup>150</sup>. Several missense and nonsense mutations in *SCYL1* have been described, but, in contrast to GORAB, primarily hepatological and neurological phenotypes were observed<sup>151–153</sup>. Cellular investigations of patient fibroblasts show an enlarged Golgi morphology as shown by immunofluorescence and impaired retrograde trafficking when perturbed with BFA<sup>151</sup>. Most interestingly, one patient demonstrated hyposialylation of both transferrin and apolipoprotein CIII as measured by isoelectric focusing (IEF) during a liver crisis, but this returned to normal after the crisis had passed<sup>151</sup>. An explanation for this might be that the secretory burden of glycoproteins in this patient was too high during the crisis, leading to abnormal glycosylation. Pathogenic variants in GORAB either affect the binding affinity of GORAB to Scyl1 or affect the assembly of GORAB in membrane domains, leading to the dysfunction of GORAB. Loss-of-function mutations in *GORAB* inhibit the retrieval of trans-Golgi resident enzyme ST6GAL1 in a COPI-mediated manner, demonstrating the necessity of GORAB for COPI-mediated intra-Golgi trafficking. Concurrently, *GORAB* mutant fibroblasts from GO patients show a reduced abundance of complex terminally sialylated glycans, suggesting deficient glycosylation by dysfunctional GORAB<sup>144</sup>. Taken together, the observed phenotypes suggest that GORAB mutations can be considered CDGs.

Once a vesicle has been captured by a Golgin, effectors such as Rab GTPases are recruited (Figure 2.3). Rabs exist in a GDP-bound inactive state and are activated by the exchange for GTP through guanine nucleotide exchange factors (GEFs). This nucleotide exchange results in a conformation switch, which enables Rabs to recruit specific effectors required for vesicular trafficking. Genetic variants within Rab proteins are associated with several neurological and metabolic disorders, including Parkinson's disease and Neumann–Pick's disease<sup>154</sup>. Certain Rabs play an active role in retrograde Golgi trafficking, such as Rab6, which is required for bidirectional transport of cargo at the Golgi<sup>87</sup>. Furthermore, Rab2 can influence the function of GMAP-210 in COPI vesicle tethering<sup>138</sup>, while Rab1, Rab2, Rab4, and Rab6 can interact with members of the COG complex and thereby tether COPI vesicles to the Golgi membrane<sup>155</sup>. Rab1, in particular, has also been identified to regulate the Golgi architecture and function and therefore has an indispensable role in glycosylation<sup>154</sup>. While genetic variants in Rabs or their regulatory proteins have not been implicated in CDGs thus far, it is conceivable that Rab dysfunction alters the identity of COPI vesicles, which results in the mislocalization of glycosylation enzymes. Thus, considering the potential effects of Rab dysfunction on glycosylation, it stands to reason that Rab CDGs are yet to be identified.

### 2.3.3 Conserved oligomeric Golgi Tethering Complex

After Golgins mediate the capture of Golgi-destined vesicles from the cytosol, the COG complex functions as a tether to anchor COPI vesicles to the Golgi membrane<sup>156–158</sup>. COG subunits have been described to interact directly with COPI coat components, as well as with SNARES and Rab GTPases involved in Golgi trafficking<sup>91,159–164</sup>. Despite the lack of transmembrane domains in COG subunits, they are membrane-associated proteins. The COG complex is a hetero-octameric protein complex, consisting of eight unique subunits COG1–8 (Figure 2.4). These subunits organize themselves into two distinct lobes: lobe A consisting of COG1–4 and lobe B consisting

of COG5-8. This in turn also dictates their localization: lobe A is primarily present on the Golgi membrane, while lobe B localizes to COPI vesicles<sup>164</sup>. The two lobes are bridged by an interaction between COG1 and COG8 through the formation of alpha-helical bundles<sup>91,159</sup>. The COG complex is therefore required for the trafficking of glycosyltransferases and cargo proteins.

Cellular models of COG-subunit deficiencies show an alteration in glycosylation homeostasis<sup>165</sup>. At a cellular level, the depletion of COG subunits 2, 3, 4, 6, 7, and 8 causes the mislocalization of glycosylation enzymes MAN2A1, MGAT1, B4GALT1, and ST6GAL1 to COG complex-dependent vesicles<sup>166,167</sup>, demonstrating their necessity in functional glycosylation<sup>168</sup>. Studies in HeLa cells depleted of COG4 by RNA interference also demonstrated glycosylation defects and the mislocalization of vesicles containing COG-interacting proteins (GEARS) around the Golgi<sup>157,159,167</sup>. Of note, the permanent membrane targeting of COG subunits 4, 7, and 8 by fusing them to the transmembrane protein TMEM115<sup>169</sup> disrupts the ribbon structure of the Golgi as visualized by electron microscopy, causing the swelling of cisternae and an increase of spherical, non-cisternal elements<sup>170</sup>. Nevertheless, membrane-anchoring of COG4 and COG7, but not COG8, rescued the glycosylation defects observed in their respective CRISPR/Cas9 knockout cell models. The N-terminal attachment of membrane-anchored COG8 interfered with overall COG structure and function, impeding the rescue of the observed glycosylation defects<sup>170</sup>. The permanent Golgi anchoring of COG4 and 7 maintains the polarization of *cis*- and *trans*-Golgi markers, but fails to restore a highly organized Golgi structure in COG4 and 7 knockout cells. These data demonstrate that the membrane association of most COG subunits is imperative for their function, and likely assists in the correct retrieval of glycosyltransferases to earlier Golgi cisternae.

Genetic variants causing CDGs have been identified for all COG subunits, except for COG3<sup>159,168,171</sup>. Most genetic variants in COG subunits are observed in lobe A subunits COG1 and COG4 and in lobe B subunit COG8 (Figure 4). While in most CDGs, N-glycosylation is mostly affected, COG-CDGs show a broader phenotype with defects in both N- and O-glycan biosynthesis<sup>168</sup>. Clinically, patients of COG-CDGs present with prominent incomplete galactosylation and sialylation<sup>168,172</sup>, and this is true for variants in both lobe A and B subunits. While the variants mostly consist of missense mutations or truncations for lobe A subunits and full loss-of-function mutations in lobe B subunits, glycan profiles of patients show the same hypogalactosylation and hyposialylation for both types of mutations<sup>173,174</sup>. This raises the question of whether mutations in one COG subunit affect the entire COG complex. Indeed, a variant in one COG subunit is associated with the instability of another subunit within that lobe, leading to the decrease in protein expression of subunits in the same lobe<sup>175</sup>. This has been shown for COG1<sup>172</sup> and COG2<sup>171</sup> in lobe A and COG6, COG7<sup>176,177</sup>, and COG8<sup>178</sup> for lobe B. Moreover, the mutations in COG1 are associated with a decrease in protein levels of COG8<sup>172</sup>. Oppositely, a truncation mutant of COG8 also decreases the protein levels of COG1<sup>179</sup>. The finding that all eight subunits are required for complete COG function is a possible explanation for the similarity in glycan profiles of COG-CDGs (see below). However, COG1- and COG4-CDG phenotypes are relatively mild, while COG7- and COG8-CDG are much more severe. This could indicate a differential necessity of COG lobe B over lobe A.

COG-CDGs have mainly been implicated through genetic variants of COG1 and COG4 for lobe

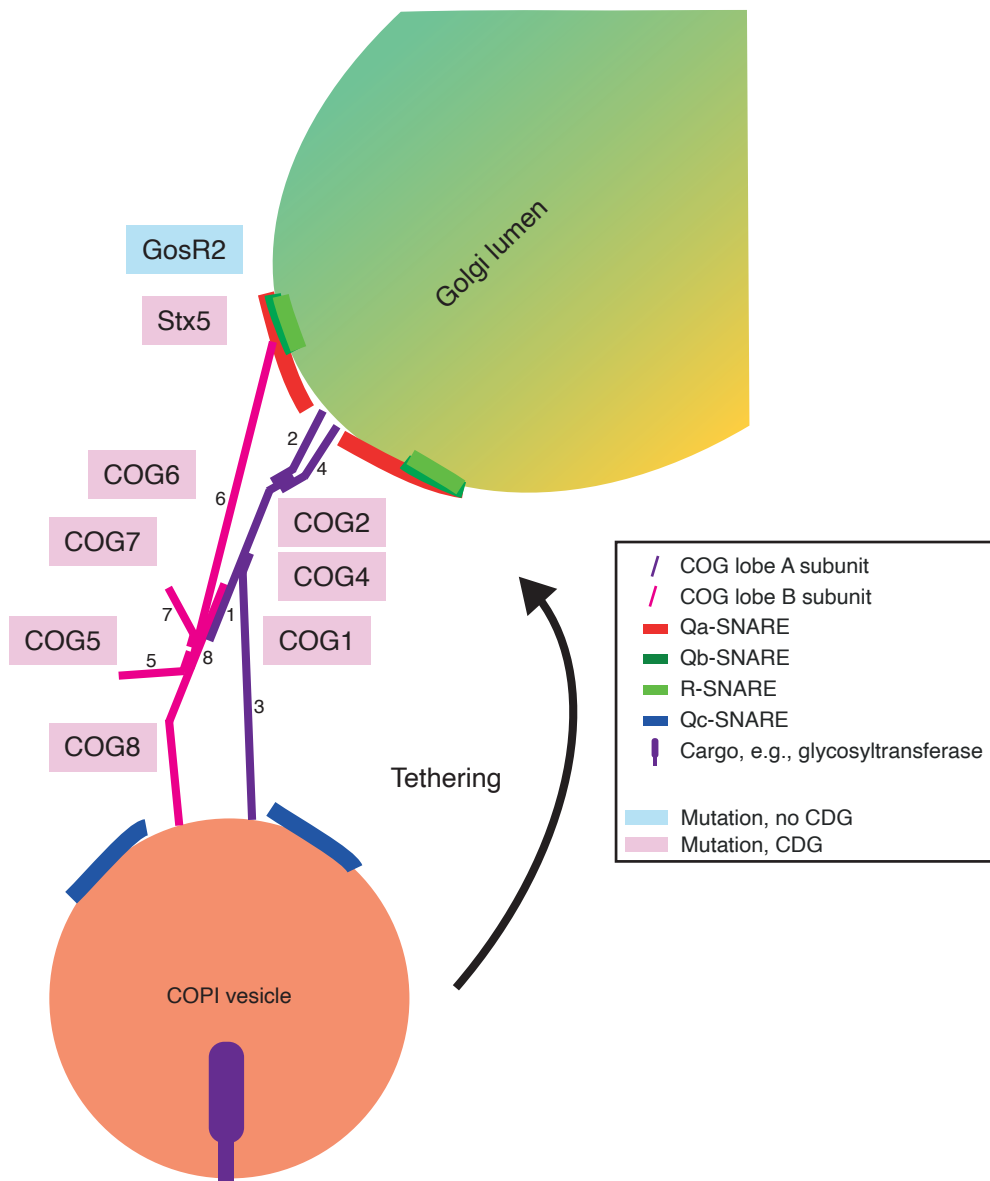


**Figure 2.4: Schematic overview of COG-mediated vesicle tethering and SNARE-mediated vesicle fusion at the Golgi.** COPI vesicles are tethered to the Golgi membrane through the interaction of COG lobes A and B. Subsequently, SNARE-mediated membrane fusion occurs, and the vesicle cargo is released to the Golgi lumen. Abbreviations: CDG, congenital disorder of glycosylation; COG complex, conserved oligomeric Golgi complex; COPI, coat protein I; SNARE, soluble N-ethylmaleimide-sensitive factor attachment protein receptor.

A. Patients with an 80 residue C-terminal truncation of COG1 present with a reduction of galactose and sialic acid moieties on N- and O-glycans. Consistent with this, fibroblasts isolated from these patients demonstrate a reduction of sialic acid incorporation on mucin-type O-glycans<sup>172</sup>. A different variant, an intronic mutation that results in a frameshift and a premature stop codon in exon 7, in *COG1* causes skeletal defects and mental retardation, together with hypogalactosylation and hyposialylation<sup>180</sup>. Moreover, the Brefeldin A assay performed on these patient fibroblasts revealed a retrograde Golgi trafficking defect. In CHO cells, depletion of COG1 by RNA interference leads to both deficient N- and O-glycosylation<sup>157,159</sup>. Fibroblasts from a patient with two heterozygous missense and nonsense mutations, respectively, in *COG4* also showed hypogalactosylation and hyposialylation<sup>181,182</sup>. Effects of these variants on other COG subunits were not investigated. Moreover, a patient with a different missense mutation in *COG4* presented with a similar glycosylation defect, but the instability of the other subunits in COG lobe A was also observed, likely due to the inability to form COG subcomplexes<sup>183</sup>. Lastly, another amino acid substitution in *COG4* was identified causing a rare form of primordial dwarfism, but patients notably have normal glycosylation of serum proteins<sup>184</sup>. Instead, the extracellular matrix protein decorin is abnormally glycated in these patients, underlying their pathology.

To date, only a single mutation, an intronic mutation leading to a decrease in *COG5* expression, has been identified in the gene coding for COG lobe B subunit COG5 with mostly neurological symptoms and similar hypogalactosylation and hyposialylation like in other COG defects<sup>173,185–187</sup>. Several studies have shown that a single missense mutation in *COG6* leads to severe neurological and hepatological symptoms and can lead to infant mortality<sup>188–190</sup>. The relative severity of COG6-CDG is likely due to the observed instability of COG lobe B, as COG6-CDG patients also have lower protein levels of COG5 and COG7. Furthermore, decreased levels of the *trans*-Golgi SNARE syntaxin-6 were detected, suggesting that stabilization of syntaxin-6 via the COG complex is necessary for its function<sup>190</sup>. Intronic mutations affecting the mRNA splicing and ultimately causing the decrease of protein levels of COG7 cause similar glycosylation defects, with patients presenting hyposialylation in their N- and O-linked glycan biosynthesis<sup>176,177,191</sup>. Another study observed that one specific variant in *COG7*, which is associated with infantile mortality<sup>192</sup>, causes a loss of sialylation on serum transferrin and on cell surface proteins of patient fibroblasts<sup>193</sup>. Moreover, this variant in *COG7* affects Golgi trafficking as shown by the impaired trafficking of ST3GAL1 from the ER to the *trans*-Golgi in patient fibroblasts. A homozygous nonsense mutation in *COG8* results in the formation of a truncated COG8 subunit, lacking 76 C-terminal residues, affecting the interaction between COG8 and COG1. Patients with this variant present with mild hyposialylation<sup>179</sup>. Similarly, a patient with a different genetic variant resulting in the truncation of COG8 with the loss of 47 C-terminal residues showed a similar deficiency in sialylation<sup>178</sup>. COG8-CDG patients present with a severe neurological phenotype and display a fragmented Golgi apparatus in patient fibroblasts. Overall, the COG defects demonstrate the importance of efficient tethering of intra-Golgi vesicles and show that even small changes are enough to destabilize the COG complex, thereby severely affecting glycosylation.

### 2.3.4 SNAREs

The final step in the delivery of glycosylation enzymes to the Golgi is SNARE-mediated membrane fusion. SNARE proteins are classified by the central residue in their SNARE motif: R-SNAREs have a central arginine residue, while Qa-, Qb-, Qbc-, and Qc-SNAREs have a central glutamine residue. A tight alpha-helical coiled-coil bundle is formed by one of each type of SNARE motif, provided by three or four cognate SNARE proteins. These are present on both the vesicular (e.g., COPI vesicle) and target membranes (e.g., *cis*-Golgi), and the coiled-coil formation provides enough energy to fuse the two opposing membranes<sup>57,58</sup>. At the mammalian ER-Golgi interface, four distinct SNARE complexes exist: Stx5 / GosR2 (also known as GS27 or membrin) / Bet1 / Sec22b (also known as ERS24) for anterograde transport from ER to ERGIC, Stx5 / GosR1 / Bet1 / Ykt6 for anterograde transport from ERGIC to *cis*-Golgi, Stx5 / GosR1 (also known as GS28) / Bet1L (also known as GS15) / Ykt6 for retrograde intra-Golgi transport, and Stx18 / Sec20 / Use1 / Sec22b for retrograde transport from *cis*-Golgi to ER<sup>21,118,194–207</sup>. While in general, R-SNAREs are present on the vesicular membrane in eukaryotic cells<sup>57</sup>, evidence suggests that the Qc-SNAREs Bet1 and Bet1L function as the vesicular SNAREs at the ER-Golgi interface<sup>21,204,207–210</sup>. This observation, together with the necessity of Sec1/Munc18 SM protein Scfd1 in ER-Golgi SNARE fusion, likely implies specificity to the fusogenic SNARE complex, by inhibiting the formation of non-functional SNARE complexes<sup>63,211–214</sup>.

Despite the essential role of SNAREs in Golgi trafficking<sup>21</sup>, there is only limited evidence for a clinical link between glycosylation and genetic variants in SNARE proteins. This also raises the question of whether SNARE CDGs mostly remain undetected due to a possible severity of the disease. Contrary to plasma membrane-localized SNARE complexes, ER-Golgi-localized SNARE complexes lack redundancy, and the loss of a single SNARE protein at this interface might result in detrimental effects for glycosylation and/or life<sup>118</sup>. Recently, the first CDG related to a SNARE protein was identified, namely a point mutation in *STX5*, the gene coding for the Qa-SNARE syntaxin-5<sup>207</sup>. In animals, the *STX5* gene is transcribed to one mRNA, which produces two different isoforms of Stx5 via an alternative starting codon: 39.6 kDa sized Stx5 Long (Stx5L) and 34.1 kDa sized Stx5 Short (Stx5S)<sup>21,215</sup>. Stx5L is characterized by a 54 residue N-terminal extension with an RKR (arginine-lysine-arginine) ER-retrieval motif and localizes at ER, ERGIC, and *cis*-Golgi. In contrast, Stx5S lacks this RKR ER-retrieval motif and primarily localizes to the Golgi (Figure 2.4). The point mutation causes the specific loss of Stx5S through the mutation of the second starting methionine residue into valine. This loss of the intra-Golgi dominant Qa-SNARE Stx5S results in a severe disorder, characterized by metabolic and developmental defects and infantile mortality. Microscopy revealed that this is caused by the mislocalization of glycosylation enzymes to the wrong compartment in the Golgi apparatus, leading to the reduced incorporation of galactose and sialic acid moieties in N-glycans and an overrepresentation of immature high-mannose glycans<sup>207</sup>.

The Qbc-SNARE SNAP29 has previously also been ascribed a role in Golgi morphology, and its dysfunction could likely result in glycosylation defects<sup>216</sup>. Of note, several missense and truncating mutations in *SNAP29* have been associated with cerebral dysgenesis, neuropathy, ichthyosis, and keratoderma syndrome (CEDNIK, a disorder of brain development, facial dys-

morphism, and skin), and Pelizaeus–Merzbacher-like disorder (PMLD, a disorder of brain development and muscle function)<sup>217–223</sup>. The first report of *SNAP29* involvement in CEDNIK noted that no N- and O-glycosylation defects were observed, although the authors did not describe how the patients were screened<sup>222</sup>. This result does not exclude that *SNAP29* is involved in glycosylation, as, assuming that custom IEF methods were applied for CDG screening, it is possible that although glycosylation of either transferrin or apolipoprotein CIII were not affected, other glycosylated proteins were. Additionally, these methods might not have been sensitive enough to detect an underlying glycosylation disorder, or only glycosylation in certain tissues could have been affected. Finally, fusion-impaired forms of *GosR2* result in a neurological phenotype in patients with progressive myoclonus epilepsy, but have not been associated with glycosylation defects (Figure 2.4)<sup>224–226</sup>. It is possible that during these studies, no diagnostics for glycosylation has been performed or that through a compensatory mechanism, sufficient glycosylation was maintained. Along these lines, more comprehensive diagnostic screening procedures might implicate more SNAREs in CDGs.

## 2.4 Discussion and Conclusions

The glycosylation process is an essential part of the secretory pathway and is a complex logistic system. Newly synthesized glycoproteins are shuttled from the ER to the Golgi apparatus, which acts as a production line that sequentially builds complex branched glycan structures on the proteins. Moreover, the Golgi can be considered a distribution center that ensures that glycoproteins are modified and sorted correctly to their final destinations. As with factories and other logistic systems, having efficient infrastructure is the key to a high efficiency and fidelity of production and delivery. Each organelle in the logistic chain needs to function optimally to avoid bottlenecks, and therefore, efficient coordination amongst organelles is of utmost importance. Here, we discussed how dysfunctional transport processes affect glycosylation and, in turn, cause a wide array of symptoms including skin and bone disorders, impaired liver function, and even infantile mortality. Mechanistically, these pathologies are the result of impaired pH homeostasis in the Golgi, incorrect tethering of Golgi-destined vesicles, and defective membrane fusion at the Golgi apparatus (Table 1).

In this review, we discussed pathogenic variants in the V-ATPase and associated proteins that affect Golgi pH homeostasis and glycosylation. Considering that glycosylation enzymes have a broad pH optimum and that the Golgi has a narrow range in pH (pH 6.7 for *cis* to pH 6.0 for *trans*), it seems unlikely that small defects in pH homeostasis result in a pronounced loss of catalytic activity of the glycosylation enzymes. Instead, the prevailing theory is that pH affects the trafficking of glycosylation enzymes to their cognate Golgi compartments and that altering the Golgi pH results in mislocalization of these enzymes to the wrong compartment<sup>31–33</sup>. This is corroborated by the observation that Golgi-to-ER recycling mediated by the KDEL receptor is indeed pH-dependent<sup>27</sup> and by the observation that the ER-Golgi SNARE protein Bos1p is absent from COPII vesicles of yeast strains lacking the V-ATPase assembly factor Vma21p<sup>119</sup>. Moreover, it has been described that the luminal pH affects the oligomerization of certain glycosylation enzymes and thereby also influences their localization<sup>227–234</sup>. Another well-characterized example of pH-mediated protein sorting is the binding of the mannose-6-phosphate receptor to the mannose-6-phosphate-labeled cargo destined for the lysosome. Proteins are bound by this receptor in the Golgi and subsequently released in the more acidic environment of late endosomes<sup>29,235,236</sup>. Finally, the pH of the TGN is also important for the correct sorting of the extracellular matrix components laminin and heparan sulfate proteoglycan to the basolateral surface of polarized epithelial cells<sup>35,235,237</sup>. Taken together, evidence shows that homeostasis of pH is of crucial importance for trafficking within, from, and to the Golgi apparatus, and thereby likely a critical factor for glycosylation. This also implicates that mislocalization of the V-ATPase and associated proteins due to pathogenic mutations in trafficking proteins such as SNAREs, COG subunits, or Golgins can affect glycosylation.

Interestingly, except for Stx5-CDG, all described CDGs in trafficking proteins primarily demonstrate defects in late glycan modifications such as galactosylation and sialylation (Table 2.1). Only in Stx5-CDG, the accumulation of an early-stage high mannose glycan is observed. Why could defects in early glycosylation steps be underrepresented? We can consider several hypotheses. First, correct glycosylation is of absolute importance for development<sup>7,10</sup>, and despite

the redundancy in glycosylation enzymes, defects affecting early glycosylation reactions might not be conducive to further development. Therefore, potential pathogenic mutations might remain undetected as they are non-viable. Second, as disorders of glycosylation are mostly a secondary effect of trafficking defects, glycosylation disorders might go undiagnosed as they simply have not been screened for in potential cases such as for *GOSR2* mutations<sup>225,226</sup>. Last, early glycosylation defects might go undiagnosed because common biochemical techniques to measure glycosylation in a clinical setting, such as isoelectric focusing of transferrin and apolipoprotein CII<sup>238</sup>, mostly interrogate late glycosylation reactions such as sialylation. Modern advances in clinical diagnostics have added mass spectrometry of intact transferrin<sup>7</sup> and glycomics on total plasma N-glycans<sup>174</sup>. These two approaches have enabled measuring all N-glycan structures on circulating serum proteins, thereby giving a more complete view of the glycosylation defects. This allows clinicians and scientists to identify more complex glycosylation disorders, including those in trafficking factors. Future advances to glycosylation screening might include measuring the glycome of all different tissues in the human body or measuring site-specific glycosylation on a large array of proteins. Understanding trafficking and glycosylation in different cellular contexts will ultimately further our knowledge of glycobiology and eventually increase therapeutic options for patients suffering from CDGs. A subcellular understanding of CDG can pave the road for targeted therapies through, for instance, gene replacement of affected genes or the development of small molecules to modulate ER-to-Golgi and intra-Golgi transport.

#### 2.4.1 Author Contributions

All authors contributed to the conceptualization and writing of the manuscript.

#### 2.4.2 Funding

G.v.d.B. is funded by a Young Investigator Grant from the Human Frontier Science Program (HFSP; RGY0080/2018) and a Vidi grant from the Netherlands Organisation for Scientific Research (NWO-ALW VIDI 864.14.001). G.v.d.B has received funding from the European Research Council (ERC) under the European Union's Horizon 2020 research and innovation program (Grant Agreement No. 862137). D.J.L. is funded by a Vidi grant (ZONMW VIDI 917.13.359), a ZONMW Medium Investment Grant (40-00506-98-9001) from the Netherlands Organisation for Scientific Research, and Erare grants EUROCDG2 and Euroglycanomics.

#### 2.4.3 Conflicts of Interest

The authors declare no conflict of interest.

## 2.5 Supplementary Information

**Table 2.1:** Overview of membrane trafficking-related CDGs and their phenotypes.

Gene	Mutation	CDG <sup>a</sup>	Clinical Phenotype <sup>b</sup>	N-Glycosylation <sup>c</sup>	Man	GlcNAc Gal	Sia	O-Glycosylation <sup>c</sup>	Screening <sup>d</sup>	References
ATP6VOA2	V66fsX107	X	+	-	=	=	-	-	IEF, IMS	77
ATP6VOA2	T643fsX683	X	+	-	=	=	-	-	IEF	77
ATP6VOA2	Q765X	X	+	-	-	-	-	-	IEF, IMS	77
ATP6VOA2	R63X	X	++	-	-	-	-	-	IEF, IMS	77/239
ATP6VOA2	K117fsX144	X	++	-	-	-	-	-	IEF, IMS	77/239
ATP6VOA2	n.d.	X	++	-	-	-	-	-	IEF, IMS	77/239
ATP6VOA2	D243fsX258 and E442fsX506	X	++	-	-	-	-	-	IEF, IMS	77
ATP6VOA2	T280fsX285	X	+++	-	-	-	-	-	IEF, IMS	77
ATP6VOA2	E442X	X	+++	-	-	-	-	-	IEF, IMS	77
ATP6AP1	M428I	X	+	-	-	-	-	-	IEF, IMS	112
ATP6AP1	L144P	X	+	-	-	-	-	-	IEF, IMS	112
ATP6AP1	E346K	X	++	-	-	-	-	-	IEF, IMS	112
ATP6AP1	Y313C	X	++	-	-	-	-	-	IEF, IMS	112
ATP6AP2	L98S	X	++	-	-	-	-	-	CZE, IEF, IMS	113
ATP6AP2	L98S	X	+	-	-	-	-	-	CZE, IEF, IMS	113
ATP6AP2	R71H	X	++	-	-	-	-	-	CZE, IEF, IMS	113
VMA21	n.d. <sup>1</sup>	X	+	-	-	-	-	-	IEF, IMS	117
VMA21	R18G*	X	+	-	-	-	-	-	IEF, IMS	117
VMA21	N63G	X	+	-	-	-	-	-	IEF, IMS	117
TMEM199	A7E	X	+	-	-	-	-	-	IEF, IMS	121
TMEM199	A14P	X	+	-	-	-	-	-	IEF, IMS	121
TMEM199	R31P	X	+	-	-	-	-	-	IEF, IMS	121
CCDC115	L31S	X	++	-	-	-	-	-	IEF, IMS	120
CCDC115	D11Y	X	++	-	-	-	-	-	IEF, IMS	120
TMEM165	n.d. <sup>2</sup>	X	++	-	-	-	-	-	IEF, ILS	130
TMEM165	R126C	X	++	-	-	-	-	-	IEF, ILS	130
TMEM165	R126C and G304R	X	+	-	-	-	-	-	IEF, ILS	130



Gene	Mutation	CDG <sup>a</sup>	Clinical phenotype <sup>b</sup>	N-Glycosylation <sup>c</sup>	Man	GlcNAc	Gal	Sia	O-Glycosylation <sup>c</sup>	Screening <sup>d</sup>	References
<i>SCYL1</i>	A504PfsX15 and Q546X	-	+	n.d.	n.d.	n.d.	n.d.	n.d.	n.d.	n.d.	153
<i>SCYL1</i>	Q57X	-	+	n.d.	n.d.	n.d.	n.d.	n.d.	n.d.	n.d.	151
<i>SCYL1</i>	E96X	-	+	n.d.	n.d.	n.d.	n.d.	n.d.	n.d.	n.d.	151
<i>SCYL1</i>	A105V	-	+	n.d.	n.d.	n.d.	n.d.	n.d.	n.d.	n.d.	151
<i>SCYL1</i>	V313GfsX6 and Q347X	-	+	n.d.	n.d.	n.d.	n.d.	n.d.	n.d.	n.d.	151
<i>SCYL1</i>	n.d. <sup>4</sup>	-	+	n.d.	n.d.	n.d.	n.d.	n.d.	n.d.	n.d.	151
<i>SCYL1</i>	D478G	-	+	n.d.	n.d.	n.d.	n.d.	n.d.	n.d.	n.d.	151
<i>SCYL1</i>	A504PfsX15	-	+	n.d.	n.d.	n.d.	n.d.	n.d.	n.d.	n.d.	151
<i>SCYL1</i>	Q546X	-	+	n.d.	n.d.	n.d.	n.d.	n.d.	n.d.	n.d.	151
<i>SCYL1</i>	Q628X	-	+	n.d.	n.d.	n.d.	n.d.	n.d.	n.d.	n.d.	151
<i>COGI</i>	900X	X	++	-	=	=	-	-	-	IEF, MS, L	172
<i>COGI</i>	n.d. <sup>4</sup>	X	++	-	=	=	-	-	-	IEF, MS	180
<i>COG2</i>	Y234X and W634G	X	+++	-	=	=	-	-	n.d.	IEF, MS	171
<i>COG4</i>	L773R	X	++	-	=	=	-	-	-	IEF, HPLC, MS	181,182
<i>COG4</i>	E233X	X	++	-	=	=	-	-	-	IEF, HPLC, MS	181,182
<i>COG4</i>	R729W	X	++	-	=	=	-	-	-	IEF, MS	183
<i>COG4</i>	G516R	X	++	-	=	=	-	-	-	MS	184
<i>COG5</i>	n.d. <sup>4</sup>	X	+/-	-	+	+	-	-	-	IEF, MS	173,185-187
<i>COG6</i>	G549V	X	+++	-	-	-	-	-	-	IEF, HPLC, MS	188-190,241
<i>COG7</i>	n.d. <sup>4</sup>	X	+++	-	-	-	-	-	-	IEF, L	176,177,192,193
<i>COG7</i>	n.d. <sup>4</sup>	X	+++	-	-	-	-	-	-	IEF, MS	191
<i>COG8</i>	Y537X	X	++	-	-	-	-	-	-	IEF, MS, L	179
<i>COG8</i>	F563HfsX4	X	++	-	-	-	-	-	-	MS, L	178
<i>STK5</i>	M55V	X	+++	-	-	-	-	-	-	IEF, MS, L	207

Gene	Mutation	CDG <sup>a</sup>	Clinical phenotype <sup>b</sup>	N-Glycosylation <sup>c</sup>	Man	GlcNAc Gal	Sia	O-Glycosylation <sup>c</sup>	Screening <sup>d</sup>	References
SNAP29	R29X	-	++	n.d.	=	=	=	n.d.	n.d.	217
SNAP29	L119AfsX15 and n.d. <sup>4</sup>	-	++	n.d.	=	=	=	n.d.	n.d.	218
SNAP29	R85X	-	++	n.d.	=	=	=	n.d.	n.d.	219
SNAP29	T130fsX17	-	++	n.d.	=	=	=	n.d.	n.d.	220
SNAP29	P10fsX42	-	++	n.d.	=	=	=	n.d.	n.d.	220
SNAP29	R90C	-	++	n.d.	=	=	=	n.d.	n.d.	220
SNAP29	E89K	-	++	n.d.	=	=	=	n.d.	n.d.	220/221
SNAP29	V75fsX28	-	+++	=	=	=	=	=	?	222
SNAP29	S163fsX5	-	++	n.d.	=	=	=	n.d.	n.d.	223
GOSR2	G144W	-	++	n.d.	n.d.	n.d.	n.d.	n.d.	n.d.	225/226
GOSR2	K164del	-	+	n.d.	n.d.	n.d.	n.d.	n.d.	n.d.	225

<sup>a</sup> X, confirmed congenital disorder of glycosylation; -, unconfirmed congenital disorder of glycosylation. <sup>b</sup> Severity of clinical symptoms. +, mild symptoms; ++, moderate symptoms; +++, severe symptoms. <sup>c</sup> Severity of glycosylation phenotype. ---, strong decrease; --, moderate decrease; -, mild decrease; =, no change; +, mild increase; ++, moderate increase; +++, strong increase. <sup>d</sup> CZE, capillary zone electrophoresis; IEF, isoelectric focusing; HPLC, high-performance liquid chromatography; MS, mass spectrometry; L, lectin staining. <sup>1</sup> New ATG start codon upstream of first exon, causing a frameshift and premature stop codon at c.26-28. <sup>2</sup> Cryptic splice donor site activation. <sup>3</sup> Intronic splice donor site; causes S793F in ITGB5. <sup>4</sup> Intronic splice site.





P.T.A. Linders, M. ter Beest, and G. van den Bogaart  
*BioRxiv* 2021.03.29.437519

# 3

Fluorescence lifetime imaging of pH  
along the secretory pathway

### 3.1 Abstract

Many cellular processes are dependent on correct pH levels, and this is especially important for the secretory pathway. Defects in pH homeostasis in distinct organelles cause a wide range of diseases, including disorders of glycosylation and lysosomal storage diseases. Ratiometric imaging of the pH-sensitive mutant of green fluorescent protein (GFP), pHLuorin, has allowed for targeted pH measurements in various organelles, but the required sequential image acquisition is intrinsically slow and therefore the temporal resolution is unsuitable to follow the rapid transit of cargo between organelles. We therefore applied fluorescence lifetime imaging microscopy (FLIM) to measure intraorganellar pH with just a single excitation wavelength. We first validated this method by confirming the pH in multiple compartments along the secretory pathway. Then, we analyze the dynamic pH changes within cells treated with Brefeldin A, a COPI coat inhibitor. Finally, we followed the pH changes of newly-synthesized molecules of the inflammatory cytokine tumor necrosis factor (TNF)- $\alpha$  while it was in transit from the endoplasmic reticulum via the Golgi to the plasma membrane. The toolbox we present here can be applied to measure intracellular pH with high spatial and temporal resolution, and can be used to assess organellar pH in disease models.

## 3.2 Introduction

Physiological pH homeostasis is crucial for many cellular processes. Not only the cytosolic pH is of importance, but defined intraorganellar pH delineates the secretory pathway. The pH of the endoplasmic reticulum (ER) is approximately 7, while the Golgi apparatus slightly acidifies from pH 6.7 at the *cis* face to pH 6.0 at the *trans* face<sup>22,242,243</sup>. Before secretory cargo is released at the plasma membrane and reaches the neutral pH of the extracellular environment, the pH in secretory vesicles is about 5.2<sup>22,242</sup>.

pH is not only crucial for proper protein folding and enzyme activity through influencing the charge of amino acid side chains, but its importance in secretory protein transport is increasingly clear<sup>13</sup>. pH affects binding affinities of cargo molecules to trafficking chaperones, and thereby pH differences facilitate intracellular transport by both influencing the transit of cargo<sup>61,62,236,237,244–246</sup> and the sorting of secretory pathway resident proteins<sup>27,28,247</sup>. Moreover, the localization of glycosylation enzymes and their substrates is determined by pH<sup>13,32,234,235,248</sup>, and defects in this homeostasis cause a wide range of human disease<sup>13,77,112,113,117,120,121,239</sup>. Being able to accurately determine intraorganellar pH along the secretory pathway is therefore of both fundamental and diagnostic importance.

Fluorescent dyes that allow the measurement of intraorganellar pH exist and are commercially available<sup>249–253</sup>, but the inability of specific organellar targeting is a major drawback. The pH in the lumen of the Golgi and ER in mammalian cells have been measured using Shiga-like toxins covalently bound to fluorescent dyes<sup>254,255</sup> and with the biotin-avidin system<sup>256</sup>. However, especially the development of pH-sensitive mutants of green fluorescent protein (GFP), such as pHLuorin<sup>257,258</sup>, which can be targeted to specific organelles by fusion proteins, have enabled specific measurement of intracellular compartments. Two classes of pHLuorin were developed by mutagenesis which altered the bimodal excitation spectrum of GFP with peaks at 395 and 475 nm<sup>257,259</sup>. First, ecliptic pHLuorin which shows a reduction of its excitation efficiency at 475 nm at pH values lower than 6. Second, ratiometric pHLuorin which shows a gradual increase in the ratio of excitation at 475/395 nm between pH 5.5 and pH 7.5<sup>257</sup>. With ecliptic pHLuorin, intraorganellar pH can be determined by first recording an image at 475 nm excitation, and then correlating the fluorescence intensities with a calibration curve. The pH can be determined with ratiometric pHLuorin using a similar approach, but now by sequentially recording images at 395 and 475 nm. A new version of ratiometric pHLuorin, ratiometric pHLuorin2 (RpHLuorin2) was later developed with 8-fold improved fluorescence<sup>258</sup>.

Ecliptic pHLuorin is less accurate than ratiometric pHLuorin, because the fluorescence intensity not only depends on the pH but also on the concentration of pHLuorin.

However, ratiometric imaging also has several drawbacks, such as sensitivity to background fluorescence leading to high variation in the ratio values and the need for two sequential image acquisitions with two different excitation wavelengths. As the exocytic pathway is highly dynamic, the sequential imaging could potentially result in misalignment of the emitted signal, compromising the calculation of ratio values.

In this study, we exploit fluorescence lifetime, an intrinsic property of fluorophores that is insensitive to changes in laser intensity or protein concentration<sup>260,261</sup> but is sensitive to pH<sup>262,263</sup>, to accurately measure intraorganellar pH with both high spatial and temporal resolution.

### 3.3 Results

#### 3.3.1 FLIM measurements of recombinant ratiometric pHLuorin2

We first measured the fluorescence excitation spectra of recombinant RpHLuorin2 (Supplementary Figure 3.5) in different pH solutions with a fluorescence spectrometer. As expected<sup>257</sup>, we observed strong dependence of the excitation efficiencies on pH, as a higher pH resulted in an increased emission brightness (at 508 nm) at an excitation wavelength of 470 nm, whereas the fluorescence brightness was reduced at an excitation wavelength of 405 nm (Supplementary Figure 3.5a). We then plotted the ratios of the emission signals with 470 nm over 405 nm excitation as a function of the pH and fitted this data with a three-parameter Michaelis-Menten function, as the (de)protonation states of RpHLuorin2 will saturate at very high and low pH values (Supplementary Figure 3.5b). The largest changes in fluorescence of RpHLuorin2 were observed between pH 5.5 and pH 7, making RpHLuorin2 an excellent candidate for pH measurements in the secretory pathway.

As ratiometric determination of pH with RpHLuorin2 requires two sequential image acquisitions with different excitation wavelengths, we investigated whether fluorescence lifetime imaging microscopy (FLIM) would be an appropriate substitute to allow for single-scan imaging. We hypothesized that as the lifetime of fluorophores is influenced by pH<sup>262,263</sup>, the pH sensitivity of RpHLuorin2 would allow for accurate pH measurement based on fluorescence lifetime. Therefore, we performed FLIM of recombinant RpHLuorin2 in different pH solutions at 488 nm excitation (Figure 3.1). We observed a similar dependency of the lifetime as a function of pH (Figure 3.1) as in the ratiometric measurements (Supplementary Figure 3.5), and the fluorescence lifetime increased upon an increasing pH. We then fused RpHLuorin2 to several intraorganellar markers in the secretory pathway to perform pH measurements in living cells.

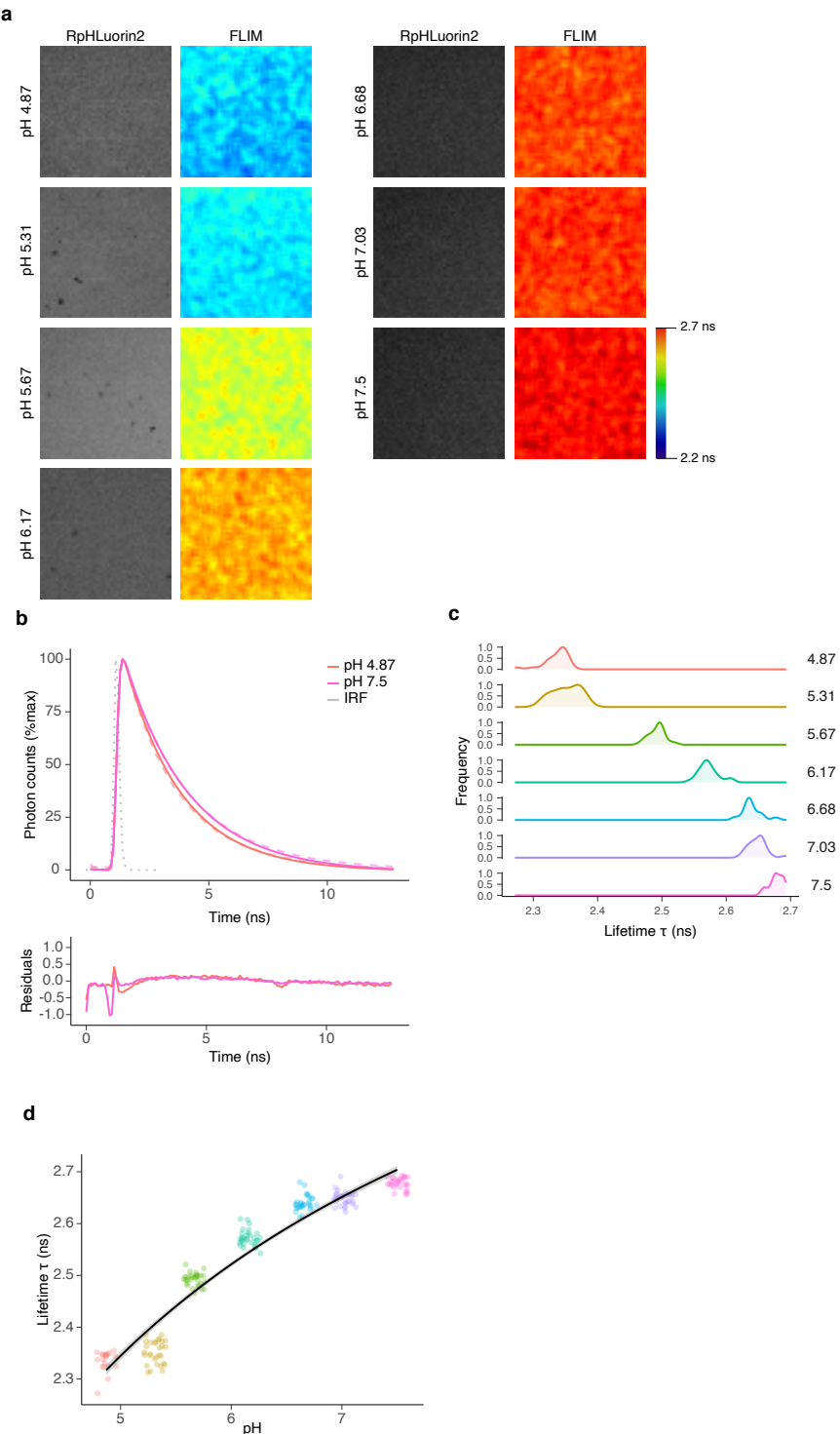


**Figure 3.1: Fluorescence lifetime imaging microscopy (FLIM) of recombinant RpHluorin2. (Continued on the following page.)**

**Figure 3.1:** (a) Representative confocal images of 10  $\mu$ M recombinant RpHluorin2 in calibration buffers with defined pH. The intensity image (left column) was convoluted with the fluorescent lifetime value per pixel and pseudo-colored (right column). (b) Representative fluorescence lifetime histograms of recombinant RpHluorin2 in pH 4.87 solution (red dashed line) or pH 7.5 solution (pink dashed line). Fits with mono-exponential decay functions (pH 4.87, solid red line; pH 7.5, solid pink line) convoluted with the instrumental response function (IRF, gray dotted line). Graphs are normalized to the maximum photon counts. (c) Average lifetime histograms from the images of panel (a). 30 regions of interest were selected per pH buffer and the average lifetime  $\tau$  was measured. (d) pH dependence of recombinant RpHluorin2 in defined pH calibration buffers from the images of panel (a).

### 3.3.2 pH measurements in the secretory pathway

In order to accurately measure intraorganellar pH of specific organelles, we targeted RpHluorin2 intracellularly by fusing it to proteins and targeting sequences that locate to specific subcellular locations in the secretory pathway (Figure ??a). To interrogate the luminal pH along the entire secretory pathway, we fused RpHluorin2 to the signal sequence of the ER-resident protein calreticulin and a C-terminal ER retention signal KDEL for ER targeting, to the luminal regions of *cis*-/medial-Golgi protein alpha-1,6-mannosyl-glycoprotein 2-beta-N-acetylglucosaminyltransferase (MGAT2), to *trans*-Golgi enzyme beta-1,4-galactosyltransferase 1 (GalT), to lysosome-associated membrane glycoprotein 1 (LAMP1) for lysosomal targeting, and finally to a GPI anchor for plasma membrane (i.e. extracellular) localization. For the Golgi enzymes (MGAT2 and GalT), we truncated each protein by removing their catalytic sites and only kept the transmembrane region and stalk regions responsible for their localization<sup>264–266</sup>.

We then expressed the fusion constructs in HeLa cells, and recorded FLIM images. We used the GPI-anchored RpHluorin2 to calibrate the probe expressed in cells using the same pH buffers as used for the calibration of purified RpHluorin2 (Figure 3.2a-c). We again observed a dependency of the fluorescence lifetime of RpHluorin2 on pH, although the absolute fluorescence lifetime values were lower than for the recombinant RpHluorin2, possibly due to crowding effects. This dependence on pH could again be fitted by a three-parameter Michaelis-Menten function. After successfully calibrating our system, we proceeded with pH measurements in the lumen of the organelles along of the secretory pathway (Figure 3.3). With ER-RpHluorin2, we measured an apparent average pH of 7.2, while with *cis*-/medial-Golgi marker MGAT2-RpHluorin2 we measured an apparent average pH of 6.1, and with *trans*-Golgi marker GalT-RpHluorin2 an apparent average pH of 5.9 (Figure 3.3b, c). Finally, for lysosomal marker LAMP1-RpHluorin2 we measured an apparent average pH of 4.7. These pH values are all consistent with previous literature<sup>22,249</sup>. Taken together, our data show that the RpHluorin2 FLIM system is highly suitable for intracellular pH measurements with only a single image acquisition.

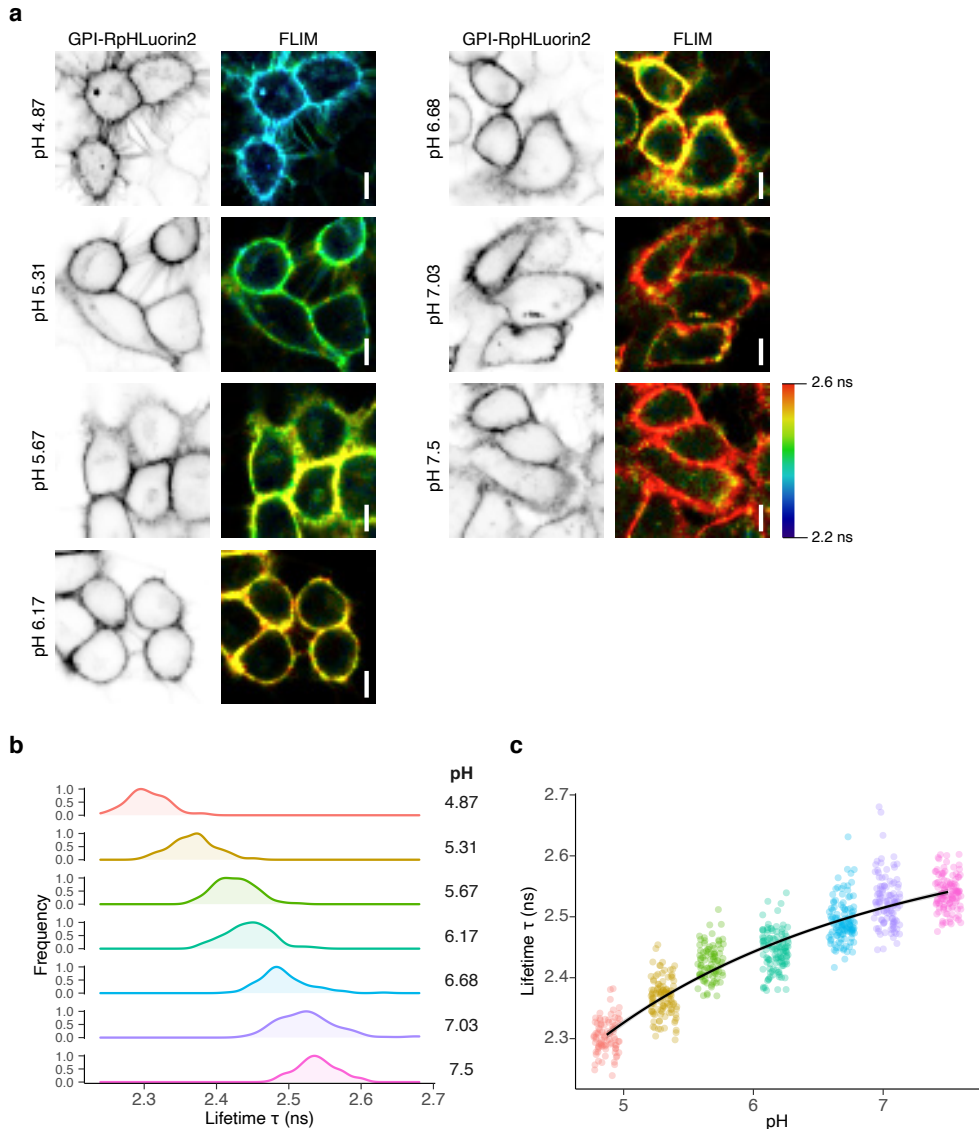


**Figure 3.2: Calibration of RpHluorin2 by fluorescence lifetime imaging microscopy (FLIM) in HeLa cells expressing GPI-RpHluorin2.** (a) Representative confocal micrographs of HeLa cells expressing GPI-RpHluorin2 in defined calibration buffers. The intensity image (left column) was convoluted with the fluorescent lifetime value per pixel and pseudo-colored (right column). Scalebars, 10  $\mu\text{m}$ . (b) Average lifetime histograms from the images of panel (a). N = 86 (pH 4.87), 108 (pH 5.31), 90 (pH 5.67), 115 (pH 6.17), 122 (pH 6.68), 113 (pH 7.03) and 120 (pH 7.5) cells from three independent experiments. (c) pH dependence of HeLa cells expressing GPI-RpHluorin2 in defined pH calibration buffers from the images of panel (a).

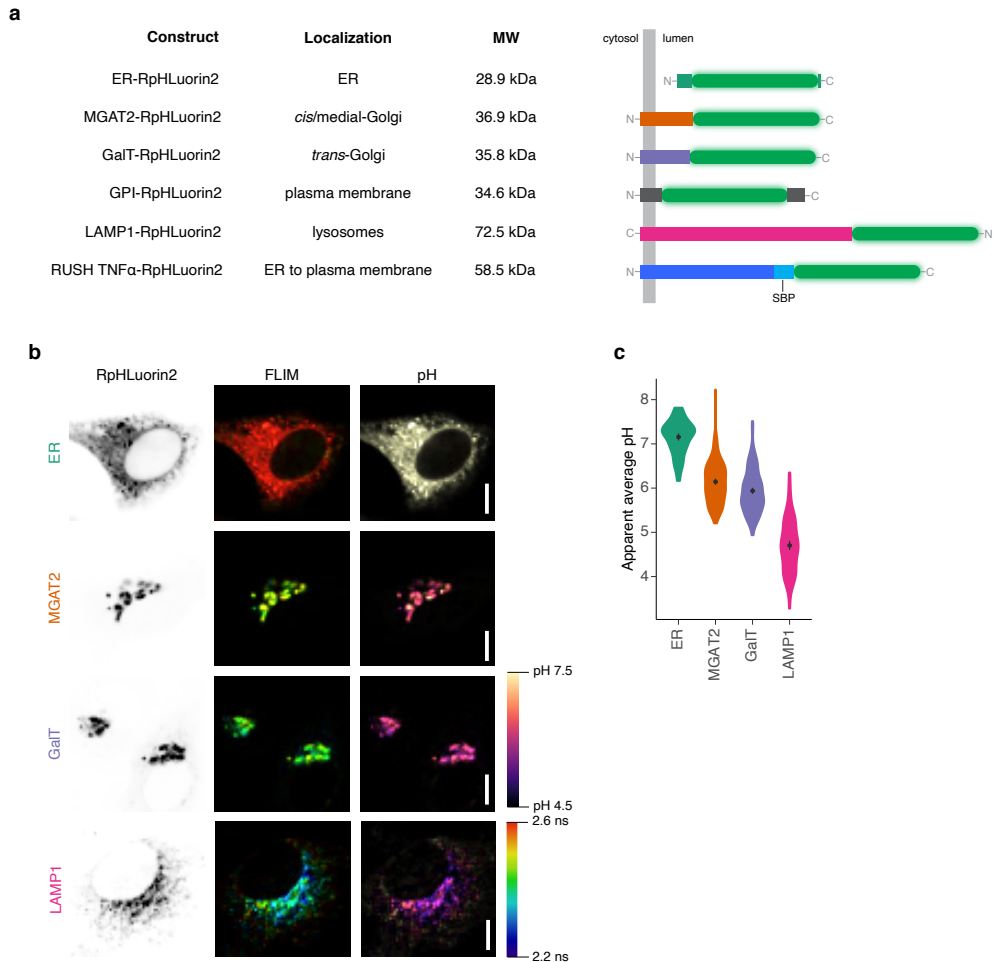


**Figure 3.3: Steady-state pH measurements of secretory pathway markers.** (a) Schematic overview of all RpHLuorin2 constructs used in this study. The signal sequence of LAMP1 is removed following co-translational ER insertion and is not shown in the diagram. MW, molecular weight. RUSH, retention using selective hooks<sup>266</sup>. SBP, streptavidin binding protein. (b) Representative confocal micrographs of HeLa cells expressing the mentioned RpHLuorin2 fusion constructs. The intensity image (left column) was convoluted with the fluorescent lifetime value per pixel and pseudo-colored (middle column). The intensity image was also convoluted with the calculated pH per pixel and pseudo-colored (right column). FLIM, fluorescence lifetime imaging microscopy. Scalebars, 10  $\mu$ m. (c) Quantification of average pH values from panel (b). N = 88 (ER), 188 (MGAT2), 193 (GaIT), and 134 (LAMP1) cells from 3 – 5 independent experiments.

### 3.3.3 Dynamic measurements of pH in the secretory pathway

To evaluate whether our method would be able to measure dynamic changes in pH, we started by measuring the pH of the medial-Golgi marker MGAT2-pHluorin2 in the presence of fungal metabolite Brefeldin A (BFA). BFA is a potent inhibitor of COPI-mediated vesicular trafficking and causes the relocation of Golgi-resident enzymes to the ER<sup>96,267</sup>. We therefore expected a substantial increase in pH when MGAT2-RpHluorin2 expressing cells were challenged with BFA. Indeed, we measured an apparent average pH of 7.1 in the BFA-challenged cells compared to an apparent average pH of 6.4 in the vehicle control cells (Figure 3.4a, b). This result means that our system is capable of measuring dynamic alterations of pH in living cells.

Next, we employed FLIM-based measurements to monitor the changes of the pH in real-time along the secretory pathway. To this end, we chose the secreted cytokine tumor necrosis factor alpha (TNF- $\alpha$ ) as a model protein that is transported through the secretory pathway. Using the Retention Using Selective Hooks (RUSH) system<sup>266</sup>, we synchronized the transit of TNF- $\alpha$  along the secretory pathway. RUSH uses the expression of two separate constructs in the cell: (i) the hook construct, which is an ER-targeting sequence fused to streptavidin, and (ii) the reporter construct which is the protein of interest (i.e., TNF- $\alpha$ ) fused in tandem to a streptavidin binding protein (SBP) and a fluorescent protein (RpHluorin2). When biotin is absent from the culture medium, the reporter construct is held at the ER through an interaction of streptavidin of the hook construct and the SBP. When biotin is added to the culture medium, biotin outcompetes this interaction and the reporter construct is released and transits along the secretory pathway in a synchronized fashion.

In our case, we used the KDEL-motif as a targeting sequence for the ER<sup>266</sup>, and used a TNF $\alpha$ -SBP-RpHluorin2 fusion protein (RUSH TNF $\alpha$ -RpHluorin2) as the reporter construct, so that we could follow the dynamic transit of TNF $\alpha$  from the ER to the plasma membrane (Figure 3.4c-e). In the absence of biotin in the cell culture medium, when all the reporter construct was trapped within the ER, we measured an apparent average pH of 7.58, which is comparable to our earlier determined pH in the ER. In the 25 min following the addition of biotin to the cells, RUSH TNF $\alpha$ -RpHluorin2 was trafficked through the Golgi and the apparent average pH gradually decreased to around pH 6. At later time points, the pH gradually increased again as more TNF $\alpha$ -RpHluorin2 reached the plasma membrane and was released in the extracellular environment. Because of the limited number of photons, we fitted the fluorescence lifetime histograms with a single exponential decay function and report the apparent average pH per cell<sup>268</sup>. This result demonstrates that FLIM-based pH measurements are a suitable method to determine intraorganellar pH with high temporal resolution.

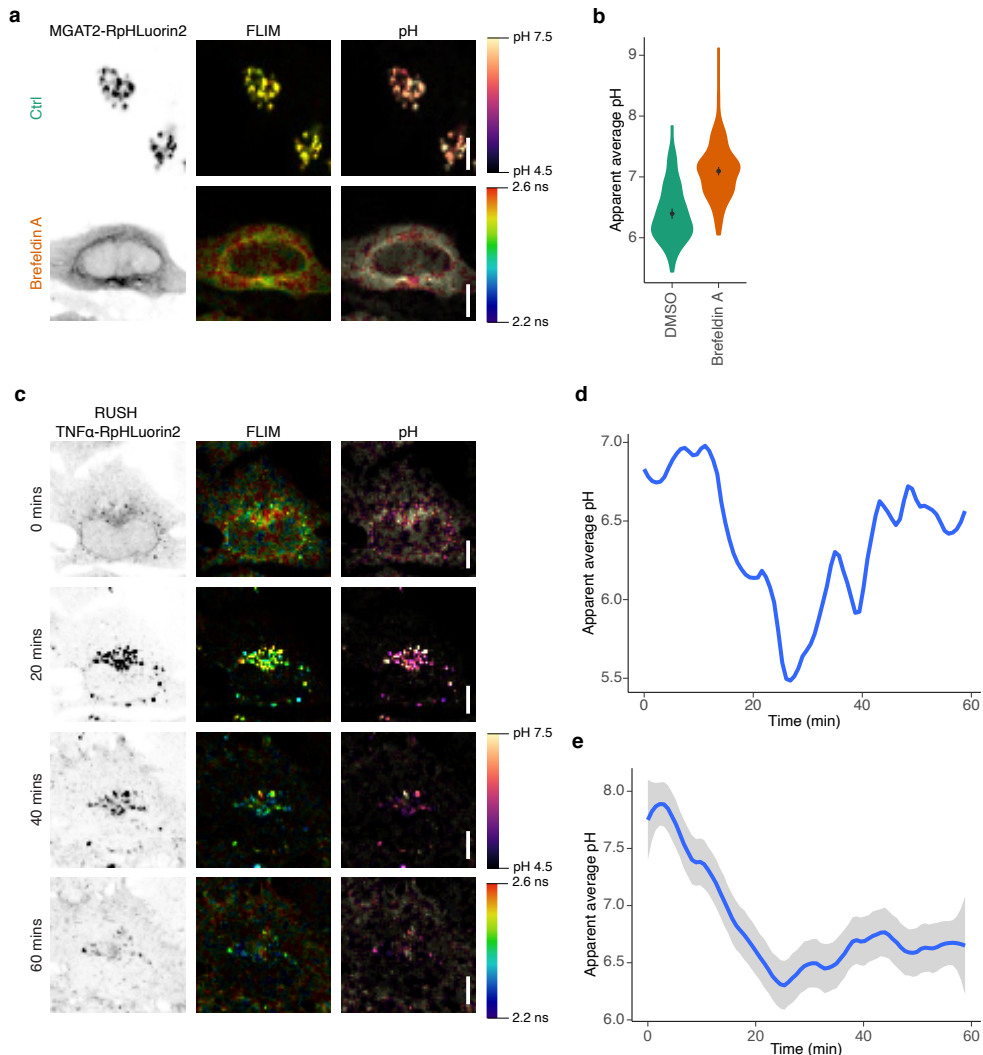


**Figure 3.4: Dynamic pH measurements along the secretory pathway.** (a) Representative confocal micrographs of HeLa cells expressing MGAT2-RpHluorin2 in the absence (Ctrl, green) or presence of Brefeldin A (Brefeldin A, orange). The intensity image (left column) was convoluted with the fluorescent lifetime value per pixel and pseudo-colored (middle column). The intensity image was also convoluted with the calculated pH per pixel and pseudo-colored (right column). FLIM, fluorescence lifetime imaging microscopy. Scalebars, 10  $\mu$ m. (b) Quantification of average pH values from panel (a). N = 110 (DMSO) and 165 (Brefeldin A) cells from 2 – 3 independent experiments. (c) Representative confocal micrographs of HeLa cells expressing RUSH TNF $\alpha$ -RpHluorin2 in the absence of biotin (0 min) or 20, 40 and 60 minutes after biotin addition. The intensity image (left column) was convoluted with the fluorescent lifetime value per pixel and pseudo-colored (middle column). The intensity image was also convoluted with the calculated pH per pixel and pseudo-colored (right column). FLIM, fluorescence lifetime imaging microscopy. Scalebars, 10  $\mu$ m. (d) Quantification of average pH values of the cell shown in panel (c). (e) Average pH measured of all cells expressing RUSH TNF $\alpha$ -RpHluorin2. N = 29 from 2 independent experiments.

## 3.4 Discussion

In this study, we measured the pH in various subcellular compartments using FLIM of the pH-sensitive fluorescent protein RpHluorin2. Consistent with previous literature, we observed a clear acidification of luminal pH through the secretory pathway<sup>22,242,243</sup>. The fusion of RpHluorin2 is not restricted to the proteins we described here; this system is applicable to any other intraorganellar measurement, provided RpHluorin2 can be fused to a luminal domain of a protein residing in the target organelle. Furthermore, additional applications include combining RpHluorin2 with other fluorescence (lifetime) based probes to measure pH and other cellular processes simultaneously within the same cell.

The key improvement of our study is the usage of FLIM as opposed to traditional ratiometric imaging. Ratiometric imaging of pHluorin and derivatives<sup>253,257,258</sup> requires the sequential recording of the fluorescent protein at both 405 and 470 nm excitation wavelengths. This sequential imaging intrinsically limits the temporal resolution and consequently limits the applicability for pH determination in dynamically moving and reshaping organelles. FLIM mitigates this issue, as only a single recording with a single excitation wavelength is required. Moreover, FLIM measurements are not dependent on laser intensity<sup>260,261</sup>, while ratiometric measurements can easily be affected by fluctuations in excitation laser power. FLIM measurements are thus more comparable between experiments.

In contrast to another study which relies on equilibrating pH with the ionophore monensin<sup>253</sup>, we used GPI-anchored RpHluorin2 to obtain calibration curves with defined pH buffers, because monensin is a known inhibitor of physiological Golgi transport, thereby likely affecting the observed fluorescence lifetime values<sup>269–275</sup>.

Defects in the regulation of pH are a hallmark of a wide range of disease, including disorders of glycosylation<sup>13,77,112,113,117,120,121</sup>, cancer<sup>276</sup>, neurodegenerative diseases<sup>277–280</sup>, mitochondrial disorders<sup>281</sup> and lysosomal storage disorders<sup>282</sup>. The tools we presented in this study offer a method to assess intraorganellar pH, both in static compartments and in transit between organelles with high temporal resolution.

### 3.4.1 Acknowledgments

We thank the following people for constructs: Hesso Farhan and Franck Perez (Str-KDEL\_ManII-SBP-EGFP; Addgene plasmid #65252, Str-KDEL\_TNF-SBP-EGFP; Addgene plasmid #65278), Lei Lu (piRFP670-N1-GalT; Addgene plasmid #87325), Carsten Schultz and André Nadler (GPI-mRFP), and Esteban Dell'Angelica (LAMP1-mGFP, Addgene plasmid #34831). We thank the Microscopy Imaging Center of the Radboud Institute for Molecular Life Sciences for use of their microscopy facilities. G.v.d.B. is funded

by a Young Investigator Grant from the Human Frontier Science Program (HFSP; RGY0080/2018) and a Vidi grant from the Netherlands Organisation for Scientific Research (NWO-ALW VIDI 864.14.001). G.v.d.B has also received funding from the European Research Council (ERC) under the European Union's Horizon 2020 research and innovation program (grant agreement No. 862137).

### 3.4.2 Author Contributions

P.T.A.L., M.t.B., and G.v.d.B. designed and performed the experiments and wrote the paper.

### 3.4.3 Declaration of Interests

The authors declare that they have no competing financial interests.

## 3.5 Methods

### 3.5.1 Cloning

The sequence of RpHluorin2<sup>258</sup> was synthesized by Genscript for both recombinant (codon optimized for *E. coli*) and mammalian cell expression. Synthetic RpHluorin2 codon optimized for *E. coli* for recombinant protein production was inserted in pET-28a(+) (EMD Biosciences) with restriction sites NdeI and XhoI. The construct for cytosolic expression of RpHluorin2 was generated by replacing EGFP in pEGFP-N1 (Clontech) with synthesized RpHluorin2 using restriction sites AgeI and BsrGI. ER-targeting of RpHluorin2 was achieved by inserting the signal sequence of calreticulin (MLLSV-PLLLGLLGLAVA) and flexible GGSGGS linker before RpHluorin2 and adding a KDEL motif for luminal ER retention after RpHluorin2. Targeting to the MGAT2-positive compartment was achieved by inserting synthetic truncated MGAT2 (residues 1-89 of Uniprot Q10469, Genscript) in the vector for cytosolic expression of RpHluorin2 with restriction sites EcoRI and BamHI. The starting codon of RpHluorin2 was removed and a flexible GGSGGS linker was added between the two protein fragments. Targeting to the GalT-positive compartment was achieved by inserting truncated GalT (Addgene plasmid #87325) in the vector for cytosolic expression of RpHluorin2 with restriction sites SmaI and BamHI. The starting codon of RpHluorin2 was removed and a flexible GGSGGS linker was added between the two protein fragments. Targeting to LAMP1-positive compartments was achieved by inserting the signal sequence of LAMP1 (LAMP1-mGFP<sup>283</sup>, Addgene plasmid #34831) N-terminal to RpHluorin2 with restriction sites HindIII and AgeI. Then, the luminal domain of LAMP1 was placed C-terminal to RpHluorin2 after a flexible GSGS linker with restriction sites BsrGI and NotI. GPI-RpHluorin2 was generated by replacing mRFP from GPI-mRFP with synthetic RpHluorin2 with restriction sites XmaI and NotI. RUSH TNF $\alpha$ -RpHluorin2 was generated by replacing EGFP from Str-KDEL\_TNF-SBP-EGFP (Addgene plasmid #65278) with synthetic RpHluorin2 (Genscript) with restriction sites SbfI and BsrGI. All sequences were verified by Sanger sequencing prior to transfection. All generated plasmids from this study have been deposited at Addgene.

### 3.5.2 Cell culture and transfection

HeLa cells (authenticated by ATCC through their human STR profiling cell authentication service) were maintained in high glucose DMEM with Glutamax (Gibco 31966021), supplemented with 10% fetal calf serum (FCS, Greiner Bio-one, Kremsmünster, Austria) and antibiotic-antimycotic solution (Gibco 15240-062). Cells were regularly tested for mycoplasma contamination. HeLa cells were transfected with plasmid vectors using

Fugene HD (Promega E2311), using the recommended protocol of the manufacturer. Cells were imaged 48 hours post-transfection. Only cells expressing low to moderate levels of the transfected plasmids, based on fluorescence intensity and manual localization scoring, were chosen for subsequent microscopic analyses.

### 3.5.3 pH calibration buffers

Buffers with defined pH for the generation of a calibration curve were prepared as described previously<sup>253</sup>. Calibration buffers contain 125 mM KCl, 25 mM NaCl, and 25 mM N-[2-hydroxyethyl]-piperazine-N-[2-ethanesulfonic acid] (HEPES, pH 7.5 or 7.0) or 25 mM 2-[N-morpholino] ethanesulfonic acid (MES, pH 6.5, 6.0, 5.5, 5.0 or 4.5). Each buffer solution was adjusted to the appropriate final pH using 1 M NaOH or 1 M HCl at 37°C.

### 3.5.4 Recombinant protein expression and purification

RpHluorin2 in pET-28(a)+ vector was transformed in BL21(DE3) *E. coli*. Cells were grown in 2× yeast extract - tryptone medium and induced with 250 µg/mL β-D-1-thiogalactopyranoside (IPTG) at an OD600 of 0.8 for 2 hrs at 37°C and 200 rpm. Cells were pelleted at 3000 × g at 4°C for 30 mins and subsequently lysed with B-PER (Thermo Scientific) supplemented with 50 U DNaseI, 1:500 lysozyme and protease inhibitor cocktail (Roche). Lysates were then cleared by centrifugation (20,000 × g at 4°C for 10 mins) and supernatants with recombinant protein were loaded onto nickel – nitrilotriacetic acid (Ni-NTA) bead columns. Ni-NTA beads were then washed five times with 10 mM Tris-HCl pH 7.6 and 150 mM KCl, and proteins were eluted in 10 mM Tris-HCl pH 7.6, 150 mM KCl and 200 mM imidazole. To remove the elution buffer, purified protein was dialyzed overnight against ddH2O using 2 mL Slide-A-Lyzer 10K MWCO tubes (Thermo Scientific). Protein concentration was determined using the Micro BCA Protein Assay Kit (Thermo Scientific). Fluorescence of recombinant pHluorin2 in each pH calibration buffer was measured using Eppendorf semimicro Vis Cuvettes on an LS 55 Fluorescence spectrometer (PerkinElmer). A xenon lamp was used as the excitation source. Samples were excited at 405 and 470 nm, and the emission was recorded at 508 nm.

### 3.5.5 Confocal microscopy

Imaging of cells took place in Leibovitz's L-15 medium, with the exception of the samples for the pH calibration curve and the recombinant protein measurements. GPI-RpHluorin2 and recombinant RpHluorin2 (10 µM) measurements were performed in the pH buffers mentioned above. For calibration with GPI-RpHluorin2, cells were

preincubated in pH buffer for 15 mins at 37°C to achieve sufficient pH equilibration. Imaging was performed on a Leica SP8 SMD system at 37°C, equipped with an HC PL APO CS2 63×/1.20 WATER objective. pHLuorin2 was excited at 488 nm with a pulsed white light laser, operating at 80 MHz. Photons were collected for one minute or 30 seconds for time-lapse experiments with a HyD detector set at 502 – 530 nm and lifetime histograms of the donor fluorophore were fitted with a monoexponential decay function convoluted with the microscope instrument response function in Leica LAS X. For reconstructing the images, tiff files with  $\tau$  values were generated using FLIMFit<sup>284</sup> and 2 × 2 spatial binning, and then convoluted with the fluorescent intensities using a custom-written ImageJ macro.

### 3.5.6 Quantification and statistical analysis

All mean values represent the average of all cells analyzed. pH calibration curves were fitted with the three-parameter Michaelis-Menten function as described by equation 3.1 with the *MM.3* function from the R package *drc*<sup>285</sup>.

$$y = c + \frac{d}{1 + \frac{e}{x}} \quad (3.1)$$

Where  $y$  is the fluorescence intensity or lifetime,  $x$  is the pH and  $c$ ,  $d$  and  $e$  are fit parameters.

All comparisons were first checked for similar mean and median values and acceptable ( $< 3x$ ) difference in variance. Statistical analysis of three or more groups was performed using a one-way ANOVA, followed by a post-hoc Tukey's honestly significant difference test.  $p < 0.05$  was considered significant. \* $p < 0.05$ , \*\* $p < 0.01$ , \*\*\* $p < 0.001$ , \*\*\*\* $p \leq 0.0001$ . All statistical analyses were performed using R statistical software. All numerical data were visualized using R package *ggplot2*<sup>286</sup>, with violins representing the overall distribution of the data and means ± 95% CI overlaid.

### 3.5.7 Data and code availability

All raw data, including R scripts and ImageJ macros, have been deposited to Zenodo.

### 3.6 Supplementary Information

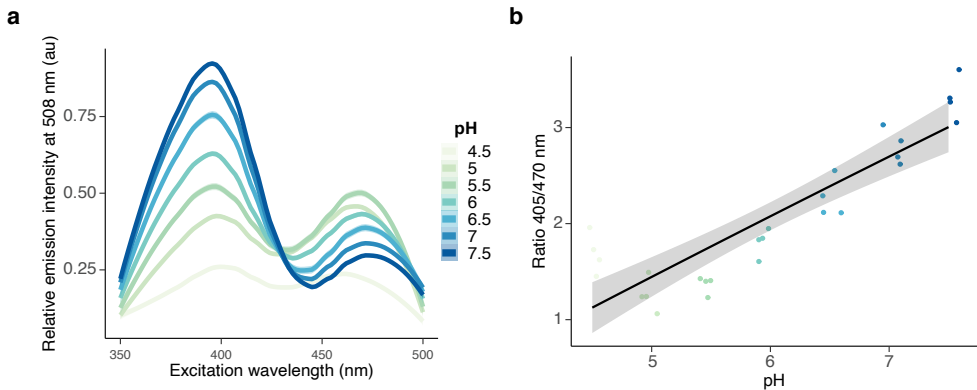


**Figure 3.5: Fluorescence excitation spectra of recombinant RpHluorin2. (a)** Representative fluorescence excitation spectra (emission 508 nm) of recombinant RpHluorin2 in buffers of defined pH were collected with a fluorescent spectrometer. **(b)** Calibration curve from panel (a). The ratios of fluorescence at 405 over 470 nm were plotted as a function of pH and fitted with a three-parameter Michaels-Menten function. Data from four independent experiments.



P.T.A. Linders, E. Peters, M. ter Beest, and G. van den Bogaart

# 4

N-glycosylation is dependent on  
TMEM199-mediated V-ATPase assembly

## 4.1 Abstract

The mammalian vacuolar H<sup>+</sup>-ATPase (V-ATPase) is an important proton pump present at the membrane of the Golgi apparatus membrane and other organelles, where it ensures luminal pH suitable for Golgi processes. The molecular mechanisms of mammalian V-ATPase assembly are still unclear, but mutations in TMEM199, the mammalian homolog of yeast V-ATPase assembly factor Vma12p, cause a disorder of glycosylation characterized by hyposialylation, hypogalactosylation and elevated liver enzymes. In this study, we generate a HeLa cell model lacking TMEM199 with CRISPR/Cas9 to dissect the molecular mechanisms of disease. We observed that several enzymes responsible for glycosylation are mislocalized in TMEM199KO cells. Then, we applied a novel method to determine intraorganellar pH along the secretory pathway and observed that intraorganellar pH is misregulated in TMEM199KO cells. Finally, we performed biochemical studies to discover that TMEM199 is involved in the specific assembly of the Golgi- and endosome-localized V<sub>0</sub>a2 subunit and that TMEM199 is required for membrane association of CCDC115, the mammalian homolog of yeast V-ATPase assembly factor Vma22p. Thus, we present the underlying molecular mechanisms of glycosylation disorders caused by mutations in TMEM199.

## 4.2 Introduction

The Golgi apparatus has a well-defined pH gradient<sup>22</sup> ranging from pH 6.7 at the *cis*-Golgi to 6.0 at the *trans*-Golgi<sup>22,242,243,254</sup>. Not only is physiological pH required for proper folding, stability and function of proteins, at the Golgi apparatus pH is of utmost importance for the correct localization and activity of Golgi-localized glycosylation enzymes<sup>13,31–34</sup>. Thus, strict maintenance of the Golgi pH gradient is critical and, in mammals, is in large part mediated by the vacuolar H<sup>+</sup>-ATPase (V-ATPase).

The mammalian V-ATPase is a large multiprotein complex ( $\approx$ 900 kDa) which acidifies intraorganellar lumina by translocating protons across the membrane<sup>69,70</sup>. The V-ATPase can be subdivided into two separate domains: the membrane V<sub>0</sub> domain, consisting of six different subunits (a, d, e, c, c', and c''), which anchors the complex, and the cytosolic V<sub>1</sub> domain, consisting of eight different subunits (A-H), which hydrolyses ATP<sup>70</sup>. In mammals, four isoforms of the V<sub>0</sub>a subunit exist (V<sub>0</sub>a1-4), and this likely provides subcellular specificity with the V<sub>0</sub>a2 subunit primarily localizing to the Golgi apparatus and endosomes<sup>74–79</sup>. This is different from *Saccharomyces cerevisiae* which only expresses two unique isoforms (Vph1p and Stv1p)<sup>69–73</sup>.

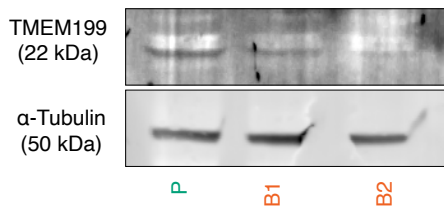
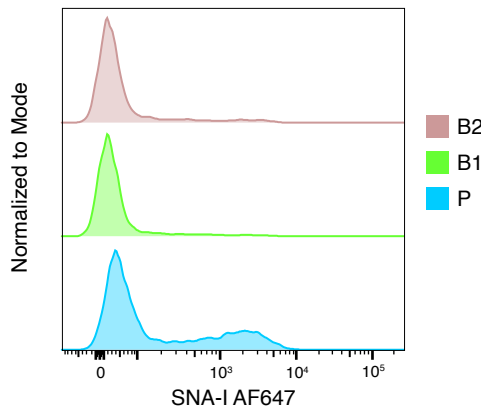
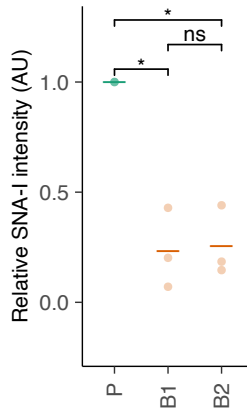
Assembly of the V<sub>0</sub> domain in yeast is dependent on a set of ER-localized chaperones: Vma12p, Vma21p and Vma22p<sup>69,100,122–124</sup>. Mammalian homologues of Vma12p (TMEM199), Vma21p (VMA21) and Vma22p (CCDC115) have recently been identified and genetic variants in these proteins are associated with disorders of glycosylation<sup>117,120,121</sup>. Moreover, TMEM199 and CCDC115 have been shown to interact and are important for physiological iron homeostasis, a process that also relies on intraorganellar pH<sup>125</sup>. However, their role in mammalian V-ATPase assembly is poorly understood.

In this study, we dissected the role of TMEM199 in mammalian V-ATPase assembly. We developed a HeLa cell line deficient of TMEM199 by CRISPR/Cas9 and, using a novel method for intraorganellar pH measurements, measured the effect of the knock-out on intracellular pH. To prove that TMEM199 is indeed an assembly factor of the mammalian V-ATPase, we performed fractionation studies and examined whether TMEM199 can tether CCDC115 to the membrane.

## 4.3 Results

### 4.3.1 Generation of a TMEM199KO model

To study the role of TMEM199 in glycosylation and V-ATPase assembly, we generated two unique partial TMEM199 knockout HeLa cell lines from the same gRNA (B1 and B2; Figure 4.1a), with different levels of residual TMEM199 expression, using CRISPR/Cas9.

**a****b****c**

**Figure 4.1: TMEM199KO HeLa cell lines show defective cell surface sialylation.** (a) Representative immunoblot for TMEM199 on cell lysates of parental HeLa cells (P, green) or TMEM199KO cells (B1 and B2, orange).  $\alpha$ -Tubulin, loading control. (b) Representative FACS histogram of parental HeLa cells (blue, P), or two TMEM199KO lines (green, B1 and pink, B2), probed with SNA-I lectin conjugated to Alexa Fluor 647. Gating strategy in Supplementary Figure 4.6. (c) Quantification of (b). Geometric means were taken and normalized to parental. 10,000 events analyzed per condition per experiment from 3 independent experiments.

To confirm that these knockout models are suitable to study the glycosylation defects observed in TMEM199-CDG patients<sup>121</sup>, we performed cell surface staining with the SNA-I lectin from *Sambucus nigra*, which binds terminal sialic acid moieties in an  $\alpha$ -2,6 linkage and to a lesser extent  $\alpha$ -2,3 linkage of N-glycans. Compared to parental HeLa cells, we observed an approximate 60% decrease in SNA-I labeling for both TMEM199KO clones (Figure 4.1b, c, flow cytometry gating strategy in Supplementary Figure 4.6). As TMEM199-CDG patients present with a similar decrease in sialylation<sup>121</sup>, we concluded from this experiment that our TMEM199KO clones are a suitable model for the glycosylation defect.

### 4.3.2 Loss of TMEM199 relocalizes glycosyltransferases

Given that our TMEM199KO cell models have defective cell surface glycosylation, we investigated whether there is a potential trafficking defect by probing for the localization of glycosyltransferases in the Golgi apparatus. We performed immunofluorescence labeling of mannosyl ( $\alpha$ -1,3)-glycoprotein  $\beta$ -1,2-N-acetylglucosaminyltransferase (MGAT1, also known as GnT1), which catalyzes the addition of N-acetylglucosamine (GlcNAc) to the early Golgi-related glycan man-5. Compared to parental HeLa cells, TMEM199KO B1 showed a slightly increased colocalization of MGAT1 with *cis*-Golgi marker GM130 (Figure 4.2a, b) and *trans*-Golgi marker TGN46 (Figure 4.2c, d), while TMEM199KO B2 shows a strongly decreased colocalization of MGAT1 with GM130 and a slightly increased colocalization with TGN46. As TMEM199-CDG patients show hypogalactosylation, we next investigated the localization of  $\beta$ -1,4-galactosyltransferase 1 (B4GALT1, also known as GalT) which catalyzes the addition of galactose to N-acetylglucosamine moieties (Supplementary Figure 4.7). Compared to parental HeLa cells, we observed a decrease of B4GALT1 colocalization with *cis*-Golgi marker ZFPL1<sup>287</sup> in B1 cells, but an increase in ZFPL1 colocalization in B2 cells. For TGN46 colocalization, no difference was observed for B1 cells but we observed a decrease in colocalization in B2 cells. Finally, N-acetylgalactosaminyltransferase 2 (GALNT2), which catalyzes the first step in mucin O-linked glycan synthesis, located slightly more to the *cis*-Golgi (marker ZFPL1), and slightly less to *trans*-Golgi (marker TGN46) in B2 cells (Supplementary Figure 4.8).

As a control, we investigated protein expression levels (inferred from the fluorescence intensity of the immunofluorescence labeling) of the markers used in the colocalization experiments, and did not find a correlation between expression and differences in colocalization (Supplementary Figure 4.9). We did observe a slight condensation of GM130 labeling area in B1 cells and a slight dilation in B2 cells, while we observed condensation of ZFPL1 labeling area only in B2 cells. A similar condensation phenotype was observed for TGN46 in B2 cells. These results suggest that the Golgi morphology is differentially altered in the two TMEM199 knockout strains.

Taken together, and despite the partially opposite phenotypes in the two TMEM199 knockout strains, the (partial) loss of TMEM199 causes the aberrant localization of glycosyltransferases to the Golgi apparatus and slight morphological differences of the Golgi. Computational simulations have shown that disruption of Golgi structure and mislocalization of glycosyltransferases can have a profound impact on glycosylation<sup>54</sup>.

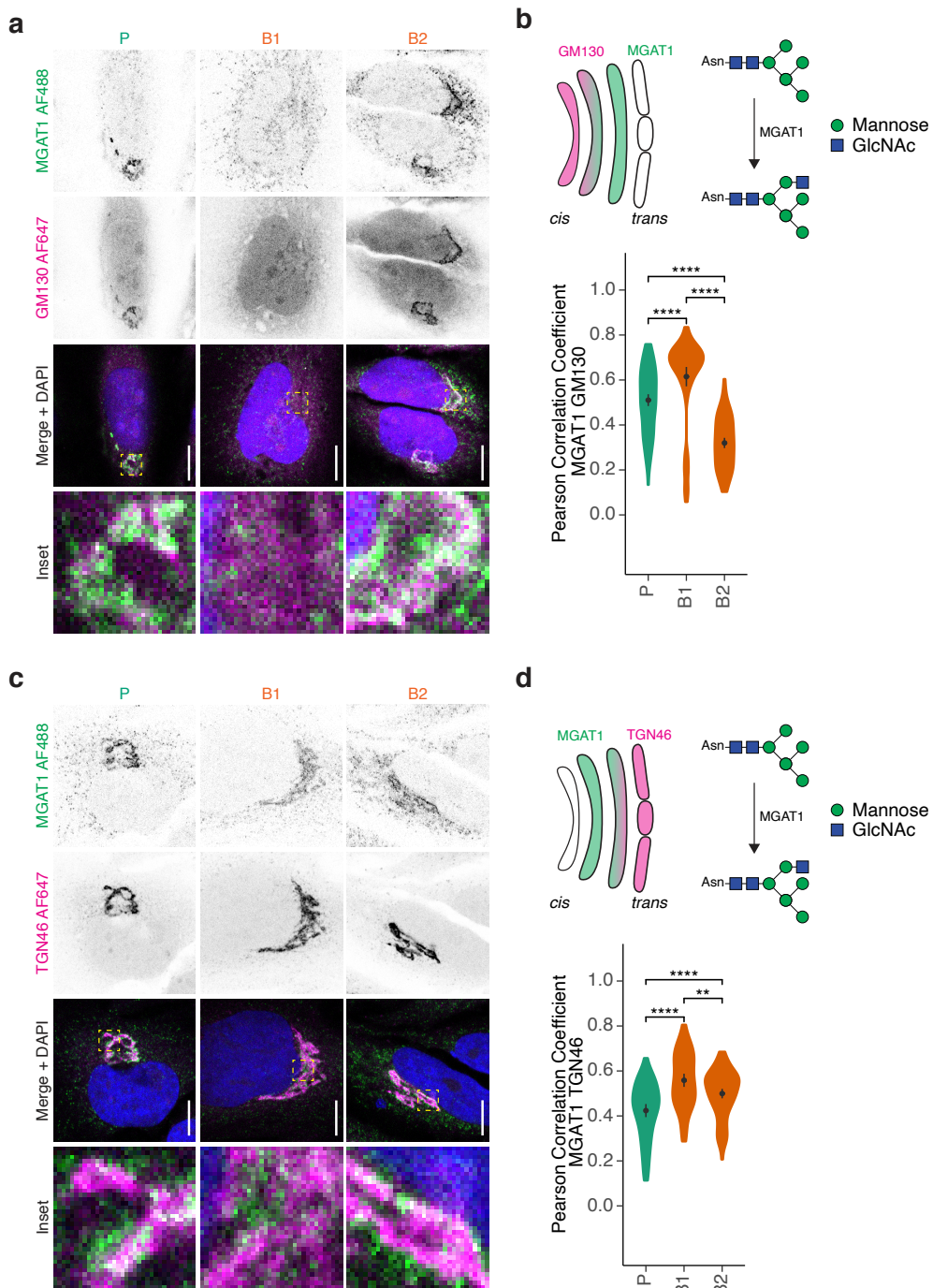


**Figure 4.2: Relocation of glycosyltransferase MGAT1 in TMEM199KO HeLa cells. (Continued on the following page.)**

**Figure 4.2:** (a) Immunofluorescence microscopy of MGAT1 (green in merge) and GM130 (magenta) in parental HeLa cells (green, P) or TMEM199KO cells (B1 and B2, orange). Representative confocal micrographs. Scale-bars, 10  $\mu$ m. DAPI in blue. (b) Pearson's correlation coefficients between MGAT1 and GM130 of panel (a). N = 118 (P), 78 (B1), and 99 (B2) from two independent experiments. (c) Same as panel (a) but now for MGAT1 (green) and TGN46 (magenta). (d) Pearson's correlation coefficients between MGAT1 and TGN46 of panel (c). N = 75 (P), 68 (B1), and 99 (B2) from two independent experiments.

#### 4.3.3 pH measurements in TMEM199KO cells

As TMEM199 is a supposed V-ATPase assembly factor and physiological pH homeostasis is necessary to maintain the delicate structure of the Golgi<sup>5–9</sup>, we then investigated whether the aberrant localization of glycosyltransferases is caused by defective Golgi lumen pH regulation. We applied our earlier developed method based on the fusion of a pH-sensitive GFP mutant, ratiometric pHLuorin2<sup>257,258</sup>, to organellar markers to measure intraorganellar pH using fluorescence lifetime imaging microscopy (FLIM)<sup>288</sup> (Figure 4.3). We measured an ER luminal pH of 7.4 for parental HeLa cells, which was strongly decreased for B1 cells (pH 6.7) and even further decreased in B2 cells (pH 6.5) (Figure 4.3a, b). Golgi pH was slightly decreased as measured by MGAT2-RpHLuorin2 (*cis*/medial-Golgi, P: pH 6.3, B1: pH 6.1, B2: pH 6.1; Figure 4.3c, d) and GALT-RpHLuorin2 (*trans*-Golgi, P: pH 6.4, B1: pH 6.0, B2: pH 5.9; Figure 4.3e, f). Finally, we observed no significant difference between parental cells and B1 cells in lysosomal pH as measured by LAMP1-RpHLuorin2 (P: pH 5.0, B1: pH 4.9; Figure 4.3g, h) but we measured a decrease in lysosomal pH for B2 cells (pH 4.5; Figure 4.3g, h). We expected that a dysfunctional V-ATPase assembly in TMEM199KO would result in an increased intraorganellar pH due to defective acidification. However, our results contrast this hypothesis as we observed stronger acidification along the entire secretory pathway.

As the observed misregulation of pH might already mislocalize the probes we applied to measure intraorganellar pH, it is possible that the localization of the probes in the B1 and B2 cells does not reflect the same localization as in the parental cells. Thus, we developed a different strategy for assessing V-ATPase activity by measuring intraorganellar pH in the absence or presence of the V-ATPase inhibitor Bafilomycin A1 (BafA1)<sup>289</sup>. We reasoned that if less V-ATPase molecules are present in organellar membranes, the difference in luminal pH ( $\Delta$ pH) between BafA1-treated cells and the DMSO control should be lower. For ER-RpHLuorin2 expressed in parental HeLa cells, we measured a lower luminal pH when treated with only DMSO compared to our previous measurements (pH 6.4 with DMSO compared to pH 7.4; Figure 4.4a, Supplementary Figure 4.10a), likely as a result of DMSO treatment, and this increased to pH 6.5 when incubated with 200 nM BafA1. Similar results with DMSO were observed for the B1 and B2 cells (pH 6.3 and pH 6.1 respectively), but  $\Delta$ pH was slightly decreased in B1 cells compared to parental HeLa, but somewhat increased in B2 cells (Figure 4.4a, b,

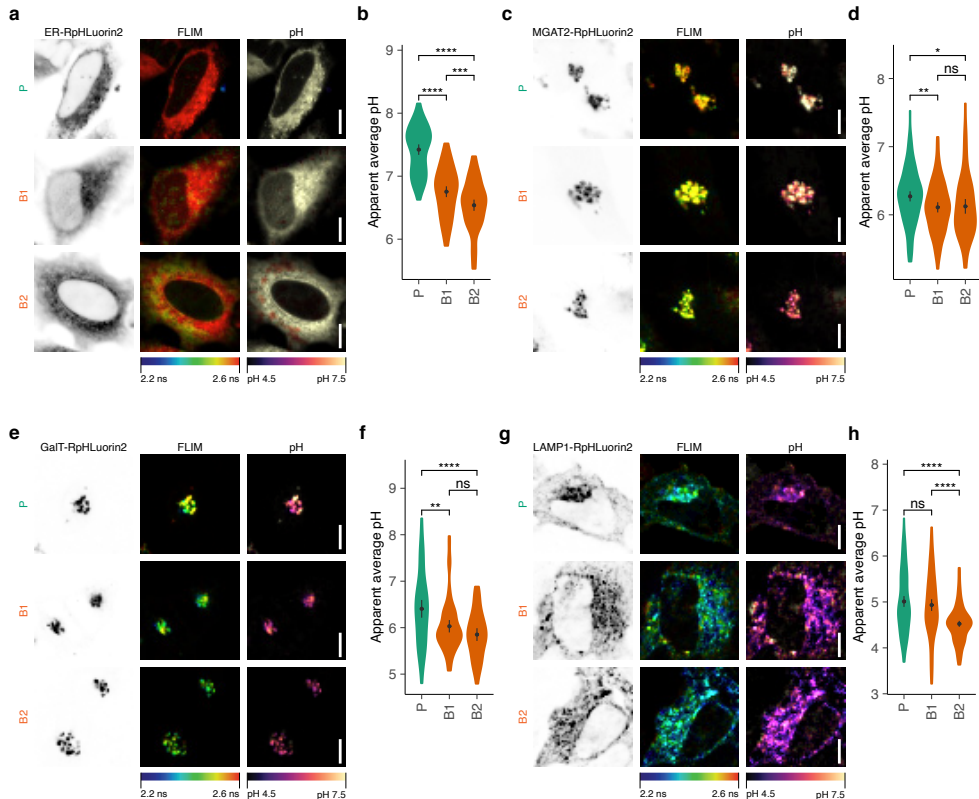


**Figure 4.3: Decreased luminal pH in TMEM199KO HeLa cells.** (a) Representative confocal micrographs of parental HeLa cells (P, green) or TMEM199KO cells (B1 and B2, orange) expressing ER-RpHluorin2. The intensity image (left column) was convoluted with the fluorescence lifetime value (middle column) and the calculated pH (right column) per pixel. FLIM, fluorescence lifetime imaging microscopy. Scalebars, 10  $\mu$ m. (b) Quantification of average pH values from panel (a). N = 79 (P), 80 (B1), and 80 (B2) from 3 independent experiments. (c) Same as panel (a) but now for MGAT2-RpHluorin2. (d) Quantification of average pH values from panel (c). N = 117 (P), 97 (B1), and 72 (B2) from 3 independent experiments. (e) Same as panel (a) but now for GalT-RpHluorin2. (f) Quantification of average pH values from panel (e). N = 65 (P), 72 (B1), and 52 (B2) from 3 independent experiments. (g) Same as panel (a) but now for LAMP1-RpHluorin2. (h) Quantification of average pH values from panel (g). N = 123 (P), 111 (B1), and 147 (B2) from 3 independent experiments.

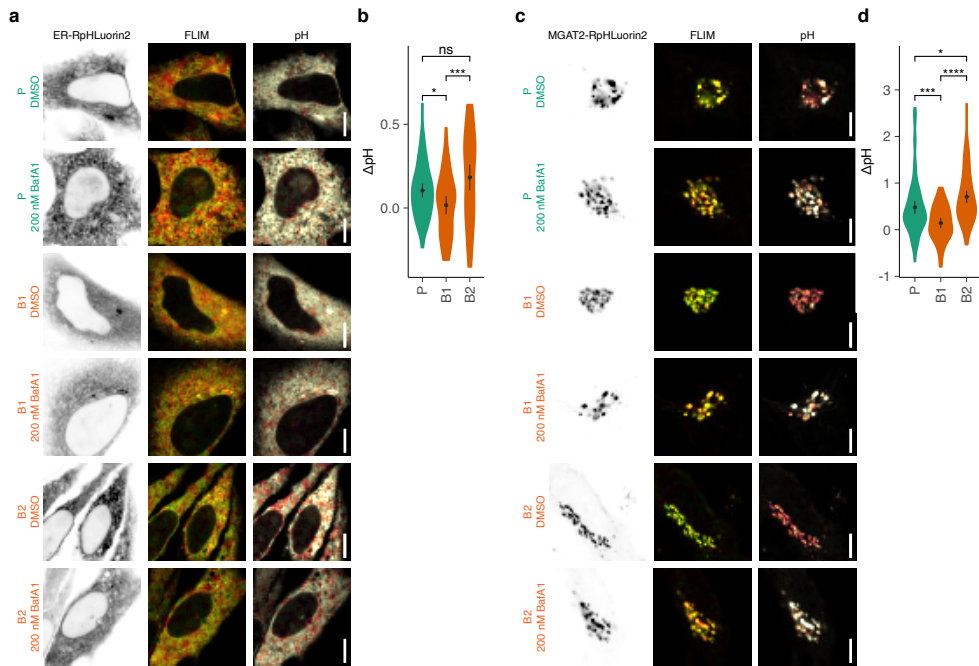


**Figure 4.4: FLIM-based pH measurements in TMEM199KO HeLa cells challenged with V-ATPase inhibitor Baflomycin A1.** (a) Representative confocal micrographs of parental HeLa cells (P, green) or TMEM199KO cells (B1 and B2, orange), in the absence (DMSO) or presence of Baflomycin A1 (200 nM BafA1). The intensity image (left column) was convoluted with the fluorescence lifetime value (middle column) and the calculated pH (right column) per pixel. FLIM, fluorescence lifetime imaging microscopy. Scalebars, 10  $\mu\text{m}$ . (b) Quantification of the difference in pH ( $\Delta\text{pH}$ ) between vehicle control (DMSO) and cells challenged with Baflomycin A1 from panel (a). N = 84 (P, DMSO), 62 (P, 200 nM BafA1), 41 (B1, DMSO), 46 (B1, 200 nM BafA1), 43 (B2, DMSO), and 50 (B2, 200 nM BafA1) from 2 independent experiments. (c) Same as panel (a) but now for MGAT2-RpHLuorin2. (d) Quantification of the difference in pH ( $\Delta\text{pH}$ ) between vehicle control (DMSO) and cells challenged with Baflomycin A1 from panel (c). N = 72 (P, DMSO), 77 (P, 200 nM BafA1), 78 (B1, DMSO), 46 (B1, 200 nM BafA1), 63 (B2, DMSO), and 71 (B2, 200 nM BafA1) from 2 independent experiments.

Supplementary Figure 4.10a). We observed similar results for *cis*-/medial-Golgi marker MGAT2-RpHLuorin2, where  $\Delta\text{pH}$  was significantly decreased for B1 cells but slightly increased for B2 cells (Figure 4.4c, d, Supplementary Figure 4.10b). Finally, we performed the same assay for *trans*-Golgi marker GalT-RpHLuorin2. Here we observed a small increase in  $\Delta\text{pH}$  for B1 cells but BafA1-sensitivity was absent for B2 cells (Supplementary Figure 4.10c-e). The observed increase in  $\Delta\text{pH}$  for the B2 cells in both ER and early Golgi compartments does not support a role of TMEM199 in V-ATPase assembly but suggests aberrant trafficking and/or processing of the V-ATPase as more V-ATPase molecules appear to be present on the ER membrane. Concurrently, less V-ATPase might be present on GalT-positive compartments which could indicate a disorganization of the pH gradient in the secretory pathway.

#### 4.3.4 Biochemical investigations of the role of TMEM199 in V-ATPase assembly

Prior to  $V_0 - V_1$  assembly, the  $V_0$  domain is first assembled in the ER<sup>69,101,102,290</sup>. Previous studies have shown that the stability of the  $V_0$ a subunits is dependent on this assembly of the  $V_0$  domain, resulting in degradation of the  $V_0$ a subunits when the  $V_0$  domain is not assembled<sup>101,102</sup>. We investigated the stability of endogenous  $V_0$ a1-3 in the parental HeLa cells and the B1 and B2 cells when chased with ribosomal inhibitor cycloheximide (Figure 4.5a-d). Stability of the subunits  $V_0$ a1 and  $V_0$ a3 was not visibly altered between parental HeLa cells, B1 and B2 cells (Figure 4.5a, b, d). However, we did observe lower stability of the Golgi- and endosome-localized  $V_0$ a2 subunit in both TMEM199 knockout strains (Figure 4.5a, c), suggesting that TMEM199 might be involved in the assembly of a Golgi- and endosome-specific  $V_0$ -domain.

To investigate whether these results have any implication on overall  $V_0 - V_1$  assembly, we fractionated parental HeLa, B1 and B2 cells into membrane and cytosolic fractions following intracellular crosslinking with dithiobis(succinimidyl propionate) (DSP) (Figure 4.5e, f). We then quantified the relative amounts of the  $V_1$ A subunit from the cytosolic  $V_1$  domain present in the membrane fraction and observed an unsignificant trend towards more overall  $V_0 - V_1$  assembly in the TMEM199KO cells. These results suggest that although less  $V_0$ a2-specific assembly might occur, complete V-ATPase assembly might be somewhat increased.

Finally, as it is known that cytosolic CCDC115 can interact with the integral membrane protein TMEM199<sup>125</sup>, we investigated whether CCDC115 would be associated with the membrane fractions. From yeast it is understood that cytosolic Vma22p can associate with membrane Vma12p<sup>122</sup> and this interaction is required for V-ATPase assembly in yeast. Thus, we hypothesized that a similar interaction is important in mammalian cells and that the loss of TMEM199 should cause less membrane association of CCDC115. We interrogated the presence of CCDC115 in the earlier obtained DSP-treated membrane fractions and we observed slightly less CCDC115 in the membrane fraction of B1 cells, and almost no CCDC115 in the membrane fraction of B2 cells (Figure 4.5g). We did not observe CCDC115 in the cytosolic fraction, which could be an indication of cytosolic instability of CCDC115. Taken together, these results suggest that TMEM199 might be important for the specific assembly of a  $V_0$ a2-containing V-ATPase, possibly together with CCDC115.

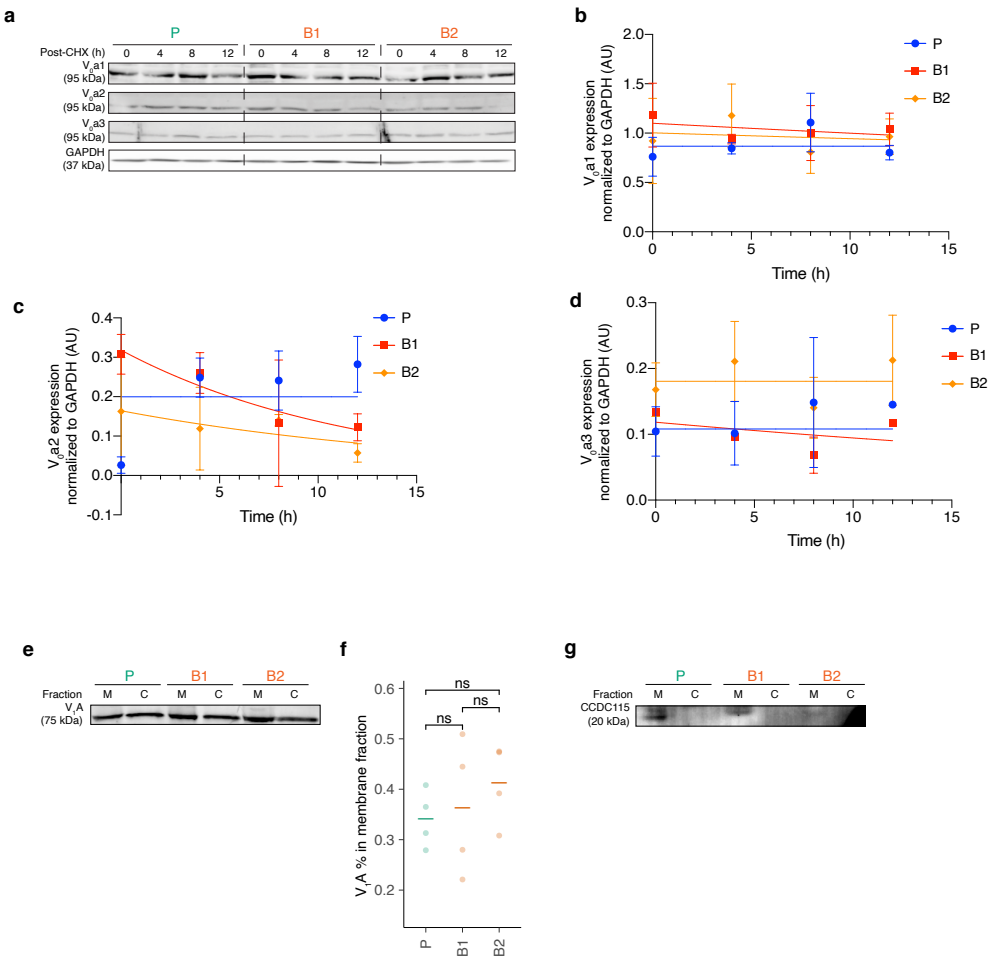


**Figure 4.5: The role of TMEM199 in mammalian V-ATPase assembly.** (a) Representative immunoblot of cell lysates for the stability of V-ATPase subunits V<sub>0</sub>a1, V<sub>0</sub>a2, and V<sub>0</sub>a3, in parental HeLa cells (P, green) or TMEM199KO cells (B1 and B2, orange) treated with cycloheximide (CHX) for the times indicated. GAPDH, loading control. (b) Quantification of panel (a) for V<sub>0</sub>a1. Protein expression levels were normalized to GAPDH signal. Data from 2 independent experiments. (c) Same as panel (b) but now for V<sub>0</sub>a2. (d) Same as panel (b) but now for V<sub>0</sub>a3. (e) Representative immunoblot of V-ATPase subunit V<sub>1</sub>A in membrane (M) and cytosolic (C) fractions of cell lysates from parental HeLa cells (P, green) or TMEM199KO cells (B1 and B2, orange) after crosslinking with DSP. Membrane and cytosolic fractions were obtained by ultracentrifugation. (f) Quantification of panel (e). Each point represents the percentage of the V<sub>1</sub>A membrane fraction, obtained by dividing the membrane signal by the total V<sub>1</sub>A signal (membrane + cytosolic fraction) from one experiment. Data from 4 independent experiments. (g) Representative immunoblot of CCDC115 in membrane (M) and cytosolic (C) fractions of cell lysates from parental HeLa cells (P, green) or TMEM199KO cells (B1 and B2, orange) after crosslinking with DSP. Membrane and cytosolic fractions were obtained by ultracentrifugation.

## 4.4 Discussion

In this study, we investigated the function of TMEM199 in intraorganellar acidification. The yeast homolog of TMEM199, Vma12p, is a known assembly factor of the V-ATPase<sup>122,124</sup> and is thereby involved in luminal pH maintenance. Our findings suggest a specific role for TMEM199 in assembly of  $V_0a2$ -containing V-ATPase, but not or less V-ATPases with the other three  $V_o$ a subunits in mammalian cells<sup>74–79</sup>. This specific role seems to contrast yeast where Vma12p has a more general function in V-ATPase assembly<sup>122,124</sup>.

In some of our experiments, we observed opposite phenotypes for the two TMEM199KO strains: the subcellular localization of glycosyltransferases and the pH measurements upon Baflomycin A1 treatment were significantly altered in opposite directions for the two strains. This might be a consequence of off-target effects of the gRNA in one of these strains. Alternatively, the contrasting phenotypes could be caused by the different residual expression of TMEM199, as strain B1 had somewhat higher levels of TMEM199 than B2. This might result in differences of residual V-ATPase activity and cause the different luminal pH values and subcellular localization of the glycosyltransferases. Moreover, Golgi pH is not only regulated by the V-ATPase, but partly also by passive backflux of  $H^+$  ions and by ion channels such as GPHR<sup>291</sup>. The activity and/or localization of these factors might also be sensitive to the levels of V-ATPase activity, and thereby contribute to the different phenotypes observed in the two TMEM199KO strains.

TMEM199 has been shown to mediate the  $V_0 - V_1$  assembly in human lung adenocarcinoma A549 cells<sup>129</sup>. However, we were not able to observe this with our TMEM199 knockout HeLa models but instead mostly observed a lower intraorganellar pH, suggesting elevated V-ATPase activity, at the ER and early Golgi compartments. The regulation and function of the V-ATPase is altered in different kinds of tumor cells<sup>276</sup> and this might explain the differences observed between HeLa cells and A549 cells lacking TMEM199. An important finding is the specific degradation of  $V_0a2$  in TMEM199-lacking cells. Therefore, a possible explanation for the discrepancy between our study and previous findings in A549 cells<sup>129</sup>, could be that A549 cells are more dependent on the  $V_0a2$ -defined V-ATPase and are therefore more sensitive to the loss of TMEM199. HeLa cells might then be more dependent on other  $V_o$ a subunits, meaning the loss of the  $V_0a2$ -defined V-ATPase would not result in a loss of acidification.

However, we even observed an increased acidification in the ER and early Golgi compartments in HeLa cells lacking TMEM199, suggesting that there is more V-ATPase present on these organellar membranes upon loss of TMEM199. This conclusion was strengthened by the increased sensitivity of ER-localized V-ATPase to Baflomycin A1

in one of the TMEM199KO strains. One possibility for the increased luminal acidification in TMEM199KO is that there might be increased assembly of V-ATPases, perhaps as a compensatory mechanism for the reduction of the V<sub>0</sub>a2-containing V-ATPase. Another possibility is that TMEM199 is involved in the trafficking of the V-ATPase from the ER to other organelles, and lack of TMEM199 results in elevated levels and activity of the V-ATPase in the ER and early Golgi compartments.

The fractionation studies we presented in this study revealed a potential molecular mechanism for the phenotypes observed in TMEM199-CDG patients <sup>121</sup>. Our results suggest that CCDC115 is recruited to membranes by TMEM199. Mutations in both CCDC115 and TMEM199 are a cause of glycosylation disorders, although the pathological condition in TMEM199-CDG seem more limited (mostly hepatological involvement) <sup>121</sup>, while CCDC115-CDG is characterized by more severe symptoms including neurological involvement <sup>120</sup>. An explanation for this difference could be that there is another mechanism for CCDC115 to exert its function in absence of TMEM199. Another, more likely, explanation is that the genetic variants found in TMEM199-CDG patients still produce TMEM199 protein, but that the binding affinity with for instance CCDC115 is reduced. This might result in a milder phenotype for TMEM199-CDG than for CCDC115-CDG.

#### 4.4.1 Acknowledgments

We thank Feng Zhang for providing the eSpCas9(1.1) construct (Addgene plasmid #71814). We also thank the Microscopic Imaging Center of the Radboud Institute for Molecular Life Sciences for use of their microscopy facilities. G.v.d.B. is funded by a Young Investigator Grant from the Human Frontier Science Program (HFSP; RGY0080/2018) and a Vidi grant from the Netherlands Organisation for Scientific Research (NWO-ALW VIDI 864.14.001). G.v.d.B has also received funding from the European Research Council (ERC) under the European Union's Horizon 2020 research and innovation program (grant agreement No. 862137).

#### 4.4.2 Author Contributions

P.T.A.L., E.P., M.t.B., and G.v.d.B. designed and performed the experiments and wrote the paper.

#### 4.4.3 Declaration of Interests

The authors declare that they have no competing financial interests.

## 4.5 Methods

### 4.5.1 Cell culture and transfection

HeLa cells (authenticated by ATCC through their human STR profiling cell authentication service) and derived TMEM199KO cells were maintained in high glucose DMEM with Glutamax (Gibco 31966021), supplemented with 10% fetal calf serum (FCS, Greiner Bio-one, Kremsmünster, Austria) and antibiotic-antimycotic solution (Gibco 15240-062). Cells were regularly tested for mycoplasma contamination. Cells were transfected with plasmid vectors using Fugene HD (Promega E2311), using the recommended protocol of the manufacturer. Cells were processed 48 hours post-transfection. Only cells expressing low to moderate levels of the transfected plasmids, based on fluorescence intensity and manual localization scoring, were chosen for subsequent microscopic analyses.

### 4.5.2 Antibodies

The following primary antibodies and dilutions were used in this study: rabbit polyclonal anti-TMEM199 (Novus Biological, NBP1-88467, 1:250), rat monoclonal anti- $\alpha$ -Tubulin (YOL1/34, Novus Biologicals NB100-1639, 1:2000) rabbit monoclonal anti-MGAT1 (Abcam, ab180578, 1:100), mouse monoclonal anti-GALNT2 (1501421, Biologend 682302, 1:100), mouse monoclonal anti-B4GALT1 (GT2/36/118, Enzo ALX-803-339-c050, 1:100), mouse monoclonal anti-GM130 (35/GM130, BD Transduction Laboratories 610822, 1:100), rabbit polyclonal anti-ZFPL1 (Sigma HPA014909, 1:100), sheep polyclonal anti-TGN46 (BioRad AHP500GP, 1:1000), rabbit monoclonal anti-GAPDH (14C10, Cell Signaling Technology 2118, 1:2000), rabbit polyclonal anti-V<sub>0</sub>a1 (Novus Biological NBP1-89342, 1:500), rabbit polyclonal anti-V<sub>0</sub>a2 (Novus Biological NBP1-59069, 1:500), mouse monoclonal anti-V<sub>0</sub>a3 (Novus Biological H00010312-M01, 1:500), mouse monoclonal anti-V<sub>1</sub>A (4F5, Santa Cruz Biotechnology sc-293336, 1:500), and rabbit polyclonal anti-CCDC115 (Proteintech, 20636-1-AP, 1:250).

### 4.5.3 CRISPR/Cas9

Knockout of TMEM199 in HeLa cells was achieved using CRISPR/Cas9. We used the prior described gRNA sequence: 5' – TATGG CGTCC TCTTT GCTTG CGG<sup>125</sup>. The gRNA sequence was cloned in eSpCas9(1.1) (Gift from Feng Zhang, Addgene no. 71814)<sup>292</sup> and transfected into HeLa cells by Fugene HD (Promega). 72 hrs after transfection, the medium of puromycin-resistant cells was changed for conditioned medium (collected from parental HeLa cells at 70% confluence) supplemented 1:1 with fresh medium. Single

clones were obtained and screened for knockout of TMEM199 by SDS-PAGE and Western blotting and finally validated by Sanger sequencing. Residual TMEM199 might be a consequence of contamination by parental HeLa cells during cell culture.

#### 4.5.4 Lectin stainings

Cells were plated in 6-well plates and incubated until confluent ( $\approx$ 72 h). Cells were released from the culture substrate with 2 mM EDTA in PBS. Cells were then blocked with Carbo-Free blocking solution (Vector Laboratories, SP-5040) and incubated with and incubated with 4  $\mu$ g/mL biotinylated SNA-I (Vector Laboratories, B-1305) diluted in Carbo-Free Blocking solution. Cells were then incubated with Streptavidin-Alexa Fluor 647 (ThermoScientific, S32357) and finally resuspended in FACS buffer (phosphate buffered saline + 0.5% FBS + 0.01% NaN<sub>3</sub>), supplemented with 300 ng/mL 4',6-diamidino-2-phenylindole (DAPI) for live/dead discrimination. Samples were run on a FACSLyric flow cytometer (BD Biosciences) and analyzed with FlowJo X (FlowJo, LLC).

#### 4.5.5 pH measurements

pH measurements were performed as described previously<sup>288</sup>. Briefly, RpHLuorin2-tagged constructs were transiently overexpressed in cells followed by FLIM. The lifetime values were subsequently calculated to pH values using the prior generated calibration curve<sup>288</sup>. For the Bafilomycin A1 experiments, cells were pre-incubated with 200 nM Bafilomycin A1 (Cayman Chemical) or DMSO (ThermoFisher) for 1 hour at 37°C.

#### 4.5.6 Confocal microscopy

Imaging of cells was performed in Leibovitz's L-15 medium (Gibco). All confocal microscopy was performed a Leica SP8 SMD system at 37°C, equipped with an HC PL APO CS2 63 $\times$ /1.20 WATER objective. pHLuorin2 was excited at 488 nm with a pulsed white light laser, operating at 80 MHz. Photons were collected for one minute or 30 seconds for time-lapse experiments with a HyD detector set at 502 – 530 nm and lifetime histograms of the donor fluorophore were fitted with a monoexponential decay function convoluted with the microscope instrument response function in Leica LAS X. For reconstructing the images, tiff files with  $\tau$  values were generated using FLIMFit<sup>284</sup> and 2  $\times$  2 spatial binning, and then convoluted with the fluorescent intensities using a custom-written ImageJ macro.

#### 4.5.7 Immunofluorescence

Immunofluorescence experiments for glycosyltransferase localization were performed as described previously<sup>207</sup>.

#### 4.5.8 Crosslinking and cell fractionation

Cells were plated in 10 cm dishes and cultured until confluent. Once confluent, cells were harvested by washing twice in ice-cold PBS followed by scraping into homogenization buffer (250 mM sucrose, 10 mM N-[2-hydroxyethyl]-piperazine-N-[2-ethanesulfonic acid] (HEPES), 1 mM Ethylenediaminetetraacetic acid (EDTA) and protease inhibitor cocktail (Roche)). Intracellular proteins were subsequently crosslinked with 500  $\mu$ M dithiobis(succinimidyl propionate) in DMSO at RT for 30 mins with agitation. The crosslinking reaction was then quenched by addition of Tris pH 7.6 to a final concentration of 20 mM and 15 mins incubation at RT with agitation. Cells were lysed by passing through a 25G needle sixteen times. Post-nuclear supernatants were acquired by centrifuging at  $500 \times g$  for 10 mins. The supernatant was subsequently ultracentrifuged at  $100,000 \times g$  for 30 mins to pellet the membrane fraction. The membrane pellet was rinsed once with homogenization buffer and resuspended in homogenization buffer with 1% SDS. Protein content was then determined and samples were subsequently analyzed by SDS-PAGE and immunoblotting.

#### 4.5.9 SDS-PAGE and immunoblotting

Whole cell lysates were prepared using SDS lysis buffer (1% SDS in 10 mM Tris-HCl pH 6.8). Prior to SDS-PAGE, protein concentrations were determined using the Micro BCA assay (ThermoFisher).

#### 4.5.10 Quantification and statistical analysis

Statistical analysis of three or more groups was performed using pair-wise t-tests, followed by p-value adjustment using Bonferroni's method.  $p < 0.05$  was considered significant. \* $p < 0.05$ , \*\* $p < 0.01$ , \*\*\* $p < 0.001$ , \*\*\*\* $p \leq 0.0001$ . All statistical analyses were performed using R statistical software, using the *ggpubr* package. All numerical data were visualized using R package *ggplot2*<sup>286</sup>, with violins representing the overall distribution of the data and means  $\pm$  95% CI overlaid.

## 4.6 Supplementary Information

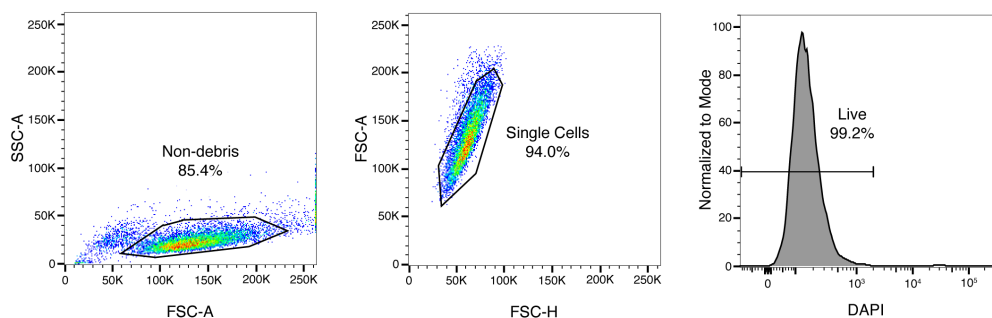


**Figure 4.6: FACS gating strategy for lectin stainings.** The cell population shown is of the parental sample shown in Figure 4.1b. FSC-A: forward scatter area, SSC-A: side scatter area, FSC-H: forward scatter height.

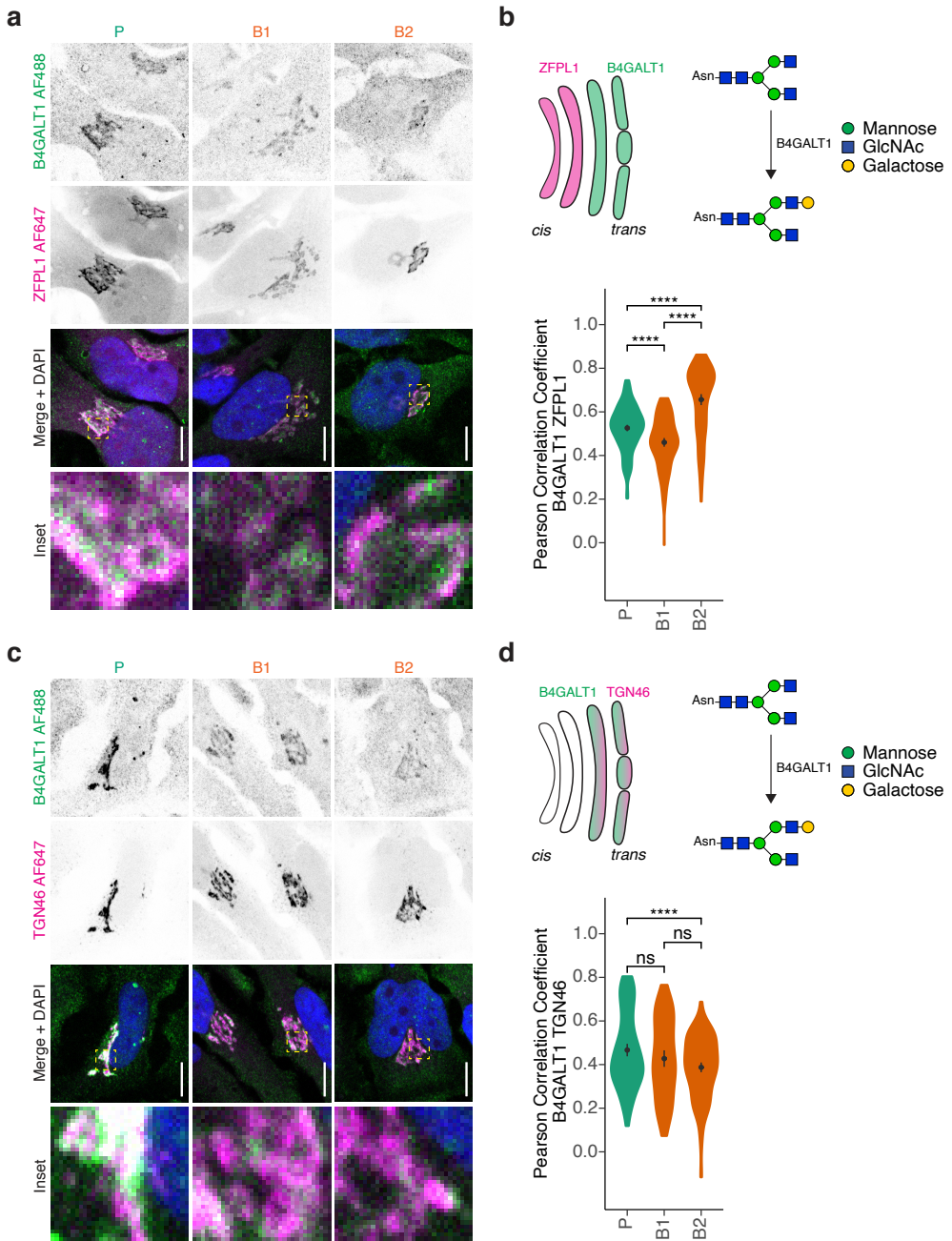


**Figure 4.7: Relocation of glycosyltransferase B4GALT1 in TMEM199KO HeLa cells.** (a) Immunofluorescence microscopy of B4GALT1 (green in merge) and ZFPL1 (magenta) in parental HeLa cells (green, P) or TMEM199KO cells (B1 and B2, orange). Representative confocal micrographs. Scalebars, 10  $\mu$ m. DAPI in blue. (b) Pearson's correlation coefficients between B4GALT1 and ZFPL1 of panel(a). N = 194 (P), 138 (B1), and 147 (B2) from two independent experiments. (c) Same as panel (a) but now for B4GALT1 (green) and TGN46 (magenta). (d) Pearson's correlation coefficients between B4GALT1 and TGN46 of panel (c). N = 139 (P), 154 (B1), and 161 (B2) from two independent experiments.

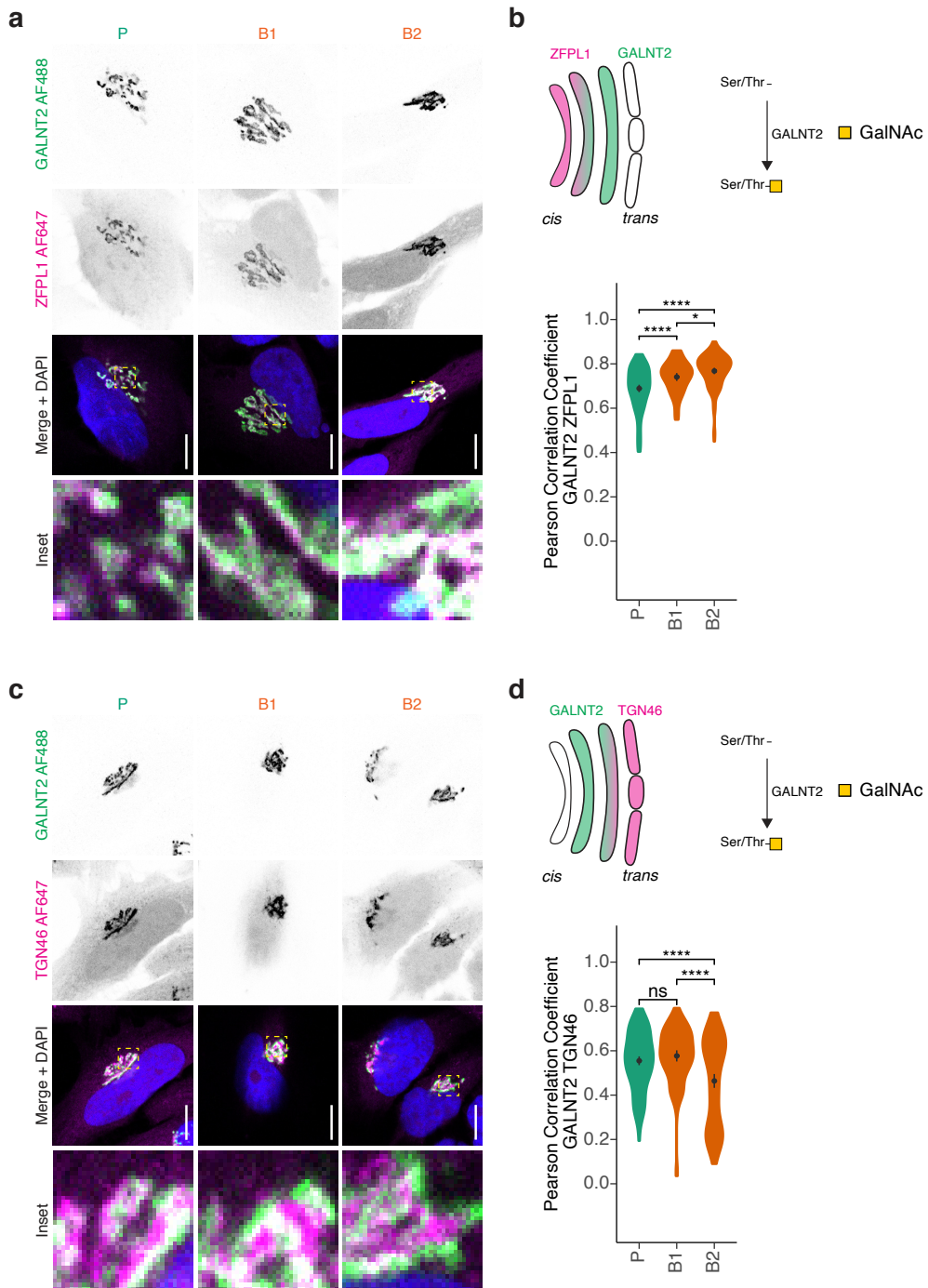


Figure 4.8: Relocation of glycosyltransferase GALNT2 in TMEM199KO HeLa cells. (Continued on the following page.)

**Figure 4.8:** (a) Immunofluorescence microscopy of GALNT2 (green in merge) and ZFPL1 (magenta) in parental HeLa cells (green, P) or TMEM199KO cells (B1 and B2, orange). Representative confocal micrographs. Scale-bars, 10  $\mu$ m. DAPI in blue. (b) Pearson's correlation coefficients between GALNT2 and ZFPL1 of panel (a). N = 142 (P), 65 (B1), and 117 (B2) from two independent experiments. (c) Same as panel (a) but now for GALNT2 (green) and TGN46 (magenta). (d) Pearson's correlation coefficients between GALNT2 and TGN46 of panel (c). N = 170 (P), 101 (B1), and 154 (B2) from two independent experiments.

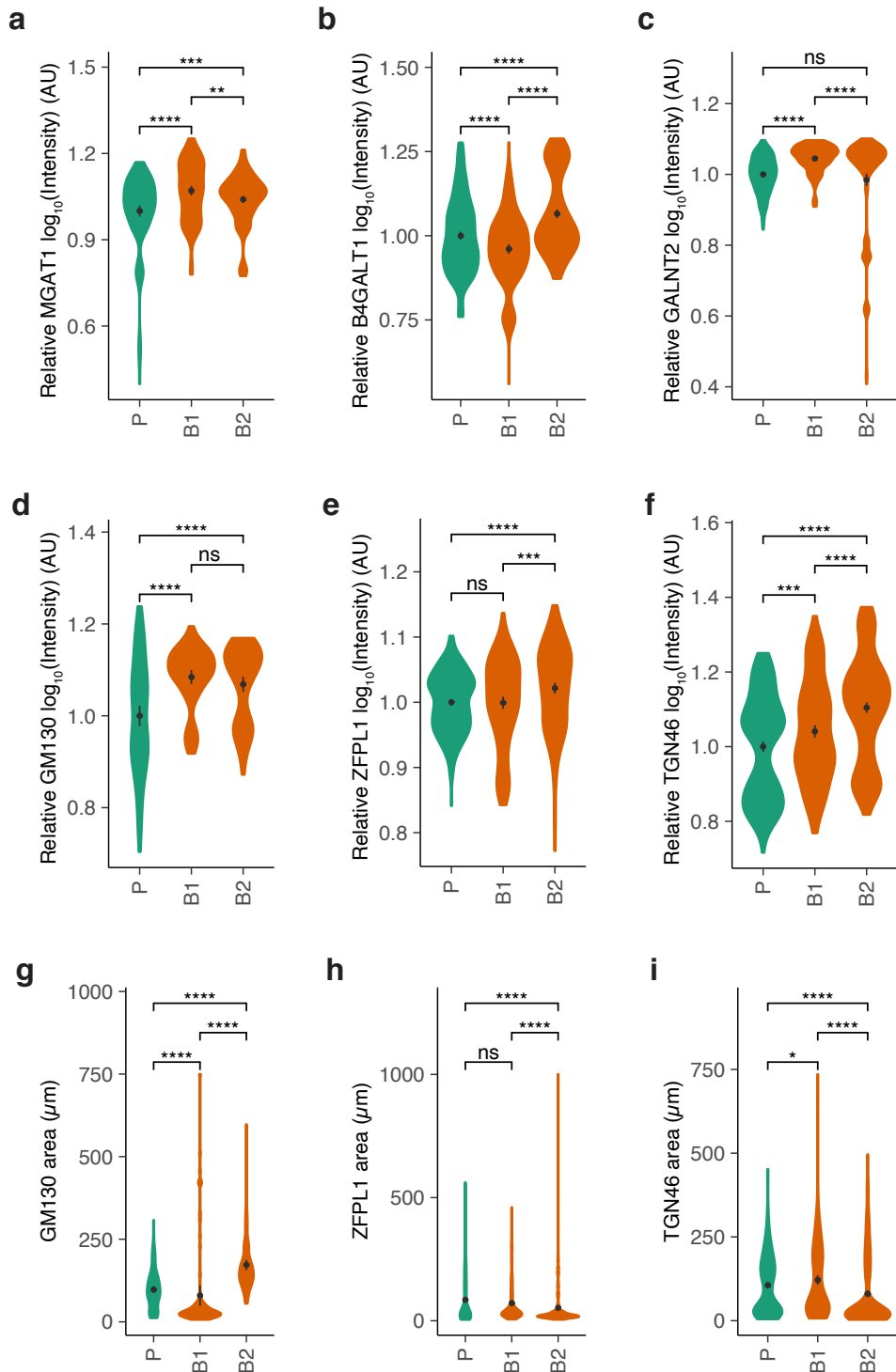


Figure 4.9: Altered glycosyltransferase expression and Golgi morphology in TMEM199KO HeLa cells. (Continued on the following page.)

**Figure 4.9:** (a) Fluorescence intensities of MGAT1 from Figure 4.2 relative to parental HeLa cells. N = 193 (P), 146 (B1), 198 (B2). (b) Same as panel (a) but now for B4GALT1 from Supplementary Figure 4.7. N = 333 (P), 226 (B1), 308 (B2). (c) Same as panel (a) but now for GALNT2 from Supplementary Figure 4.7. N = 312 (P), 166 (B1), 271 (B2). (d) Same as panel (a) but now for GM130 from Figure 4.2. N = 118 (P), 78 (B1), 99 (B2). (e) Same as panel (a) but now for ZFPL1 from Supplementary Figures 4.7 and 4.8. N = 336 (P), 203 (B1), 264 (B2). (f) Same as panel (a) but now for TGN46 from Figure 4.2 and Supplementary Figures 4.7 and 4.8. N = 384 (P), 257 (B1), 414 (B2). (g) Quantification of GM130 fluorescence labeling area from Figure 4.2. N = 118 (P), 78 (B1), 99 (B2). (h) Same as panel (g) but now for ZFPL1 from Supplementary Figures 4.7 and 4.8. N = 336 (P), 203 (B1), 264 (B2). (i) Same as panel (g) but now for TGN46 from Figure 4.2 and Supplementary Figures 4.7 and 4.8. N = 384 (P), 257 (B1), 414 (B2).

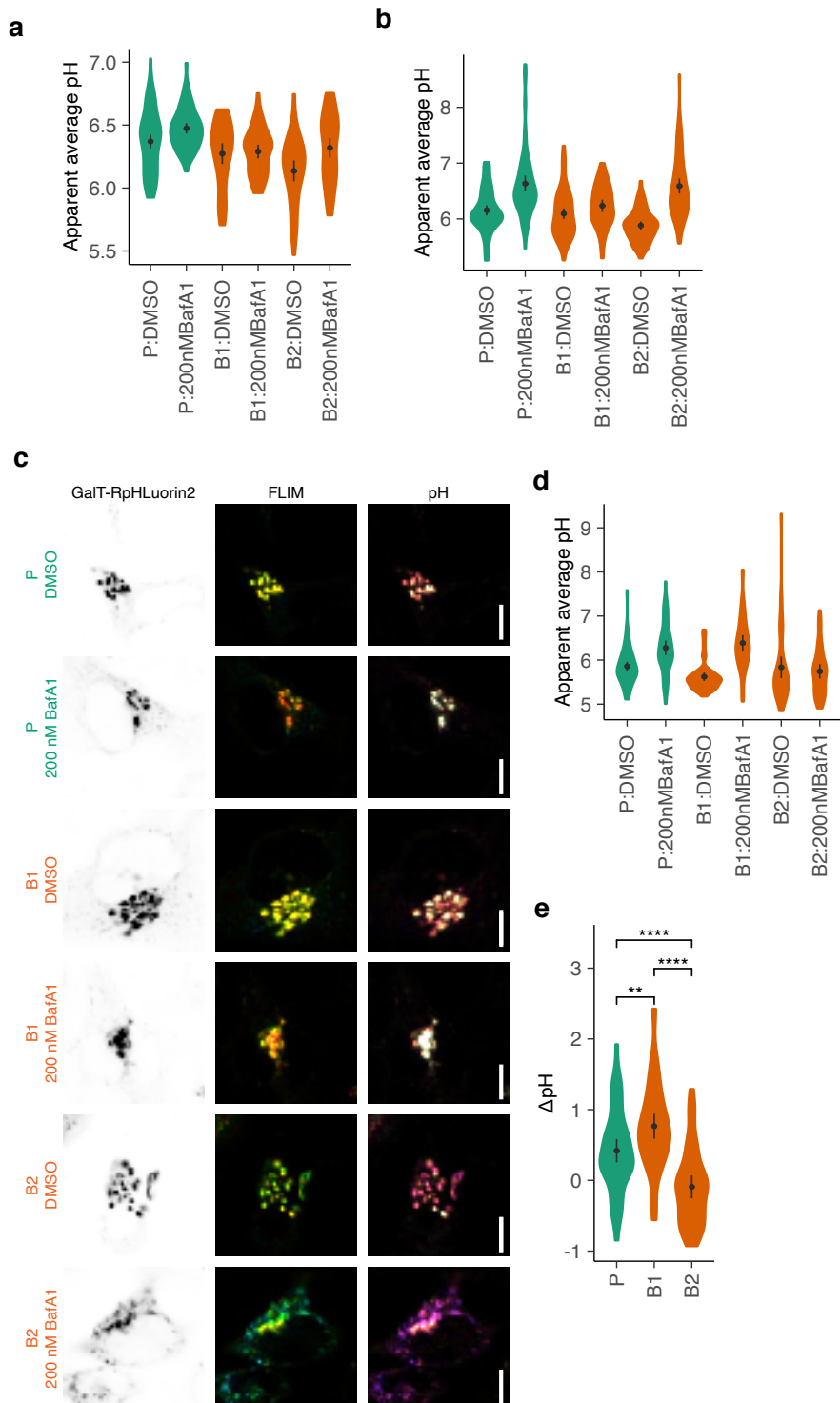


Figure 4.10: FLIM-based pH measurements in TMEM199KO HeLa cells challenged with V-ATPase inhibitor  $\beta$ -filomycin A1. (Continued on the following page.)

**Figure 4.10:** (a) Full quantification of pH from Figure 4.4a. The values presented here were used to generate the  $\Delta\text{pH}$  plot. (b) Same as panel (a) but now for Figure 4.4c. (c) Representative confocal micrographs of parental HeLa cells (P, green) or TMEM199KO cells (B1 and B2, orange) expressing GalT-RpHLuorin2, in the absence (DMSO) or presence of Bafilomycin A1 (200 nM BafA1). The intensity image (left column) was convoluted with the fluorescence lifetime value (middle column) and the calculated pH (right column) per pixel. FLIM, fluorescence lifetime imaging microscopy. Scalebars, 10  $\mu\text{m}$ . (d) Same as panel (a) but now for panel (c). (e) Quantification of the difference in pH ( $\Delta\text{pH}$ ) between vehicle control (DMSO) and cells challenged with Bafilomycin A1 from panel (c). N = 68 (P, DMSO), 50 (P, 200 nM BafA1), 48 (B1, DMSO), 49 (B1, 200 nM BafA1), 46 (B2, DMSO), and 44 (B2, 200 nM BafA1) from 2 independent experiments.



P.T.A. Linders, C. van der Horst, M. ter Beest and G. van den Bogaart  
*Cells* 2019, 8(8), 780

# 5

## Stx5-Mediated ER-Golgi Transport in Mammals and Yeast

## 5.1 Abstract

The soluble N-ethylmaleimide-sensitive factor attachment protein receptor (SNARE) syntaxin 5 (Stx5) in mammals and its ortholog Sed5p in *Saccharomyces cerevisiae* mediate anterograde and retrograde endoplasmic reticulum (ER)-Golgi trafficking. Stx5 and Sed5p are structurally highly conserved and are both regulated by interactions with other ER-Golgi SNARE proteins, the Sec1/Munc18-like protein Scfd1/Sly1p and the membrane tethering complexes COG, p115, and GM130. Despite these similarities, yeast Sed5p and mammalian Stx5 are differently recruited to COPII-coated vesicles, and Stx5 interacts with the microtubular cytoskeleton, whereas Sed5p does not. In this review, we argue that these different Stx5 interactions contribute to structural differences in ER-Golgi transport between mammalian and yeast cells. Insight into the function of Stx5 is important given its essential role in the secretory pathway of eukaryotic cells and its involvement in infections and neurodegenerative diseases.

## 5.2 Introduction

The secretory pathway is essential for secretion of cytokines, hormones, growth factors, and extracellular matrix proteins, as well as for the delivery of receptors and transporters to the cell membrane and lytic proteins to endo-lysosomal compartments. Proteins destined for the secretory pathway are synthesized at the endoplasmic reticulum (ER) and subsequently transported to their destination by vesicular trafficking via the *cis*- to medial- to *trans*-Golgi cisternae and finally to the *trans*-Golgi network<sup>14,202,293</sup>. ER-Golgi transport has been mostly studied in mammalian cells and the yeast *Saccharomyces cerevisiae*, and although the basic mechanisms of this ER-Golgi trafficking are well conserved among eukaryotic cells, there are three pronounced differences between the yeast *S. cerevisiae* and mammalian cells (Figure 5.1).

The first difference concerns the spatial organization of the Golgi apparatus. In most mammalian cell types, a single large Golgi apparatus is juxtaposed with the nucleus and surrounds the microtubule organizing center (MTOC)<sup>14–16</sup>. In contrast, in *S. cerevisiae*, the Golgi is organized into discrete cisternae, consisting of individual cisternae that are scattered throughout the cytoplasm, while in other yeast, such as budding *Pichia pastoris* and *Schizosaccharomyces pombe*, the Golgi is present as mini-stacks that are dispersed in the cytoplasm<sup>15,16</sup>.

The second difference is the presence of an intermediate compartment between the ER and *cis*-Golgi in mammals called the ER-Golgi intermediate compartment (ERGIC) or vesicular-tubular cluster (VTC)<sup>63</sup>. Yeast does not have an ERGIC, and anterograde trafficking from the ER occurs directly to the *cis*-Golgi<sup>294</sup> via vesicles coated with the cage protein complex COPII, while retrograde trafficking in the reverse direction occurs via vesicles coated with COPI<sup>14,15</sup>. In mammalian cells, anterograde trafficking from the ER also occurs via COPII-coated vesicles, but in this case, proceeds to the ERGIC<sup>14–16</sup>. In mammalian cells, not only retrograde trafficking from the ERGIC back to the ER but also further anterograde trafficking to the *cis*-Golgi might occur via COPI-coated vesicles<sup>64</sup>.

A final difference in ER-Golgi trafficking is the involvement of microtubules in mammalian cells, but not in yeast<sup>14–16</sup>.

In this review, we argue that these mechanistic differences between mammals and yeast are partly attributable to one of the central players in ER-Golgi trafficking: the SNARE protein syntaxin 5 (Stx5) in mammals and its yeast ortholog Sed5p.

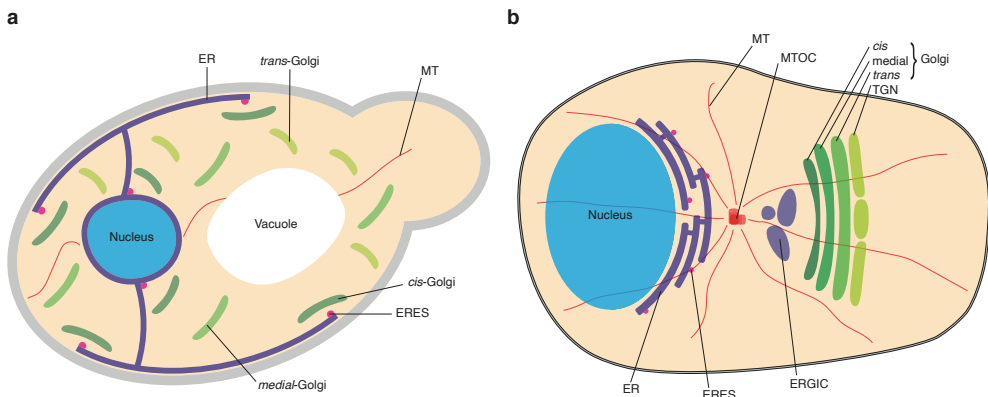


**Figure 5.1: Schematic overview of the early secretory pathway in *Saccharomyces cerevisiae* (A) and mammalian cells (B). Abbreviations: ER, endoplasmic reticulum; ERES, endoplasmic reticulum exit sites; ERGIC, endoplasmic reticulum-Golgi intermediate compartment; MT, microtubule; MTOC, microtubule organizing center; TGN, trans-Golgi network.**

### 5.3 SNARE Proteins in ER-Golgi and Intra-Golgi Transport

The SNARE protein family consists of about 38 members in humans and about 24 in yeast and is responsible for most intracellular fusion events of organelar trafficking<sup>57,58,118</sup>. The central hallmark of SNARE proteins is the presence of one or two SNARE motifs of 50–70 residues in size. Based on the structures of these motifs, SNAREs can be grouped into R-SNAREs, with an arginine residue located at the center of the SNARE-motif, and Qa-, Qb- and Qc-SNAREs, with a central glutamine residue<sup>57,58</sup>. Membrane fusion requires three or four cognate SNARE proteins that together contribute four SNARE motifs, one of each group (R, Qa, Qb, Qc). For membrane fusion, these cognate SNARE proteins need to be anchored to both the donor membrane (e.g., COPII vesicle) and acceptor membrane (e.g., *cis*-Golgi) via a C-terminal transmembrane helix or by lipid modifications<sup>57,58</sup>. SNAREs in the donor membrane are called v-SNAREs (vesicular-SNAREs) and SNAREs in the acceptor membrane t-SNAREs (target-SNAREs). Cognate SNARE proteins can form a tight  $\alpha$ -helical coiled-coil bundle, called the SNARE complex, which overcomes the energy barrier of membrane fusion. In addition to this, the fusogenic activity of ER-Golgi SNAREs is tightly regulated by numerous interacting proteins and by N-terminal-regulating motifs, which are present on most SNAREs<sup>57,58</sup>. After membrane fusion, the SNARE complex is disassembled by the AAA ATPase N-ethylmaleimide-sensitive factor (NSF) in mammals and Sec18p in yeast, which are recruited by the adaptor protein-soluble NSF-attachment protein  $\alpha$  ( $\alpha$ -SNAP) in mammals and Sec17p in yeast<sup>57,58</sup>.

In mammalian cells, the Qa-SNARE Stx5 is an integral component of ER-derived

COPII transport vesicles and is required for the docking and fusion of these vesicles to assemble the ERGIC<sup>64,295</sup> by forming a SNARE complex with GosR2 (GS27, membrin; Qb-SNARE) or GosR1 (GS28; Qb), Bet1 (Qc), and Ykt6 (R) or Sec22b (Ers24; R) (Figure 5.2)<sup>194–200</sup>. This process is well conserved in yeast, where the fusion of COPII vesicles is believed to occur directly at the Golgi<sup>294</sup> by interactions of the orthologs of the mammalian SNAREs Sed5p (Qa), Bos1p (Qb), Bet1p (Qc), and Sec22p (R)<sup>201,296,297</sup>. Stx5/Sed5p is not involved in COPI-mediated retrograde transport from the Golgi to the ER, but this is mediated by Stx18 (Qa), Sec20 (Qb), Use1 (Qc), and Sec22b (R) in mammals and Ufe1p (Qa), Sec20p (Qb), Use1p (Qc), and Sec22p (R) in yeast<sup>202,203,298</sup>. However, Stx5 is involved in COPI-dependent intra-Golgi retrograde trafficking between cisternae and/or retrograde trafficking from endosomes to the *trans*-Golgi network by forming a SNARE complex with GosR1 (Qb), Bet1L (GS15; Qc), and Ykt6 (R)<sup>195,198,202,204–206</sup>. In yeast, intra-Golgi retrograde trafficking is mediated by Sed5p forming a SNARE complex with Gos1p (Qb), Sft1p (Qc), and Ykt6p (R)<sup>202,208,210</sup>. Anterograde vesicular trafficking is in principle not required for intra-Golgi transport, as in the widely-accepted cisternal maturation model, the cisternae are very dynamic entities, constantly forming at the *cis*-side by homotypic or/and heterotypic vesicular fusion, and disassembling into anterograde and retrograde membrane carriers at the *trans*-side<sup>14</sup>. In this model, all intra-Golgi vesicular traffic is going in a retrograde direction to recycle Golgi enzymes, cargo receptors and SNAREs<sup>14</sup>. In contrast, according to the vesicular transport model, the cisternae are relatively static with a constant enzyme composition. In this case, the cisternae accept anterograde vesicles with cargo molecules and shed retrograde vesicles with recycling SNAREs and cargo receptors<sup>14</sup>. In favor of the vesicular transport model, Stx5 was found to mediate anterograde trafficking within the Golgi, at least in *Drosophila melanogaster*<sup>299</sup>.

Both knockdown and overexpression of Stx5 induce Golgi fragmentation in mammalian cells<sup>196,300,301</sup> and *D. melanogaster*<sup>302</sup>. Because ER-Golgi transport is at the base of most exocytic trafficking, knockdown of Stx5 also causes downstream defects in lysosomal trafficking and autophagy<sup>303</sup>. In yeast, Sed5p is rate-limiting for ER-Golgi transport, because overexpression of Sed5p and to a lesser extent other SNAREs involved in ER-Golgi trafficking (Bos1p, Bet1p, Sec22p) resulted in higher secretion of overexpressed cellulase<sup>304</sup>. Most importantly, Stx5/Sed5p is an essential protein, and Stx5/Sed5p knockout is lethal for mammalian cells<sup>305</sup> and yeast<sup>306</sup>, while the STX5 gene knockout is not viable for mice<sup>307</sup> and *D. melanogaster*<sup>308</sup>.

There are two notable differences between the function of SNAREs in ER-Golgi transport and exocytic and endocytic trafficking. First, in mammals, Bet1 is proposed to be the v-SNARE for anterograde trafficking<sup>200,202,204–206</sup>, although another study reported that this is Sec22b<sup>194</sup>, and Bet1L is the v-SNARE for retrograde trafficking in intra-Golgi

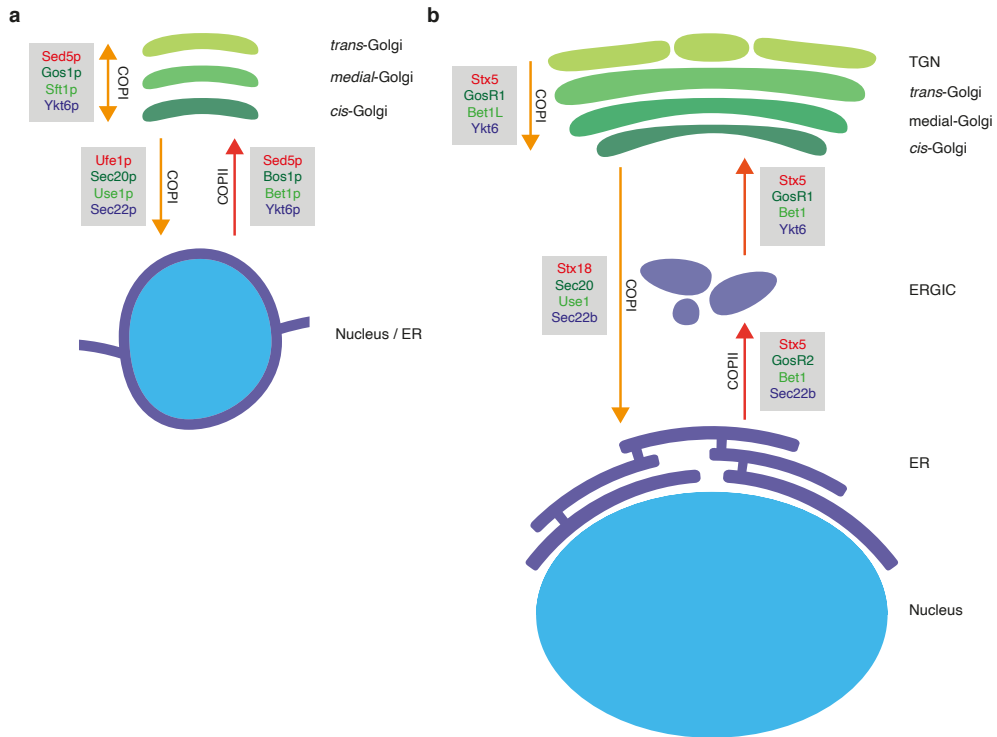


**Figure 5.2: Schematic overview of SNARE complexes of the early secretory pathway in *Saccharomyces cerevisiae* (A) and mammalian cells (B).** The grey boxes indicate the known SNARE complexes and their location along the secretory pathway. Colors of the SNAREs: red, Qa-SNAREs; dark green, Qb-SNAREs; light green, Qc-SNAREs; blue, R-SNAREs. Abbreviations: ER, endoplasmic reticulum; ERGIC, endoplasmic reticulum-Golgi intermediate compartment; TGN, *trans*-Golgi network.

transport<sup>200,202,204–206</sup>. Similarly, in yeast, the v-SNAREs for antero- and retrograde traffic are the yeast orthologs Bet1p and Sft1p, respectively<sup>208–210</sup>. This differs from other described SNARE-mediated trafficking routes, where R-SNAREs generally act as v-SNAREs, e.g., synaptobrevin in exocytosis, and the Qa-, Qb-, and Qc-SNAREs form an acceptor t-SNARE complex in the target membrane<sup>57,58,118</sup>. The second difference is in the promiscuity of SNAREs. Most SNAREs involved in exocytic and endocytic trafficking are very promiscuous, and nearly every combination of a Qa-, Qb-, Qc-, and R-SNARE can form a SNARE complex *in vitro*<sup>118</sup>. Because of this promiscuity, exocytic and endocytic SNAREs are often functionally redundant, and knockout or knockdown mostly has no or a very minor phenotype<sup>118</sup>. This is different for Stx5/Sed5p and other ER-Golgi SNAREs, which have been shown in *in vitro* studies to be highly stringent with purified Sed5p only being able to form a SNARE complex with other SNAREs involved in Golgi-ER trafficking Gos1p (Qb), Bos1p (Qb), Sft1p (Qc), Bet1p (Qc), Ykt6p (R), and Sec22p (R)<sup>309,310</sup>. In line with this, Sed5p forms two distinct non-overlapping Golgi SNARE complexes *in vivo* (Sed5p-Bos1p-Bet1p-Sec22p and Sed5p-Gos1p-Ykt6p-Sft1p)<sup>210</sup>.

In contrast to Stx5, which distributes evenly throughout the Golgi stack, electron microscopy revealed that Bet1L and Bet1 have opposite distributions within the Golgi stack with Bet1L more present at the *trans*-Golgi and Bet1 more present at the *cis*-Golgi<sup>205</sup>. This finding is the base of the SNARE gradient model, where retrograde trafficking is mediated by SNARE complex formation of Bet1L with Stx5, GosR1, and Ykt6 and anterograde trafficking by complex formation of Bet1 with Stx5, GosR2, and Sec22b<sup>202,205,293</sup>. Electron microscopy also revealed that within each Golgi layer, the SNAREs are also heterologously distributed with Bet1L, Stx5, and GosR1 more located to the center of each stack, whereas Bet1, Sec22b, and GosR2 locate more to the rims where they can be more efficiently incorporated into transport vesicles<sup>311</sup>. As Bet1 and Bet1L mediate anterograde and retrograde intra-Golgi trafficking, respectively<sup>200,202,204–206</sup>, this finding suggests that SNAREs involved in retrograde trafficking might be Golgi resident, whereas the SNAREs involved in anterograde trafficking might dynamically cycle through the Golgi layers. However, it is unclear how this relates to the cisternal maturation model that mainly relies on retrograde vesicular transport and in principle does not require any anterograde intra-Golgi vesicular transport<sup>14</sup>.

Stx5 is also involved in ER-Golgi trafficking of specialized cargo molecules. First, Stx5 is required for ER exit of pro-collagens, which are too large to fit in COPII transport vesicles, because its knockdown results in a reduction of pro-collagen I and VII secretion and accumulation of these pro-collagens in the ER<sup>312</sup>. Second, Stx5 mediates the specific export of very low-density lipoproteins (VLDLs) from the ER. VLDLs are synthesized in the ER of liver cells and then transported to the Golgi prior to secretion at the plasma membrane. This transport occurs via unique ER-derived vesicles called

5

VTVs (VLDL-transport vesicles)<sup>313</sup>. These vesicles differ from the other protein exporting vesicles as they are larger, have a lower buoyant density, and have different cargo and protein compositions<sup>313</sup>. It was found that VTVs contain Sec22b, which is able to make a SNARE complex at the *cis*-Golgi together with Stx5, GosR1, and Bet1<sup>314</sup>. Stx5 is able to bind to the cytoplasmic C-terminal domain of the VLDL receptor (VLDL-R), thereby influencing the receptor's glycosylation and trafficking<sup>315</sup>. Overexpression of Stx5 was found to prevent Golgi-maturation of VLDL-R and resulted in the decreased presence of VLDL-R at the *trans*-Golgi<sup>315</sup>. However, VLDL-R did not accumulate at the ER nor Golgi and was still translocated from the ER to the cell surface, indicating that overexpression of Stx5 resulted in circumvention of the regular secretory pathway and immature VLDL-R reached the cell surface via an alternative pathway<sup>315</sup>. In addition to VLDL, Stx5 mediates trafficking of another lipoprotein in intestinal cells. Dietary long-chain fatty acids are esterified to triacylglycerol and packaged in the chylomicron, which is the unique lipoprotein of the intestine. Rate-limiting for the transit of chylomicrons through the enterocyte is the exit of chylomicrons from the ER to the *cis*-Golgi in specialized 250 nm-sized transport vesicles. This process involves a t-SNARE complex of Stx5, Vti1a, and Bet1 and the v-SNARE VAMP7, which, based on inhibition of these SNAREs with antibodies, is believed to mediate the fusion of the chylomicrons with the *cis*-Golgi<sup>316</sup>. Note that in contrast to canonical ER-Golgi transport, where Bet1 acts as the v-SNARE<sup>200,202,204–206</sup>, in these lipoprotein trafficking routes, Bet1 is believed to act as a t-SNARE together with Stx5. However, this has never been studied side-by-side with the same assays, and whether the dual function as Bet1 as both a t- and v-SNARE is true remains to be established.

## 5.4 Subcellular Localization of Stx5 Isoforms

In mammalian cells, translation of Stx5 can occur at two different starting methionines resulting in two distinct isoforms: a 34.1-kDa short isoform of 301 residues and a 39.6-kDa long isoform that is extended by 54 N-terminal residues (Figure 5.3)<sup>215</sup>. In yeast, only a single 38.8-kDa and 340 residue-long isoform of Sed5p is expressed, which corresponds to the short isoform of Stx5 in mammalian cells. Both the short and long Stx5 isoforms in mammalian cells and yeast Sed5p are so-called tail-anchored proteins that contain a C-terminal transmembrane helix, which after translation is inserted into the ER membrane by AsnA1 in mammals<sup>317</sup> and its yeast ortholog Get3p<sup>318</sup> of the tail recognition complex (TRC) pathway. The subcellular localization of Stx5 and Sed5p at the ER-Golgi interface is largely determined by its transmembrane helix. Stx5 and Sed5p have a short transmembrane helix of only 20 residues in length, which is much shorter than most other SNAREs ( $\approx$ 24 residues), and this supports their recycling

## 5.4. Subcellular Localization of Stx5 Isoforms

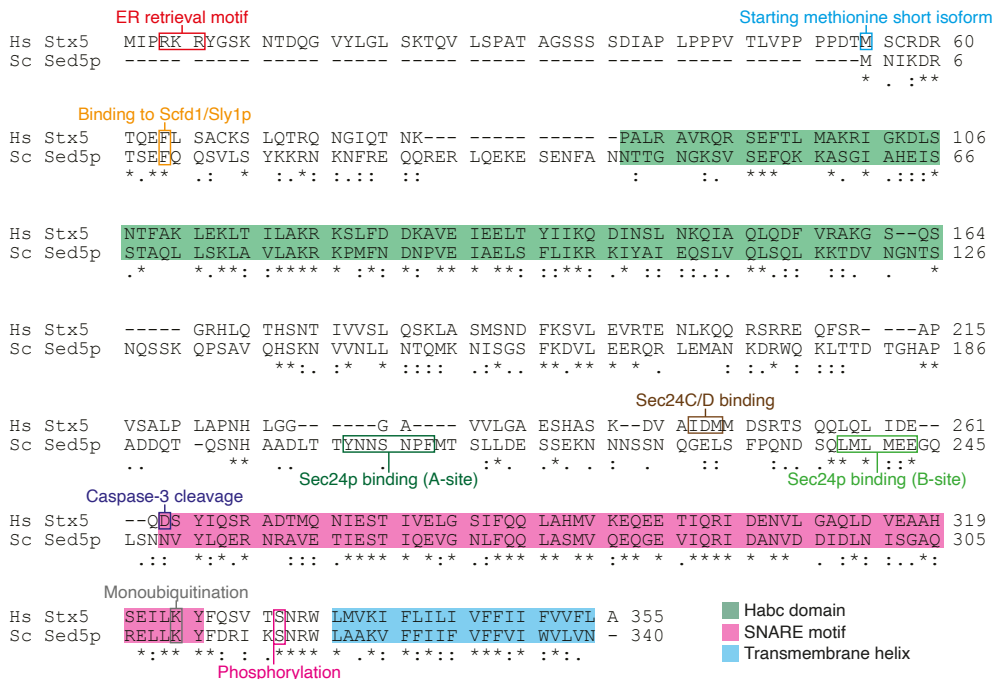


**Figure 5.3: Conserved and distinct interactions of mammalian Stx5 and yeast Sed5p.** Alignment of human (Hs) Stx5 and *S. cerevisiae* (Sc) Sed5p. Indicated are: the double arginine ER retrieval motif of the long isoform of Stx5<sup>215,324</sup>; the alternative starting methionine of the short isoform of Stx5<sup>215</sup>; the binding site to Scfd1 (mammals) and Sly1p (yeast)<sup>211,212</sup>; Sec24C/D binding site to the IxM motif of Stx5<sup>201,325</sup>; Sec24p binding sites to the YNNSNPF motif (A-site) and LxxME motif (B-site) of Sed5p<sup>326</sup>; Caspase-3 cleavage site of Stx5<sup>327</sup>; monoubiquitination site of Stx5<sup>328</sup>; phosphorylation site of Sed5p<sup>329</sup>.

to the *cis*-Golgi and ER<sup>319,320</sup>. The membranes of the ER and Golgi have thinner membranes than other organelles, because they contain less cholesterol, and thereby provide a better matching with the short lengths of the short transmembrane helices of Stx5 and Sed5p<sup>320</sup>. In fact, overexpression of truncation constructs revealed that the transmembrane domains of Stx5 and Sed5p are sufficient for proper localization to the *cis*-Golgi<sup>321–323</sup>. Both isoforms of mammalian Stx5 and yeast Sed5p contain an N-terminal Habc domain, which, at least for Stx5, can interact with its SNARE motif and thereby inhibit SNARE complex formation<sup>194</sup>, similar to many other syntaxins<sup>118</sup>.

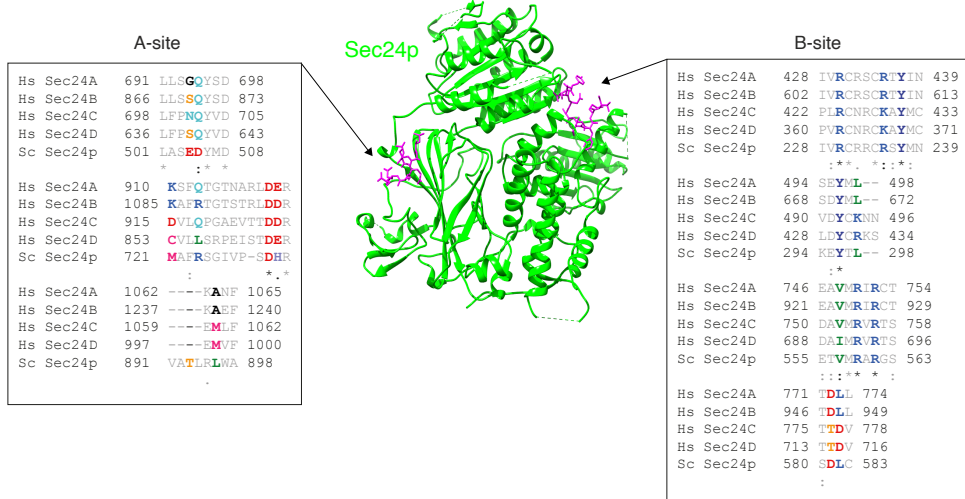
Although both the short and the long isoforms of mammalian Stx5 can be found at ER-derived COPII vesicles<sup>63</sup>, the long isoform carries a double-arginine ER retrieval motif, which makes it localize more at the ER (Figure 5.3)<sup>215,324,330</sup>. The short isoform of mammalian Stx5 lacks this ER retrieval motif and can be found more at the Golgi<sup>215,324,330</sup>. Yeast Sed5p does not contain an ER retrieval motif, and when it is heterologously expressed in mammalian cells Sed5p, locates to the *cis*-Golgi and ER-

GIC, similar to the short isoform of Stx5<sup>322</sup>. In yeast, Sed5p localizes to COPII vesicles, and Sed5p immune-isolated vesicles carry early Golgi mannosyltransferases (Mnt1p, Van1p, and Mnn9p), whereas late Golgi and ER proteins are almost completely absent<sup>331</sup>.

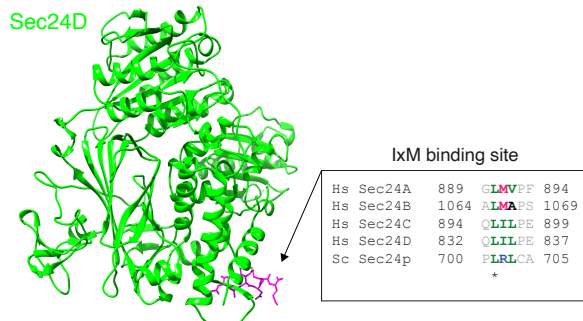
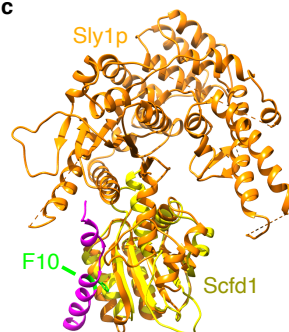
The presence of an ER retrieval motif argues that the long isoform of Stx5 might be more involved in retrograde transport, while the short isoform mediates anterograde transport. However, this might be too simplistic, as immunoprecipitation revealed that Bet1L, the v-SNARE of retrograde intra-Golgi trafficking, forms a SNARE complex mainly with the short and less with the long isoform of Stx5, whereas GosR1, which has both retro- and anterograde trafficking roles, exclusively interacted with the short Stx5 isoform<sup>161,197</sup>, indicating that retrograde Golgi transport is mainly mediated by the short isoform of Stx5. Instead, the long form of Stx5 is involved in the regulation of the ER structure by linking the ER membrane to microtubules (Figure 5.3)<sup>332</sup> possibly via the adapter protein CLIMP-63<sup>332,333</sup>. In addition to regulation of ER structure, Stx5 has been implicated in calcium storage at the ER. Both the long and short isoform of Stx5 directly interact with the calcium channel polycystin-2 (PC2) via their SNARE motifs, and this blocks channel activity and prevents calcium leakage from the ER<sup>326</sup>.

The localization of both the long and short isoform of mammalian Stx5 and yeast Sed5p is regulated not only by the presence or absence of an ER retrieval motif and their transmembrane helices but also by a number of protein-protein interactions. First, Stx5 is regulated by other SNAREs, because in mammalian cells, overexpression of mutant forms of Bet1L, the v-SNARE of retrograde trafficking, results in altered distribution of Stx5, its SNARE partner GosR1, and the medial-Golgi protein Golgi mannosidase II to *cis*-Golgi and ER<sup>204</sup>, possibly because of increased retrograde transport of Stx5. Second, the subcellular localization of Stx5 is mediated by the COG (conserved oligomeric Golgi) tethering complex as experiments targeting the Cog4 subunit of COG to mitochondria showed that this interaction resulted in delocalization of Stx5 to mitochondria<sup>162</sup>. Third, in both mammals and yeast, the sorting of Stx5 and Sed5p to COPII vesicles is mediated by the COPII subunit Sec24. In mammals, Sec24 is present in four different isoforms from gene duplication, called Sec24A–D. Sec24A and B recruit Sec22b, whereas Sec24C and D recruit a Q-SNARE complex of Stx5, GosR2, and Bet1 to COPII-coated vesicles<sup>201,325</sup>, but the functional role of this differential binding is still unclear. In yeast, only a single form of Sec24p is present that interacts with Sed5p via two distinct sites (Figure 5.3 and Figure 5.4A)<sup>334,335</sup>. The first site of Sec24p, called the A-site, binds to a YNNSNPF motif of Sed5p (residues 203–209)<sup>334</sup> and is not conserved in mammalian Sec24 isoforms (Figure 5.3 and Figure 5.4A). Binding of Sec24p to a pre-assembled t-SNARE complex of Sed5p, Bos1p, and Sec22p is favored compared to single Sed5p, as this assembly results in a conformation change that exposes the YNNSNPF

motif<sup>334</sup>. The second site of Sec24p, called the B-site, binds to a LxxME motif present in both Bet1p and Sed5p (residues 238–242)<sup>334</sup>. The LxxME motif seems conserved in Stx5 (Figure 5.3), and the B-site seems conserved in Sec24A and B (not in C and D) (Figure 5.4A), suggesting that mammalian Sec24A and B can also bind to Stx5, but this has not been proven. The recruitment of mammalian Stx5 to Sec24C and D occurs by direct interactions of the open form of Stx5 (thus the N-terminal Habc-domain not bound to its SNARE motif) to the IxM cargo-binding site of Sec24C or D via a conserved region on Stx5 (residues 242–249; Figure 5.3 and Figure 5.4B)<sup>201,325</sup>. This recruitment of Stx5 to COPII-coated vesicles, therefore, differs markedly from the recruitment of Sed5p in yeast.

**a**

5

**b****c**

**Figure 5.4: Interactions of Stx5/Sed5p with Sec24 and Scfd1/Sly1p.** (a) Crystal structure of yeast Sec24p (green) bound to the YNNSNPF motif of Sed5p (A-site) and the LxxME motif of Bet1p (B-site)<sup>326</sup>. Alignments of interacting regions of Sec24p with mammalian Sec24A-D are shown. Substrate-interacting residues are in bold and colored. Note that the A-site is not conserved, whereas the B-site seems conserved in mammalian Sec24A and B (not C and D). (b) Crystal structure of mammalian Sec24D (green) with the IxM motif of Stx5 (magenta; residues 241–248)<sup>325</sup>. Note that the IxM binding site is not conserved in mammalian Sec24A–D. (c) Conserved interactions between Stx5/Sed5p and Scfd1/Sly1p. Crystal structure of yeast Sly1p (orange) with the N-terminal region of Sed5p (magenta; residues 1–21)<sup>212</sup> aligned with an NMR structure of mammalian Scfd1 (yellow)<sup>211</sup>. Interacting residue F10 of the short isoform of Stx5 and Sed5p is indicated<sup>211,212</sup>.

## 5.5 Posttranslational Modifications

Stx5 is dynamically regulated during the cell cycle by ubiquitination. During mitosis, particularly the short isoform of Stx5 is monoubiquitinated at K270 (K324 in the long isoform)<sup>328</sup> by HACE1, and this prevents its complex formation with Bet1 and results in Golgi fragmentation<sup>328</sup> [65]. After mitosis, Stx5 is deubiquitinated by VCIP135, enabling SNARE complex formation with Bet1 and reassembly of the Golgi fragments<sup>328,336</sup>. K324 is conserved in yeast Sed5p (K310) (Figure 5.3), but since the nucleus remains intact during budding of yeast, it is a question if Sed5p is regulated in a similar manner as Stx5 in mammals. In mammalian cells, Golgi reassembly after cell division is also regulated by interactions of Stx5 with the triple AAA ATPase p97/VCP (valosin-containing protein) subunit p47<sup>336,337</sup>. The activity of Stx5 is not only blocked during mitosis but also in cells undergoing apoptosis. In this case, Stx5 is cleaved by caspase-3 at conserved D263 resulting in a 26-kDa product (Figure 5.3)<sup>327</sup>, which might well be the same as the prominent 31-kDa breakdown product originally reported<sup>197</sup>. Finally, in yeast, Sed5p is regulated by phosphorylation at serine 317, presumably by protein kinase A<sup>329</sup>, which is conserved in mammalian cells (human: S331; Figure 5.3). The phosphomimetic mutant (serine to aspartate) of Sed5p results in enlarged ER, disruption of Golgi trafficking, and impaired cell growth, whereas the phospho-dead mutant (serine to alanine) does not affect ER-Golgi transport nor cell growth, but results in enlargement of the Golgi<sup>329</sup>. The precise role of this phosphorylation of Sed5p is not known, but it is speculated that it might play a role in Golgi inheritance during mitosis, as it allows for the Golgi to cycle between ordered and dispersed states<sup>329</sup>.

## 5.6 Scfd1/Sly1p

ER-Golgi transport and trafficking within the Golgi stack are regulated by the Sec1/Munc18-like protein Scfd1 in mammals and its ortholog Sly1p in yeast. Sec1/Munc18-like proteins regulate the assembly and activity of SNARE complexes in membrane fusion events<sup>338</sup>, and in mammals, Scfd1 functions with Stx5 in ER-Golgi trafficking and also functions in the assembly of pre-Golgi intermediates through interactions with Stx17 and Stx18<sup>63,211,212,214,339,340</sup>. In yeast, Sly1p is implicated in antero- and retrograde ER-Golgi trafficking<sup>339</sup>. Scfd1/Sly1p binds to Stx5/Sed5p in the Golgi via a well-conserved N-terminal region upstream of the Habc-domain (Figure 5.3)<sup>211,212,214,339</sup>. This N-terminal region is also present in mammalian Stx17 and Stx18 and in yeast Ufe1p (Stx18 ortholog), which also bind Scfd1/Sly1p. In mammalian cells, Scfd1 regulates ER-Golgi anterograde transport via the assembly of pre-Golgi Stx5 SNARE intermediates<sup>63,214,340</sup> and retrograde trafficking via association with the Cog4

subunit of the COG tethering complex<sup>341</sup>. Scfd1 is also involved in a secretory pathway that is independent of COPII, as in zebrafish chondroblasts, the loss of Scfd1 blocks the transport of type II collagen from the ER<sup>342</sup>. Scfd1 mediates pro-collagen export from the ER in mammalian cells as well by binding to the protein TANGO1<sup>312</sup>.

The crystal structure of yeast Sly1p bound to the N-terminal fragment of Sed5p has been resolved<sup>212</sup> and an NMR structure for mammalian Scfd1 bound to the short isoform of Stx5<sup>211</sup>, showing that the high-affinity binding of the N-terminal fragment of Stx5/Sed5p to Scfd1/Sly1p is well conserved (Figure 5.3 and Figure 5.4C). Given the conservation and location of this interaction site, Scfd1 is predicted to bind to both the short and long isoforms of Stx5, and Scfd1/Sly1p is predicted to bind to both unbound Stx5/Sed5p and to Stx5/Sed5p in complex with other SNAREs<sup>14,213</sup>. However, at least for yeast Sly1p, this high-affinity binding to Sed5p is not required for its regulation of ER-Golgi transport, but this is mediated by a second lower affinity binding to Sed5p and other SNAREs<sup>343</sup>. This second binding mode might accelerate the assembly of the Sed5p-Bos1p-Bet1p-Sec22p SNARE complex by releasing the Habc-domain from the SNARE motif of Sed5p<sup>344,345</sup>, although in another study, they found no significant difference in the kinetics of SNARE complex formation<sup>213</sup>. In mammalian cells, Scfd1 might have no effect on SNARE complex formation as well, because although it is required for ER-Golgi transport, Scfd1 does not promote accessibility of the Stx5 SNARE motif for an antibody that only binds Stx5 in its open conformation<sup>346</sup>. An alternative, or complementary, explanation for how Sly1p regulates ER-Golgi transport is by preventing the interactions of Sed5p with non-cognate SNAREs, which would avert the formation of non-productive SNARE complexes<sup>213</sup>. In line with this, overexpression of Scfd1 in mammalian cells was found to neutralize the dominant-negative effects of excess Stx5 on ER-Golgi trafficking<sup>340</sup>. Finally, Sly1p/Scfd1 might prevent the dissociation of partly-formed SNARE complexes prior to fusion, as in yeast, Sly1p co-assembles with the  $\alpha$ -SNAP ortholog Sec17p to prevent disassembly of the Sed5p-Bet1p-Bos1p-Sec22p SNARE complex by the NSF ortholog Sec18p<sup>347</sup>. In contrast to Ufe1p, another interacting SNARE of Sly1p, Sly1p binding does not affect the stability of Sed5p<sup>348</sup>. Both the short and long isoform of Stx5 also interact with the chaperone hsc70, and at least *in vitro*, this promotes SNARE complex formation of Stx5, GosR2, Bet1, and Sec22b<sup>349</sup>.

## 5.7 Tethering Complexes

Prior to SNARE complex formation, Golgi transport vesicles are captured to the target organelle by two types of membrane tethering complexes<sup>154,350</sup>. The first family consists of long coiled-coil proteins and includes the Golgins p115 and GM130, which mediate ER-Golgi transport, intra-Golgi transport, and Golgi biogenesis<sup>14,350</sup>. The second

family consists of multi-subunit tethering complexes of a heterogeneous structure and composition and includes the COG complex, which organizes vesicle tethering in intra-Golgi retrograde trafficking<sup>14,154</sup>. These tethering complexes regulate the specificity of Golgi trafficking by interacting with SNARE proteins, Rab-GTPases, and COPI and COPII vesicle coats, and this, in turn, facilitates the complex formation of cognate SNARE proteins<sup>14,154,202,350</sup>.

In mammalian cells, the COG complex has been shown to interact with Stx5 and other Golgi SNAREs, and this interaction enhances the fusogenic assembly of SNARE complexes<sup>161,351–353</sup>. The COG complex is composed of eight different subunits called Cog1–Cog8. Cog1–Cog4 are organized in lobe A, which is mainly located at the Golgi stacks, whereas Cog5–Cog8 form lobe B, which locates predominantly at vesicle-like structures<sup>164</sup>. The COG complex is well conserved in yeast<sup>14</sup>, and yeast COG interacts with Sed5p<sup>161,354</sup>. In mammalian cells, Stx5 interacts with Cog6<sup>161,162,353</sup> and Cog8<sup>162</sup>, and these interactions are required for the assembly of the Stx5-GosR1-Bet1L-Ykt6 SNARE complex<sup>352</sup>. However, the best-characterized COG interactions of Stx5 are with subunit Cog4<sup>161,162,341,353</sup>. Cog4 interacts with the SNARE domain of the short isoform of Stx5<sup>161</sup>, and as this domain is present in both Stx5 isoforms, it seems likely that Cog4 interacts with the long isoform of Stx5 as well. Adjacent to the Stx5 binding site of Cog4 is a site that interacts with Scfd1, and this promotes SNARE complex formation<sup>161</sup>. Knockdown of COG subunits or overexpression of a dominant-negative Cog4 fragment containing the Stx5 and Scfd1 binding sites results in blockage of Golgi-ER retrograde trafficking, mislocalization of Stx5, GosR1, and Bet1L away from the Golgi, and impaired SNARE complex formation of the short Stx5 isoform with GosR1, Bet1L, and Ykt6, whereas SNARE complex formation of the short and long isoforms of Stx5 with Bet1 is not affected<sup>161,341,353</sup>.

The Golgins p115 and GM130 also interact with Stx5. The C-terminal region of p115 contains four coiled-coil domains (CC1–CC4), and the first coiled-coil domain CC1 bears weak sequence homology to a SNARE motif and can bind to Stx5<sup>355</sup>. In addition to Stx5, CC1 can bind to other SNAREs involved in both antero- and retrograde Golgi trafficking (GosR1, GosR2, Ykt6, Sec22, Bet1, Bet1L) and to Scfd1<sup>350</sup>. These interactions of p115 with Stx5 and other ER-Golgi SNAREs enhance *in vitro* SNARE complex assembly<sup>355</sup>. p115 is conserved in yeast, and its ortholog Uso1p binds to Sed5p by a region containing CC1 and CC2<sup>356</sup>. Not only CC1, but also CC4 are required for Golgi trafficking by interacting with multiple Golgi SNAREs (GosR1, GosR2, Ykt6, Bet1, and Bet1L)<sup>350</sup>. Thereby, p115 might connect t- and v-SNAREs in opposing membranes<sup>350</sup> and facilitate SNARE complex formation preceding membrane fusion<sup>293</sup>. Knockdown of p115 results in Golgi fragmentation and blocks ER-Golgi trafficking<sup>293</sup>. p115 also interacts with the Golgin GM130, which in turn also binds to Stx5<sup>357</sup> via a membrane-

proximal region of GM130<sup>358</sup>. However, in this case, GM130 binding to Stx5 is proposed to prevent its interaction with other SNAREs<sup>358</sup>. Binding of p115 to GM130 releases Stx5 from GM130 and allows SNARE complex formation and membrane fusion downstream of tethering<sup>358</sup>. During mitosis, the interactions of GM130 with p115 are inhibited, whereas binding of GM130 to Stx5 is increased, likely due to phosphorylation of GM130, which would reduce membrane fusion, and hence suggests a role for GM130–Stx5 interactions in the disassembly of the Golgi during cell division<sup>358</sup>.

## 5.8 Infections and Neurodegenerative Disease

Stx5 is involved in neurodegenerative diseases and infections of intracellular parasites and viruses. This makes it a therapeutic target, and in a screen for small molecule inhibitors of retrograde Golgi-ER transport of Shiga toxin, the compounds Retro-1 and Retro-2 were identified, which result in mislocalization of Stx5 away from the Golgi apparatus<sup>359,360</sup>. Stx5 localizes to vacuoles containing the intracellular pathogen *Leishmania amazonensis*, where it mediates the communication with early secretory vesicles, and knockdown or blockage of Stx5 using the small molecule inhibitor Retro-2 was found to reduce the size of these parasitophorous vacuoles and impair *Leishmania* replication and infection<sup>359,361</sup>. Stx5 has also been described to play a role in viral infections. First, infection with human cytomegalovirus (HCMV) results in increased cellular levels of Stx5, which is recruited to the viral assembly site and is required for the efficient production of viral particles<sup>362</sup>. Second, Stx5 is required for infection with adeno-associated virus (AAV), although here, it is likely responsible for viral transport from endosomes to the *trans*-Golgi network<sup>363</sup>.

Both in Alzheimer's and Parkinson's disease, Stx5 has been implicated. The short and the long isoforms of Stx5 mediate ER-Golgi transport of presenilin 1 and 2, which are subunits of the  $\gamma$ -secretase that cleaves  $\beta$ -amyloid pre-protein (APP) and is responsible for  $\beta$ -amyloid peptide production<sup>324,364,365</sup>. Stx5 interacts directly with presenilin 1 and 2 via both its Habc regulatory domain and transmembrane helix, and these interactions are reduced in a mutant of presenilin 1 that is associated with Alzheimer's disease<sup>324,364,365</sup>. Moreover, Stx5 expression is upregulated in neurons under ER and Golgi stress<sup>366</sup>, and overexpression of the short, but not long, isoform of Stx5 causes accumulation of APP in the ER and inhibits the formation of  $\beta$ -amyloid peptides<sup>324,365,366</sup>. Stx5 may also play a role in Parkinson's disease, as a disease-related mutant of  $\alpha$ -synuclein (A53T) binds to Stx5 and GosR2, and this reduces the formation of the Stx5–GosR2–Bet1–Sec22b SNARE complex, thereby possibly impairing ER-Golgi transport<sup>367</sup>.

## 5.9 Discussion

Despite the high conservation in mammals and *S. cerevisiae* of Stx5/Sed5p and its well-conserved interactions with cognate ER-Golgi SNAREs, the Sec1/Munc18-like protein Scfd1/Sly1p, and the tethering complexes COG, p115, and GM130, there are several important differences in the function and regulation of Stx5/Sed5p. First, Stx5/Sed5p interacts differently with the COPII coat protein Sec24p in yeast and Sec24C/D in mammalian cells<sup>201,213,325,335</sup>, indicating a different mechanism of recruitment to COPII-coated vesicles. Based on sequence alignments (Figure 5.3 and Figure 5.4A), one of the two sites of Sed5p binding to Sec24p in yeast seems to be conserved for Stx5 binding to Sec24A/B in mammals, but this remains to be proven. The different binding of Sed5p/Stx5 to Sec24 might relate to differences in COPII function among yeast and mammals. In yeast, COPII mediates anterograde trafficking from the ER directly to the *cis*-Golgi<sup>294</sup>, whereas in mammals, COPII vesicles fuse together to form the ERGIC<sup>14,15</sup>. Second, Stx5 is present as two isoforms in mammalian cells, but there is only one short isoform of Sed5p in yeast. The long isoform of Stx5 interacts with microtubules<sup>332</sup>, which correlates with the finding that the microtubular cytoskeleton is involved in ER-Golgi trafficking in mammalian cells, but not in yeast<sup>14–16</sup>. Moreover, the long isoform of Stx5 is retrieved to the ER, while the short isoform of Stx5 locates more to the Golgi<sup>215,324,330</sup>. These findings suggest that in mammalian cells, the long isoform of Stx5 has a role in early ER and *cis*-Golgi trafficking, whereas the short isoform of Stx5 is involved in later trafficking at the medial- and *trans*-Golgi. These potentially distinct trafficking roles of Stx5 isoforms might contribute to how mammalian cells maintain a complex Golgi structure of intercalated tubular networks of *cis*-, medial, and *trans*-Golgi intercalating into a large network, whereas in yeast, with only a single Sed5p isoform, the Golgi is organized into discrete cisternae that are scattered throughout the cell<sup>14–16</sup>. An intriguing possibility that thus emerges from this review is that the different organization of ER-Golgi trafficking between yeast and mammalian cells might be partly attributable to the interactions of a single SNARE protein: Stx5/Sed5p, although there are presumably other reasons for this such as the differential role of microtubules and the larger number of proteins involved in ER-Golgi trafficking in mammals versus yeast. This might not be surprising, given the rate-limiting function of Stx5/Sed5p in ER-Golgi transport<sup>304</sup> and its central role in the organization of the Golgi structure<sup>196,300,301</sup>. Moreover, Stx5 is tightly regulated during cell division<sup>328,336,337,358</sup> and is hijacked by several pathogens to promote their replication within infected cells<sup>361–363,368</sup>, and dysregulation of Stx5-mediated trafficking is implicated in neurodegenerative diseases<sup>324,364,365</sup>. Thus, Stx5/Sed5p plays a pivotal role in the early secretory pathway, and understanding its function is important for un-

derstanding the organization of eukaryotic cells and disease mechanisms.

### 5.9.1 Author Contributions

All authors contributed to the conceptualization and writing of the manuscript.

### 5.9.2 Funding

This work was supported by a Young Investigator Grant from the Human Frontier Science Program (HFSP; RGY0080/2018) and the Netherlands Organization for Scientific Research (NWO-ALW VIDI 864.14.001).

### 5.9.3 Conflicts of Interest

The authors declare no conflict of interest.





P.T.A. Linders, E. Gerretsen, A. Ashikov, M.-A. Vals, R. de Boer, N.H. Revelo, R. Arts, M. Baerenfaenger, F. Zijlstra, K. Huijben, K. Raymond, K. Muru, O. Fjodorova, S. Pajusalu, K. Õunap, M. ter Beest, D.J. Lefeber and G. van den Bogaart

*medRxiv* 2020.03.30.20044438

# 6

## Congenital disorder of glycosylation caused by starting site-specific variant in syntaxin-5

## 6.1 Abstract

The SNARE (soluble N-ethylmaleimide-sensitive factor attachment protein receptor) protein syntaxin-5 (Stx5) is essential for Golgi transport. In humans, the *STX5* mRNA encodes two protein isoforms, Stx5 Long (Stx5L) from the first starting methionine and Stx5 Short (Stx5S) from an alternative starting methionine at position 55. In this study, we identified a novel human disorder caused by a single missense substitution in the second starting methionine (p.M55V), resulting in complete loss of the short isoform. Patients suffer from an early fatal multisystem disease, including severe liver disease, skeletal abnormalities and abnormal glycosylation. Primary human dermal fibroblasts isolated from these patients showed defective glycosylation, altered Golgi morphology as measured by electron microscopy and mislocalization of glycosyltransferases. Measurements of anterograde trafficking, based on biotin-synchronizable forms of Stx5 (the RUSH system), and of cognate binding SNAREs, based on Förster resonance energy transfer (FRET), revealed that the short isoform of Stx5 is essential for intra-Golgi transport. This is the first time a mutation in an alternative starting codon is linked to human disease, demonstrating that the site of translation initiation is an important new layer of regulating protein trafficking.

## 6.2 Introduction

In eukaryotes, proteins destined for the secretory pathway are synthesized at the endoplasmic reticulum (ER) and then transported to the Golgi apparatus, where they are sorted for their ultimate destinations at the *trans*-Golgi network. Central to this process is intracellular membrane fusion, which is mediated by members of the SNARE (soluble *N*-ethylmaleimide-sensitive factor attachment protein receptor) protein family. Cognate SNARE proteins that are present in both the carrier vesicle and target membranes, called v- and t-SNAREs respectively, engage and form a tight alpha-helical coiled-coil bundle that overcomes the energy barrier of membrane fusion. Membrane fusion requires a single R-SNARE, characterized by an arginine residue located central in the SNARE bundle, and three Q-SNAREs, with glutamine residues instead. Generally in mammalian cells, the R-SNAREs act as vesicle (v-) SNAREs and the Q-SNAREs together form the t-SNARE complex on the target membrane<sup>57</sup>. In contrast, the Qc-SNAREs Bet1 and Bet1L (GS15) function as the v-SNAREs at the ER/Golgi interface<sup>204,208–210</sup>, while, for anterograde ER to Golgi trafficking, the recipient t-SNARE complex is formed by the Qa-SNARE syntaxin-5 (Stx5)<sup>63,194,196,295</sup>, together with the Qb-SNAREs GosR1 (also known as GS27 or membrin) or GosR2 (GS28), and R-SNAREs Ykt6 or Sec22b (Ers24)<sup>195,198,199</sup>. This different allocation of the Qc-SNAREs Bet1 and Bet1L as v-SNARE instead of t-SNARE possibly prevents the formation of non-functional SNARE complexes during ER to Golgi transit. In addition, Stx5 functions in retrograde intra-Golgi transport by forming a recipient t-SNARE complex with GosR1, and Ykt6<sup>21,204</sup> and in retrograde trafficking from endosomes to the *trans*-Golgi network (TGN)<sup>202,206</sup>, making it a unique SNARE protein involved in both anterograde and retrograde Golgi transport.

STX5 is highly conserved and is an essential gene in animals and fungi<sup>307,369</sup>. In animals, Stx5 exists as a long and a short isoform translated from the same mRNA: 39.6 kDa sized Stx5 Long (Stx5L) and 34.1 kDa sized Stx5 Short (Stx5S)<sup>21,215</sup>. This is in contrast to lower organisms such as *Saccharomyces cerevisiae*, which only express a single isoform of Stx5 (Sed5p). Although Sed5p was originally believed to resemble mammalian Stx5S<sup>21</sup>, it is now clear that it likely more resembles Stx5L, since an N-terminal COPI-binding tribasic motif has been identified in Sed5p<sup>370</sup>. The emergence of a second Stx5 isoform can be traced back to the pacific purple sea urchin, *Strongylocentrotus purpuratus*, and is also present in the model organism *Danio rerio*, but not in *Drosophila melanogaster* nor *Caenorhabditis elegans*. Compared to Stx5S, Stx5L contains 54 extra N-terminal residues bearing an Arginine—Lysine—Arginine (RKR) ER retrieval motif, and as a result, Stx5L locates more to the ER whereas Stx5S locates more to the Golgi network<sup>21,215,324,330,332</sup>. The evolutionary necessity of the two Stx5 isoforms remains unclear but it has been suggested that Stx5L is important to maintain ER structure

by binding microtubules, possibly via CLIMP-63<sup>332,333</sup>. In addition, immunoprecipitations showed that GosR1 and Bet1L preferentially interact with Stx5S over Stx5L<sup>161,197</sup>, suggesting that Stx5S might act in more fusogenic complexes later at the ER-Golgi interface whereas Stx5L might be more involved in earlier fusion steps.

In the present study, we identified a genetic variant in the second translation codon methionine-55, fully abrogating the production of Stx5S and providing a unique opportunity to study the physiological relevance of the existence of two isoforms in humans. Patients homozygous for this mutation have a very severe clinical phenotype associated with infantile mortality and defective protein glycosylation. We demonstrate that although Stx5L can largely compensate for the lack of Stx5S, the loss of Stx5S leads to defects in intra-Golgi trafficking with mislocalization of glycosyltransferases, which results in pronounced defects in glycosylation. Moreover, by synchronizing the intracellular trafficking of Stx5 isoforms, we reveal differential trafficking routes for either isoform and identify Stx5S as the dominant Qa-SNARE for intra-Golgi transport. This is the first time that a mutation in an alternate starting site of ribosomal translation is related to human disease. This finding reveals that protein function can be regulated at the level of translation initiation and has profound effects on intracellular membrane trafficking and Golgi function.

## 6.3 Results

### 6.3.1 Clinical data

The family history (Supplementary Figure 6.8) revealed multiple deceased individuals (IV:3, IV:9, IV:10) shortly after birth, spontaneous abortions (IV:5, IV:6, IV:7), and elective abortions in the 20th-21st week of pregnancy due to abnormal fetal ultrasound (US) (IV:4, IV:8). Fetal US of individuals IV:8, IV:9, and IV:10 (Figure 6.1a-c, respectively) showed shortening of the long bones with suspicion of chondrodysplasia. Patients IV:9 and IV:10 showed highly dysmorphic facial features (high forehead, frontal bossing, prominent glabella, short and upturned nose, long philtrum, micrognathia and dysplastic ears), skeletal dysplasia (short extremities and narrow thorax), profound hypotonia, hepatomegaly, and many abnormal laboratory parameters including elevated cholesterol (Figure 6.1b,c, Supplementary Table 6.1). After birth, the main clinical problem for both patients IV:9 and IV:10 was progressive liver failure with cholestasis and hyperinsulinemic hypoglycemia (Supplementary Table 6.1). Liver failure was the main cause of death at the age of 28 days and 8 months, in patients IV:9 and IV:10, respectively. Autopsy of fetus IV:8 revealed bilateral hydronephrosis and sacral lordosis. Autopsy of patient IV:9 showed hepatomegaly with stage 3 to 4 liver fibrosis, agenesis of left kidney, hyperemia of internal organs, ventricular septal defect

and suggestive pathohistological features of chondrodysplasia. Autopsy of patient IV:10 showed biliary cirrhosis and nodular regenerative hyperplasia, pancreatic hypertrophy/hyperplasia, and narrow thorax with normal lung development.

### 6.3.2 Abnormal protein glycosylation suggests a defect in Golgi trafficking

Known genetic causes for skeletal dysplasias were excluded (IV:8), no submicroscopic chromosomal abnormalities were found, while most metabolic investigations were normal except for the Congenital Disorders of Glycosylation (CDG) (IV:9 and IV:10). CDG screening revealed a strong hyposialylation of protein N-glycosylation and mucin-type O-glycosylation, as analyzed by isofocusing of respectively plasma transferrin (Figure 6.1d, Supplementary Table 6.2) and apolipoprotein CIII (ApoCIII-IEF, Figure 6.1e, Supplementary Table 6.2). ApoCIII-IEF showed a strong increase of non-sialylated apoCIII (ApoCIII-0) band intensities compared to the intensities of the fully glycosylated form, even stronger than observed for genetic defects in the Conserved Oligomeric Golgi (COG) complex, a known group of disorders with disturbed Golgi homeostasis and abnormal glycosylation<sup>13</sup>.

To gain more insight into the abnormal N-glycan structures, mass spectrometry was performed of intact transferrin (Figure 6.1f, g, Supplementary Figure 6.9) and of total plasma protein derived N-glycans (Figure 6.1f, h, Supplementary Figure 6.10). Analysis of intact transferrin of individuals IV:9 and IV:10 revealed multiple abnormal glycan structures, divided into two categories: high mannose structures and truncated glycans. Compared to the peak height of completely glycosylated transferrin, a dominant accumulation was found of high-mannose glycans (Supplementary Table 3, Man5, mass/peak number) suggesting a problem with MGAT1, the enzyme that adds the next *N*-acetylglucosamine during N-glycosylation. Furthermore, a series of transferrin isoforms was observed with reduced incorporation of galactose and sialic acid residues. Similar glycosylation patterns were observed in COG5-CDG<sup>173,185–187</sup>. Analysis of N-glycans released from total plasma proteins recapitulated the two categories of abnormal glycans with the accumulation of high mannose glycans, as well as reduced incorporation of galactose and sialic acid residues (Supplementary Table 4). Together, these data indicate that the activities of multiple glycosyltransferases in the Golgi apparatus are affected, covering both N- and O-glycosylation, thereby suggesting a general disturbance in Golgi trafficking.

### 6.3.3 Molecular investigations result in the identification of variants in *STX5*

Chromosomal microarray analysis (CMA) using HumanCytoSNP-12 microarrays revealed multiple long contiguous stretches of homozygosity (LCSH, >5 Mb) distributed

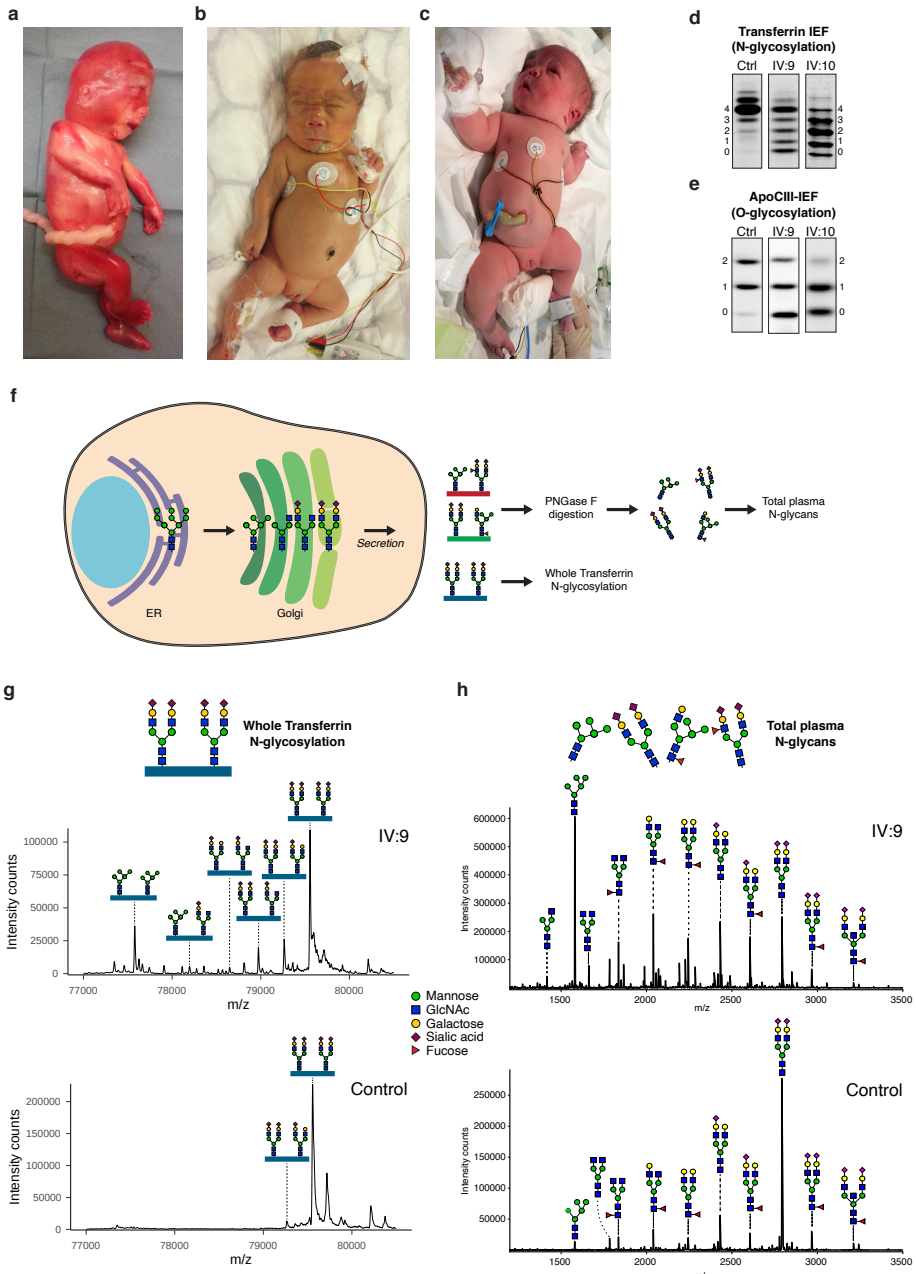


Figure 6.1: A novel, lethal, genetic variant suggests a defect in protein glycosylation related to Golgi trafficking. (Continued on the following page.)

**Figure 6.1:** (a-c) Clinical images of Stx5M55V patients IV:8 (a), IV:9 (b), IV:10 (c). (d) Glycosylation screening by isoelectric focusing (IEF) of serum transferrin. The accompanying numbers represent the total number of sialic acids in the different proteoforms. Both patients show a reduction in the number of sialic acids. Quantification of bands is shown in Supplementary Table 6.2. (e) Glycosylation screening by IEF of serum Apolipoprotein C3 (ApoCIII). ApoCIII has one mucin-type O-linked glycan with one or two sialic acids in controls. Both patients show a reduction in the number of sialic acids. Quantification of bands is shown in Supplementary Table 6.2. (f) Schematic overview of N-glycosylation intermediates in the Golgi. For mass spectrometry analysis of glycan structures, glycosylated transferrin was enriched from all secreted glycoproteins in human serum and subjected to intact protein mass spectrometry. In parallel, a different serum sample was treated with PNGase F to cleave and analyze N-glycans from all plasma proteins. (g) Nanochip-C8 QTOF mass spectra of enriched intact serum Transferrin of Stx5M55V patient IV:9 (top spectrum) and healthy control (lower spectrum). Key transferrin glycoforms are shown, indicating a strong increase of high-mannose glycans and glycans lacking sialic acid and galactose. Annotation of all peaks of patients IV:9 and IV:10 is shown in Supplementary Table 3. (h) MALDI-TOF mass spectra of total plasma N-glycans of Stx5M55V patient IV:9 (top spectrum) and healthy control (lower spectrum). Structural analysis shows a strong increase of high-mannose glycans and glycans lacking sialic acid and galactose. Annotation of all peaks of patients IV:9 and IV:10 is shown in Supplementary Table 4.

across the entire genome, with several regions of homozygosity on chromosome 11 in all three affected sibs (IV:8, IV:9 and IV:10, Supplementary Table 6.3). Exome sequencing was performed in proband IV:9 to find the genetic variant that could be associated with the disease. Only two homozygous rare protein-altering variants without homozygous individuals in the gnomAD v3 database were identified in shared homozygous stretches on chromosome 11. First, a missense variant in the VPS37C gene was discovered (NM\_017966.4:c.760G>T p.(Gly254Cys) rs201088253). However, as this variant reaches an allele frequency of 0.9% in Estonia, it is unlikely to cause a rare genetic disorder. The second variant was identified in the *STX5* gene (NM\_003164.4:c.163A>G p.(Met55Val), Figure 6.2a). This is a missense mutation affecting the alternative starting codon for the production of the short Stx5 isoform. The variant is absent from the gnomAD v3 database and was thus classified as a potentially disease-causing variant. The variant was confirmed by Sanger sequencing as homozygous in all affected individuals (IV:8, IV:9, and IV:10) and as heterozygous in the mother (III:2). Paternal DNA was not available for testing.

To confirm the effect of the genetic variant on both Stx5 proteoforms, immunoblotting was performed in primary dermal fibroblasts of patients IV:9 and IV:10. While Stx5L was present, a total absence of Stx5S was found in both patient fibroblasts (Figure 6.2b, c). We next tested the expression of known interaction partners of Stx5. The levels of Qc-SNARE Bet1L, which forms a complex with Stx5 upon retrograde intra-Golgi trafficking<sup>21,202,204,206</sup>, were also reduced. In contrast (Figure 6.2b, c), the expression of Qc-SNARE Bet1, which forms a complex with Stx5 upon anterograde ER-Golgi trafficking<sup>21,195,198,200</sup> was not reduced (Figure 6.2b, c). Likewise, the expression of Qb-SNAREs GosR1 and GosR2, which can complex with Stx5 for anterograde ER-Golgi trafficking and retrograde intra-Golgi trafficking<sup>21,194,195,197,198,204</sup> were unaltered in patient der-

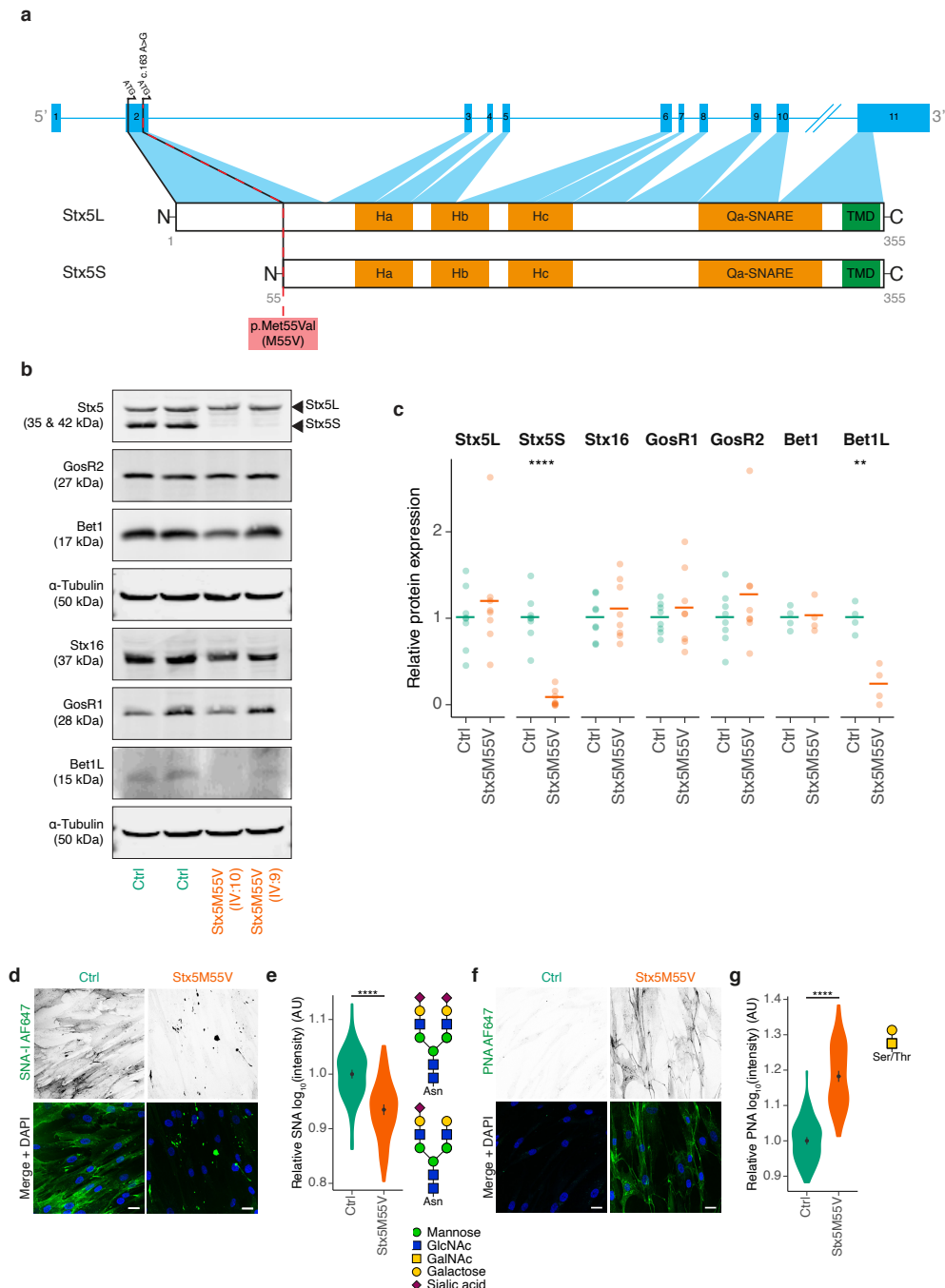


Figure 6.2: Primary dermal fibroblasts are an accurate model of the glycosylation defect observed in Stx5M55V patients. (Continued on the following page.)

**Figure 6.2:** (a) Schematic representation of the intron-exon structure of STX5 and the encoded proteoforms resulting from the two starting codons in exon 2. The Stx5M55V genetic variant is indicated by a dashed red line. Orange regions have a secondary helical structure. TMD, transmembrane domain. Ha, Hb, Hc: regulatory Habc-domain. (b) Representative immunoblot for SNARE proteins of cell lysates of primary human dermal fibroblasts from two unique individual healthy donors (green, Ctrl) or Stx5M55V patients (orange, Stx5M55V).  $\alpha$ -Tubulin, loading control. (c) Quantification of (b). Protein levels were first normalized to the loading control, then to the average expression of both control lines. Each point represents one cell line from 2 independent experiments. (d) Fibroblasts of healthy donors (green, Ctrl) or Stx5M55V patients (orange, Stx5M55V) were probed with SNA-I lectin (green in merge). Representative confocal micrographs. Scalebars, 25  $\mu$ m. DAPI in blue. (e) Quantification of (d). All data were  $\log_{10}$ -transformed and then normalized to the healthy donor. N = 124 (Ctrl) and 111 (Stx5M55V) cells from 2 unique individuals tested twice. (f-g) Same as panels (d-e), but now for PNA lectin. N = 117 (Ctrl) and 122 (Stx5M55V) cells from 2 unique individuals tested twice.

mal fibroblast lysates. We hypothesized that a compensatory mechanism might exist by upregulating the expression of the trans-Golgi Qa-SNARE Stx16<sup>371</sup>, usually involved in endosome-to-TGN trafficking<sup>118</sup>, but we did not detect a change of Stx16 expression in patient fibroblast lysates (Figure 6.2b, c). As a first step to confirm that fibroblasts offer a useful model to recapitulate the cell biological abnormalities due to loss of the Stx5S isoform, we studied glycosylation by fluorescently-labeled lectins.

#### 6.3.4 Glycosylation defects in Stx5M55V patient fibroblasts

Patient fibroblasts could be cultured normally and we did not observe apparent differences in growth rate or viability between healthy control and patient-derived cell lines. Cell surface staining with the lectin SNA-I from *Sambucus nigra*, which binds terminal sialic acid in an  $\alpha$ -2,6 linkage of fully-formed N-glycan moieties and, to a lesser extent, sialic acid in an  $\alpha$ -2,3 linkage, showed that glycosylation was also impaired at the cellular level in patient fibroblasts. Compared to fibroblasts of healthy donors, we observed a more than two-fold reduced SNA-I labeling intensity in Stx5M55V patient fibroblasts (Figure 6.2d,e). Moreover, most signal came from punctuated structures in the Stx5M55V patient fibroblasts, instead of the more uniform cell membrane labeling observed in the healthy donor fibroblasts. To confirm this glycosylation defect, we performed cell surface staining with the lectin PNA (Peanut agglutinin) from *Arachis hypogaea*, which binds terminal galactose residues present on mucin O-glycan moieties of incompletely glycosylated proteins. Opposite to our findings with SNA-I, we observed an increased labeling intensity in Stx5M55V patient fibroblasts relative to healthy control by about six-fold (Figure 6.2f,g). These findings show that patient-derived fibroblasts, which express Stx5L but lack Stx5S, have a glycosylation defect.

Next, we evaluated the expression levels of Stx5S and Stx5L in lysates of peripheral blood mononuclear cells (PBMCs) obtained from four different healthy donors (Supplementary Figure 6.11). While total Stx5 expression levels varied strongly (more than two-fold), the ratio of Stx5S and Stx5L was approximately equimolar for all individu-

als, demonstrating that the expression ratio is similar in PBMCs of different healthy subjects.

To determine the role of Stx5S in Golgi transport, we generated a Stx5L-lacking fibroblast cell line from one of the prior used control lines, using CRISPR/Cas9 (Fib Stx5 $\Delta$ L, Supplementary Figure 6.12a). We then performed the same cell surface staining as described above. While we observed a similar decrease in SNA-I labeling intensity in Stx5 $\Delta$ L fibroblasts as in Stx5M55V patient fibroblasts, the staining pattern was more similar to healthy control and showed a uniform plasma membrane-localized SNA-I labeling (Supplementary Figure 6.12b-c). In addition, opposite to Stx5M55V fibroblasts, the low PNA labeling intensity was reduced further in Fib Stx5 $\Delta$ L (Supplementary Figure 6.12d-e). To investigate this difference further, we generated two clonal HeLa cell lines lacking Stx5L using the same method (Stx5 $\Delta$ L: B1A7 and C1F4, Supplementary Figure 6.12f), and we observed a decrease in the already low SNA-I labeling intensity as measured by FACS compared to the parental HeLa cells, while PNA labeling resulted in opposite changes between the two Stx5 $\Delta$ L lines (Supplementary Figure 6.12g-k). The difference in PNA labeling between the HeLa Stx5 $\Delta$ L cell lines therefore likely is attributable by clonal variation and/or off-target effects of CRISPR/Cas9. These results demonstrate that while the loss of Stx5S or Stx5L both result in N-glycosylation defects, the defect is stronger upon the loss of Stx5S, as this results in lower levels and a punctuated distribution of sialic acid moieties. Moreover, the mucin-type O-glycosylation defect seems specific to the loss of Stx5S. As these results reiterate the glycosylation defect observed on serum transferrin, total plasma N-glycans and apoCIII mucin O-glycans, patient fibroblasts are a suitable model to investigate the cell biological consequences of the complete disruption of the Stx5S isoform.

## 6

### 6.3.5 Stx5M55V mutation results in mislocalization of glycosyltransferases

Given that Stx5 mediates ER-Golgi trafficking<sup>21,194–200,204,206</sup>, we next investigated whether the glycosylation defect in Stx5M55V patient fibroblasts was caused by the mislocalization of glycosyltransferases. We performed immunofluorescence labeling of mannosyl ( $\alpha$ -1,3)-glycoprotein  $\beta$ -1,2-N-acetylglucosaminyltransferase (MGAT1, also known as GnT1), which catalyzes the addition of GlcNAc to the immature man-5 N-glycan. Compared to healthy donor fibroblasts, MGAT1 colocalizes only slightly less with the *cis*-Golgi marker GM130 in patient fibroblasts (Figure 6.3a, b), but colocalized substantially less with the *trans*-Golgi network marker TGN46 (Figure 6.3c, d). In addition, alpha-mannosidase 2 (MAN2A1), which catalyzes the final hydrolytic step in the N-glycan maturation pathway after MGAT1 conversion, colocalized substantially less with both GM130 (Supplementary Figure 6.13a, b) and TGN46 in patient fibroblasts (Supplementary Figure 6.13c, d). Similarly to MGAT1, beta-galactoside alpha-2,6-

sialyltransferase 1 (ST6GAL1), which catalyzes the transfer of sialic acid to galactose residues of N-glycans in an  $\alpha$ -2,6 linkage, colocalized less with both GM130 (Supplementary Figure 6.13e, f) and TGN46 in patient fibroblasts (Supplementary Figure 6.13g, h). Finally, *N*-acetylgalactosaminyltransferase 2 (GALNT2), which catalyzes the initial reaction in mucin O-linked glycan synthesis, localized more to the *cis*-Golgi (marker Zinc finger protein-like 1 (ZFPL1)<sup>287</sup>) (Figure 6.3e, f) and less to the *trans*-Golgi in patient fibroblasts (Figure 6.3g, h).

To exclude the possibility that our conclusions were affected by potential mislocalization of TGN46 in the patient cells, we repeated these experiments but now co-stained for another *trans*-Golgi marker, the *trans*-Golgi coiled-coil protein p230<sup>372</sup> (Supplementary Figure 6.14). Indeed, we observed similar Pearson correlation coefficients for p230 as for TGN46 with MGAT1, GALNT2, MAN2A1, and ST6GAL1 (Supplementary Figure 6.14). Moreover, to confirm that the observed changes in colocalization were not due to lower expression of glycosyltransferases, we performed immunoblotting for several glycosyltransferases and could not detect consistent differences between control and Stx5M55V fibroblasts, although we noticed substantial variation in protein expression levels of some of the glycosyltransferases between the samples (Supplementary Figure 6.15), reflecting expression differences among individuals and/or fibroblast lines.

Taken together, the loss of Stx5S results in irregular localization of glycosyltransferases to the Golgi apparatus. An altered Golgi organization and mislocalization of glycosyltransferases can have a profound impact on glycosylation as shown by computational simulations<sup>54</sup>. We investigated the organization of the Golgi complex in Stx5M55V fibroblasts in more detail.

### 6.3.6 Stx5S mediates retrograde Golgi-ER and intra-Golgi trafficking

Transmission electron microscopy showed dilation of rough ER and Golgi cisternae in the Stx5M55V patient fibroblasts (Figure 4.4a-c, gallery Supplementary Figure 6.16), similar to previously observed alteration in the ultrastructure of the Golgi in several COG defects<sup>156,170,183</sup>. Notwithstanding these large alterations in Golgi morphology, the polarized arrangement of Golgi apparatus cisternae was still present in Stx5M55V, as observed by immunofluorescence labeling of *cis*- and *trans*-Golgi markers (Supplementary Figure 6.17). These results indicate that although Stx5L is sufficient to maintain normal Golgi apparatus cisterna polarization, Stx5S is required for physiological ER and Golgi ultrastructure and proper trafficking of glycosylation enzymes.

To address the role of the Stx5 isoforms in more detail, we studied the distribution of Stx5 isoforms in the Golgi network. Because Stx5L contains an RKR ER-retrieval motif in its N-terminal extension, it locates more at the ER compared to Stx5S<sup>21,215,330,332</sup>.

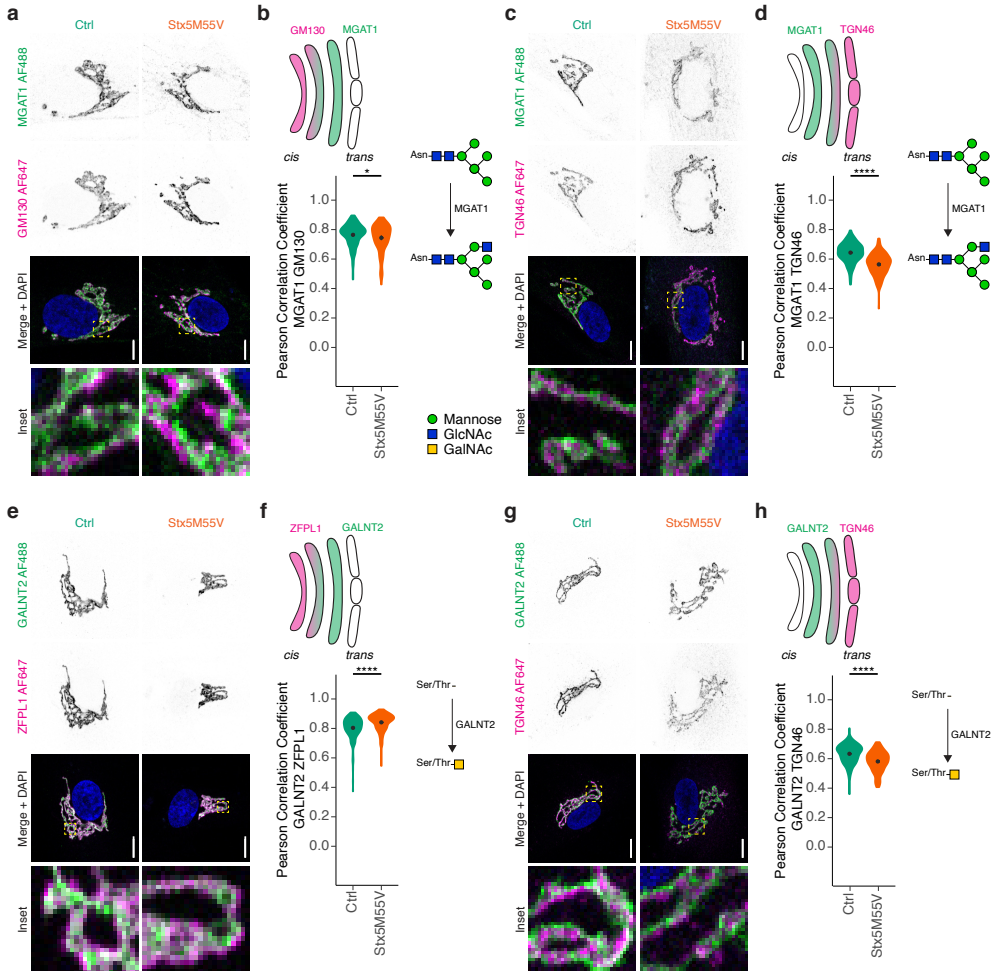


**Figure 6.3: Glycosylation enzymes mislocalize in Stx5M55V patient fibroblasts.** (a) Immunofluorescence microscopy of MGAT1 (green in merge) and GM130 (magenta) in primary dermal fibroblasts of healthy donors (green, Ctrl) or Stx5M55V patients (orange, Stx5M55V). Representative confocal micrographs. Scalebars, 10  $\mu$ m. DAPI in blue. N = 157 (Ctrl) and 126 (Stx5M55V) cells from 2 unique individuals tested twice. (b) Pearson's correlations coefficients between MGAT1 and GM130 of panel (a). N = 157 (Ctrl) and 126 (Stx5M55V) from 2 unique individuals tested twice. (c-d) Same as panels (a-b), but now for MGAT1 (green) and TGN46 (magenta). N = 157 (Ctrl) and 162 (Stx5M55V) cells from 2 unique individuals tested twice. (e-f) Same as panels (a-b), but now for GALNT2 (green) and ZFPL1 (magenta). N = 240 (Ctrl) and 146 (Stx5M55V) cells from 2 unique individuals tested twice. (g-h) Same as panels (a-b), but now for GALNT2 (green) and TGN46 (magenta). N = 172 (Ctrl) and 152 (Stx5M55V) cells from 2 unique individuals tested twice.

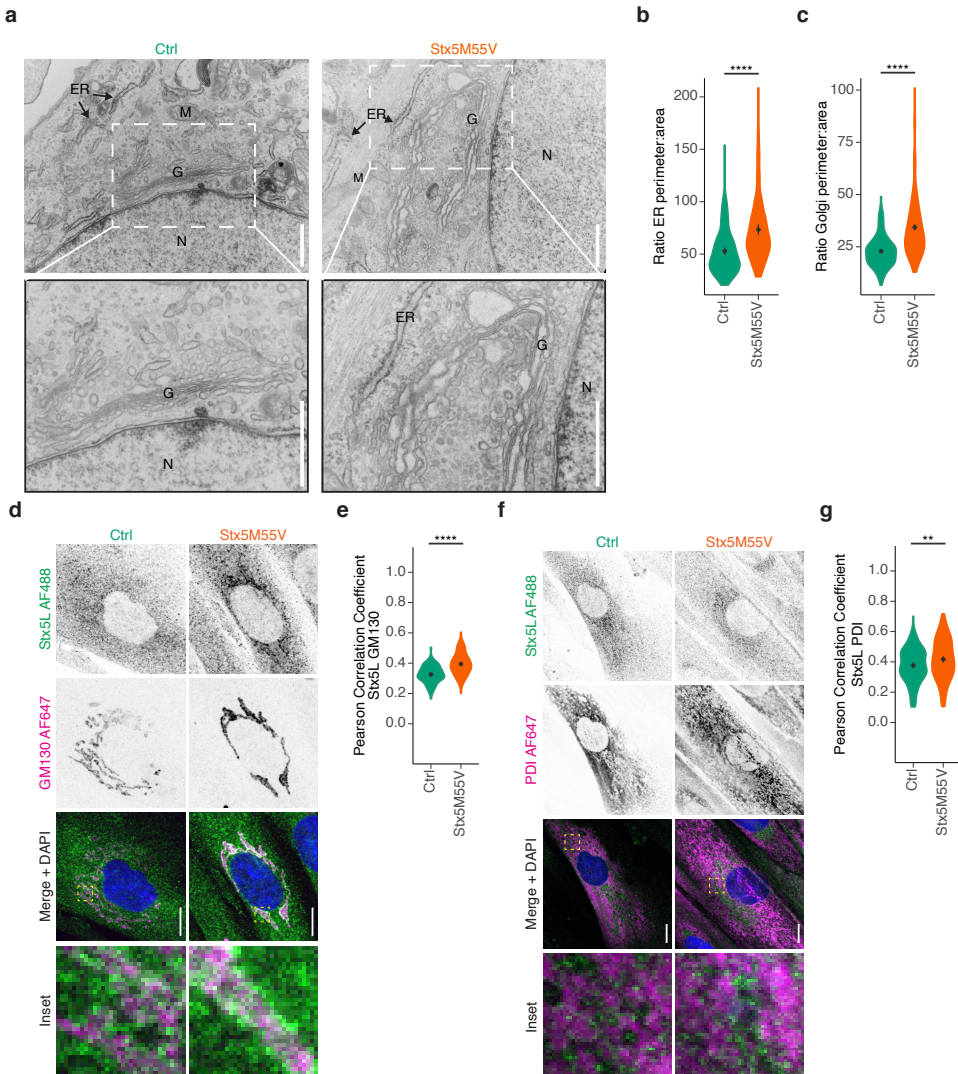


**Figure 6.4: Loss of Stx5S alters ER and Golgi morphology.** (a) Representative transmission electron micrographs from healthy donor fibroblasts (left) or Stx5M55V patient fibroblasts (right). Scalebars, 1  $\mu$ m. N, nucleus; G, Golgi apparatus; ER, endoplasmic reticulum; M, mitochondrion. More electron micrographs in Supplementary Figure 6.16. (b) ER perimeter and area quantification of panel (a), the ratios of the perimeters over the areas are plotted. N = 144 (both Ctrl and Stx5M55V) ER sections. (c) Same as panel (b), but now for Golgi. N = 400 (both Ctrl and Stx5M55V) Golgi sections. (d) Immunofluorescence microscopy of Stx5L (green in merge) and GM130 (magenta) in primary dermal fibroblasts of healthy donors (green, Ctrl) or Stx5M55V patients (orange, Stx5M55V). Representative confocal micrographs. Scalebars, 10  $\mu$ m. DAPI in blue. (e) Pearson's correlations coefficients between Stx5L and GM130 of panel (d). N = 102 (Ctrl) and 135 (Stx5M55V) cells from 2 unique individuals tested twice. (f-g) Same as panels (d-e), but now for Stx5L (green) and TGN46 (magenta). N = 147 (Ctrl) and 156 (Stx5M55V) from 2 unique individuals tested twice.

In line with this, we observed a more dominant localization of Stx5L at the ER and less at various Golgi compartments in Stx5M55V fibroblasts compared to total Stx5 localization in healthy control fibroblasts (Supplementary Figure 6.18a, b, d, e, Supplementary Figure 6.19a, b, d, e).

A notable difference was the far more diffuse staining in Stx5M55V patients of the COPI coat protein  $\beta$ COP (Supplementary Figure 6.18a, c) and of TGN46 (Supplementary Figure 6.18d, f). In contrast, we observed a small increase in GM130 fluorescence in Stx5M55V patients (Supplementary Figure 6.19f). Since Western blot showed that total cellular levels of  $\beta$ COP and GM130 were not consistently altered in Stx5M55V patients (Supplementary Figure 6.18g), the more diffuse staining of  $\beta$ COP is suggestive of reduced association with COPI-coated vesicles, while the higher staining intensity of GM130 suggests more association with the *cis*-Golgi. In contrast, total TGN46 protein levels were somewhat reduced in patient fibroblasts (Supplementary Figure 6.18h). These findings suggest that loss of Stx5S results in reduced COPI trafficking between GM130-marked *cis*- and TGN46-marked *trans*-Golgi compartments.

Using an antibody specific to Stx5L (antibody specificity validated in Supplementary Figure 6.20), we next investigated whether the loss of Stx5S affects the intracellular distribution of Stx5L. An altered cellular localization of Stx5L might imply a compensatory mechanism. Indeed, in Stx5M55V, Stx5L localizes more to the *cis*-Golgi as measured by increased colocalization with GM130 (Figure 6.4d, e). A slight increase in ER localization as measured by PDI colocalization was also observed (Figure 6.4f, g). Taken together, the loss of Stx5S causes Stx5L to relocalize more towards the *cis*-Golgi.

As COPI is involved in retrograde Golgi-ER transport<sup>80</sup>, we investigated whether trafficking at this interface is compromised in Stx5M55V fibroblasts by using the fungal metabolite Brefeldin A (BFA), which inhibits COPI vesicle formation<sup>96</sup>. If loss of Stx5S results in reduced retrograde Golgi-ER transport, we expect reduced relocalization of Golgi-resident proteins to ER upon BFA treatment. Indeed, redistribution of GALNT2 from the Golgi to the ER was incomplete in patient fibroblasts (Figure 6.5a-c), supporting a role for Stx5S in retrograde COPI trafficking. In addition, washout of BFA caused a more rapid localization of GALNT2 to the Golgi apparatus in Stx5M55V, likely due to its incomplete redistribution to the ER (Figure 6.5a, b, d, Supplementary Figure 6.21a-c). We investigated the role of Stx5L in Golgi trafficking further using temperature-synchronizable vesicular stomatitis virus G protein (VSVG) fused to GFP<sup>373</sup> in patient fibroblasts. At 40°C, VSVG does not fold correctly and the VSVG-GFP protein remains trapped in the ER. A temperature shift to 32°C enables the correct refolding of VSVG resulting in the synchronized release of VSVG-GFP from the ER, transit through the Golgi network, and finally delivery at the plasma membrane where it becomes accessible to antibody labeling. VSVG-EGFP appears at a Golgi-like compartment in both control

and Stx5M55V fibroblasts at 30 mins after temperature shift from 40°C to 32°C (Supplementary Figure 6.21d), but after 60 mins plasma membrane localization of VSVG is strongly reduced in Stx5M55V fibroblasts (Figure 6.5e-g). Taken together, these findings show that Stx5L is sufficient for anterograde trafficking until the Golgi, but the loss of Stx5S significantly impairs intra- and/or post-Golgi trafficking, likely by the decrease of Stx5S-mediated intra-Golgi trafficking.

To further delineate the role of Stx5L in retrograde Golgi-ER trafficking, we performed a BFA experiment in the Stx5L-lacking HeLa cells. In these cells, BFA resulted in faster relocalization of GALNT2 to the ER compared to parental HeLa (Supplementary Figure 6.22a, b), indicating that Stx5S suffices for retrograde COPI trafficking and the expression of Stx5L counteracts this process. Further investigation of anterograde ER-Golgi trafficking in Stx5 $\Delta$ L cells with H-89 washout (Supplementary Fig. 15c, d), the retention using selective hooks (RUSH) system for synchronized ER-Golgi transport<sup>266</sup> (Supplementary Figure 6.22e, f) and temperature-synchronizable VSVG<sup>373</sup> (Supplementary Figure 6.22g, h) revealed no phenotype relating to the loss of Stx5L. Thus, these data suggest Stx5L has no necessary function in ER-Golgi trafficking as Stx5S can compensate, while Stx5L can only partly compensate for the loss of Stx5S in retrograde Golgi-ER and intra-Golgi transport.

### 6.3.7 Faster Golgi exit of Stx5L due to ER-retrieval motif

Our results in patient fibroblasts indicate differential trafficking roles of the two Stx5 isoforms in ER-Golgi trafficking. To gain more insight in this process, we fused each Stx5 isoform to streptavidin-binding protein (SBP) and mCitrine (Stx5L-SBP-mCitrine and Stx5S-SBP-mCitrine; Stx5L-SBP-mCitrine carries the M55V mutation to suppress expression of Stx5S). Moreover, we generated a mutant form of Stx5L where the RKR ER-retrieval motif was converted to 3 $\times$  alanine (AAA) (Stx5L $\Delta$ ER-SBP-mCitrine)<sup>215</sup>, to delineate the role of this motif in ER-Golgi transport. The co-expression of these constructs with ER-localized streptavidin enabled the synchronized release of the Stx5 fusion proteins from the ER using biotin, which is the so-called RUSH system<sup>266</sup> (Figure 6.6a). Co-expressing each Stx5 isoform with the Golgi marker Giantin fused to mScarlet<sup>374</sup> in HeLa cells, allowed to visualize the trafficking of Stx5-SBP-mCitrine to the Golgi following the addition of biotin (Figure 6.6a, b). All three constructs were expressed at similar levels, as judged from the fluorescent intensities, and all Stx5 forms reached the Golgi with the same rate and achieved maximal Golgi localization after about 20 minutes (Figure 6.6c). However, the subsequent decrease in Golgi localization, attributed to recycling to the ER or degradation of the fusion proteins, was faster for Stx5L-SBP-mCitrine than for Stx5S or Stx5L $\Delta$ ER (Figure 6.6c, d). Thus, the RKR ER retrieval motif of Stx5L is necessary and sufficient for the attenuated presence of Stx5L at the Golgi,

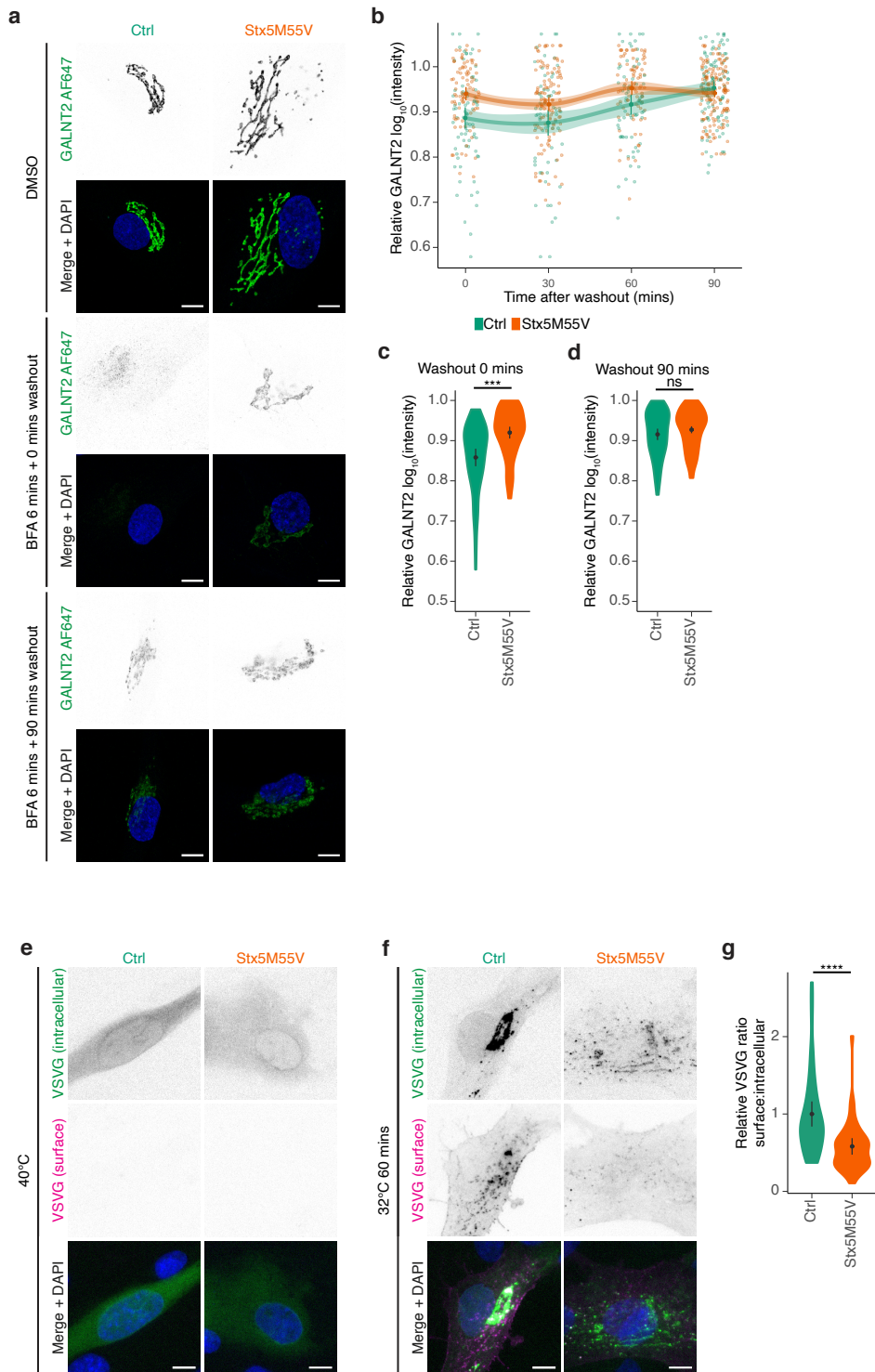


Figure 6.5: Loss of Stx5S compromises ER-Golgi trafficking. (Continued on the following page.)  
126

**Figure 6.5:** (a) Immunofluorescence microscopy of GALNT2 (green in merge) in primary human dermal fibroblasts of healthy donors (green, Ctrl) or Stx5M55V patients (orange, Stx5M55V) in the absence or presence of Brefeldin A (BFA) for 6 min and washout for the indicated times. Representative confocal micrographs are shown. Scalebars, 10  $\mu$ m. DAPI in blue. (b) Timecourse of relative maximum fluorescence intensities of GALNT2 from panel (a). All data were normalized to the DMSO condition (vehicle). (c) Quantification of the 0 min washout timepoint from panels (a) and (b). N = 76 (Ctrl) and 85 (Stx5M55V) cells from 2 unique individuals tested twice. (d) Same as (c), but now for the 90 min timepoint. N = 97 (Ctrl) and 152 (Stx5M55V) cells from 2 unique individuals tested twice. (e) Immunofluorescence microscopy of VSVG-EGFP in primary human dermal fibroblasts of healthy donors (green, Ctrl) or Stx5M55V patients (orange, Stx5M55V) cultured overnight at 40°C. Representative confocal micrographs are shown. Scalebars, 10  $\mu$ m. DAPI in blue. (f) Same as (e), but now after 60 mins at 32°C. (g) Quantification of the ratio of surface to intracellular of VSVG after 60 mins at 32°C. N = 45 (Ctrl) and 39 (Stx5M55V) cells from 2 unique individuals tested twice.

supporting that the main role of Stx5S is COPI trafficking specifically at the Golgi.

### 6.3.8 The two isoforms of Stx5 differently engage in SNARE complexes

Since interactions of Stx5 with Bet1 and Bet1L mediate anterograde ER-Golgi transport and retrograde intra-Golgi transport, respectively<sup>204,208–210</sup>, we hypothesized that Stx5S would interact more strongly with Bet1L, whereas Stx5L would interact more strongly with Bet1. We set out to test this hypothesis by performing co-immunoprecipitation with our RUSH Stx5 constructs. However, we were unable to consistently resolve differences in binding to endogenous cognate Qc-SNAREs between the two Stx5 isoforms, either with or without 30 mins biotin (Supplementary Figure 6.23). A likely explanation is that interactions might occur *in vitro* during the immunoprecipitation. Therefore, we developed an approach to visualize SNARE complexes based on a combination of the RUSH system<sup>266</sup> and our previously developed Förster resonance energy transfer-fluorescence lifetime imaging microscopy (FRET-FLIM) approach for visualization of SNARE complexes<sup>268</sup> (Figure 6.7a). This FRET-FLIM approach employed Stx5 isoforms C-terminally fused with a donor fluorophore (mCitrine) and Bet1L C-terminally fused with an acceptor fluorophore (mCherry). The formation of a post-fusion SNARE complex results in the close proximity of the donor and an acceptor fluorophore resulting in FRET which can be measured from a decreased donor fluorescence lifetime ( $\tau$ ). Contrary to ratiometric FRET, FRET-FLIM is not dependent on local concentration differences or excitation intensities of the donor and acceptor fluorophores, as  $\tau$  is an intrinsic property of the fluorophore itself. By combining the FRET-FLIM approach with the RUSH system, we were able to control the spatial localization of Stx5 isoforms and measure interactions specifically at the ER (no biotin) or the Golgi apparatus (20 min after biotin addition). 30 minutes prior to imaging, cells were incubated with cycloheximide in culture medium to make sure background interaction from any ER-localized newly-synthesized acceptor construct was mitigated.

For the mCitrine donor-only Stx5 constructs, we measured similar lifetimes for both

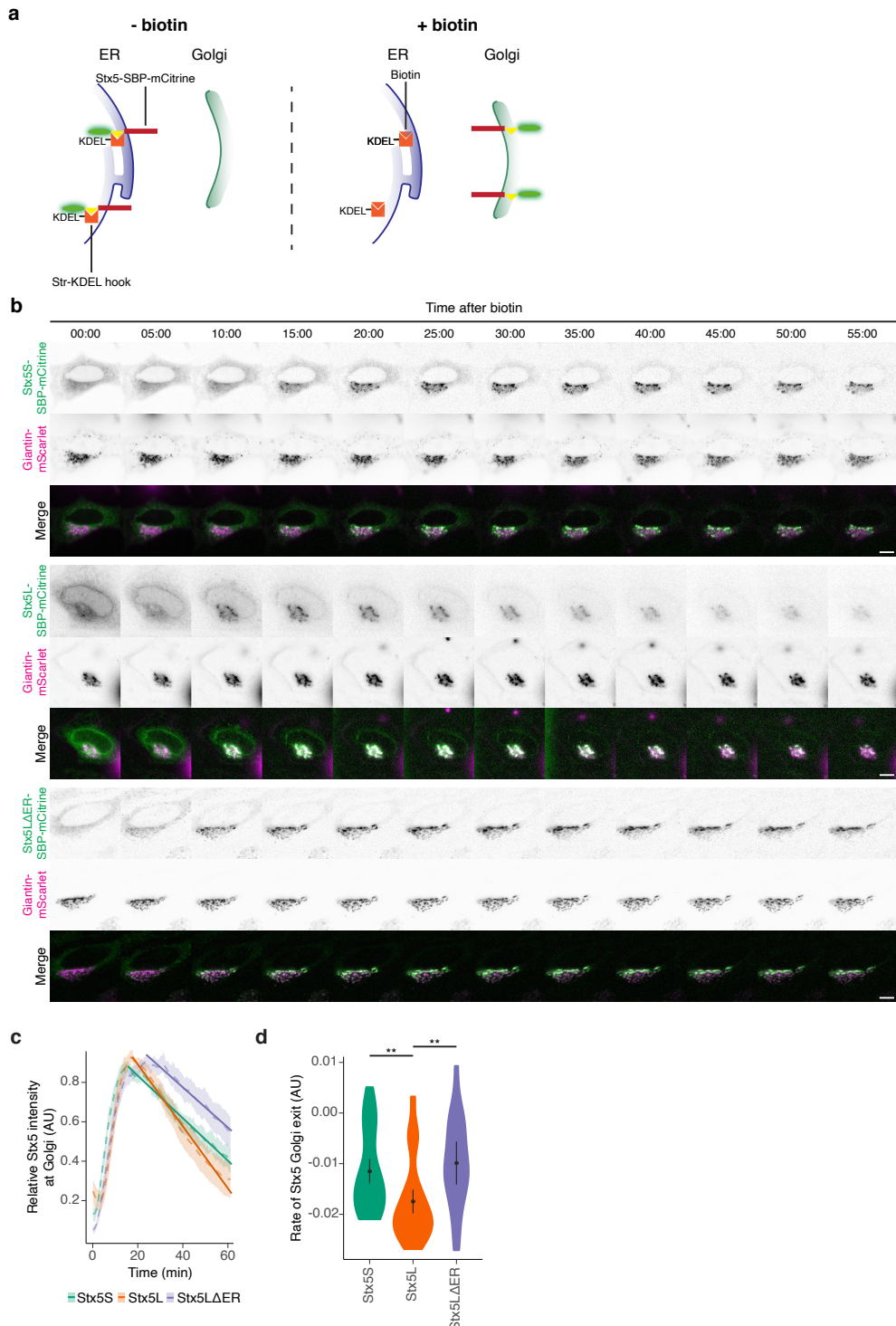
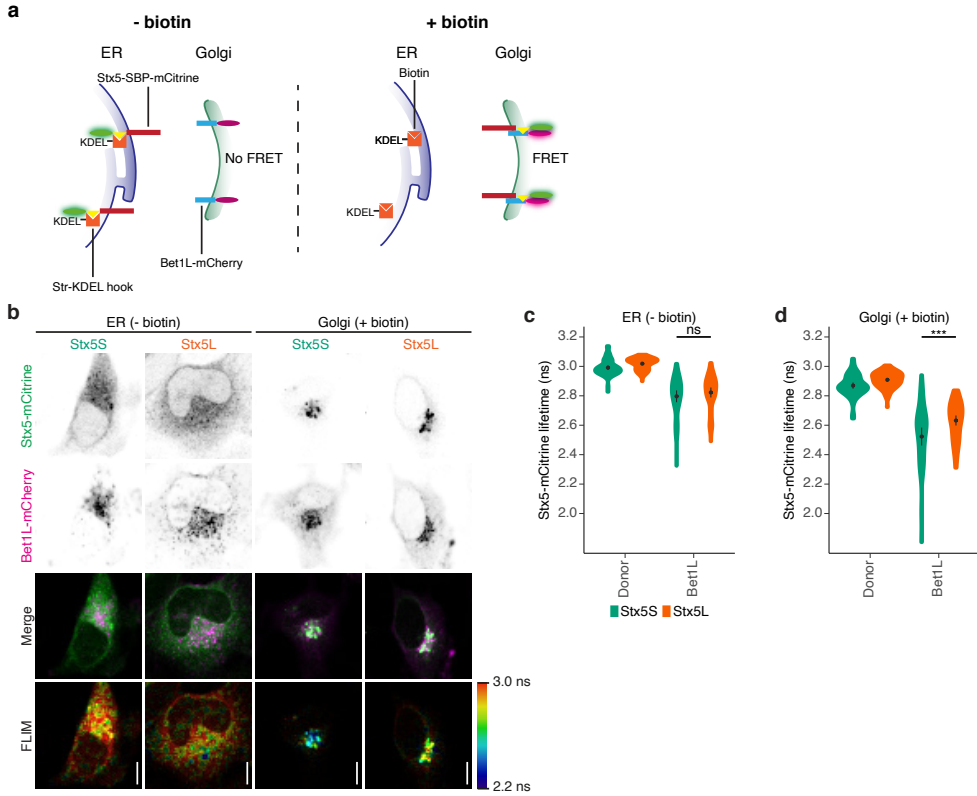


Figure 6.6: Faster Golgi exit of Stx5L than Stx5S. (Continued on the following page.)

**Figure 6.6:** (a) Schematic overview of the design of Stx5 trafficking experiment, based on the RUSH system. In absence of biotin (left panel), the reporter cargo (Stx5-SBP-mCitrine) is trapped at the ER by the luminal Str-KDEL hook. When biotin is added (right panel), biotin outcompetes the interaction with streptavidin, allowing Stx5-SBP-mCitrine to traffic freely to its destination compartment. SBP, streptavidin binding protein; Str, streptavidin. (b) Snapshots of live-cell imaging of Stx5-SBP-mCitrine (green in merge). Magenta: Golgi marker Giantin-mScarlet. Scale bars, 10  $\mu\text{m}$ . (c) Quantification of mCitrine fluorescence at the Golgi of Stx5S-SBP-mCitrine (green), Stx5L-SBP-mCitrine (orange) and Stx5L $\Delta$ ER-SBP-mCitrine (blue) over time from panel (b). N = 44 (Stx5S), 47 (Stx5L) and 19 (Stx5L $\Delta$ ER) cells from 4 independent experiments. (d) Quantification of the slopes from panel (c) of the post-Golgi section ( $\approx$ 20 mins onwards).

isoforms (Figure 6.7c, Supplementary Figure 6.24a, Stx5L: 3.02 ns  $\pm$  0.004, Stx5S: 2.99 ns  $\pm$  0.007) prior to biotin addition, while these lifetimes slightly decreased following biotin addition (Figure 6.7d, Supplementary Figure 6.24a, Stx5L: 2.90 ns  $\pm$  0.006, Stx5S: 2.86 ns  $\pm$  0.011). We attribute this reduced lifetime to the fact that mCitrine is somewhat pH-sensitive<sup>375</sup> and the pH of the Golgi apparatus is lower than in the ER lumen<sup>22</sup>. We then co-expressed the Stx5 isoforms with mCherry-tagged Bet1L (Bet1L-mCherry) (Figure 6.7a,b). At the ER, thus before the release of Stx5 with biotin, we observed reduced lifetimes for both Stx5S and Stx5L with Bet1L-mCherry, compared to the donor-only controls (Figure 6.7b, c, Stx5L: 2.82 ns  $\pm$  0.01, Stx5S: 2.79  $\pm$  0.01), whereas the lifetimes of Stx5S and Stx5L did not significantly differ from each other. After the release in the presence of biotin, this difference between Stx5L and Stx5S became significant and lifetimes were 2.63 ns ( $\pm$  0.01) for Stx5L while Stx5S dropped to 2.52 ns ( $\pm$  0.03) (Figure 6.7b, d). To validate that the observed effect is indeed caused by functional SNARE complex formation, we repeated this experiment with VAMP8 instead of Bet1L as the acceptor R-SNARE. VAMP8 has no role in ER-Golgi membrane fusion but rather associates with the late endosomal/lysosomal compartment<sup>58,118,268,376–379</sup>. We only observed minor decreases in fluorescence lifetimes for both Stx5L and Stx5S (Supplementary Figure 6.24b, c, prior to biotin Stx5L: 2.92 ns  $\pm$  0.01, Stx5S: 2.86  $\pm$  0.02, upon biotin addition Supplementary Figure 6.24b, d, Stx5L: 2.82 ns  $\pm$  0.01, Stx5S: 2.76  $\pm$  0.02). These FLIM results demonstrate that Stx5S interacts more strongly with Bet1L at the Golgi than Stx5L. Thus, Stx5S is the dominant Qa-SNARE for intra-Golgi trafficking.



**Figure 6.7: Stx5S is the dominant Qa-SNARE for intra-Golgi trafficking.** (a) Schematic overview of experimental design for complex formation of Stx5 isoforms with Bet1L, based on the RUSH system and SNARE complex measurement by FRET-FLIM. In absence of biotin (left panel), the reporter cargo (Stx5-SBP-mCitrine) is trapped at the ER by the luminal Str-KDEL hook, and no FRET with Golgi-localized Bet1L-mCherry occurs. When biotin is added (right panel), biotin outcompetes the interaction with streptavidin, allowing Stx5-SBP-mCitrine to traffic freely to its destination compartment, and SNARE complex formation with Golgi-localized Bet1L-mCherry results in FRET. SBP, streptavidin binding protein; Str, streptavidin; FRET, Förster resonant energy transfer. FLIM, fluorescence lifetime imaging microscopy. (b) Representative confocal micrographs of HeLa cells co-expressing Stx5-mCitrine (green in merge) and Bet1L-mCherry (magenta) without (ER) or with (Golgi) biotin. Scalebars, 10  $\mu$ m. (c-d) Stx5-mCitrine lifetimes at the ER (c) and Golgi (d) from panel (b). N = 52 (Stx5S Donor ER), 74 (Stx5L Donor ER), 47 (Stx5S Bet1L ER), 51 (Stx5L Bet1L ER), 50 (Stx5S Donor Golgi), 71 (Stx5L Donor Golgi), 58 (Stx5S Bet1L Golgi) and 58 (Stx5L Bet1L Golgi) cells from 3 independent experiments.

## 6.4 Discussion

Since the advent of the genomic age, close to 6,000 monogenic disorders have been discovered<sup>380</sup>. While nearly all of these disorders result in a truncated, unstable and/or nonfunctional protein, e.g., due to a genetic variant in the catalytic site or protein misfolding, isoform-specific mutations are rare. Here we present the first known mutation in an alternate site of ribosomal translation leading to human disease, namely the mutation of the second starting methionine of Stx5. This mutation leads to the complete and specific loss of Stx5S. Although *STX5* is an essential gene for embryonic development in mice<sup>307,369</sup>, here we show that in humans the loss of Stx5S still allowed a completed pregnancy. Nevertheless, patients have a very severe clinical pathology characterized by infantile mortality due to liver disease, skeletal abnormalities and protein glycosylation defects. While the exact mechanism for alternative translation is unclear, this might be an actively regulated process. It could also be simply regulated by the affinity of the ribosome for the nucleotide sequence upstream of the starting codon. Supporting the latter option, analysis of translation initiation sites with NetStart<sup>381</sup> revealed that the starting codon of Stx5S is located in a more optimal nucleotide context than the starting codon for Stx5L (Supplementary Figure 6.25). This could lead to more leaky ribosomal scanning<sup>382,383</sup>, resulting in the more or less equimolar ratio of expression of Stx5L and Stx5S that we observed in fibroblasts and PBMCs of healthy individuals. On the other hand, Western blot revealed different ratios of the two Stx5 isoforms in different organs in rats<sup>215</sup>, suggesting (i) that different cell types express different levels of Stx5S and Stx5L and this is probably related to their exocytic function, and (ii) that the initiation of starting translation might be regulated and not merely dependent on the binding affinities of the ribosome.

Cofractionation and microscopy studies have revealed that the localization of Stx5L and Stx5S overlap to a large extent, but that they are generally distributed as a gradient between ER, ERGIC, and Golgi apparatus<sup>330</sup>. This observation has previously led to the suggestion that Stx5L might play a role in early Golgi trafficking, while Stx5S functions in late Golgi trafficking<sup>21,194–200,204,206</sup>. Our data now shows that this is not the case and that both Stx5 isoforms can mediate both early and late anterograde and retrograde Golgi trafficking with sufficient fidelity to keep the layered Golgi morphology intact. However, the role of Stx5S is more important for retrograde Golgi-ER and intra-Golgi trafficking, and its absence leads to an altered ER and Golgi morphology, distribution of glycosylation enzymes and trafficking proteins. The cumulative effect of slight mislocalization of all glycosyltransferases might well explain the observed hypoglycosylation in the Stx5M55V patients. Indeed, recent modeling showed that the slight mislocalization of glycosyltransferases can result in large differences in glyco-

sylation patterns, because glycosylation is the result of the sequential addition and removal of different sugar moieties at the various Golgi compartments<sup>384</sup>.

The dominant role of Stx5S in retrograde Golgi-ER and intra-Golgi trafficking is corroborated by the observation that cellular levels of Bet1L, with known roles in intra-Golgi trafficking, are lower in Stx5M55V patient cells. Interestingly, genetic variants in conserved oligomeric Golgi (COG) tethering complex components, which are also implicated in CDGs, also resulted in lower levels of Bet1L as well and this was attributed to a mislocalization of Bet1L to the ER where it was degraded<sup>157</sup>. Possibly, a similar mechanism might explain the reduction in Bet1L levels in Stx5M55V patients. Although the Stx5-Bet1L interaction has been reported in several studies<sup>80,202</sup>, our study now shows this interaction *in situ* using FLIM. This interaction is localization dependent and occurs mostly when Stx5 is localized at the Golgi. Moreover, we observed stronger interaction of Bet1L with Stx5S compared to Stx5L at the Golgi, which is likely the result of the differential localization of both isoforms.

An important function of the Golgi apparatus is protein glycosylation<sup>385</sup>. Collectively, somatic mutations affecting glycosylation are classified as CDGs and currently over 100 monogenic diseases affecting glycosylation have been identified<sup>31,56</sup>. A significant number of these include defects in Golgi trafficking, such as the components of the conserved oligomeric Golgi tethering complex (COG)<sup>165,172,176–179,183,193,386</sup>, mutations in genes coding for the vacuolar H<sup>+</sup>-ATPase and its assembly factors<sup>112,120,121,387</sup>, and novel genes involved in Golgi ion homeostasis<sup>130,131,388</sup>. Furthermore, defects are known in components associated with COPI-coated vesicles<sup>144</sup> that result in deficient protein glycosylation in patient cells, but are not linked to abnormal glycosylation of proteins in plasma and thus escape routine CDG screening. Our study is the first example of an ER-Golgi SNARE being implicated in CDG, thus highlighting the potential of glycosylation screening in patients to uncover novel cell biological mechanisms.

While the cellular effects of the loss of Stx5S in Stx5M55V mutant fibroblasts are subtle, there can be pronounced consequences in secretory cells, such as exocrine and endocrine cells, which are sensitive to minor disruptions of the secretory pathway<sup>144,385,389,390</sup>. Not only can the defects in intra-Golgi trafficking explain the hypoglycosylation in Stx5M55V patients, but also of other pathologies. For instance, Stx5 can participate in the trafficking and processing of the very low-density lipoprotein receptor (VLDL-R) and this role is heavily dependent on the expression of Stx5<sup>315</sup>, thus providing an explanation for the observed cholesterol homeostasis defect with elevated cholesterol in all Stx5M55V patients.

In summary, we have demonstrated that a mutation in an alternative translation start site in Stx5 has a severe impact on intracellular membrane trafficking, leading to the discovery of a novel CDG. While there are many previous descriptions of alterna-

tive start site variations leading to disease<sup>391</sup>, this is the first known mutation in an alternative starting codon leading to human disease by the loss of an isoform.

#### 6.4.1 Acknowledgments

We thank the family for participating in this study. We thank the following people for constructs: Hesso Farhan and Franck Perez (Str-KDEL\_ManII-SBP-EGFP; Addgene plasmid #65252), Jennifer Lippincott-Schwartz (pEGFP-VSVG; Addgene plasmid #11912), Feng Zhang (pSpCas9n(BB)-2A-Puro (PX462) V2.0; Addgene plasmid #62987) and Dorus Gadella (pmScarlet-i\_Giantin\_C1, Addgene plasmid #85050). We also thank the Microscopic Imaging Center of the Radboud Institute for Molecular Life Sciences for use of their microscopy facilities. N.H.R. is funded by a Long-Term Fellowship from the European Molecular Biology Organization (EMBO-LTF, ALTF 232-2016) and a Veni grant from the Netherlands Organization for Scientific Research (016.VENI.171.097). G.v.d.B. is funded by a Young Investigator Grant from the Human Frontier Science Program (HFSP; RGY0080/2018) and a Vidi grant from the Netherlands Organisation for Scientific Research (NWO-ALW VIDI 864.14.001). G.v.d.B has also received funding from the European Research Council (ERC) under the European Union's Horizon 2020 research and innovation program (grant agreement No. 862137). D.J.L. is funded by a Vidi grant (ZONMW VIDI 917.13.359), a ZONMW Medium Investment Grant (40-00506-98-9001) from the Netherlands Organisation for Scientific Research, and Erare grants EUROCDG2 and Euroglycanomics. K.Õ, M.-A.V., S.P., and K.M. were supported by the Estonian Research Council grants GARLA8175, PUT355, PUTJD827 and PRG471.

#### 6.4.2 Author Contributions

P.T.A.L., M.t.B., D.J.L., and G.v.d.B. designed the experiments and wrote the paper. E.C.F.G. contributed to the Stx5 kinetics, co-immunoprecipitation, and FLIM experiments. A.A., M.-A.V., M.B., F.Z., K.H., K.R., K.M., and K.Õ. contributed to the clinical data, exome sequencing and glycomics. O.F. and S.P. performed homozygosity mapping and prioritization of exome variants. N.H.R. and R.d.B. performed TEM. R.A. contributed to the Stx5 $\Delta$ L experiments. P.T.A.L. and M.t.B. performed all other experiments. All authors contributed to writing the manuscript.

#### 6.4.3 Declaration of Interests

The authors declare that they have no competing financial interests.

## 6.5 Methods

### 6.5.1 Ethics

The study was approved by Research Ethics Committee of the University of Tartu (approval dates 19.12.2011, 20.02.2012 and 17.03.2014, and approval numbers 210/M-17, 212/M-31 and 235/M-13, 17.03.2014, respectively) and were strictly in accordance with the Declaration of Helsinki. Informed consent for carrying out research was obtained from the family of investigated individuals. Buffy coats and whole blood were obtained as anonymous coded specimens from the Dutch blood bank (Sanquin) and were handled according to known practice and legal guidelines. The research with human blood samples at the Department of Tumor Immunology complies with all institutional and national ethics regulations and has been approved by the ethics committee of Sanquin.

### 6.5.2 Glycosylation studies

Screening for CDG was carried out as described before<sup>120</sup>. Plasma N-glycan profiling was performed by MALDI-TOF mass spectrometry of permethylated glycans<sup>93</sup>, using 10 µL of plasma. High resolution mass spectrometry of intact transferrin was performed on a 6540 nanochip QTOF (Agilent), according to published protocols<sup>392</sup>.

### 6.5.3 Microarray analysis

DNA was extracted either from peripheral blood according to the standard salting out protocol (IV:9 and IV:10) or from amniotic fluid cell culture (IV:8). Screening for chromosomal abnormalities was performed using HumanCytoSNP-12 BeadChips (Illumina Inc., San Diego, CA, USA). 200 ng of total DNA per sample was processed according to the protocol supplied by the manufacturer. Genotypes were called by GenomeStudio v2011.1 software and the data were analyzed using GenomeStudio Genome Viewer tool (Illumina Inc.). The minimum threshold for LCSH (long contiguous stretches of homozygosity) regions was set at 5 Mb.

### 6.5.4 Exome sequencing

Genomic DNA was extracted from fibroblasts from patient IV:9 according to the manufacturer's protocol using a Qiagen Mini Kit (Qiagen) and was checked for DNA degradation on agarose gels. Next generation sequencing (NGS) and analysis were performed as described<sup>121</sup>. In brief, exome enrichment was performed using the SureSelect Human All Exon 50 Mb Kit (Agilent), covering ≈21,000 genes. The exome library was se-

quenced on a SOLiD 5500xl sequencer (Life Technologies). Color space reads were iteratively mapped to the hg19 reference genome with the SOLiD LifeScope software version 2.1. Called variants and indels were annotated using an in-house annotation pipeline<sup>393,394</sup> and common variants were filtered out based on a frequency of >0.5% in dbSNP and a frequency of >0.3% in our in-house database of >5,000 exomes. Quality criteria were applied to filter out variants with less than 5 variant reads and less than 20% variation. Furthermore, synonymous variants, deep intronic, intergenic and UTR variants were excluded. The identified variant was confirmed by Sanger sequencing in all affected individuals (IV:8, IV:9, and IV:10) and their mother (III:2). Paternal DNA (III:1) was not available.

### 6.5.5 Cell culture

HeLa cells (authenticated by ATCC through their human STR profiling cell authentication service), including Stx5 $\Delta$ L cell lines, were maintained in high glucose DMEM with Glutamax (Gibco 31966021). Human primary dermal fibroblasts were obtained from patients or healthy donors and maintained in Medium 199 with EBSS and L-glutamine (Lonza BE12-119F). All media were supplemented with 10% fetal calf serum (FCS, Greiner Bio-one, Kremsmünster, Austria) and antibiotic-antimycotic solution (Gibco 15240-062). All cells were regularly tested for mycoplasma contamination. Human peripheral blood mononuclear cells (PBMCs) were obtained from buffy coats as previously described<sup>395</sup>.

### 6.5.6 Plasmids and transfection

Str-KDEL\_ManII-SBP-EGFP was a gift from Franck Perez (Addgene plasmid #65252). VAMP8-mCherry was constructed earlier<sup>268</sup> and previously deposited to Addgene (Addgene plasmid #92424). Str-KDEL\_Stx5L-SBP-mCitrine and Str-KDEL\_Stx5S-SBP-mCitrine were constructed by replacing the ManII-SBP-EGFP cassette in Str-KDEL\_ManII-SBP-EGFP using the AscI and XbaI restriction sites. Stx5 coding sequences were codon-optimized for Homo sapiens using JCat and ordered from Genscript, the Stx5L coding sequence carries the M55V mutation to suppress production of Stx5S. Stx5L $\Delta$ ER coding sequence was generated with Q5-polymerase site-directed mutagenesis, using the Stx5L cDNA as a template with the following primer: 5'- CTTCG AATGA TTCCG GCCGC CGCCT ACGGC AGCAA GAACA CC. Sequences were verified with Sanger sequencing. HeLa cells were transfected with plasmid vectors using Fugene HD (Promega E2311), using the recommended protocol of the manufacturer. Only cells expressing low to moderate levels of the transfected plasmids, based on

fluorescence intensity and manual localization scoring, were chosen for subsequent microscopic analyses.

### 6.5.7 CRISPR/Cas9

Stable knock out of Stx5L in fibroblasts and HeLa cells was obtained using the CRISPR-CAS9 method. For this, pairs of gRNA sequences were designed upstream of the *STX5* initiation codon ([crispr.mit.edu](http://crispr.mit.edu), pair 1: ATAAC CTCGG ACTGT TGTGG AGG and ATGAT CCCGC GGAAA CGCTA CGG; pair 2: TAACC TCGGA CTGTT GTGGA GGG and TGATC CCGCG GAAAC GC-TAC GGG). The gRNA sequences were cloned in pSpCas9n(BB)-2A-Puro (PX462) V2.0 (gift from Feng Zhang, Addgene no. 62987)<sup>396</sup> and transfected into fibroblasts or HeLa cells by electroporation (Neon Transfection System, ThermoFisher, MA). After initial selection with puromycin, the medium was changed for conditioned medium (collected from parental fibroblasts or wildtype HeLa cells at 70% confluence) supplemented 1:1 with fresh medium. Single clones were obtained and screened for knockout of Stx5L by SDS-PAGE and Western blotting.

### 6.5.8 Immunofluorescence

Cells were plated on cleaned 12 mm glass coverslips (Electron Microscopy Services, 72230-01) and the following day fixed with 4% paraformaldehyde for 15 minutes at room temperature. Following quenching with 50 mM NH<sub>4</sub>Cl in PBS, cells were permeabilized and blocked in 2% normal donkey serum (Rockland, 017-000-121) and 0.1% saponin (permeabilization buffer) for 30 mins at RT. Primary and secondary antibodies (list of antibodies and dilutions in Table 6.4) were diluted in permeabilization buffer and incubated for 1 hour at room temperature. Finally, cells were washed with 0.1% Triton X-100 in PBS to remove background staining and mounted with mounting medium containing 0.01% Trolox (6-hydroxy-2,5,7,8-tetramethylchroman-2-carboxylic acid) and 68% glycerol in 200 mM sodium phosphate buffer at pH 7.5 with 0.1 µg/ml DAPI. Coverslips were sealed with nail polish. Cells were imaged on a Leica SP8 SMD confocal laser scanning microscope, equipped with an HC PL APO CS2 63×/1.20 WATER objective. Colocalization analysis was performed using the *pearsonr* function from the Python package SciPy<sup>397</sup>. Briefly, individual cells were saved to separate .tiff files with ImageJ without any modifications, and then processed in a fully automated and unbiased fashion using the *pearsonr* function.

### 6.5.9 Lectin stainings

Cells were plated on cleaned 12 mm glass coverslips for microscopy or 6-wells plates for flow cytometry and after 72 hours culturing fixed with 4% paraformaldehyde. Cells

were blocked with Carbo-Free Blocking solution (Vector Laboratories, SP-5040) and incubated with 4  $\mu$ g/mL biotinylated SNA-I (Vector Laboratories, B-1305) or PNA (Vector Laboratories, B-1075) diluted in Carbo-Free Blocking solution. Cells were then incubated with Streptavidin-Alexa Fluor 647 (ThermoScientific, S32357) before coverslips were mounted as described above. Cells were imaged on a Leica SP8 SMD confocal laser scanning microscope, equipped with an HC PL APO CS2 63 $\times$ /1.20 WATER objective. For flow cytometry, cells were resuspended in FACS buffer (phosphate buffered saline + 0.5% FBS + 0.01% NaN<sub>3</sub>). Flow cytometry samples were run on a FACSLyric flow cytometer (BD Biosciences) and analyzed with FlowJo X (FlowJo, LLC).

#### 6.5.10 Brefeldin A assay

Fibroblasts were plated on 12 mm coverslips and cultured until 80% confluent. Cells were either treated with 10  $\mu$ g/mL Brefeldin A in DMSO (Cayman Chemicals, 11861) or DMSO alone for 6 minutes in a humified incubator. Washout was performed by washing five times with Leibovitz's L-15 (Gibco 21083027) with 10% FBS, then incubating in Leibovitz's L-15 with 10% FBS at 37°C for the indicated times. After incubation, plates were transferred immediately to ice and cells were fixed with 4% paraformaldehyde, after which the above immunofluorescence protocol was performed. Microscopy images were acquired using a Leica SP8 SMD confocal laser scanning microscope, equipped with an HC PL APO CS2 63 $\times$ /1.20 WATER objective. HeLa cells were plated on 12 mm coverslips and incubated in the same way with Brefeldin A, but fixed with 100% methanol at -20°C for 15 mins. Imaging of these samples was performed using a Leica DMI6000B epifluorescence microscope equipped with an HC PL APO 63x1.40 OIL objective. Cells were analyzed using Fiji (<http://fiji.sc/>) by first removing noise outliers (bright outliers, radius 2.0 pixels, threshold 50), then manually selecting cells and measuring the maximum fluorescence intensity in these ROIs. Data were normalized to the mean of the DMSO control of each group.

#### 6.5.11 H-89 assay

HeLa cells were plated on 12 mm coverslips and incubated the following day for 30 mins with 100  $\mu$ M H-89 (Cayman Chemicals, 10010556) in DMSO or DMSO alone (vehicle) and H-89 was washed out with fresh medium for 5 mins. Cells were fixed with 4% paraformaldehyde for 15 mins at RT and permeabilized with 100% methanol at -20°C for 15 mins prior to immunostaining with ERGIC53 mouse monoclonal antibody (G1/93 or OTI1A8) before epifluorescence imaging as described for the BFA assay. Cells were analyzed using Fiji and the number of ERGIC53-positive spots was quantified with the Spot Counter plugin. Data were normalized to the mean fluorescence

of the DMSO control of each group. Data was analyzed with a Mann-Whitney U non-parametric test.

### 6.5.12 Transmission electron microscopy

Fibroblasts were grown in 12-wells plates and fixed with 2% glutaraldehyde (Sigma-Aldrich, G5882) in PB (0.1 M phosphate buffer, pH 7.4) for 60 mins at room temperature. Subsequently, cells were washed four times with PB and post-fixed with 1% osmium tetroxide and 1% potassium ferrocyanide in PB for 60 mins at room temperature. Then, cells were again washed four times with PB and four times with water. Cells were incubated overnight in 0.5% uranyl acetate and dehydrated with graded steps of ethanol (30%, 50%, 70%, 96%, 100%) and embedded in Epon resin. 70 nm sections were stained with 2% uranyl acetate solution and lead citrate solution. Stained sections were then examined using a CM12 transmission electron microscope (Phillips).

### 6.5.13 Live-cell epifluorescence microscopy

Cells were seeded in four-compartment dishes (Greiner 627870) and transfected as described above (3:1 weight ratio reporter construct:Golgi label). Before imaging, the culture medium was exchanged for Leibovitz's L-15 (Gibco 21083027). Samples were imaged using a DMI6000B (Leica Microsystems) with a heated stage (Pecon) and objective heater. All samples were imaged using an HC PL APO 63 $\times$ /1.40–0.60 OIL objective. VSVG-ts045-EGFP experiments were performed at 32°C after overnight incubation at 40°C, while all other epifluorescence experiments were performed at 37°C. For RUSH experiments, an equal amount of Leibovitz's L-15 supplemented with biotin was added to the well immediately before imaging, to reach a final concentration of 40  $\mu$ M biotin. Live cell imaging was started immediately with 15 sec or 30 sec frame rates. Analysis was performed with Fiji, after registration of the image stacks, the increase in fluorescence was measured in the Golgi area by using the thresholded mScarlet-Giantin signal as an image mask.

### 6.5.14 FRET-FLIM

All imaging took place in Leibovitz's L-15 supplemented with 10  $\mu$ g/mL cycloheximide (Sigma-Aldrich, C4859) and cells were pulsed with biotin as described above. Imaging was performed on a Leica SP8 SMD system at 37°C, equipped with an HC PL APO CS2 63 $\times$ /1.20 WATER objective. Fluorophores were excited with a pulsed white light laser, operating at 80 MHz. mCitrine was excited at 514 nm, two separate HyD detectors were used to collect photons, set at 521-565 nm and 613-668 nm respectively. Photons were collected for one minute and lifetime histograms of the donor fluorophore were fitted

with monoexponential decay functions convoluted with the microscope instrument response function in Leica LAS X.

### 6.5.15 Immunoprecipitation

HeLa cells were lysed 48 hours post-transfection with IP lysis buffer (20 mM Tris-HCl pH 7.6, 137 mM NaCl, 1% IGEPAL, 2 mM EDTA and complete protease inhibitors (Roche 5892791001)). Protein levels were equilibrated and lysates were immunoprecipitated with 1  $\mu$ g anti-GFP-antibody (Rockland 600-401-215) and protein A beads (ThermoFisher, 20333) for 1 hour at 4°C with constant agitation. After three washes with IP lysis buffer, samples were boiled in 5x SDS sample buffer with  $\beta$ -mercaptoethanol and resolved with SDS-PAGE and subsequent immunoblotting.

### 6.5.16 SDS-PAGE and immunoblotting

Cells were plated in 12-wells plates in culture medium and lysed the following day with SDS lysis buffer (1% SDS, 10 mM Tris-HCl pH 6.8). Lysates were diluted to equal protein content (30  $\mu$ g per lane) with SDS lysis buffer, separated with SDS-PAGE on 4–20% Mini-PROTEAN TGX Precast Protein Gels (Biorad, 4561094) and subsequently transferred onto 0.45  $\mu$ m PVDF membranes. Small molecular weight proteins (Bet1 and Bet1L) were separated on 16% Schaegger gels<sup>398</sup>.

### 6.5.17 Quantification and statistical analysis

All mean values represent the average of all cells analyzed. All comparisons between two groups were first checked for similar mean and median values and acceptable (< 3x) difference in variance, before statistical analysis with an unpaired two-sided Student's t-test. Relative intensity data was first transformed using the binary logarithm before analysis with an unpaired two-sided Student's t-test. H-89 data was analyzed with a Mann-Whitney U non-parametric test. Stx5 kinetics data were analyzed with a one-way ANOVA, followed by a post-hoc Tukey's honestly significant difference test. Stx5 FLIM data were analyzed with a two-way ANOVA, with the isoform and timepoint as independent variables, followed by a post-hoc Tukey's honestly significant difference test.  $p < 0.05$  was considered significant. \* $p < 0.05$ , \*\* $p < 0.01$ , \*\*\* $p < 0.001$ , \*\*\*\* $p \leq 0.0001$ . All statistical analyses were performed using R statistical software. All numerical data were visualized using R package *ggplot2*<sup>286</sup>, with violins representing the overall distribution of the data and means  $\pm$  95% CI overlaid.

### 6.5.18 Data and code availability

Microarray data, exome sequencing data and ImageJ macros for quantification of the RUSH experiments are available upon request. Primary microscopy data was deposited to Zenodo.

## 6.6 Supplementary Information

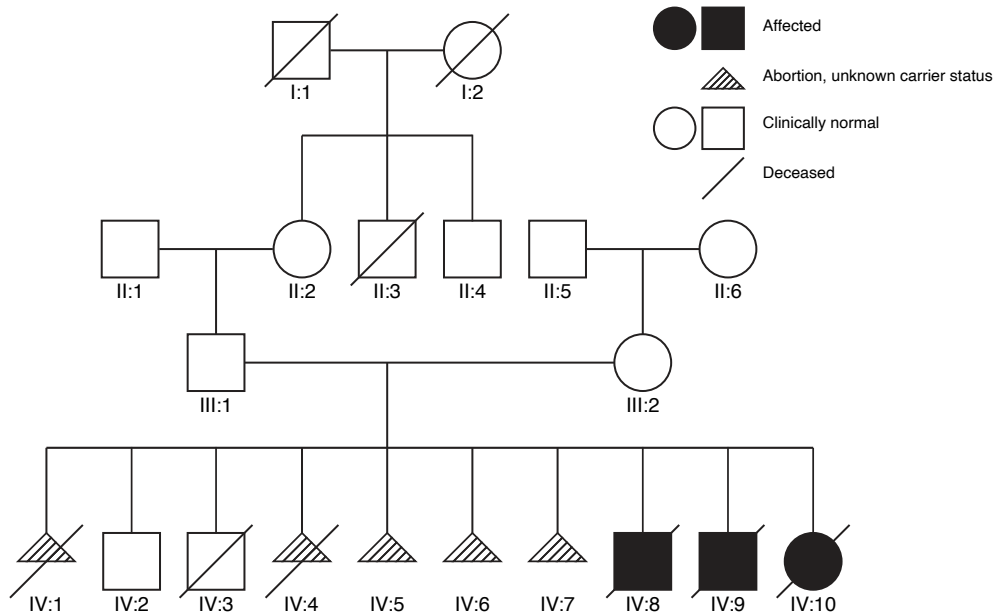


**Figure 6.8: Family pedigree of *Stx5M55V* patients.** Black filled squares and circles indicate affected patients. Empty squares and circles indicate clinically normal individuals. Triangles with diagonal stripes indicate aborted individuals or individuals with unknown carrier status. The diagonal line indicates deceased individuals.

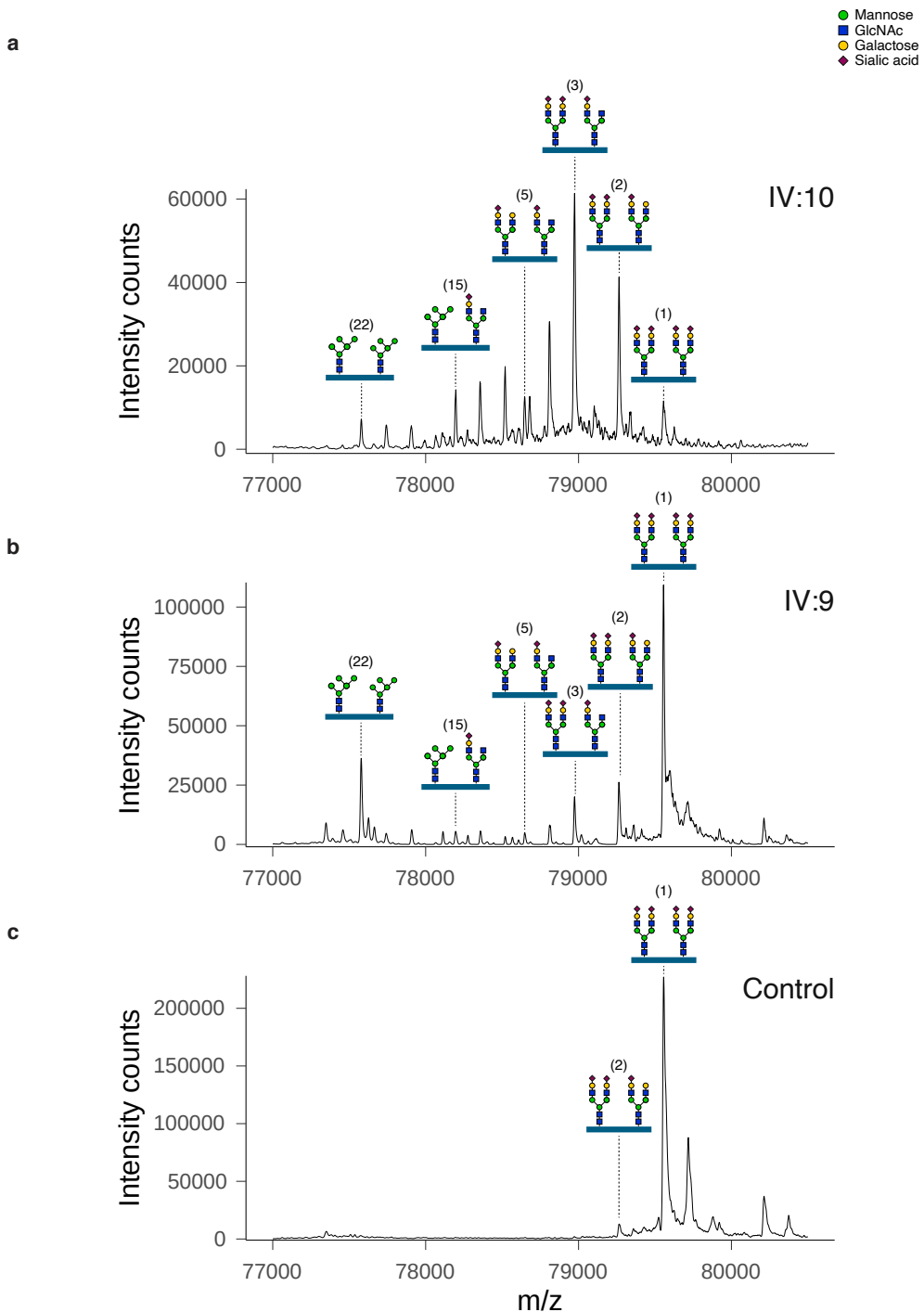


**Figure 6.9: Glycan structural changes in STX5M55V patients by intact transferrin mass spectrometry.** (Continued on the following page.)

**Figure 6.9:** The nanochip-C8 QTOF mass spectra of enriched intact serum transferrin of Stx5M55V patient IV:10 (a), patient IV:9 (b) and healthy control (c) are shown. Annotation of all transferrin glycoforms is shown in Supplementary Table 3.

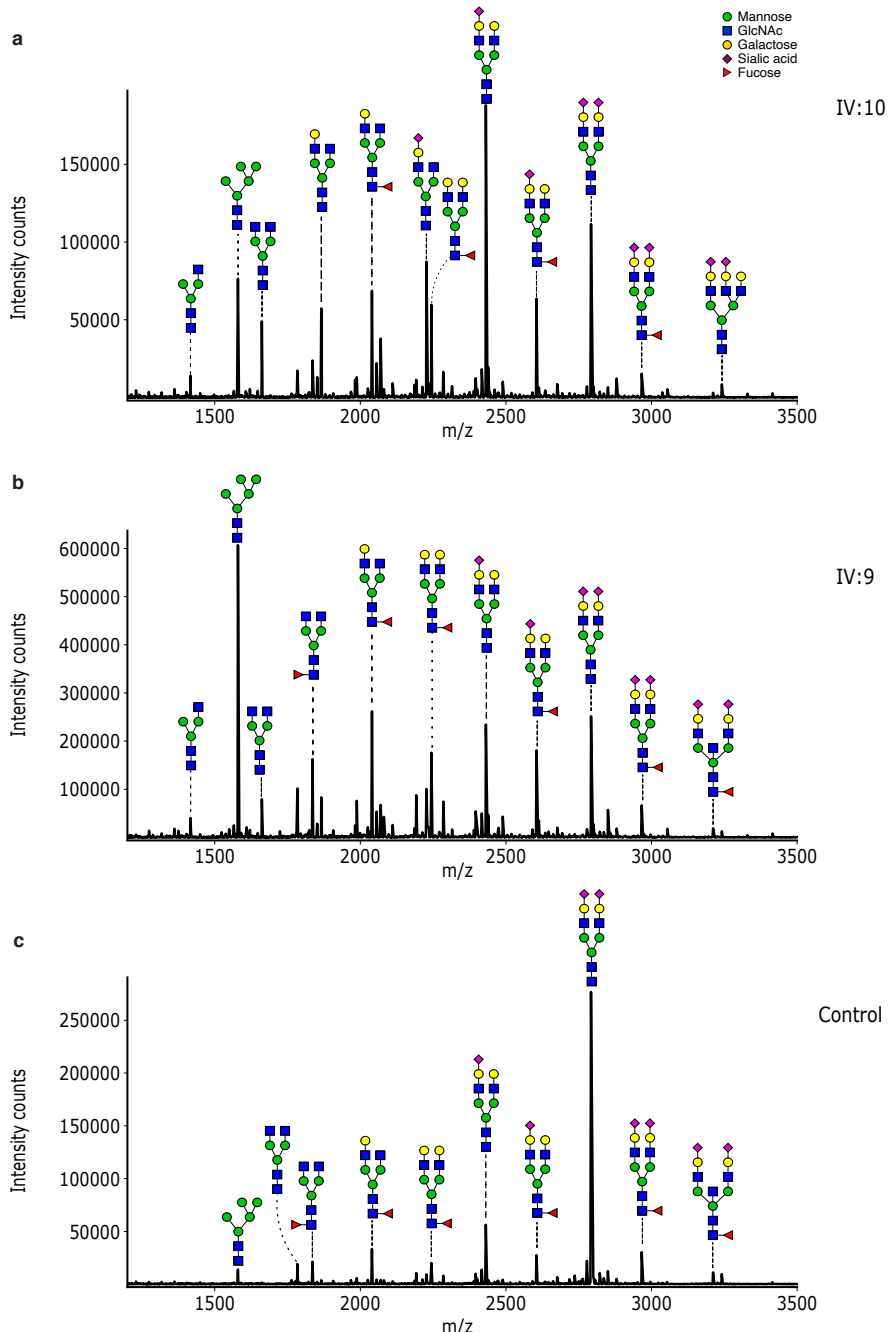
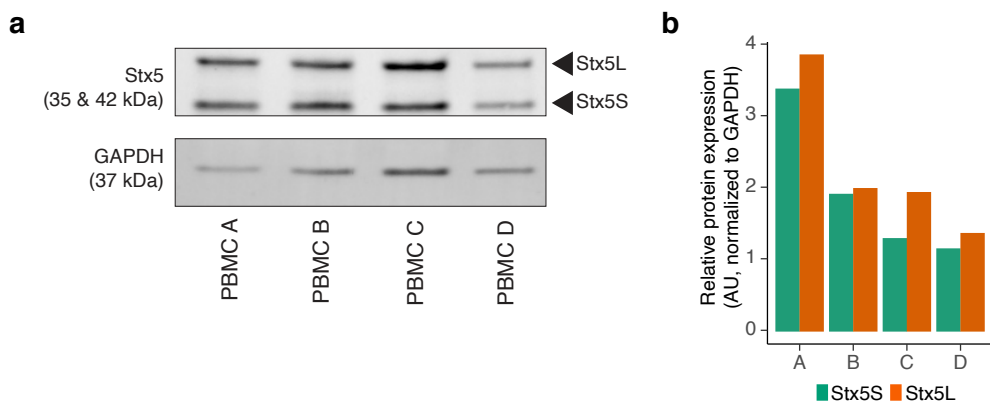


Figure 6.10: Glycan structural changes in STX5M55V patients by MALDI-TOF mass spectrometry of total plasma protein derived N-glycans. (Continued on the following page.)

**Figure 6.10:** The MALDI-TOF mass spectra of all plasma N-glycans of Stx5M55V patient IV:10 (a), patient IV:9 (b) and healthy control (c) are shown. Annotation of all glycan structures is shown in Supplementary Table 4.



**Figure 6.11: Interindividual Stx5 expression variation.** (a) Representative immunoblot for Stx5 on lysates of peripheral blood mononuclear cells (PBMCs) isolated from four healthy donors. GAPDH, loading control. (b) Quantification of (a).

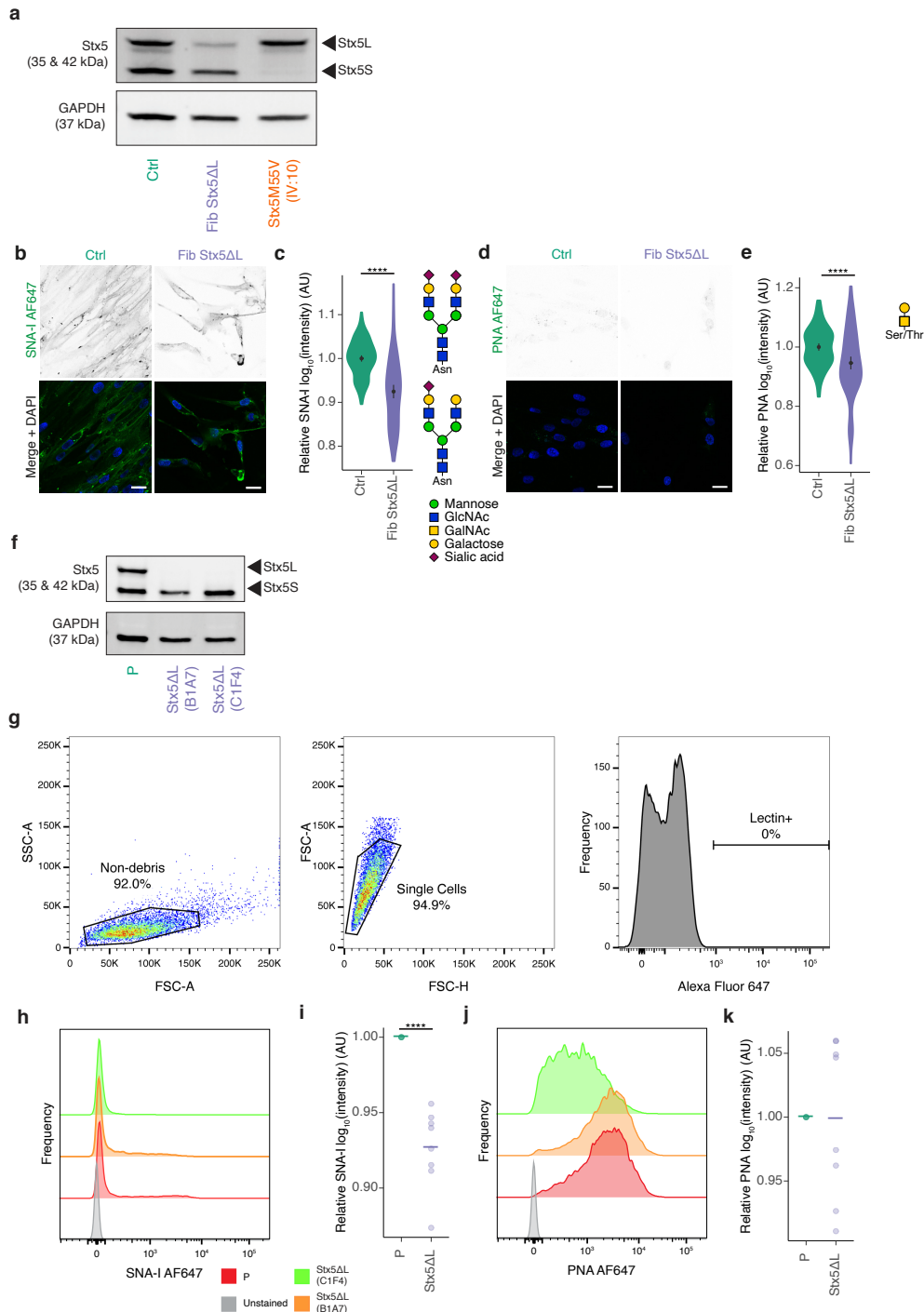
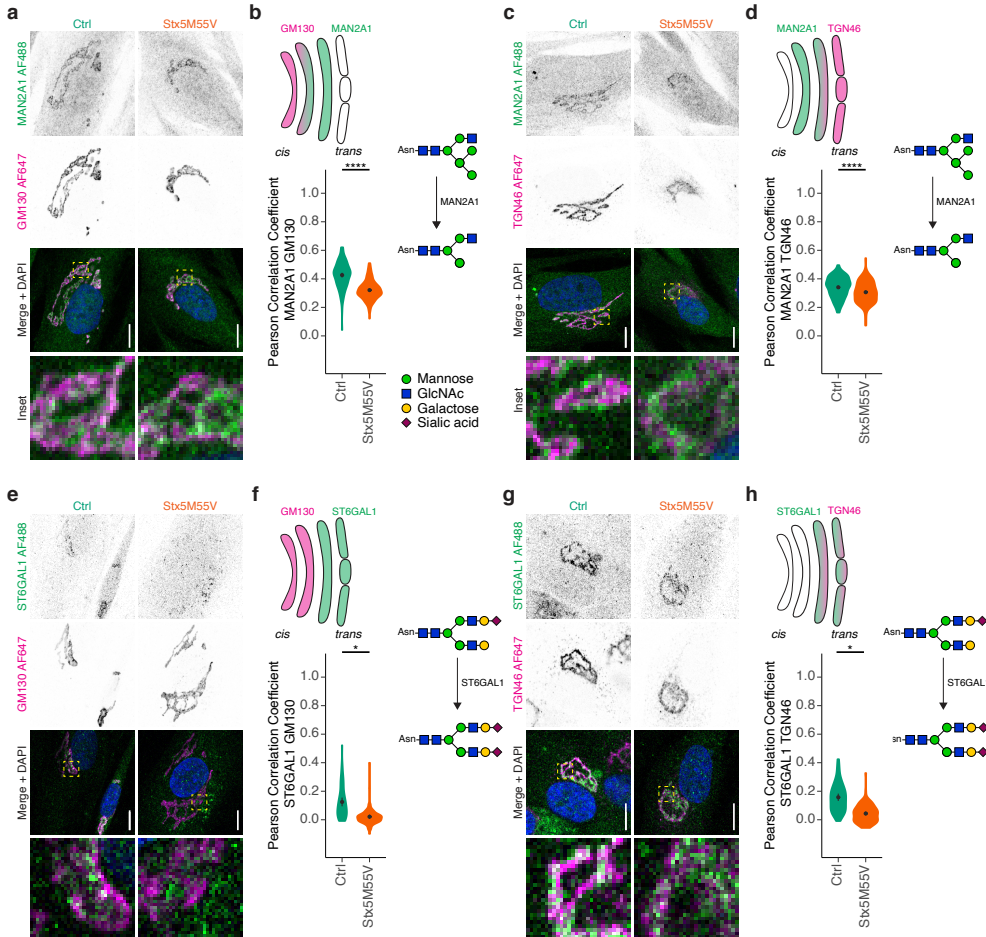
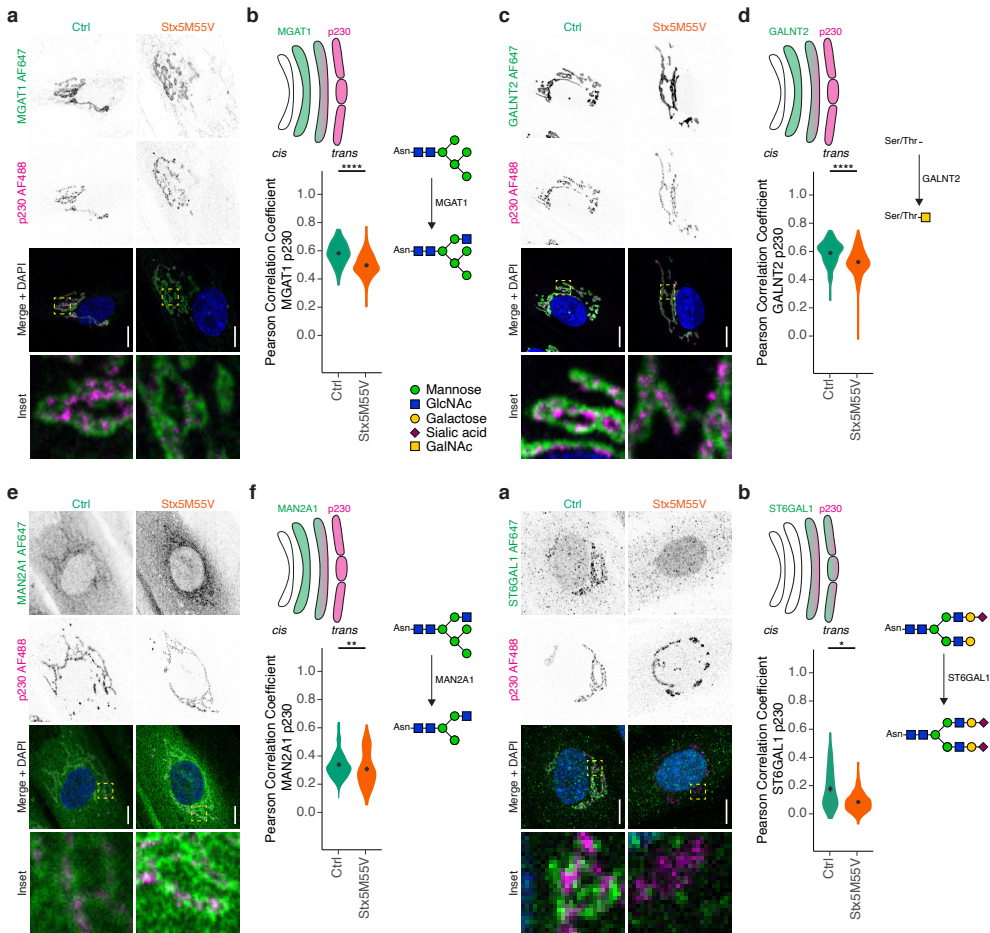


Figure 6.12: Stx5L-lacking cell line generation and lectin stainings. (Continued on the following page.)

**Figure 6.12:** (a) Representative immunoblot for Stx5 of cell lysates of primary human dermal fibroblasts of a healthy donor (green, Ctrl), Stx5L-lacking (blue, Fib Stx5 $\Delta$ L) or Stx5M55V patients (orange, Stx5M55V). GAPDH, loading control. The band corresponding to Stx5L in Fib Stx5 $\Delta$ L shows residual Stx5 $\Delta$ L expression due to incomplete CRISPR/Cas9 knockout. (b) Fibroblasts of healthy donors (green, Ctrl) or Stx5 $\Delta$ L (blue, Fib Stx5 $\Delta$ L) were probed with SNA-I lectin (green in merge). Representative confocal micrographs. Scalebars, 25  $\mu$ m. DAPI in blue. (c) Quantification of (b). All data were  $\log_{10}$ -transformed and then normalized to the healthy donor. N = 134 (Ctrl) and 107 (Stx5 $\Delta$ L) from 2 independent cell lines repeated twice. (d-e) Same as panels (b-c), but now for PNA lectin. N = 113 (Ctrl) and 111 (Stx5 $\Delta$ L) from 2 independent cell lines repeated twice. (f) Representative immunoblot for Stx5 of cell lysates of HeLa cells of parental (green, P) or two clonal Stx5L-lacking lines (blue, Stx5 $\Delta$ L B1A7 and C1F4). GAPDH, loading control. (g) FACS gating strategy for lectin stainings, cell population shown is the unstained control. FSC-A: forward scatter area, SSC-A: side scatter area, FSC-H: forward scatter height. (h) Quantification of parental HeLa (green, P) or Stx5 $\Delta$ L (blue, Stx5 $\Delta$ L), probed with SNA-I lectin followed by FACS. Geometric means were taken and  $\log_{10}$ -transformed, then normalized to wildtype. 10.000 events analyzed per condition per experiment from 4 independent experiments. (i) Same as panel (h), but now for PNA lectin. 10.000 events analyzed per condition per experiment from 4 independent experiments.



**Figure 6.13: Glycosylation enzymes mislocalize in Stx5M55V patient fibroblasts.** (a) Immunofluorescence microscopy of MAN2A1 (green in merge) and GM130 (magenta) in primary dermal fibroblasts of healthy donors (green, Ctrl) or Stx5M55V patients (orange, Stx5M55V). Representative confocal micrographs. Scalebars, 10  $\mu$ m. DAPI in blue. N = 127 (Ctrl) and 143 (Stx5M55V) cells from 2 independent cell lines repeated twice. (b) Pearson's correlations coefficients between MAN2A1 and GM130 of panel (a). (c-d) Same as panels (a-b), but now for MAN2A1 (green) and TGN46 (magenta). N = 155 (Ctrl) and 171 (Stx5M55V) cells from 2 independent cell lines repeated twice. (e-f) Same as panels (a-b), but now for ST6GAL1 (green) and GM130 (magenta). N = 56 (Ctrl) and 78 (Stx5M55V) cells from 2 independent cell lines repeated twice. (g-h) Same as panels (a-b) but now for ST6GAL1 (green) and TGN46 (magenta). N = 57 (Ctrl) and 86 (Stx5M55V) cells from 2 independent cell lines repeated twice.



**Figure 6.14: Glycosylation enzymes mislocalize in Stx5M55V patient fibroblasts.** (a) Immunofluorescence microscopy of MGAT1 (green in merge) and p230 (magenta) in primary dermal fibroblasts of healthy donors (green, Ctrl) or Stx5M55V patients (orange, Stx5M55V). Representative confocal micrographs. Scalebars, 10  $\mu$ m. DAPI in blue. N = 153 (Ctrl) and 147 (Stx5M55V) cells from 2 independent cell lines repeated twice. (b) Pearson's correlations coefficients between MGAT1 and p230 of panel (a). (c-d) Same as panels (a-b), but now for GALNT2 (green) and p230 (magenta). N = 166 (Ctrl) and 160 (Stx5M55V) cells from 2 independent cell lines repeated twice. (e-f) Same as panels (a-b), but now for MAN2A1 (green) and p230 (magenta). N = 184 (Ctrl) and 75 (Stx5M55V) cells from 2 independent cell lines repeated twice. (g-h) Same as panels (a-b) but now for ST6GAL1 (green) and p230 (magenta). N = 128 (Ctrl) and 149 (Stx5M55V) cells from 2 independent cell lines repeated twice.

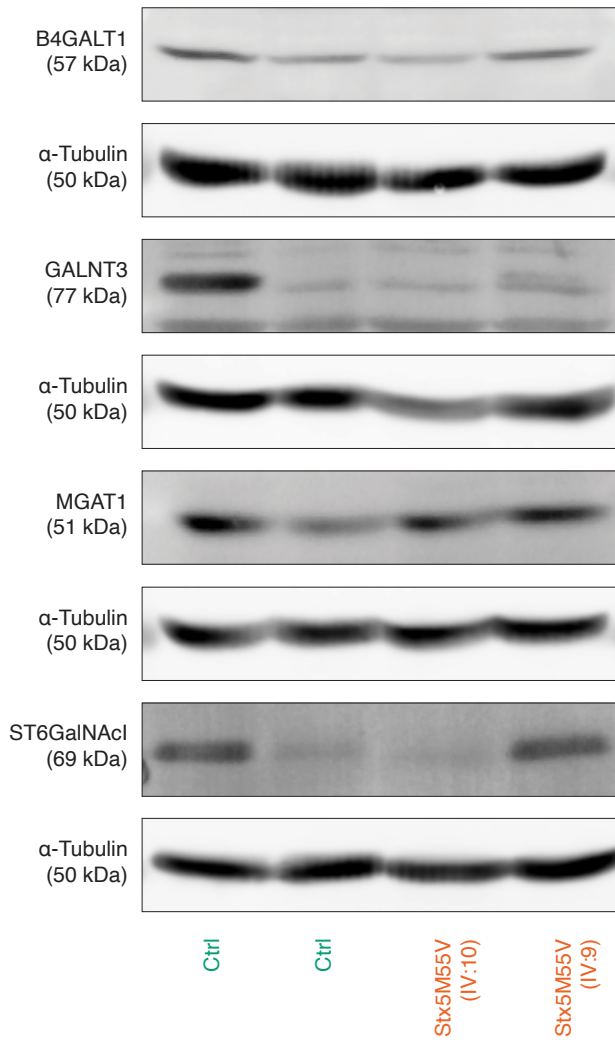


**Figure 6.15: No consistent changes in expression of glycosyltransferases in healthy and patient fibroblasts.**  
Representative immunoblot for glycosyltransferases of cell lysates of primary human dermal fibroblasts of healthy donors (green, Ctrl) or Stx5M55V patients (orange, Stx5M55V).  $\alpha$ -Tubulin, loading control.

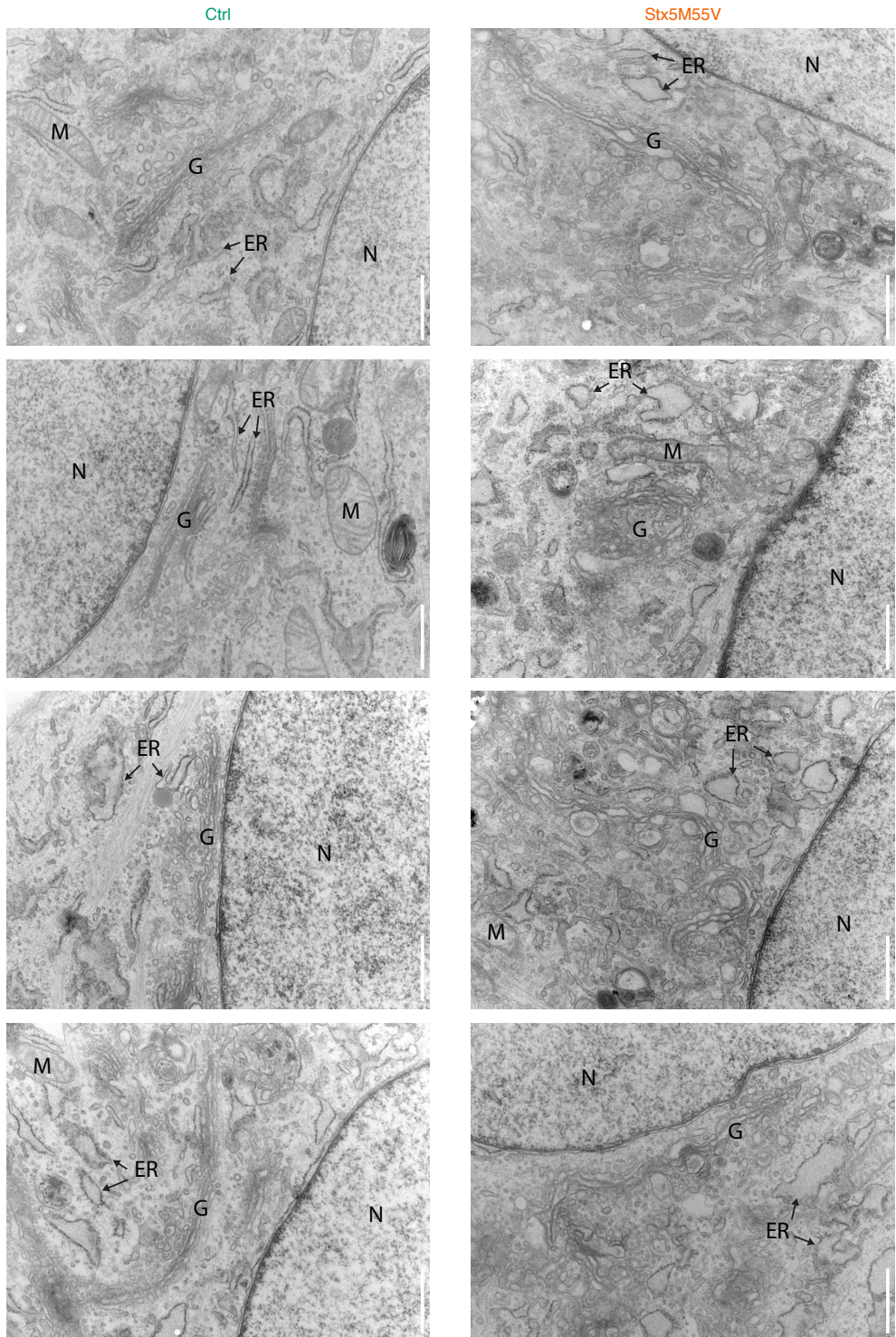
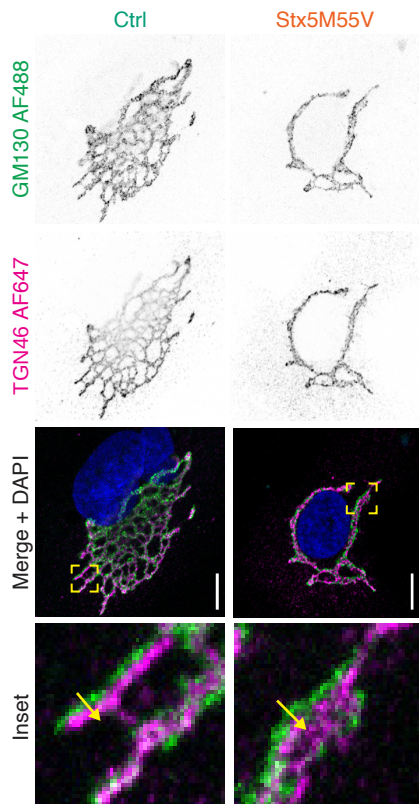


**Figure 6.16:** Gallery of transmission electron micrographs of healthy donor and Stx5M55V fibroblasts. Scale-bars,  $1\text{ }\mu\text{m}$ . N, nucleus; G, Golgi apparatus; ER, endoplasmic reticulum; M, mitochondrion.

a



6

b

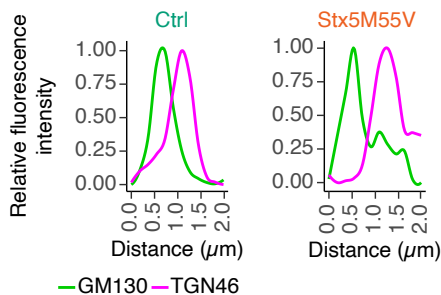


**Figure 6.17: Golgi cisterna polarization is maintained in Stx5M55V patient fibroblasts.** (a) Immunofluorescence microscopy of GM130 (green in merge) and TGN46 (magenta) in primary dermal fibroblasts of healthy donors (green, Ctrl) or Stx5M55V patients (orange, Stx5M55V). Representative confocal micrographs. Scale-bars, 10  $\mu\text{m}$ . DAPI in blue. The yellow arrows indicate the cross-sections used for the line plots in panel (b). (b) Fluorescence intensity line plots from panel (a). Data for each marker was normalized to the maximum fluorescent intensity per cross-section.

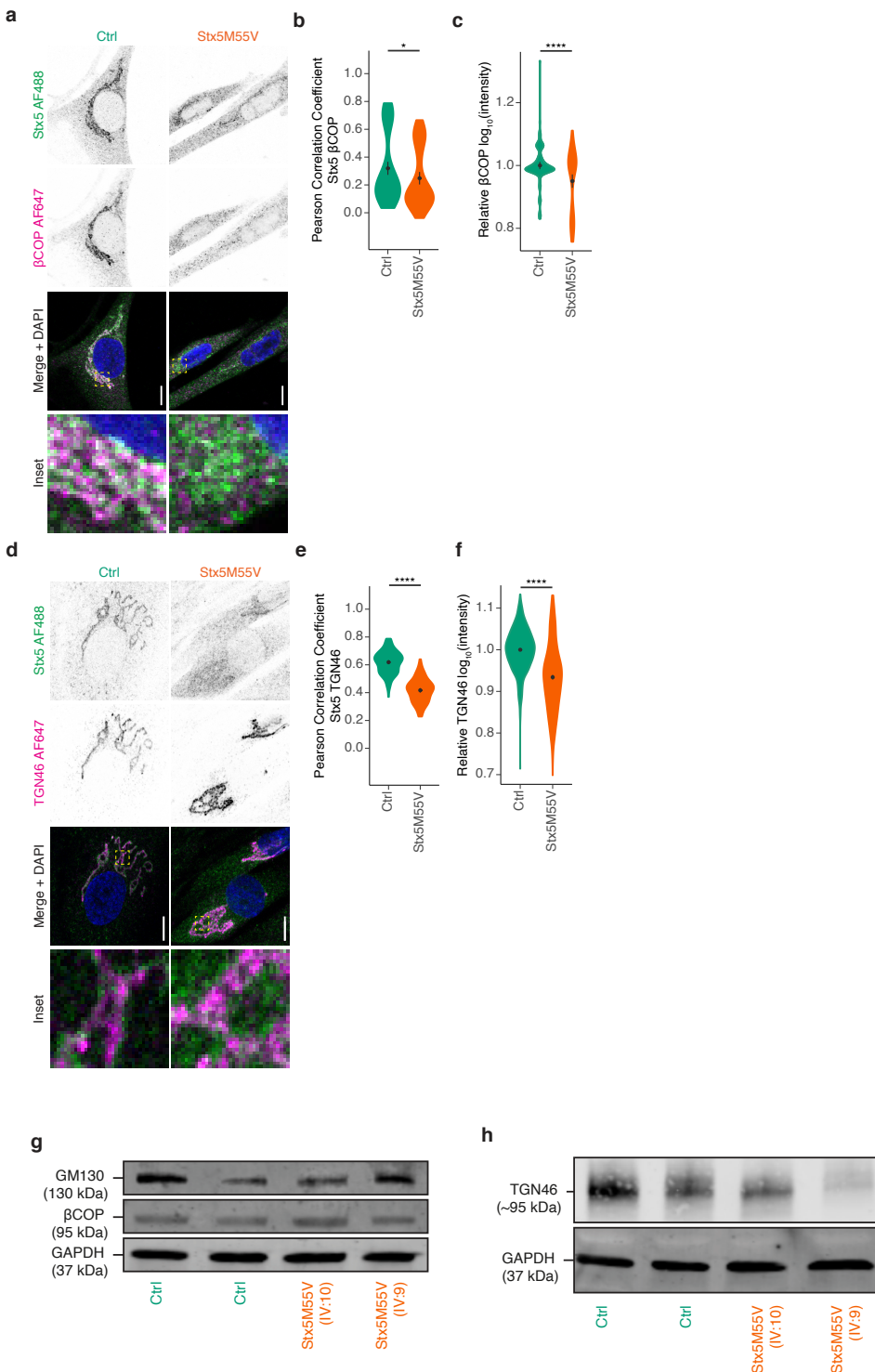


**Figure 6.18: Reduced localization of Stx5 to trans-Golgi network in Stx5M55V patients.** (Continued on the following page.)

**Figure 6.18:** (a) Immunofluorescence microscopy of Stx5 (green in merge) and  $\beta$ COP (magenta) in primary dermal fibroblasts of healthy donors (green, Ctrl) or Stx5M55V patients (orange, Stx5M55V). Representative confocal micrographs. Scalebars, 10  $\mu$ m. DAPI in blue. (b) Pearson's correlations coefficients between Stx5 and  $\beta$ COP of panel (a). N = 109 (Ctrl) and 87 (Stx5M55V) cells from 2 independent cell lines repeated twice. (c) Fluorescence intensities of  $\beta$ COP from panel (a) relative to the healthy control. N = 109 (Ctrl) and 87 (Stx5M55V) cells from 2 independent cell lines repeated twice. (d-f) Same as panels (a-c), but now for Stx5 (green) and TGN46 (magenta). N = 128 (Ctrl) and 114 (Stx5M55V) cells from 2 independent cell lines repeated twice for colocalization, N = 822 (Ctrl) and 783 (Stx5M55V) cells from 2 independent cell lines repeated six times for intensity measurements. (g) Representative immunoblot for GM130 and  $\beta$ COP of the cells from panel A. GAPDH, loading control. (h) Same as panel (g), but now for TGN46.

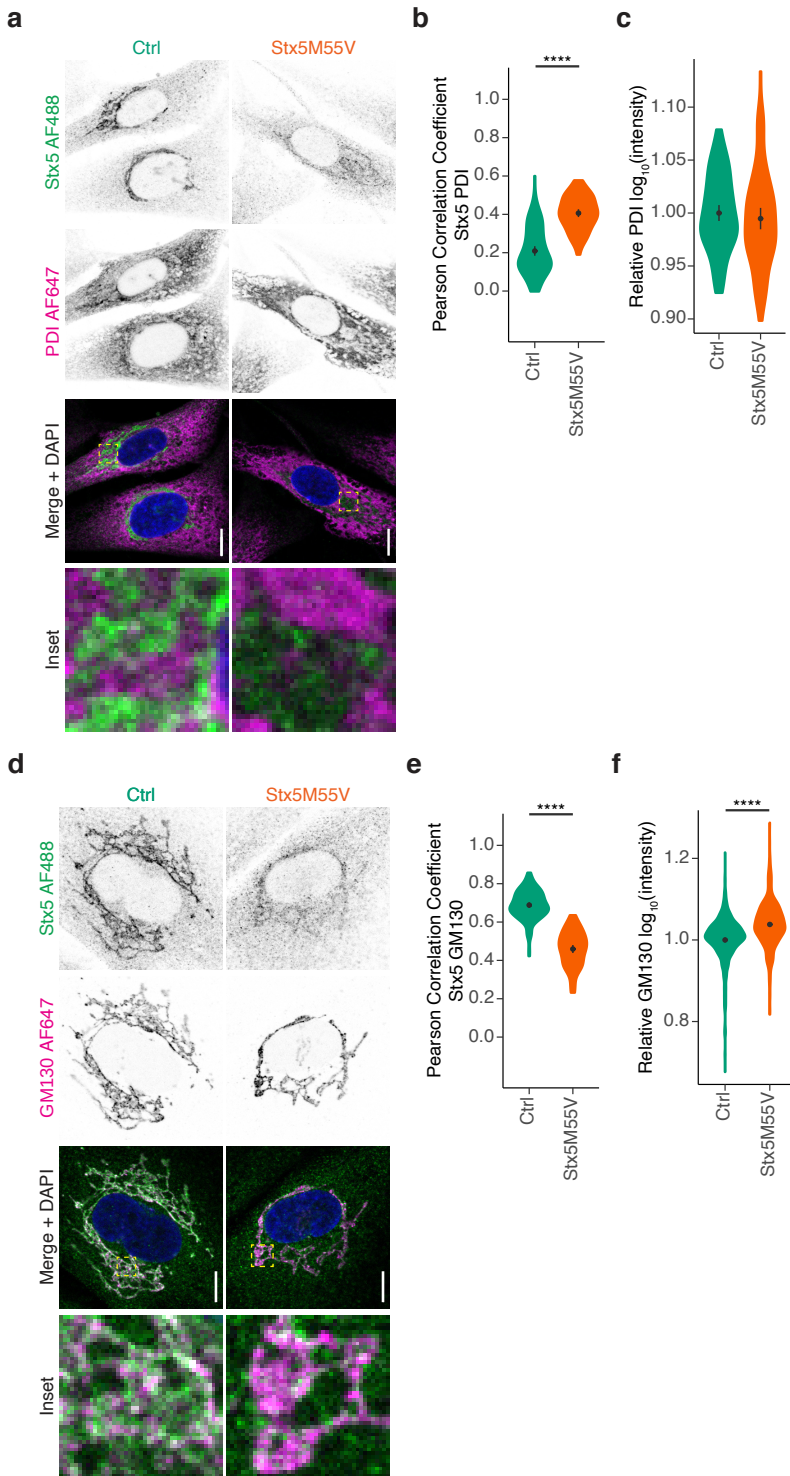


**Figure 6.19: Stronger localization of Stx5 to ER in Stx5M55V patient fibroblasts.** (Continued on the following page.)

**Figure 6.19:** (a) Immunofluorescence microscopy of Stx5 (green in merge) and PDI (magenta) in primary dermal fibroblasts of healthy donors (green, Ctrl) or Stx5M55V patients (orange, Stx5M55V). Scalebars, 10  $\mu\text{m}$ . DAPI in blue. (b) Pearson's correlations coefficients between Stx5 and PDI of panel (a). N = 101 (Ctrl) and 76 (Stx5M55V) cells from 2 independent cell lines repeated twice. (c) Fluorescence intensity of PDI from panel (a) relative to healthy donor. N = 93 (Ctrl) and 84 (Stx5M55V) cells from 2 independent cell lines repeated twice. (d-f) Same as panels (a-c), but now for Stx5 (green) and GM130 (magenta). N = 105 (Ctrl) and 80 (Stx5M55V) cells from 2 independent experiments for colocalization, N = 415 (Ctrl) and 436 (Stx5M55V) cells from 2 independent cell lines repeated four times for intensity.

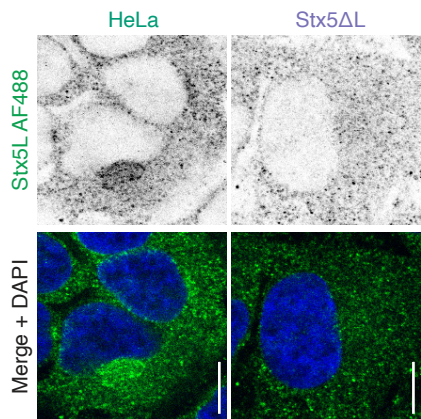


**Figure 6.20: Stx5L-specific antibody validation.** Immunofluorescence microscopy of Stx5L (green in merge) in parental HeLa (HeLa, green) or HeLa Stx5 $\Delta$ L (Stx5 $\Delta$ L, blue). Representative epifluorescence micrographs. Scalebars, 10  $\mu$ m. DAPI in blue.

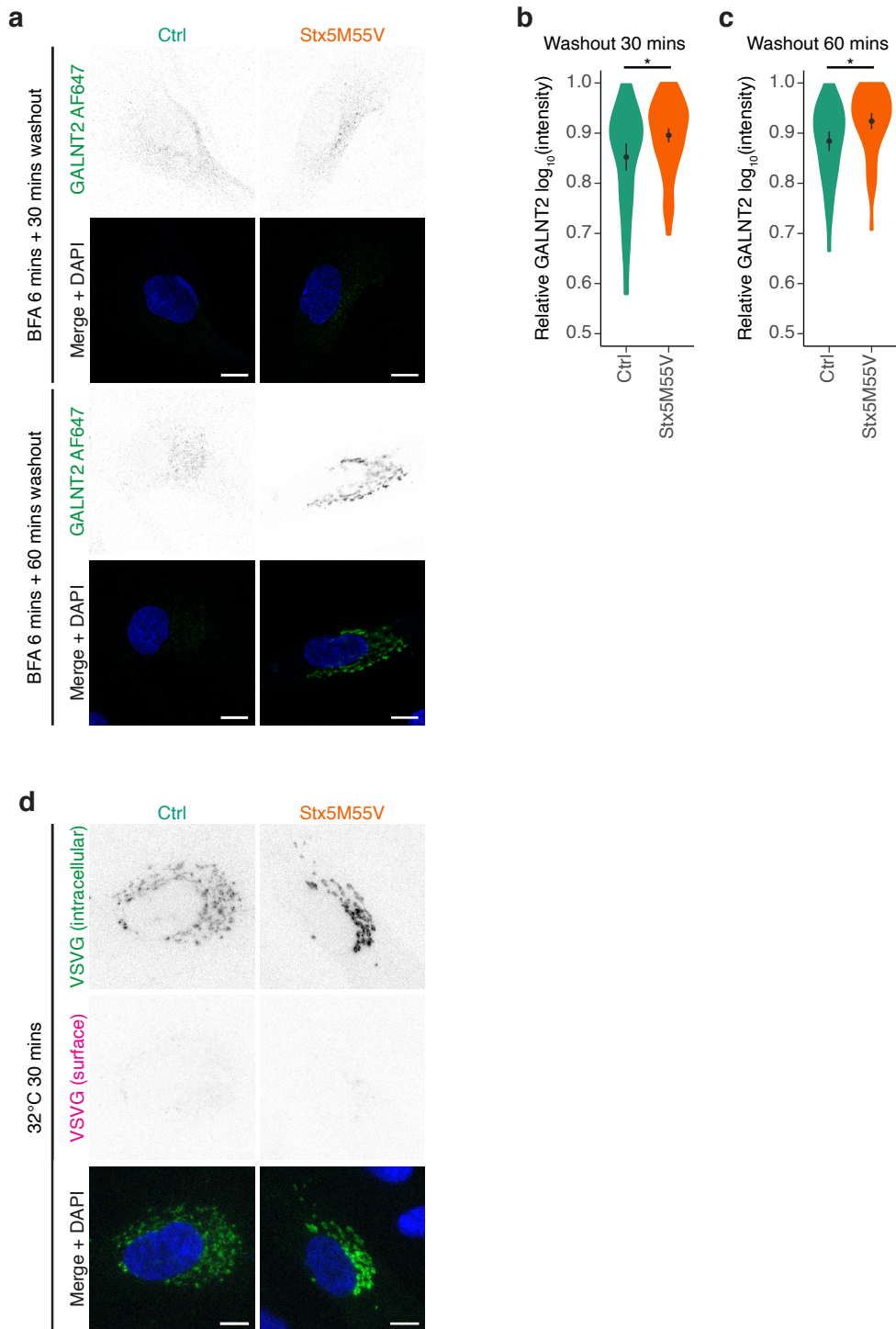
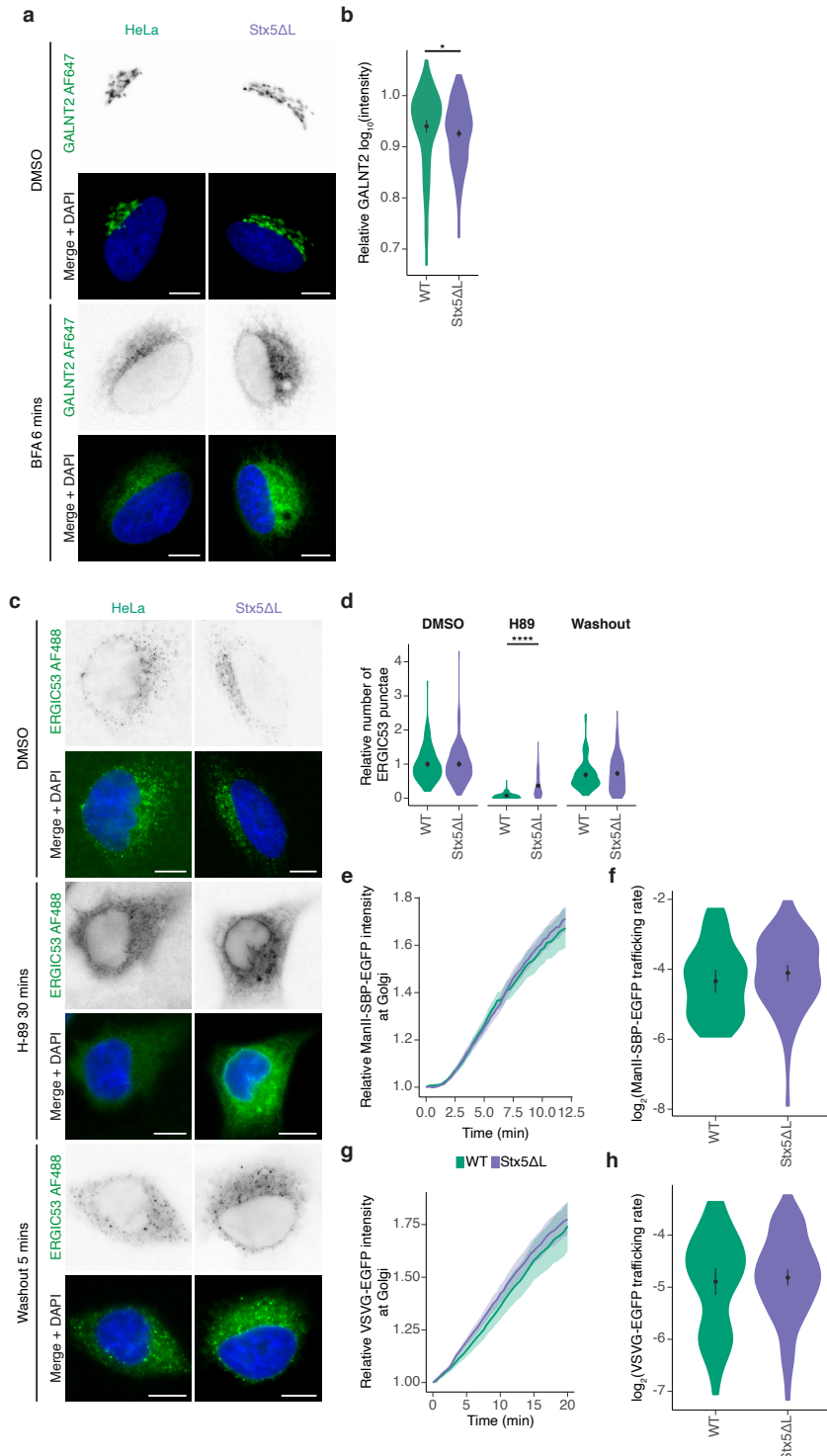


Figure 6.21: BFA and VSVG experiments in Stx5M55V fibroblasts. (Continued on the following page.)

**Figure 6.21:** (a) Immunofluorescence microscopy of GALNT2 (green in merge) in primary human dermal fibroblasts of healthy donors (green, Ctrl) or Stx5M55V patients (orange, Stx5M55V) in the absence or presence of Brefeldin A (BFA) for 6 min and washout for the indicated times. Representative confocal micrographs. Scalebars, 10  $\mu$ m. DAPI in blue. (b) Quantification of the 30 min timepoint from panel (a). N = 64 (Ctrl) and 119 (Stx5M55V) cells from 2 independent cell lines repeated twice. (c) Same as (b), but now for the 60 min timepoint. N = 68 (Ctrl) and 83 (Stx5M55V) cells from 2 independent cell lines repeated twice. (d) Immunofluorescence microscopy of VSVG-EGFP in primary human dermal fibroblasts of healthy donors (green, Ctrl) or Stx5M55V patients (orange, Stx5M55V) cultured overnight at 40°C and then 32°C for 30 mins. Representative confocal micrographs are shown. Scalebars, 10  $\mu$ m. DAPI in blue.



**Figure 6.22: Loss of Stx5L does not affect anterograde ER-Golgi trafficking.** (Continued on the following page.)

**Figure 6.22:** (a) Immunofluorescence microscopy of GALNT2 (green in merge) in parental HeLa (WT, green) or HeLa Stx5 $\Delta$ L (Stx5 $\Delta$ L, blue) in the absence or presence of Brefeldin A (BFA) for 6 min. Representative epifluorescence micrographs. Scalebars, 10  $\mu$ m. DAPI in blue. (b) Relative maximum fluorescence intensities of GALNT2 from panel (a). All data were normalized to the DMSO condition (vehicle). N = 103 (WT) and 212 (Stx5 $\Delta$ L) cells from 2 independent experiments. (c) Immunofluorescence microscopy of ERGIC53 (green in merge) in the absence or presence of H-89 and after washout of H-89 in parental HeLa (WT, green) or HeLa Stx5 $\Delta$ L (Stx5 $\Delta$ L, blue). H-89 inhibits export of cargo from ER exit sites via inhibition of protein kinase A, and causes redistribution of ERGIC53 to the ER, both of which are restored upon washout<sup>399,400</sup>. Representative epifluorescence micrographs. Scalebars, 10  $\mu$ m. DAPI in blue. (d) The relative number of ERGIC53 punctae of panel (a). All data were normalized to the average of the DMSO condition of each of the lines. N = 140 (WT DMSO), 90 (WT H-89), 92 (WT Washout), 169 (Stx5 $\Delta$ L), 188 (Stx5 $\Delta$ L H-89) and 167 (Stx5 $\Delta$ L Washout) cells from 2 independent experiments. (e) Trafficking of ManII-SBP-EGFP in parental HeLa (WT, green) or HeLa Stx5 $\Delta$ L (Stx5 $\Delta$ L, blue) over time (n  $\approx$  40 cells/condition). As part of the RUSH system<sup>266</sup>, ManII-SBP-EGFP is held at the ER in absence of biotin by interaction with a streptavidin-KDEL hook protein. After addition of biotin at t = 0, ManII-SBP-EGFP can exit the ER normally and traffic to the Golgi. ManII-SBP-EGFP intensity at the Golgi was measured, corrected to the total cellular intensity of ManII-SBP-EGFP per frame, and normalized to t = 0. SBP, streptavidin binding protein. (f) Quantification of slope coefficients from panel (c) of the linear section (3-6 min). No differences between WT and Stx5 $\Delta$ L were observed. N = 38 (WT) and 79 (Stx5 $\Delta$ L) cells from 2 independent experiments. (g) Trafficking of VSVG-ts045-EGFP in parental HeLa (WT, green) or HeLa Stx5 $\Delta$ L (Stx5 $\Delta$ L, blue) over time after shift to 32°C (n  $\approx$  40 cells/condition). When cells expressing VSVG-ts045-EGFP are cultured at 40°C, the tagged protein misfolds and is retained at the ER. Shifting the cells to 32°C at t = 0 refolds the protein and enables it to exit the ER normally and traffic to the Golgi<sup>373</sup>. VSVG-ts045-EGFP intensity at the Golgi was measured, corrected to the total cellular intensity of VSVG-ts045-EGFP per frame, and normalized to t = 0. (h) Quantification of slope coefficients from panel (e) of the linear section (3-15 min). No differences between WT and Stx5 $\Delta$ L were observed. N = 51 (WT) and 103 (Stx5 $\Delta$ L) cells from 2 independent experiments.

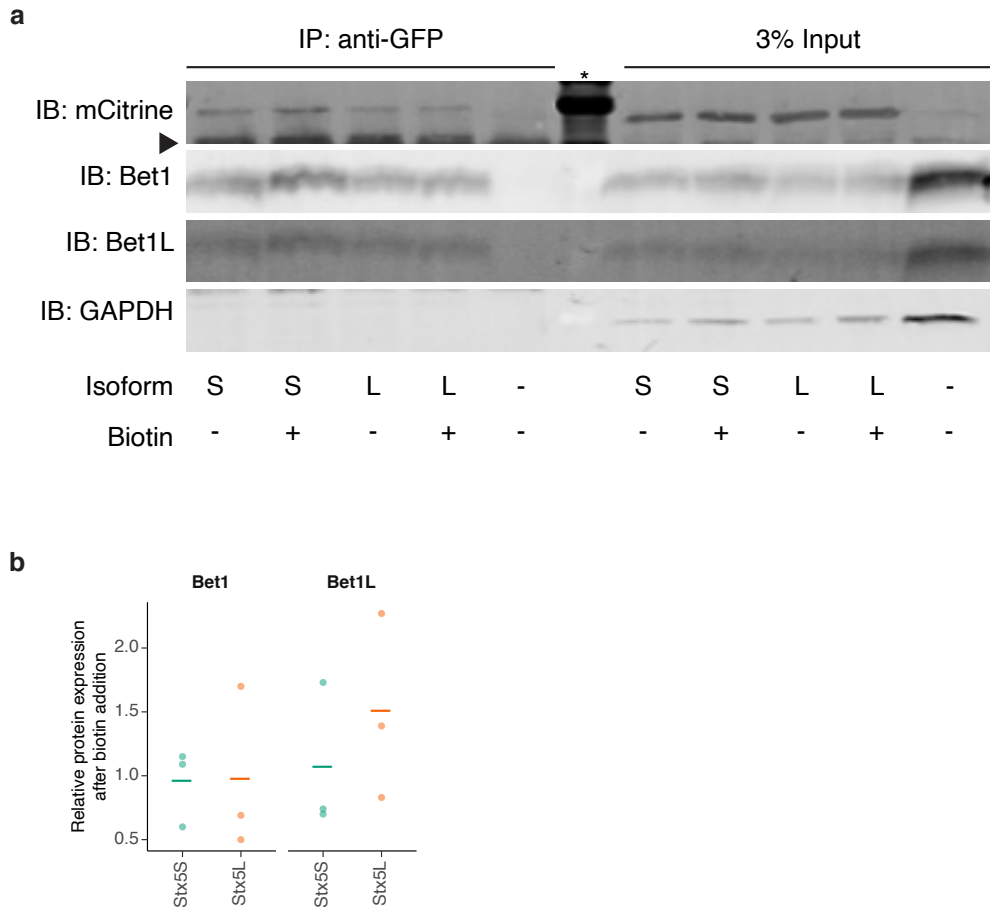


**Figure 6.23: Co-immunoprecipitation of RUSH Stx5-mCitrine with cognate Qc-SNAREs.** (a) HeLa cells were transfected with Stx5L-SBP-mCitrine (L), Stx5S-SBP-mCitrine (S), or left untransfected (-), lysates were immunoprecipitated by anti-GFP, then blotted for Bet1 and Bet1L. Biotin was added 30 minutes prior to lysis. Shown is a representative immunoblot from 3 independent experiments. Arrowhead, heavy IgG chain; asterisk, molecular weight marker; GAPDH, loading control; SBP, streptavidin binding protein. (b) Quantification of band intensities from panel (a). Each band intensity was first normalized to the loading control, and then to the condition without biotin. Each point represents one independent experiment.

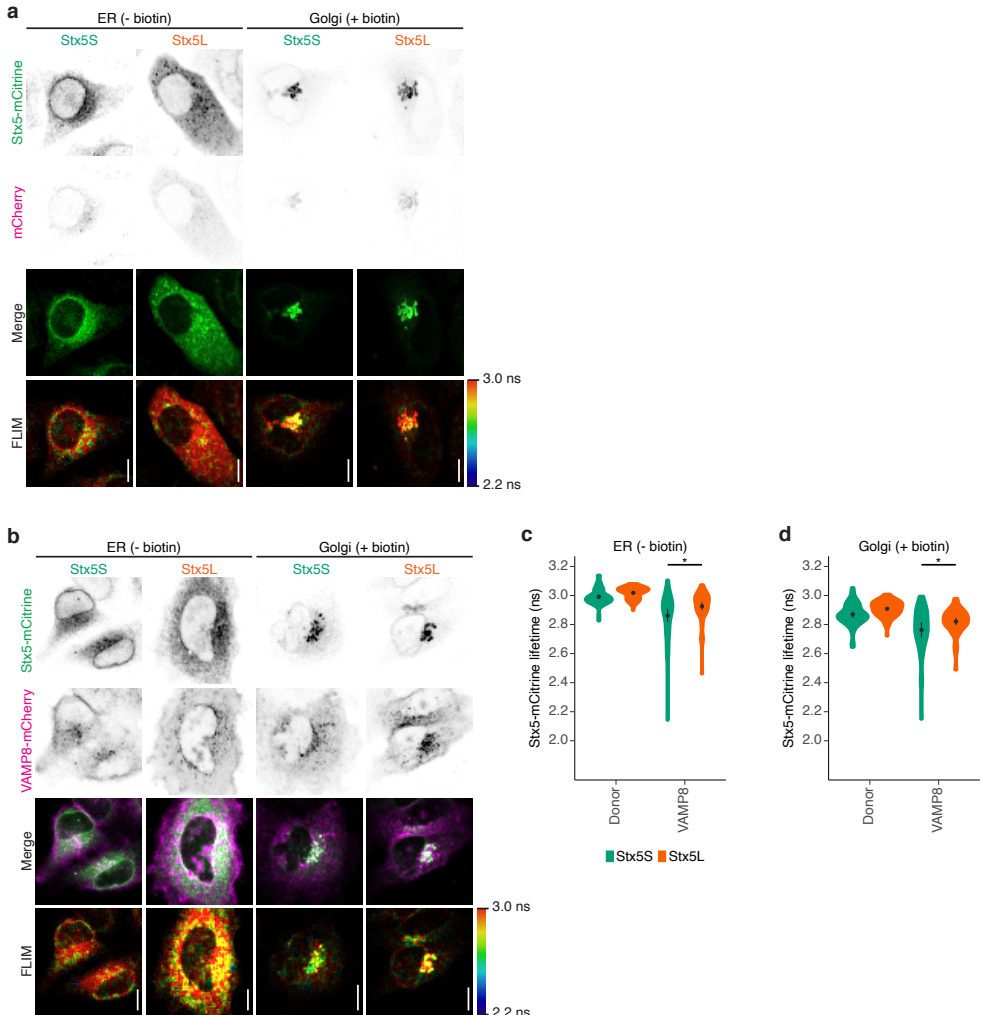


**Figure 6.24: Fluorescence lifetime imaging microscopy (FLIM) of Stx5-mCitrine or with co-expression of VAMP8-mCherry.** (a) Representative confocal micrographs of HeLa cells expressing Stx5S-mCitrine or Stx5L-mCitrine (green in merge) without (ER) or with (Golgi) biotin. Scale bars, 10  $\mu$ m. (b) Same as panel (a), but now for HeLa cells co-expressing Stx5-mCitrine (green in merge) and VAMP8-mCherry (magenta). (c-d) Stx5-mCitrine lifetimes at the ER (c) and Golgi (d) from panel (b). N = 52 (Stx5S Donor ER), 74 (Stx5L Donor ER), 51 (Stx5S VAMP8 ER), 61 (Stx5L VAMP8 ER), 50 (Stx5S Donor Golgi), 71 (Stx5L Donor Golgi), 39 (Stx5S VAMP8 Golgi) and 53 (Stx5L VAMP8 Golgi) cells from 3 independent experiments.

mRNA AGTCTTGGTCGGTTCGCGGCTTCAGTGCTCGGGAGGAGGCAGTGACGCCGGTGAGATTGAAAGTGGCGG  
AA  
**NetStart**

CGGCGGCAGGCAGGAGGGAGTCCGAGGTTATCGTCTCA**ATG**ATCCCAGGAAACGCTACGGGTCTAAGAAC  
M I P R K R Y G S K N  
0.445 **0.351**

ACGGATCAGGGTGTCTACCTGGGTCTCTCAAAGACACAGGTCTGTCCCCCTGCAACTGCTGGCAGTAGCAGCAGC  
T D Q G V Y L G L S K T Q V L S P A T A G S S S S  
GACATCGCCCCCTCTGCCCCCCCCAGTGACCCCTCGTCCCTCCCCCTCCCGACACC**ATG**TCCCTGCCGGATCGGACC  
D I A P L P P P V T L V P P P D T M S C R D R T  
**0.713**

6

**Figure 6.25:** Translation initiation predictions of STX5. NetStart 1.0<sup>381</sup> (<https://services.healthtech.dtu.dk/service.php?NetStart-1.0>) was used to predict translation start of the STX5 mRNA transcript (accession code: NM\_003164.5). The starting codons of Stx5L and Stx5S respectively are shown in bold red. In gray is the 5' UTR of STX5. AA, amino acid.

**Table 6.1: Phenotypes of patients affected by Stx5M55V genetic variant**

	Patient IV:9	Patient IV:10
Gestational age (weeks)		
Birth	29	37
weight/length/head circumference	1380 gr/36.2 cm/29.5 cm	2656 gr/41.5 cm/34 cm
Cardiovascular involvement	Ventricular septal defect	Delayed closure of ductus arteriosus, patent ductus venosus
Renal involvement	Agenesis of left kidney	Unilateral hydronephrosis
Liver involvement	Liver failure, hepatomegaly, stage 3 to 4 liver fibrosis on autopsy	Liver failure, hepatomegaly, biliary cirrhosis and nodular regenerative hyperplasia on autopsy
Skeletal involvement	Narrow thorax, shortening of long bones, bilateral clubfeet and flexion contracture of both knees	Narrow thorax, shortening of long bones
Nervous system	Hypotonia	Severe hypotonia, delayed motor development, brain MRI - slight enlargement of cerebrospinal fluid spaces
Laboratory abnormalities	Cholestasis with increased aspartate aminotransferase, high alkaline phosphatase (1611 U/L), hyperammonaemia, coagulation abnormalities (antithrombin III 6%, and protein C 20%), hypercholesterolemia (8.5 mmol/L), hyperinsulinemic (33.5 mU/L) hypoglycemia, lower TSH (1.36 mU/L) and ft4 (8.1 pmol/L), very low IGF-I (<25 µg/L)	Cholestasis with increased transaminases, high alkaline phosphatase (2732 U/L), hyperammonaemia, coagulation abnormalities (antithrombin III 17%, protein C 25%, factor VII 46%, factor XI 21%), hypercholesterolemia (9.2 mmol/L), low ceruloplasmin (0.083 g/L), hyperinsulinemic (28 mU/L) hypoglycemia, hypokalemia, -natremia, and -phosphatemia

**Table 6.2: Quantification of Transferrin-IEF and ApoCIII-IEF bands**

	IV:9	IV:10
Transferrin isofocusing (Figure 6.1d)		
TF-6	2.1 (3.2-7.8)	n.d. (3.2-7.8)
TF-5	9 (18.7-31.5)	2.66 (18.7-31.5)
TF-4	31.1 (47.3-62.7)	9.09 (47.3-62.7)
TF-3	12.9 (4.9-10.6)	22.03 (4.9-10.6)
TF-2	14.6 (3.3-7.6)	32.73 (3.3-7.6)
TF-1	13.2 (0-5.0)	22.35 (0-5.0)
TF-0	17.2 (0-3.2)	11.14 (0-3.2)
Apolipoprotein CIII isofocusing (Figure 6.1e)		
ApoCIII-2	15.1 (26.2-56.7)	9.3 (40.4-60.9)
ApoCIII-1	29.1 (42.7-69.8)	49.6 (37.1-54.5)
ApoCIII-0	55.8 (0.2-4.5)	41.1 (1.3-11.7)

The numbers behind TF and ApoCIII refer to the number of sialic acids. The numbers indicate the relative distribution of the individual protein isoforms (in %). The range between brackets indicates the reference range (age-related for ApoCIII).

**Table 6.3: Chromosomal microarray analysis**

Chromosome	Starting position (bp) hg19	Ending position (bp) hg19
Common LCSH areas in two patients (IV:8 and IV:9)		
2	41 051 123	47 273 511
5	113 980 360	123 909 500
11	23 410 903	32 583 695
11	33 423 590	48 994 066
11*	55 091 268	76 733 313
Common LCSH areas in three patients (IV:8, IV:9, and IV:10)		
11	23 410 903	32 583 695
11	33 423 590	48 994 066
11*	55 091 268	70 906 073

\*STX5 gene is located on the chromosome 11 (62 806 897 - 62 832 088). The variant was confirmed by Sanger sequencing as homozygous in all affected individuals, and heterozygous in the mother.

**Table 6.4: Antibodies used in this study**

Target	Catalog number	Application
Stx5 (polyclonal)	Synaptic Systems, 110 053	IF (5 µg/mL)
Stx5 (B-8)	Santa Cruz Biotechnology, sc-365124	WB (0.4 µg/mL), IF (4 µg/mL)
Stx5L	Abcam, ab217130	WB
GAPDH (14C10)	Cell Signaling Technology, 2118	WB WB (0.5 µg/mL)
MGAT1	Abcam, ab180578	IF (10 µg/mL), WB (2 µg/mL)
MAN2A1	Abcam, ab12277	IF (5 µg/mL)
ST6GAL1	Abcam, ab225793	IF (20 µg/mL)
GALNT2 (1501421)	Biolegend, 682302	IF (5 µg/mL)
B4GALT1 (GT2/36/118)	Enzo, ALX-803-339-c050	WB (2 µg/mL)
GALNT3	R&D Systems AF7174	WB (2.9 µg/mL)
ST6GalNacI	Abcam ab69066	WB (4 µg/mL)
GM130 (35/GM130)	BD Biosciences, 610822	WB (0.5 µg/mL), IF (2.5 µg/mL)
TGN46	BioRad, AHP500GT	WB (0.25 µg/mL), IF (0.25 µg/mL)
βCOP	Abcam, ab2899	WB (4.4 µg/mL), IF (2.2 µg/mL)
Alpha-Tubulin (YOL1/34)	Novus Biologicals, NB100-1639	WB (0.2 µg/mL)
GosR1 (1/GS28)	BD Biosciences, 611185	WB (0.25 µg/mL)
GosR2 (25/GS27)	BD Biosciences, 611034	WB (0.25 µg/mL)
Stx16	Synaptic Systems, 110 162	WB (1 µg/mL)
Bet1 (17)	Santa Cruz Biotechnology, sc-136390	WB (0.2 µg/mL)
Bet1L (19/GS15)	BD Biosciences, 610960	WB (1 µg/mL)
ERGIC53 (G1/93)	Alexis Biochemicals, 802-602-C100	IF (10 µg/mL)
PDI (RL90)	Novus Biologicals, NB300-517	IF (10 µg/mL)
ERGIC53 (OTI1A8)	Enzo, enz-ABS300-0100	IF (10 µg/mL)
VSV-G (8G5F11)	Kerafast EB0010	IF (20 µg/mL)

## 6.6. Supplementary Information

6



# 7

## Discussion & Future Perspectives

## 7.1 The Clinical Foundation of this Thesis

The field of membrane trafficking in glycobiology is rapidly advancing. The work presented in this thesis represents only a fraction of the new developments of the past five years. While much is still unknown, many advancements have contributed to the formation of this thesis. The starting point for much of the experimental work presented in this thesis was found in the clinic: chapters 4 and 6 originate from novel genetic variants in the genes coding for the membrane trafficking-related proteins TMEM199 and syntaxin-5 observed in patients with congenital disorders of glycosylation (CDG). Recent advances in the diagnostics of CDG have not only improved the sensitivity of detection of various glycosylation defects but also provide insights as to where exactly in the glycosylation process the defects occur. Where classic diagnostic approaches only interrogate the sialic acid content of glycans using isoelectric focusing (IEF)<sup>238</sup>, modern approaches use mass spectrometry to investigate full glycan structure profiles in an unbiased fashion<sup>174,392,401</sup>. For Stx5-CDG, discussed in chapter 6, the combination of IEF and mass spectrometry-based diagnostics allowed me to identify a glycan profile unique to Stx5-CDG patients (strong decrease of sialic acid and galactose incorporation, but strong increase in Man-5 glycan abundance). Moreover, this observation can already be linked to a step in the glycosylation pathway: as the Man-5 glycan is a very early N-glycan, the defect must relate to a component early in the Golgi apparatus. This information would have been overlooked if only the IEF data would have been considered. Together with advances in next-generation sequencing<sup>94,95</sup>, the genomic location of the variant could quickly be identified in STX5. This offered a stepping stone to understanding the cell biological mechanism behind the clinical presentation. Human disease therefore can bring an understanding of the function of proteins in the cell, and chapters 4 and 6 are good examples of how advancements in CDG diagnostics pave the way to elucidate the role of membrane trafficking components.

Inversely, understanding the cell biological mechanisms in disease is paramount for the development of treatment options. As CDGs are rare diseases that do not affect many individuals<sup>13</sup>, treatment options are scarce but desirable. A better understanding of the underlying cell biological and biochemical processes affected in the cells of CDG patients opens up new therapeutic opportunities, which can be as straightforward as monosaccharide supplementation<sup>402–404</sup>. In some cases, such as the Stx5-CDG patients presented in chapter 6, treatment options are currently not feasible. Considering the breadth of the disorder, and that it likely affects embryonic development, straightforward supplementation strategies would not be sufficient to ameliorate the patient phenotypes. Possible therapeutic opportunities include the use of gene replacement therapy, similar to the treatment of spinal muscular atrophy (SMA)<sup>405</sup>. For

Stx5-CDG patients, this would need to be performed early in development and is therefore technologically and ethically complicated.

These rare diseases also offer the opportunity for new initiatives both for patients and researchers. One such opportunity is the Noordzeeziekte foundation<sup>406</sup>, which is a patient organization for individuals suffering from the homozygous G144W mutation in the Golgi trafficking protein GOSR2<sup>224–226</sup>, partner SNARE for syntaxin-5. Noordzeeziekte has been identified in 25 patients so far worldwide, with most of them living in the north of the Netherlands, and is characterized by muscle spasms and epilepsy. The Noordzeeziekte foundation offers a platform for (family of) patients to understand the disease and the therapeutic options, as well as to share the research progress of scientists affiliated with the foundation. Similarly, the foundation enables the continuation of basic research through donations, advancing the understanding and treatment options of the disease. Analogous patient organizations also exist for CDG in many different countries<sup>407</sup>.

## 7.2 On Tissue-Specific Glycosylation

Many CDGs are characterized by tissue-specific defects, even though the affected machinery is present in most cells of the human body. In this thesis, I discuss Stx5M55V-CDG (chapter 6) which primarily has skeletal and hepatological involvement, TMEM199-CDG (chapter 4) which mainly affects the liver<sup>121</sup>, and CCDC115-CDG<sup>120</sup> which affects the liver, spleen and, brain. Especially TMEM199 and CCDC115 are of interest as it is hypothesized that they act in concert to facilitate V-ATPase assembly<sup>125</sup>, and my data in chapter 4 suggests that TMEM199 recruits CCDC115 to membranes, raising the question why the patient phenotype is different. Another clear example of tissue-specific glycosylation is found in GNE-CDG, caused by genetic variants in GNE (Glucosamine (UDP-N-Acetyl)-2-Epimerase/N-Acetylmannosamine Kinase), the enzyme responsible for the two first steps in sialic acid biosynthesis<sup>408–412</sup>. In GNE-CDG, all skeletal muscle tissue is affected except for the quadriceps. A likely explanation for this phenomenon is that the expression levels of glycosyltransferases vary between tissues and cell types<sup>13,15,41,65–68</sup>. Several distinct isoforms exist of most glycosyltransferases<sup>10</sup>, which is likely important for the tissue distribution of glycans. Moreover, differences in expression levels of glycosyltransferases can shift the balance towards distinct glycosylation steps, similarly how the ratio of syntaxin-5 isoform expression can dictate intracellular trafficking as seen in chapter 6. The ratio of glycosylation enzymes might hence alter both the substrate and product levels of certain intermediate glycans, producing different glycans on the same protein in different cell types.

The studies I performed in chapters 3, 4, and 6 in this thesis made use of one or

two different cell types, but it would be much more valuable to interrogate glycosylation disorders caused by mutant trafficking proteins in various types of tissues. induced pluripotent stem cells (iPSCs) are ideal with their capacity to differentiate in multiple tissues. Coupled with the retention using selective hooks (RUSH) system<sup>266</sup> and glycoproteomics, glycoproteins can be followed almost in real-time during their transit through the secretory pathway in multiple cell types, with concurrent analysis of the attached glycan structures. Proteins of interest fused to fluorescent proteins can be imaged by live-cell microscopy, while the same tag can be used to purify the glycoprotein via immunoprecipitation for downstream mass spectrometry analysis of not only glycans but also interacting proteins at each step in the trafficking pathway. In theory, this system could also be multiplexed by using multiple different cargo molecules (e.g., cytokines, ECM proteins, or immunoglobulins) with different (fluorescent) tags. Using such high spatial and temporal resolution where glycosylation and trafficking meet is highly interesting to elucidate how and where differential glycosylation occurs. Moreover, the same processes can be studied in iPSCs derived from CDG patients to observe how mutations affect the transit of glycoproteins.

### 7.3 The Use of Primary Human Material in Cell Biological Studies

One important limitation from chapter 6 concerns the use of primary human dermal fibroblasts. While primary patient material is the most accurate model to study disease effects on a cellular level, there are three important aspects to using patient-derived cells: (1) high interindividual variation, (2) primary patient material is mostly difficult to manipulate by i.e., fluorescent protein expression, and (3) primary human dermal fibroblasts are often not the most relevant cell type with regards to the pathophysiology.

First, as all individuals are unique, so are the cells derived from both healthy donors and patients. As opposed to studies performed in genetically uniform cell lines or animals, many considerations need to be taken when working with material from humans. Many different aspects including age, treatment, diet, environment, and genetic makeup influence the biology of cells in the human body and therefore influence the results of cell-based assays. We observed this by different protein expression levels between donors as measured by Western blot, as well as by the different glycosylation results dependent on the availability of N-glycans in blood serum. While this affects the interpretation of these experiments, an important improvement would be to include more different patients to account for the variation. Ultimately, the observations in chapter 6 are a testament to how humans are all unique.

Second, cell biological techniques often use the exogenous expression of fluores-

cent proteins in live cells to interrogate many different processes. For short-term experiments, a suitable technique involves transient delivery, or transfection, of plasmid DNA for temporary expression of the desired protein. Many different methods for transient transfection exist, such as complexing plasmid DNA with cationic lipids for endosomal uptake<sup>413,414</sup> or high voltage electroporation<sup>415</sup>, but these are often not ideal for the transfection of primary material compared to transformed and immortalized cell lines<sup>416,417</sup>. This severely limits the options for studying cell biological processes in live primary cells. Viral delivery of plasmid DNA is generally a more suitable option for stable transduction of primary human cells and offers high levels of transduction efficiency. Unfortunately, viral transduction methods come with severe drawbacks regarding the production of viral particles, toxicity, and immunogenicity which are undesirable in certain experimental contexts<sup>413,418–420</sup>.

The most ideal method would be to generate cell lines that express fluorescent (fusion) proteins in a mostly endogenous context. CRISPR/Cas9 technology has enabled robust genomic engineering with a relatively small investment necessary, enabling wide-spread applications<sup>421–424</sup>. Recently, improvements to the CRISPR/Cas9 system facilitate the development of genome-edited cells even further by increased specificity and less off-target effects<sup>292</sup> and by inferring resistance to a potent cytotoxic drug concurrently with the desired edit to improve the selection of positive cells<sup>425</sup>. Most importantly, well-designed CRISPR/Cas9 constructs do not affect the nucleotide context of the edited gene, therefore maintaining physiological promoter function and expression regulation. This eliminates artifacts commonly associated with overexpression<sup>426,427</sup>. Experiments of use would be to perform the same FLIM-FRET-based approach as outlined in chapter 6 but with endogenous SNAREs, to truly measure SNARE fusion *in situ* in an endogenous system. The same is true for other trafficking assays; when the RUSH system is introduced endogenously rather than with overexpression, all copies of the protein of interest can be captured, thereby removing the effect of the unedited protein from the experiment. Another noteworthy avenue would be to perform CRISPR/Cas9 genome editing in iPSCs<sup>428,429</sup>. The pluripotent property of these cells would allow the investigation of protein function in many different tissue types, all arising from a single progenitor. Moreover, robust iPSC generation can be performed using patient-derived fibroblasts from patients with uncharacterized mutations resulting in, for example, CDGs.

Another interesting addition to the genome editing arsenal is the development of base editing and prime editing<sup>430–432</sup>. Base and prime editing use a similar genomic targeting strategy to CRISPR/Cas9 and allow for precise single nucleotide changes. New generation prime editing tools use a catalytically impaired Cas9 fused to reverse transcriptase<sup>432</sup>. A prime editing guide RNA (pegRNA) specifies both the tar-

get site for the fusion complex and the desired genomic edit, which is then inserted using a single strand DNA break. Contrary to CRISPR/Cas9, base and prime editing do not induce double-strand breaks in DNA which are the source of random insertions and deletions at the target locus<sup>433,434</sup>. Moreover, double-strand breaks can induce a p53-mediated DNA damage response which strongly inhibits the application of CRISPR/Cas9 in pluripotent stem cells<sup>435,436</sup>.

While prime and base editing can only edit a single nucleotide, the technology is of major interest to deploy in patient cells. In our case, we could have repaired the single nucleotide mutation in Stx5M55V patient cells (chapter 6) to investigate whether restoring Stx5S protein expression would rescue the patient phenotype. These technologies are currently only feasible in laboratory settings, however, in the future, these strategies could also be applied to efficiently and safely restore congenital mutations in humans.

## 7.4 How Advancements in Microscopy Advance Golgi and Glycosylation Research

Other advancements that are of interest regarding this thesis are advances in optical microscopy. Most optical microscopy presented in this thesis was performed using confocal microscopy systems, which have a maximum resolution of 200 nm in the  $x$  and  $y$  dimensions and about 1  $\mu\text{m}$  in the  $z$  dimension (depending on the wavelength of the emitted light)<sup>437</sup>. A major drawback is that the space between cisterna, approximately 20 nm, is indiscernible using confocal microscopy, and the highly compact nature of the Golgi makes it very difficult to resolve fluorescent signals belonging to different Golgi cisternae<sup>438</sup>. This is of particular importance for chapters 4 and 6, where I used confocal microscopy to investigate the localization of glycosyltransferases in Golgi cisternae. As confocal microscopy lacks the resolution to accurately separate the different cisternae, I could only make general conclusions about the localization of the glycosyltransferases instead of accurately naming the cisternae where the protein of interest resides in. The latter would be of much interest for understanding glycosylation in the context of different disorders. Using computational approaches, it is currently possible to resolve cargo in transit between different cisternae<sup>439</sup> but this is still relatively complicated and does not offer a high temporal resolution.

Recently, super-resolution microscopy techniques such as STED (stimulated emission depletion), SIM (structured illumination microscopy), PALM (photo-activated localization microscopy), and STORM (stochastic optical reconstruction microscopy) have become much more accessible and could therefore be of interest to image Golgi trafficking and related processes. Traditionally, electron microscopy has been applied

to visualizing Golgi membranes, but more recent approaches combine both electron microscopy and optical fluorescence microscopy as correlated light and electron microscopy (CLEM)<sup>440</sup>. CLEM allows maintaining the flexibility of fluorescence-based optical microscopy experiments, potentially with super-resolution modalities<sup>441</sup>, with the robust lateral resolution of electron microscopy. Improving the resolution axially and laterally is possible through focused ion beam milling combined with scanning electron microscopy (FIB-SEM) and cryogenic super-resolution to obtain images at 4 nm isotropic resolution with 40 nm accuracy in fluorescence imaging<sup>442</sup>. While the lateral and axial resolution is unparalleled with FIB-SEM with cryo-SIM, it is highly restricted in temporal resolution as live samples cannot be imaged and full image acquisition per sample can be very long. Moreover, depending on the complexity and dimensions of the sample, datasets can be restrictively large and typically range from 100 GB to about 19.5 TB<sup>442,443</sup>, making FIB-SEM with cryo-SIM difficult to scale.

As in many optical microscopy techniques, any increases in spatial resolution decrease the temporal resolution. This raises the question: what is the highest spatial resolution achievable with high temporal resolution? A perfect technique for the time-lapse experiments I performed in this thesis would be lattice light sheet microscopy (LLSM)<sup>444</sup>. LLSM can currently achieve the highest spatiotemporal resolution in biological samples with SIM-levels of spatial resolution and temporal resolution of only a few milliseconds<sup>444</sup>. The underlying principle is the creation of a structured light sheet that only illuminates a very small volume in the cell (approx. 1  $\mu\text{m}$  deep) which is then captured by a camera. This enables confocal-like imaging (i.e., imaging a small focal plane rather than the whole sample as with epifluorescence microscopy) with the capture speed of epifluorescence microscopy as images are not reconstructed from single-pixel scans. Furthermore, phototoxicity is significantly reduced by the decrease of sample illumination, thus making LLSM particularly suitable for imaging cells in all dimensions of spacetime. Current LLSM setups are also suitable for fluorescence lifetime imaging microscopy (FLIM)<sup>445</sup>, a technique I applied to several research questions throughout this thesis (chapters 3, 4, and 6).

LLSM could greatly improve the time-lapse studies I performed in this thesis. For instance, following the transit of tumor necrosis factor (TNF)- $\alpha$  in chapter 3 was currently performed at a temporal resolution of 1 minute per frame. LLSM could speed this imaging up by orders of magnitude, thereby enabling highly accurate pH measurements in time. The same holds for the syntaxin-5 trafficking experiments of chapter 6. With LLSM, the localization of the syntaxin-5 isoforms could much more accurately be determined, both spatially and temporally. LLSM hence allows for much more precise analyses of intracellular trafficking dynamics. As the exact mechanisms of Golgi transport are still unclear, LLSM could offer additional insights into how Golgi-

related trafficking processes occur.

## 7.5 Intersecting Membrane Trafficking and Glycosylation

The work I performed in this thesis contributes to the understanding of intracellular membrane trafficking in the context of glycosylation. Understanding the fundamental transport processes of the Golgi improves our understanding of glycosylation, and vice versa, understanding the exact mechanism of glycosylation improves our understanding of Golgi membrane trafficking.

Even though the complexity of Golgi transport transcends current advances in biology, a variation of the cisternal maturation model seems the most likely transport theory<sup>80,446,447</sup>. Cisternal maturation postulates that a new *cis*-Golgi cisterna is formed from vesicles containing newly synthesized (glyco)proteins emanating from the ER. This new cisterna is then matured by renewing its biochemical contents, through donating some of its Golgi-resident proteins to younger cisternae and receiving other Golgi-resident proteins from older cisternae. This is a continuous process until the cisterna becomes part of the *trans*-Golgi network and subsequently fragments into secretory vesicles and other carriers<sup>80,446,447</sup>. The cisternal maturation theory improves upon the thought that Golgi cisternae are stable entities with specific compositions, as this compartmentalized idea is not compatible with observations of the distribution of glycosyltransferases and other Golgi-associated proteins<sup>19,68,230,447–449</sup>. The control of trafficking pathways to, from, and within the Golgi are also needed to dictate Golgi transport dynamics<sup>447</sup> and important components include adapter proteins<sup>447</sup>, GTPases<sup>450</sup>, tethering proteins<sup>133,134</sup> and SNARE proteins<sup>202</sup>.

Not only the basal dynamics of the Golgi apparatus itself but also the kinetics of proteins that pass through the Golgi are of importance for the entire Golgi trafficking model. Considering two different types of secretory cargo, one transmembrane and the other soluble, large differences appear between their trafficking routes<sup>451</sup>. In this case, albumin, a soluble, non-glycosylated, protein that is secreted can traverse the Golgi within 5 minutes while a model transmembrane glycoprotein VSVG (vesicular stomatitis virus G protein) moves much slower through the Golgi<sup>451</sup>. Similarly, the transport of procollagen is also distinct as its large size (> 250 nm) is incompatible with the size of transport vesicles<sup>451,452</sup>. These observations suggest that (glyco)protein topology and potential post-translational modifications influence the transport of proteins through the Golgi apparatus, meaning that separate transport routes for each protein must exist.

Further insights into the role of glycosylation in the transit of proteins through the Golgi can be gathered by engineering a model protein with one or more glycosylation

sites, potentially with different locations in the amino acid sequence, and observing how the trafficking of the protein is altered. Moreover, Golgi transport in different cell types can be fundamentally different, depending on the expression levels of trafficking machinery and Golgi-resident proteins. This is an important point as the glycosylation requirement of certain cell types (i.e., cell types highly dependent on secretion) can reshape intracellular membrane trafficking pathways. The opposite is also true: differences in intracellular membrane trafficking pathways can reshape glycosylation mechanisms in different cell types. Evidence for this also arises from this thesis, as I demonstrated in chapters 4 and 6 that modulating Golgi trafficking components (a putative factor in Golgi acidification in chapter 4, and SNARE protein syntaxin-5 in chapter 6) strongly affects the structure of the Golgi and the localization of glycosyltransferases with striking downstream effects on glycosylation.

## 7.6 Concluding Remarks

Ultimately, the various insights gathered from advances in microscopy, Golgi transport, glycobiology and diagnostic strategies for CDGs together strengthen our knowledge and will benefit patients down the line. The results presented in this thesis identify the mechanism behind two distinct glycosylation disorders and thus offer the basis for novel therapeutic opportunities. Fundamentally understanding how both Golgi transport and glycosylation are linked to each other is therefore of utmost importance for the treatment of CDG.



# References

- [1] Dröscher, A. The history of the Golgi apparatus in neurones from its discovery in 1898 to electron microscopy. *Brain Research Bulletin* **47**, 199–203 (1998).
- [2] Fabene, P. & Bentivoglio, M. 1898–1998: Camillo Golgi and “the Golgi”: one hundred years of terminological clones. *Brain research bulletin* **47**, 195–198 (1998). URL [https://doi.org/10.1016/S0361-9230\(98\)00079-3](https://doi.org/10.1016/S0361-9230(98)00079-3).
- [3] Davidson, M. W. Molecular Expressions Cell Biology: The Golgi Apparatus. URL <https://micro.magnet.fsu.edu/cells/golgi/golgiapparatus.html>.
- [4] The Nobel Prize in Physiology or Medicine 1906. URL <https://www.nobelprize.org/prizes/medicine/1906/summary/>.
- [5] Potelle, S., Klein, A. & Foulquier, F. Golgi post-translational modifications and associated diseases. *Journal of Inherited Metabolic Disease* **38**, 741–751 (2015). URL <https://onlinelibrary.wiley.com/doi/abs/10.1007/s10545-015-9851-7>. \_eprint: <https://onlinelibrary.wiley.com/doi/pdf/10.1007/s10545-015-9851-7>.
- [6] Dennis, J. W., Lau, K. S., Demetriou, M. & Nabi, I. R. Adaptive Regulation at the Cell Surface by N-Glycosylation. *Traffic* **10**, 1569–1578 (2009). URL <https://onlinelibrary.wiley.com/doi/abs/10.1111/j.1600-0854.2009.00981.x>. \_eprint: <https://onlinelibrary.wiley.com/doi/pdf/10.1111/j.1600-0854.2009.00981.x>.
- [7] Haltiwanger, R. S. & Lowe, J. B. Role of Glycosylation in Development. *Annual Review of Biochemistry* **73**, 491–537 (2004). URL <https://www.annualreviews.org/doi/10.1146/annurev.biochem.73.011303.074043>. Publisher: Annual Reviews.
- [8] Hoseki, J., Ushioda, R. & Nagata, K. Mechanism and components of endoplasmic reticulum-associated degradation. *The Journal of Biochemistry* **147**, 19–25 (2010). URL <https://academic.oup.com/jb/article/147/1/19/753995>. Publisher: Oxford Academic.
- [9] Kollmann, K. et al. Mannose phosphorylation in health and disease. *European Journal of Cell Biology* **89**, 117–123 (2010). URL <http://www.sciencedirect.com/science/article/pii/S0171933509003227>.
- [10] Moremen, K. W., Tiemeyer, M. & Nairn, A. V. Vertebrate protein glycosylation: diversity, synthesis and function. *Nature Reviews Molecular Cell Biology* **13**, 448–462 (2012). URL <https://www.nature.com/articles/nrm3383>. Number: 7 Publisher: Nature Publishing Group.
- [11] Rothman, J. E. & Fine, R. E. Coated vesicles transport newly synthesized membrane glycoproteins from endoplasmic reticulum to plasma membrane in two successive stages. *Proceedings of the National Academy of Sciences* **77**, 780–784 (1980). URL <https://www.pnas.org/content/77/2/780>. Publisher: National Academy of Sciences Section: Research Article.
- [12] Varki, A. Biological roles of oligosaccharides: all of the theories are correct. *Glycobiology* **3**, 97–130 (1993). URL <https://academic.oup.com/glycob/article/3/2/97/822943>. Publisher: Oxford Academic.
- [13] Linders, P. T. A., Peters, E., ter Beest, M., Lefeber, D. J. & van den Bogaart, G. Sugary Logistics Gone Wrong: Membrane Trafficking and Congenital Disorders of Glycosylation. *International Journal of Molecular*

## References

- Sciences* **21**, 4654 (2020). URL <https://www.mdpi.com/1422-0067/21/13/4654>. Number: 13 Publisher: Multidisciplinary Digital Publishing Institute.
- [14] Cottam, N. P. & Ungar, D. Retrograde vesicle transport in the Golgi. *Protoplasma* **249**, 943–955 (2012). URL <https://doi.org/10.1007/s00709-011-0361-7>.
  - [15] Papanikou, E. & Glick, B. S. The yeast Golgi apparatus: Insights and mysteries. *FEBS Letters* **583**, 3746–3751 (2009). URL <https://febs.onlinelibrary.wiley.com/doi/abs/10.1016/j.febslet.2009.10.072>. \_eprint: <https://febs.onlinelibrary.wiley.com/doi/pdf/10.1016/j.febslet.2009.10.072>.
  - [16] Jackson, C. L. Mechanisms of transport through the Golgi complex. *Journal of Cell Science* **122**, 443–452 (2009). URL <https://jcs.biologists.org/content/122/4/443>. Publisher: The Company of Biologists Ltd Section: Commentary.
  - [17] Dejgaard, S. Y., Murshid, A., Dee, K. M. & Presley, J. F. Confocal microscopy-based linescan methodologies for intra-Golgi localization of proteins. *The Journal of Histochemistry and Cytochemistry: Official Journal of the Histochemistry Society* **55**, 709–719 (2007).
  - [18] Freeze, H. H. & Ng, B. G. Golgi glycosylation and human inherited diseases. *Cold Spring Harbor Perspectives in Biology* **3**, a005371 (2011).
  - [19] Rabouille, C. *et al.* Mapping the distribution of Golgi enzymes involved in the construction of complex oligosaccharides. *Journal of Cell Science* **108** (Pt 4), 1617–1627 (1995).
  - [20] Stanley, P. Golgi Glycosylation. *Cold Spring Harbor Perspectives in Biology* **3**, a005199 (2011). URL <http://cshperspectives.cshlp.org/content/3/4/a005199>. Company: Cold Spring Harbor Laboratory Press Distributor: Cold Spring Harbor Laboratory Press Institution: Cold Spring Harbor Laboratory Press Label: Cold Spring Harbor Laboratory Press Publisher: Cold Spring Harbor Lab.
  - [21] Linders, P. T., van der Horst, C., ter Beest, M. & van den Bogaart, G. Stx5-Mediated ER-Golgi Transport in Mammals and Yeast. *Cells* **8**, 780 (2019). URL <https://www.mdpi.com/2073-4409/8/8/780>.
  - [22] Casey, J. R., Grinstein, S. & Orlowski, J. Sensors and regulators of intracellular pH. *Nature reviews. Molecular cell biology* **11**, 50–61 (2010). URL <http://www.ncbi.nlm.nih.gov/pubmed/19997129>.
  - [23] Potelle, S. *et al.* Glycosylation abnormalities in Gdt1p/TMEM165 deficient cells result from a defect in Golgi manganese homeostasis. *Human Molecular Genetics* **25**, 1489–1500 (2016). URL <https://academic.oup.com/hmg/article/25/8/1489/2384622>. Publisher: Oxford Academic.
  - [24] Alberts, B. *Essential cell biology* (Norton, New York, 2019).
  - [25] Lodish, H. F. *Molecular cell biology* (Freeman : Macmillan Higher Education, New York, NY, 2016).
  - [26] Hetz, C. The unfolded protein response: controlling cell fate decisions under ER stress and beyond. *Nature Reviews Molecular Cell Biology* **13**, 89–102 (2012). URL <https://www.nature.com/articles/nrm3270>. Number: 2 Publisher: Nature Publishing Group.
  - [27] Bräuer, P. *et al.* Structural basis for pH-dependent retrieval of ER proteins from the Golgi by the KDEL receptor. *Science* **363**, 1103–1107 (2019). URL <https://science/sciencemag.org/content/363/6431/1103>.
  - [28] Wilson, D. W., Lewis, M. J. & Pelham, H. R. pH-dependent binding of KDEL to its receptor in vitro. *Journal of Biological Chemistry* **268**, 7465–7468 (1993). URL [https://www.jbc.org/article/S0021-9258\(18\)53197-5/abstract](https://www.jbc.org/article/S0021-9258(18)53197-5/abstract). Publisher: Elsevier.
  - [29] Ghosh, P., Dahms, N. M. & Kornfeld, S. Mannose 6-phosphate receptors: new twists in the tale. *Nature Reviews Molecular Cell Biology* **4**, 202–213 (2003). URL <https://www.nature.com/articles/nrm1050>. Number: 3 Publisher: Nature Publishing Group.

- [30] Olson, L. J. *et al.* Allosteric regulation of lysosomal enzyme recognition by the cation-independent mannose 6-phosphate receptor. *Communications Biology* **3**, 1–15 (2020). URL <https://www.nature.com/articles/s42003-020-01211-w>. Number: 1 Publisher: Nature Publishing Group.
- [31] Fisher, P. & Ungar, D. Bridging the Gap between Glycosylation and Vesicle Traffic. *Frontiers in Cell and Developmental Biology* **4** (2016). URL <https://www.frontiersin.org/articles/10.3389/fcell.2016.00015/full>.
- [32] Rivinoja, A., Hassinen, A., Kokkonen, N., Kauppila, A. & Kellokumpu, S. Elevated Golgi pH impairs terminal N-glycosylation by inducing mislocalization of Golgi glycosyltransferases. *Journal of Cellular Physiology* **220**, 144–154 (2009). URL <http://dx.doi.org/10.1002/jcp.21744>.
- [33] Maeda, Y. & Kinoshita, T. Chapter Twenty-Three - The Acidic Environment of the Golgi Is Critical for Glycosylation and Transport. In Fukuda, M. (ed.) *Methods in Enzymology*, vol. 480 of *Glycobiology*, 495–510 (Academic Press, 2010). URL <http://www.sciencedirect.com/science/article/pii/S0076687910800229>.
- [34] Gawlitzeck, M., Ryll, T., Lofgren, J. & Sliwkowski, M. B. Ammonium alters N-glycan structures of recombinant TNFR-IgG: Degradative versus biosynthetic mechanisms. *Biotechnology and Bioengineering* **68**, 637–646 (2000). URL <https://onlinelibrary.wiley.com/doi/abs/10.1002/%28SICI%291097-0290%2820000620%2968%3A6%3C637%3A%3AAID-BIT6%3E3.0.CO%3B2-C>. \_eprint: <https://onlinelibrary.wiley.com/doi/pdf/10.1002/%28SICI%291097-0290%2820000620%2968%3A6%3C637%3A%3AAID-BIT6%3E3.0.CO%3B2-C>.
- [35] Guo, Y., Sirkis, D. W. & Schekman, R. Protein Sorting at the trans-Golgi Network. *Annual Review of Cell and Developmental Biology* **30**, 169–206 (2014). URL <https://doi.org/10.1146/annurev-cellbio-100913-013012>. \_eprint: <https://doi.org/10.1146/annurev-cellbio-100913-013012>.
- [36] Lombard, V., Golaconda Ramulu, H., Drula, E., Coutinho, P. M. & Henrissat, B. The carbohydrate-active enzymes database (CAZy) in 2013. *Nucleic Acids Research* **42**, D490–D495 (2014). URL <https://academic.oup.com/nar/article/42/D1/D490/1057423>. Publisher: Oxford Academic.
- [37] Gabius, H.-J. The sugar code: Why glycans are so important. *Biosystems* **164**, 102–111 (2018). URL <https://www.sciencedirect.com/science/article/pii/S0303264717301983>.
- [38] Cummings, R. D. The repertoire of glycan determinants in the human glycome. *Molecular BioSystems* **5**, 1087–1104 (2009). URL <https://pubs.rsc.org/en/content/articlelanding/2009/mb/b907931a>. Publisher: The Royal Society of Chemistry.
- [39] Joshi, H. J. *et al.* Glycosyltransferase genes that cause monogenic congenital disorders of glycosylation are distinct from glycosyltransferase genes associated with complex diseases. *Glycobiology* **28**, 284–294 (2018).
- [40] Nairn, A. & Moremen, K. *Handbook of Glycomics* (Academic Press, 2009).
- [41] Nairn, A. V. *et al.* Regulation of Glycan Structures in Animal Tissues TRANSCRIPT PROFILING OF GLYCAN-RELATED GENES. *Journal of Biological Chemistry* **283**, 17298–17313 (2008). URL <http://www.jbc.org/content/283/25/17298>. Publisher: American Society for Biochemistry and Molecular Biology.
- [42] Narimatsu, Y. *et al.* An Atlas of Human Glycosylation Pathways Enables Display of the Human Glycome by Gene Engineered Cells. *Molecular Cell* **75**, 394–407.e5 (2019).
- [43] Riemersma, M. *et al.* Human ISPD Is a Cytidyltransferase Required for Dystroglycan O-Mannosylation. *Chemistry & Biology* **22**, 1643–1652 (2015). URL <http://www.sciencedirect.com/science/article/pii/S1074552115004421>.

## References

- [44] Kornfeld, R. & Kornfeld, S. Assembly of asparagine-linked oligosaccharides. *Annual Review of Biochemistry* **54**, 631–664 (1985). URL <https://www.annualreviews.org/doi/10.1146/annurev.bi.54.070185.003215>. Publisher: Annual Reviews.
- [45] Lizak, C., Gerber, S., Numao, S., Aebi, M. & Locher, K. P. X-ray structure of a bacterial oligosaccharyltransferase. *Nature* **474**, 350–355 (2011). URL <https://www.nature.com/articles/nature10151>. Number: 7351 Publisher: Nature Publishing Group.
- [46] Ruiz-Canada, C., Kelleher, D. J. & Gilmore, R. Cotranslational and Posttranslational N-Glycosylation of Polypeptides by Distinct Mammalian OST Isoforms. *Cell* **136**, 272–283 (2009). URL <http://www.sciencedirect.com/science/article/pii/S0092867408015626>.
- [47] Kelleher, D. J. & Gilmore, R. An evolving view of the eukaryotic oligosaccharyltransferase. *Glycobiology* **16**, 47R–62R (2006). URL <https://academic.oup.com/glycob/article/16/4/47R/603609>. Publisher: Oxford Academic.
- [48] Schreiner, R., Schnabel, E. & Wieland, F. Novel N-glycosylation in eukaryotes: laminin contains the linkage unit beta-glucosylasparagine. *Journal of Cell Biology* **124**, 1071–1081 (1994). URL <https://rupress.org/jcb/article/124/6/1071/14829/Novel-N-glycosylation-in-eukaryotes-laminin>. Publisher: The Rockefeller University Press.
- [49] Vulliere-Douglass, J. F. *et al.* Glutamine-linked and Non-consensus Asparagine-linked Oligosaccharides Present in Human Recombinant Antibodies Define Novel Protein Glycosylation Motifs. *Journal of Biological Chemistry* **285**, 16012–16022 (2010). URL <http://www.jbc.org/content/285/21/16012>. Publisher: American Society for Biochemistry and Molecular Biology.
- [50] Zielinska, D. F., Gnad, F., Wiśniewski, J. R. & Mann, M. Precision Mapping of an In Vivo N-Glycoproteome Reveals Rigid Topological and Sequence Constraints. *Cell* **141**, 897–907 (2010). URL [https://www.cell.com/cell/abstract/S0092-8674\(10\)00386-7](https://www.cell.com/cell/abstract/S0092-8674(10)00386-7). Publisher: Elsevier.
- [51] Helenius, A. & Aebi, M. Roles of N-Linked Glycans in the Endoplasmic Reticulum. *Annual Review of Biochemistry* **73**, 1019–1049 (2004). URL <https://www.annualreviews.org/doi/10.1146/annurev.biochem.73.011303.073752>. Publisher: Annual Reviews.
- [52] Ledermann, G. Z. Glycoprotein folding, quality control and ER-associated degradation. *Current Opinion in Structural Biology* **19**, 515–523 (2009). URL <http://www.sciencedirect.com/science/article/pii/S09594440X09000943>.
- [53] Varki, A. Essentials of glycobiology (2017). URL <https://www.ncbi.nlm.nih.gov/books/NBK310274/>. Archive: /z-wcorg/ Library Catalog: http://worldcat.org.
- [54] Jaiman, A. & Thattai, M. Golgi compartments enable controlled biomolecular assembly using promiscuous enzymes. *eLife* **9**, e49573 (2020). URL <https://doi.org/10.7554/eLife.49573>. Publisher: eLife Sciences Publications, Ltd.
- [55] Freeze, H. H. Genetic defects in the human glycome. *Nature Reviews Genetics* **7**, 537–551 (2006). URL <https://www.nature.com/articles/nrg1894>. Number: 7 Publisher: Nature Publishing Group.
- [56] Freeze, H., Chong, J., Bamshad, M. & Ng, B. Solving Glycosylation Disorders: Fundamental Approaches Reveal Complicated Pathways. *The American Journal of Human Genetics* **94**, 161–175 (2014). URL <http://www.sciencedirect.com/science/article/pii/S0002929713004813>.
- [57] Jahn, R. & Scheller, R. H. SNARES — engines for membrane fusion. *Nature Reviews Molecular Cell Biology* **7**, 631–631 (2006). URL <http://dx.doi.org/10.1038/nrm2002>.

- [58] Hong, W. SNAREs and traffic. *Biochimica et Biophysica Acta (BBA) - Molecular Cell Research* **1744**, 120–144 (2005). URL <http://www.sciencedirect.com/science/article/pii/S0167488905000571>.
- [59] Weimbs, T. *et al.* A conserved domain is present in different families of vesicular fusion proteins: A new superfamily. *Proceedings of the National Academy of Sciences* **94**, 3046–3051 (1997). URL <https://www.pnas.org/content/94/7/3046>. Publisher: National Academy of Sciences Section: Biological Sciences.
- [60] Appenzeller, C., Andersson, H., Kappeler, F. & Hauri, H.-P. The lectin ERGIC-53 is a cargo transport receptor for glycoproteins. *Nature Cell Biology* **1**, 330–334 (1999). URL [http://www.nature.com/articles/ncb1099\\_330](http://www.nature.com/articles/ncb1099_330).
- [61] Appenzeller-Herzog, C., Roche, A.-C., Nufer, O. & Hauri, H.-P. pH-induced conversion of the transport lectin ERGIC-53 triggers glycoprotein release. *The Journal of biological chemistry* **279**, 12943–50 (2004). URL <http://www.ncbi.nlm.nih.gov/pubmed/14718532>.
- [62] Kamiya, Y. *et al.* Molecular Basis of Sugar Recognition by the Human L-type Lectins ERGIC-53, VIPL, and VIP36. *Journal of Biological Chemistry* **283**, 1857–1861 (2008). URL <http://www.jbc.org/content/283/4/1857.abstract>.
- [63] Rowe, T., Dascher, C., Bannykh, S., Plutner, H. & Balch, W. E. Role of vesicle-associated syntaxin 5 in the assembly of pre-Golgi intermediates. *Science (New York, N.Y.)* **279**, 696–700 (1998). URL <http://www.ncbi.nlm.nih.gov/pubmed/9445473>.
- [64] Appenzeller-Herzog, C. & Hauri, H.-P. The ER-Golgi intermediate compartment (ERGIC): in search of its identity and function. *Journal of Cell Science* **119**, 2173 LP–2183 (2006). URL <http://jcs.biologists.org/content/119/11/2173.abstract>.
- [65] Mogelsvang, S., Marsh, B. J., Ladinsky, M. S. & Howell, K. E. Predicting Function from Structure: 3D Structure Studies of the Mammalian Golgi Complex. *Traffic* **5**, 338–345 (2004). URL <https://onlinelibrary.wiley.com/doi/abs/10.1111/j.1398-9219.2004.00186.x>. \_eprint: <https://onlinelibrary.wiley.com/doi/pdf/10.1111/j.1398-9219.2004.00186.x>.
- [66] Nilsson, T. *et al.* Overlapping distribution of two glycosyltransferases in the Golgi apparatus of HeLa cells. *Journal of Cell Biology* **120**, 5–13 (1993). URL <https://rupress.org/jcb/article/120/1/5/14583/Overlapping-distribution-of-two>. Publisher: The Rockefeller University Press.
- [67] Ripoche, J., Link, B., Yucel, J. K., Tokuyasu, K. & Malhotra, V. Location of Golgi membranes with reference to dividing nuclei in syncytial Drosophila embryos. *Proceedings of the National Academy of Sciences* **91**, 1878–1882 (1994). URL <https://www.pnas.org/content/91/5/1878>. Publisher: National Academy of Sciences Section: Research Article.
- [68] Velasco, A. *et al.* Cell type-dependent variations in the subcellular distribution of alpha-mannosidase I and II. *Journal of Cell Biology* **122**, 39–51 (1993). URL <https://rupress.org/jcb/article/122/1/39/59473/Cell-type-dependent-variations-in-the-subcellular>. Publisher: The Rockefeller University Press.
- [69] Forgac, M. Vacuolar ATPases: rotary proton pumps in physiology and pathophysiology. *Nature Reviews Molecular Cell Biology* **8**, 917–917 (2007). URL <http://dx.doi.org/10.1038/nrm2272>.
- [70] Nishi, T. & Forgac, M. The vacuolar (H<sup>+</sup>)-ATPases—nature's most versatile proton pumps. *Nature Reviews Molecular Cell Biology* **3**, 94–103 (2002).
- [71] Kawasaki-Nishi, S., Bowers, K., Nishi, T., Forgac, M. & Stevens, T. H. The Amino-terminal Domain of the Vacuolar Proton-translocating ATPase a Subunit Controls Targeting and in Vivo Dissociation, and the Carboxyl-terminal Domain Affects Coupling of Proton Transport and ATP Hydrolysis. *Journal of Biological Chemistry* **276**, 47411–47420 (2001). URL <http://www.jbc.org/content/276/50/47411>. Publisher: American Society for Biochemistry and Molecular Biology.

## References

- [72] Kawasaki-Nishi, S., Nishi, T. & Forgac, M. Yeast V-ATPase complexes containing different isoforms of the 100-kDa  $\alpha$ -subunit differ in coupling efficiency and in vivo dissociation. *The Journal of Biological Chemistry* **276**, 17941–17948 (2001).
- [73] Manolson, M. F. *et al.* STV1 gene encodes functional homologue of 95-kDa yeast vacuolar H(+) -ATPase subunit Vph1p. *Journal of Biological Chemistry* **269**, 14064–14074 (1994). URL <http://www.jbc.org/content/269/19/14064>. Publisher: American Society for Biochemistry and Molecular Biology.
- [74] Sun-Wada, G.-H., Tabata, H., Kawamura, N., Aoyama, M. & Wada, Y. Direct recruitment of H+-ATPase from lysosomes for phagosomal acidification. *Journal of Cell Science* **122**, 2504–2513 (2009). URL <https://jcs.biologists.org/content/122/14/2504>. Publisher: The Company of Biologists Ltd Section: Research Article.
- [75] Toyomura, T. *et al.* From Lysosomes to the Plasma Membrane LOCALIZATION OF VACUOLAR TYPE H+-ATPase WITH THE a3 ISOFORM DURING OSTEOCLAST DIFFERENTIATION. *Journal of Biological Chemistry* **278**, 22023–22030 (2003). URL <http://www.jbc.org/content/278/24/22023>. Publisher: American Society for Biochemistry and Molecular Biology.
- [76] Saw, N. M. N. *et al.* Vacuolar H+-ATPase subunits Voa1 and Voa2 cooperatively regulate secretory vesicle acidification, transmitter uptake, and storage. *Molecular Biology of the Cell* **22**, 3394–3409 (2011). URL <https://www.molbiolcell.org/doi/10.1091/mbc.e11-02-0155>. Publisher: American Society for Cell Biology (mbc).
- [77] Kornak, U. *et al.* Impaired glycosylation and cutis laxa caused by mutations in the vesicular H+-ATPase subunit ATP6VOA2. *Nature Genetics* **40**, 32–34 (2008). URL <https://www.nature.com/articles/ng.2007.45>.
- [78] Pietrement, C. *et al.* Distinct Expression Patterns of Different Subunit Isoforms of the V-ATPase in the Rat Epididymis. *Biology of Reproduction* **74**, 185–194 (2006). URL <https://academic.oup.com/biolreprod/article/74/1/185/2666994>. Publisher: Oxford Academic.
- [79] Hurtado-Lorenzo, A. *et al.* V-ATPase interacts with ARNO and Arf6 in early endosomes and regulates the protein degradative pathway. *Nature Cell Biology* **8**, 124–136 (2006). URL <https://www.nature.com/articles/ncb1348>. Number: 2 Publisher: Nature Publishing Group.
- [80] Glick, B. S. & Nakano, A. Membrane Traffic Within the Golgi Apparatus. *Annual Review of Cell and Developmental Biology* **25**, 113–132 (2009). URL <http://www.annualreviews.org/doi/10.1146/annurev.cellbio.24.110707.175421>.
- [81] Muschalik, N. & Munro, S. Golgins. *Current Biology* **28**, R374–R376 (2018). URL [https://www.cell.com/current-biology/abstract/S0960-9822\(18\)30008-3](https://www.cell.com/current-biology/abstract/S0960-9822(18)30008-3). Publisher: Elsevier.
- [82] Wong, M., Gillingham, A. K. & Munro, S. The golgin coiled-coil proteins capture different types of transport carriers via distinct N-terminal motifs. *BMC Biology* **15**, 3–3 (2017). URL <http://bmcbiol.biomedcentral.com/articles/10.1186/s12915-016-0345-3>.
- [83] Drin, G., Morello, V., Casella, J.-F., Gounon, P. & Antonny, B. Asymmetric Tethering of Flat and Curved Lipid Membranes by a Golgin. *Science* **320**, 670–673 (2008). URL <https://science.sciencemag.org/content/320/5876/670>. Publisher: American Association for the Advancement of Science Section: Report.
- [84] Fridmann-Sirkis, Y., Siniossoglou, S. & Pelham, H. R. TMF is a golgin that binds Rab6 and influences Golgi morphology. *BMC Cell Biology* **5**, 18 (2004). URL <https://doi.org/10.1186/1471-2121-5-18>.
- [85] Setty, S. R. G., Shin, M. E., Yoshino, A., Marks, M. S. & Burd, C. G. Golgi Recruitment of GRIP Domain Proteins by Arf-like GTPase 1 Is Regulated by Arf-like GTPase 3. *Current Biology* **13**, 401–404 (2003). URL [https://www.cell.com/current-biology/abstract/S0960-9822\(03\)00089-7](https://www.cell.com/current-biology/abstract/S0960-9822(03)00089-7). Publisher: Elsevier.

- [86] Kelly, E. E. *et al.* Rab30 is required for the morphological integrity of the Golgi apparatus. *Biology of the Cell* **104**, 84–101 (2012). URL <https://onlinelibrary.wiley.com/doi/abs/10.1111/boc.201100080>. \_eprint: <https://onlinelibrary.wiley.com/doi/pdf/10.1111/boc.201100080>.
- [87] Miserey-Lenkei, S. *et al.* Rab and actomyosin-dependent fission of transport vesicles at the Golgi complex. *Nature Cell Biology* **12**, 645–654 (2010). URL <https://www.nature.com/articles/ncb2067>. Number: 7 Publisher: Nature Publishing Group.
- [88] Hayes, G. L. *et al.* Multiple Rab GTPase Binding Sites in GCC185 Suggest a Model for Vesicle Tethering at the Trans-Golgi. *Molecular Biology of the Cell* **20**, 209–217 (2009). URL <https://www.ncbi.nlm.nih.gov/pmc/articles/PMC2613123/>.
- [89] Zerial, M., McBride, H., Woodman, P. G. & Allan, V. J. Rab proteins as membrane organizers. *Nature reviews. Molecular cell biology* **2**, 107–17 (2001). URL <http://www.ncbi.nlm.nih.gov/pubmed/11252952>.
- [90] Wandinger-Ness, A. & Zerial, M. Rab Proteins and the Compartmentalization of the Endosomal System. *Cold Spring Harbor Perspectives in Biology* **6** (2014). URL <https://www.ncbi.nlm.nih.gov/pmc/articles/PMC4413231/>.
- [91] Lees, J. A., Yip, C. K., Walz, T. & Hughson, F. M. Molecular organization of the COG vesicle tethering complex. *Nature Structural & Molecular Biology* **17**, 1292–1297 (2010). URL <http://www.nature.com/doifinder/10.1038/nsmb.1917>.
- [92] Yu, I.-M. & Hughson, F. M. Tethering Factors as Organizers of Intracellular Vesicular Traffic. *Annual Review of Cell and Developmental Biology* **26**, 137–156 (2010). URL <http://www.annualreviews.org/doi/10.1146/annurev.cellbio.042308.113327>.
- [93] Morelle, W. & Michalski, J.-C. Analysis of protein glycosylation by mass spectrometry. *Nature Protocols* **2**, 1585–1602 (2007). URL <https://www.nature.com/articles/nprot.2007.227>. Number: 7 Publisher: Nature Publishing Group.
- [94] de Ligt, J. *et al.* Diagnostic Exome Sequencing in Persons with Severe Intellectual Disability. *New England Journal of Medicine* **367**, 1921–1929 (2012). URL <https://doi.org/10.1056/NEJMoa1206524>. Publisher: Massachusetts Medical Society \_eprint: <https://doi.org/10.1056/NEJMoa1206524>.
- [95] Gilissen, C. *et al.* Genome sequencing identifies major causes of severe intellectual disability. *Nature* **511**, 344–347 (2014). URL <https://www.nature.com/articles/nature13394>. Number: 7509 Publisher: Nature Publishing Group.
- [96] Galea, G., Bexiga, M. G., Panarella, A., O'Neill, E. D. & Simpson, J. C. A high-content screening microscopy approach to dissect the role of Rab proteins in Golgi-to-ER retrograde trafficking. *Journal of Cell Science* **128**, 2339–2349 (2015). URL <https://jcs.biologists.org/content/128/13/2339>.
- [97] Axelsson, M. A. B. *et al.* Neutralization of pH in the Golgi apparatus causes redistribution of glycosyltransferases and changes in the O-glycosylation of mucins. *Glycobiology* **11**, 633–644 (2001). URL <https://academic.oup.com/glycob/article/11/8/633/650599>. Publisher: Oxford Academic.
- [98] Ben-Tekaya, H., Miura, K., Pepperkok, R. & Hauri, H.-P. Live imaging of bidirectional traffic from the ERGIC. *Journal of Cell Science* **118** (2005).
- [99] Davis-Kaplan, S. R. *et al.* PKR1 encodes an assembly factor for the yeast V-type ATPase. *The Journal of Biological Chemistry* **281**, 32025–32035 (2006).
- [100] Malkus, P., Graham, L. A., Stevens, T. H. & Schekman, R. Role of Vma21p in assembly and transport of the yeast vacuolar ATPase. *Molecular Biology of the Cell* **15**, 5075–5091 (2004).

## References

- [101] Esmail, S. *et al.* N-Linked Glycosylation Is Required for Vacuolar H<sup>+</sup>-ATPase (V-ATPase) a4 Subunit Stability, Assembly, and Cell Surface Expression. *Journal of Cellular Biochemistry* **117**, 2757–2768 (2016).
- [102] Esmail, S. *et al.* N-linked glycosylation of a subunit isoforms is critical for vertebrate vacuolar H<sup>+</sup>-ATPase (V-ATPase) biosynthesis. *Journal of Cellular Biochemistry* **119**, 861–875 (2017). URL <https://doi.org/10.1002/jcb.26250>.
- [103] Graham, L. A., Flannery, A. R. & Stevens, T. H. Structure and assembly of the yeast V-ATPase. *Journal of Bioenergetics and Biomembranes* **35**, 301–312 (2003).
- [104] Feng, H. *et al.* Cytoplasmic Terminus of Vacuolar Type Proton Pump Accessory Subunit Ac45 Is Required for Proper Interaction with V0 Domain Subunits and Efficient Osteoclastic Bone Resorption. *Journal of Biological Chemistry* **283**, 13194–13204 (2008). URL <http://www.jbc.org/content/283/19/13194>. Publisher: American Society for Biochemistry and Molecular Biology.
- [105] Hodi, F. S. *et al.* ATP6S1 elicits potent humoral responses associated with immune-mediated tumor destruction. *Proceedings of the National Academy of Sciences* **99**, 6919–6924 (2002). URL <https://www.pnas.org/content/99/10/6919>. Publisher: National Academy of Sciences Section: Biological Sciences.
- [106] Holthuis, J. C. M., Jansen, E. J. R., Schoonderwoert, V. T. G., Burbach, J. P. H. & Martens, G. J. M. Biosynthesis of the vacuolar H<sup>+</sup>-ATPase accessory subunit Ac45 in Xenopus pituitary. *European Journal of Biochemistry* **262**, 484–491 (1999). URL <https://febs.onlinelibrary.wiley.com/doi/abs/10.1046/j.1432-1327.1999.00396.x>. \_eprint: <https://febs.onlinelibrary.wiley.com/doi/pdf/10.1046/j.1432-1327.1999.00396.x>.
- [107] Supek, F. *et al.* A novel accessory subunit for vacuolar H<sup>(+)</sup>-ATPase from chromaffin granules. *Journal of Biological Chemistry* **269**, 24102–24106 (1994). URL <http://www.jbc.org/content/269/39/24102>. Publisher: American Society for Biochemistry and Molecular Biology.
- [108] Jansen, E. J. R., Scheenen, W. J. J. M., Hafmans, T. G. M. & Martens, G. J. M. Accessory subunit Ac45 controls the V-ATPase in the regulated secretory pathway. *Biochimica Et Biophysica Acta* **1783**, 2301–2310 (2008).
- [109] Jansen, E. J. R., Hafmans, T. G. M. & Martens, G. J. M. V-ATPase-Mediated Granular Acidification Is Regulated by the V-ATPase Accessory Subunit Ac45 in POMC-Producing Cells. *Molecular Biology of the Cell* **21**, 3330–3339 (2010). URL <https://www.ncbi.nlm.nih.gov/pmc/articles/PMC2947469/>.
- [110] Qin, A. *et al.* Versatile Roles of V-ATPases Accessory Subunit Ac45 in Osteoclast Formation and Function. *PLOS ONE* **6**, e27155 (2011). URL <https://journals.plos.org/plosone/article?id=10.1371/journal.pone.0027155>. Publisher: Public Library of Science.
- [111] Yang, D.-Q. *et al.* V-ATPase subunit ATP6AP1 (Ac45) regulates osteoclast differentiation, extracellular acidification, lysosomal trafficking, and protease exocytosis in osteoclast-mediated bone resorption. *Journal of Bone and Mineral Research: The Official Journal of the American Society for Bone and Mineral Research* **27**, 1695–1707 (2012).
- [112] Jansen, E. J. R. *et al.* ATP6AP1 deficiency causes an immunodeficiency with hepatopathy, cognitive impairment and abnormal protein glycosylation. *Nature Communications* **7**, 11600–11600 (2016). URL <http://dx.doi.org/10.1038/ncomms11600>.
- [113] Rujano, M. A. *et al.* Mutations in the X-linked ATP6AP2 cause a glycosylation disorder with autophagic defects. *The Journal of Experimental Medicine* **214**, 3707–3729 (2017).
- [114] Kinouchi, K. *et al.* The Role of Individual Domains and the Significance of Shedding of ATP6AP2/(pro)renin Receptor in Vacuolar H<sup>+</sup>-ATPase Biogenesis. *PLOS ONE* **8**, e78603 (2013). URL <https://journals.plos.org/plosone/article?id=10.1371/journal.pone.0078603>. Publisher: Public Library of Science.

- [115] Kinouchi Kenichiro *et al.* The (Pro)renin Receptor/ATP6AP2 is Essential for Vacuolar H<sup>+</sup>-ATPase Assembly in Murine Cardiomyocytes. *Circulation Research* **107**, 30–34 (2010). URL <https://www.ahajournals.org/doi/10.1161/CIRCRESAHA.110.224667>. Publisher: American Heart Association.
- [116] Kissing, S. *et al.* Disruption of the vacuolar-type H<sup>+</sup>-ATPase complex in liver causes MTORC1-independent accumulation of autophagic vacuoles and lysosomes. *Autophagy* **13**, 670–685 (2017). URL <https://doi.org/10.1080/15548627.2017.1280216>. Publisher: Taylor & Francis \_eprint: <https://doi.org/10.1080/15548627.2017.1280216>.
- [117] Cannata Serio, M. *et al.* Mutations in the V-ATPase Assembly Factor VMA21 Cause a Congenital Disorder of Glycosylation With Autophagic Liver Disease. *Hepatology* **72**, 1968–1986 (2020). URL <https://doi.org/10.1002/hep.31218>. Publisher: John Wiley & Sons, Ltd.
- [118] Dingjan, I. *et al.* Endosomal and Phagosomal SNAREs. *Physiological Reviews* **98**, 1465–1492 (2018). URL <https://www.physiology.org/doi/10.1152/physrev.00037.2017>.
- [119] Welsh, L. M., Tong, A. H. Y., Boone, C., Jensen, O. N. & Otte, S. Genetic and molecular interactions of the Erv41p-Erv46p complex involved in transport between the endoplasmic reticulum and Golgi complex. *Journal of Cell Science* **119**, 4730–4740 (2006). URL <https://jcs.biologists.org/content/119/22/4730>. Publisher: The Company of Biologists Ltd Section: Research Article.
- [120] Jansen, J. *et al.* CCDC115 Deficiency Causes a Disorder of Golgi Homeostasis with Abnormal Protein Glycosylation. *The American Journal of Human Genetics* **98**, 310–321 (2016).
- [121] Jansen, J. *et al.* TMEM199 Deficiency Is a Disorder of Golgi Homeostasis Characterized by Elevated Aminotransferases, Alkaline Phosphatase, and Cholesterol and Abnormal Glycosylation. *The American Journal of Human Genetics* **98**, 322–330 (2016).
- [122] Graham, L. A., Hill, K. J. & Stevens, T. H. Assembly of the Yeast Vacuolar H<sup>+</sup>-ATPase Occurs in the Endoplasmic Reticulum and Requires a Vma12p/Vma22p Assembly Complex. *Journal of Cell Biology* **142**, 39–49 (1998). URL <https://rupress.org/jcb/article/142/1/39/1031/Assembly-of-the-Yeast-Vacuolar-H-ATPase-Occurs-in>. Publisher: The Rockefeller University Press.
- [123] Hill, K. J. & Stevens, T. H. Vma22p Is a Novel Endoplasmic Reticulum-associated Protein Required for Assembly of the Yeast Vacuolar H<sup>+</sup>-ATPase Complex. *Journal of Biological Chemistry* **270**, 22329–22336 (1995). URL <http://www.jbc.org/content/270/38/22329>. Publisher: American Society for Biochemistry and Molecular Biology.
- [124] Jackson, D. D. & Stevens, T. H. VMA12 Encodes a Yeast Endoplasmic Reticulum Protein Required for Vacuolar H<sup>+</sup>-ATPase Assembly. *Journal of Biological Chemistry* **272**, 25928–25934 (1997). URL <http://www.jbc.org/content/272/41/25928>. Publisher: American Society for Biochemistry and Molecular Biology.
- [125] Miles, A. L., Burr, S. P., Grice, G. L. & Nathan, J. A. The vacuolar-ATPase complex and assembly factors, TMEM199 and CCDC115, control HIF1 $\alpha$  prolyl hydroxylation by regulating cellular iron levels. *eLife* **6**, e22693–e22693 (2017). URL <https://doi.org/10.7554/eLife.22693>.
- [126] Nishi, T. & Forgac, M. Molecular cloning and expression of three isoforms of the 100-kDa a subunit of the mouse vacuolar proton-translocating ATPase. *The Journal of Biological Chemistry* **275**, 6824–6830 (2000).
- [127] Schulz, N., Dave, M. H., Stehberger, P. A., Chau, T. C. & Wagner, C. A. Differential Localization of Vacuolar H<sup>+</sup>-ATPases Containing a1, a2, a3, or a4 (ATP6V0A1-4) Subunit Isoforms Along the Nephron. *Cellular Physiology and Biochemistry* **20**, 109–120 (2007). URL <https://www.karger.com/DOI/10.1159/000104159>.

## References

- [128] Toyomura, T., Oka, T., Yamaguchi, C., Wada, Y. & Futai, M. Three Subunit a Isoforms of Mouse Vacuolar H<sup>+</sup>-ATPase PREFERENTIAL EXPRESSION OF THE a3 ISOFORM DURING OSTEOCLAST DIFFERENTIATION. *Journal of Biological Chemistry* **275**, 8760–8765 (2000). URL <http://www.jbc.org/content/275/12/8760>. Publisher: American Society for Biochemistry and Molecular Biology.
- [129] Li, B. *et al.* Genome-wide CRISPR screen identifies host dependency factors for influenza A virus infection. *Nature Communications* **11** (2020). URL <https://www.ncbi.nlm.nih.gov/pmc/articles/PMC6952391/>.
- [130] Foulquier, F. *et al.* TMEM165 Deficiency Causes a Congenital Disorder of Glycosylation. *The American Journal of Human Genetics* **91**, 15–26 (2012). URL <http://www.sciencedirect.com/science/article/pii/S000292971200256X>.
- [131] Park, J. *et al.* SLC39A8 Deficiency: A Disorder of Manganese Transport and Glycosylation. *The American Journal of Human Genetics* **97**, 894–903 (2015). URL <http://www.sciencedirect.com/science/article/pii/S0002929715004486>.
- [132] Powell, J. T. & Brew, K. Metal ion activation of galactosyltransferase. *Journal of Biological Chemistry* **251**, 3645–3652 (1976). URL <http://www.jbc.org/content/251/12/3645>. Publisher: American Society for Biochemistry and Molecular Biology.
- [133] Wong, M. & Munro, S. Membrane trafficking. The specificity of vesicle traffic to the Golgi is encoded in the golgin coiled-coil proteins. *Science (New York, N.Y.)* **346**, 1256898–1256898 (2014). URL <http://www.ncbi.nlm.nih.gov/pubmed/25359980>.
- [134] Witkos, T. M. & Lowe, M. The Golgin Family of Coiled-Coil Tethering Proteins. *Frontiers in Cell and Developmental Biology* **3**, 86–86 (2016). URL <http://journal.frontiersin.org/Article/10.3389/fcell.2015.00086/abstract>.
- [135] Barr, F. A., Puype, M., Vandekerckhove, J. & Warren, G. GRASP65, a protein involved in the stacking of Golgi cisternae. *Cell* **91**, 253–62 (1997). URL <http://www.ncbi.nlm.nih.gov/pubmed/9346242>.
- [136] Smits, P. *et al.* Lethal Skeletal Dysplasia in Mice and Humans Lacking the Golgin GMAP-210. *New England Journal of Medicine* **362**, 206–216 (2010). URL <https://doi.org/10.1056/NEJMoa0900158>. eprint: <https://doi.org/10.1056/NEJMoa0900158>.
- [137] Robotti, P., Sato, K. & Lowe, M. The golgin GMAP-210 is required for efficient membrane trafficking in the early secretory pathway. *Journal of Cell Science* **128**, 1595–1606 (2015).
- [138] Sato, K., Robotti, P., Mironov, A. A. & Lowe, M. Coupling of vesicle tethering and Rab binding is required for in vivo functionality of the golgin GMAP-210. *Molecular Biology of the Cell* **26**, 537–553 (2014). URL <https://www.molbiolcell.org/doi/10.1091/mbc.E14-10-1450>. Publisher: American Society for Cell Biology (mboC).
- [139] Wehrle, A. *et al.* Hypomorphic mutations of TRIP11 cause odontochondrodysplasia. *JCI Insight* **4** (2019). URL <https://insight.jci.org/articles/view/124701#BIBL>. Publisher: American Society for Clinical Investigation.
- [140] Lan, Y., Zhang, N., Liu, H., Xu, J. & Jiang, R. Golgb1 regulates protein glycosylation and is crucial for mammalian palate development. *Development* **143**, 2344–2355 (2016). URL <https://dev.biologists.org/content/143/13/2344>. Publisher: Oxford University Press for The Company of Biologists Limited Section RESEARCH ARTICLE.
- [141] Satoh, A. *et al.* The Golgin Protein Giantin Regulates Interconnections Between Golgi Stacks. *Frontiers in Cell and Developmental Biology* **7** (2019). URL <https://www.frontiersin.org/articles/10.3389/fcell.2019.00160/full>. Publisher: Frontiers.

- [142] Koreishi, M. *et al.* The Golgin Tether Giantin Regulates the Secretory Pathway by Controlling Stack Organization within Golgi Apparatus. *PLOS ONE* **8**, e59821 (2013). URL <https://journals.plos.org/plosone/article?id=10.1371/journal.pone.0059821>. Publisher: Public Library of Science.
- [143] Xiang, Y. *et al.* Regulation of protein glycosylation and sorting by the Golgi matrix proteins GRASP55/65. *Nature Communications* **4**, 1659–1659 (2013). URL <http://www.nature.com/articles/ncomms2669>.
- [144] Witkos, T. M. *et al.* GORAB scaffolds COPI at the trans -Golgi for efficient enzyme recycling and correct protein glycosylation. *Nature Communications* **10**, 1–18 (2019). URL <https://www.nature.com/articles/s41467-018-08044-6>.
- [145] Lowe, M. The Physiological Functions of the Golgin Vesicle Tethering Proteins. *Frontiers in Cell and Developmental Biology* **7** (2019). URL <https://www.frontiersin.org/articles/10.3389/fcell.2019.00094/full>. Publisher: Frontiers.
- [146] Hennies, H. C. *et al.* Geroderma osteodysplastica is caused by mutations in SCYL1BP1 , a Rab-6 interacting golgin. *Nature Genetics* **40**, 1410–1412 (2008). URL <https://www.nature.com/articles/ng.252>. Number: 12 Publisher: Nature Publishing Group.
- [147] Chan, W. L. *et al.* Impaired proteoglycan glycosylation, elevated TGF- $\beta$  signaling, and abnormal osteoblast differentiation as the basis for bone fragility in a mouse model for geroderma osteodysplastica. *PLOS Genetics* **14**, e1007242 (2018). URL <https://journals.plos.org/plosgenetics/article?id=10.1371/journal.pgen.1007242>.
- [148] Hunter, A. G. W., Martolf, J. T., Baker, C. G. & Reed, M. H. Geroderma osteodysplastica. *Human Genetics* **40**, 311–324 (1978). URL <https://doi.org/10.1007/BF00272192>.
- [149] Lisker, R. *et al.* Geroderma osteodysplastica hereditaria: Report of three affected brothers and literature review. *American Journal of Medical Genetics* **3**, 389–395 (1979). URL <https://onlinelibrary.wiley.com/doi/abs/10.1002/ajmg.1320030410>. \_eprint: <https://onlinelibrary.wiley.com/doi/pdf/10.1002/ajmg.1320030410>.
- [150] Burman, J. L. *et al.* Scyl1, mutated in a recessive form of spinocerebellar neurodegeneration, regulates COPI-mediated retrograde traffic. *The Journal of biological chemistry* **283**, 22774–86 (2008). URL <http://www.ncbi.nlm.nih.gov/pubmed/18556652>.
- [151] Lenz, D. *et al.* SCYL1 variants cause a syndrome with low  $\beta$ -glutamyl-transferase cholestasis, acute liver failure, and neurodegeneration (CALFAN). *Genetics in Medicine* **20**, 1255–1265 (2018). URL <https://www.nature.com/articles/gim2017260>. Number: 10 Publisher: Nature Publishing Group.
- [152] Schmidt, W. M. *et al.* Mutation in the Scyl1 gene encoding amino-terminal kinase-like protein causes a recessive form of spinocerebellar neurodegeneration. *EMBO reports* **8**, 691–697 (2007). URL <https://www.embopress.org/doi/full/10.1038/sj.embor.7401001>. Publisher: John Wiley & Sons, Ltd.
- [153] Schmidt, W. M. *et al.* Disruptive SCYL1 Mutations Underlie a Syndrome Characterized by Recurrent Episodes of Liver Failure, Peripheral Neuropathy, Cerebellar Atrophy, and Ataxia. *The American Journal of Human Genetics* **97**, 855–861 (2015). URL [https://www.cell.com/ajhg/abstract/S0002-9297\(15\)00413-9](https://www.cell.com/ajhg/abstract/S0002-9297(15)00413-9). Publisher: Elsevier.
- [154] Climer, L. K., Dobretsov, M. & Lupashin, V. Defects in the COG complex and COG-related trafficking regulators affect neuronal Golgi function. *Frontiers in Neuroscience* **9** (2015). URL <https://www.frontiersin.org/articles/10.3389/fnins.2015.00405/full>. Publisher: Frontiers.
- [155] Fukuda, M. Regulation of secretory vesicle traffic by Rab small GTPases. *Cellular and molecular life sciences: CMLS* **65**, 2801–2813 (2008).

## References

- [156] Oka, T. *et al.* Genetic Analysis of the Subunit Organization and Function of the Conserved Oligomeric Golgi (COG) Complex STUDIES OF COG5- AND COG7-DEFICIENT MAMMALIAN CELLS. *Journal of Biological Chemistry* **280**, 32736–32745 (2005). URL <http://www.jbc.org/content/280/38/32736>. Publisher: American Society for Biochemistry and Molecular Biology.
- [157] Oka, T., Ungar, D., Hughson, F. M. & Krieger, M. The COG and COPI Complexes Interact to Control the Abundance of GEARs, a Subset of Golgi Integral Membrane Proteins. *Molecular Biology of the Cell* **15**, 2423–2435 (2004). URL <https://www.molbiolcell.org/doi/10.1091/mbc.e03-09-0699>.
- [158] Witkos, T. M. & Lowe, M. Recognition and tethering of transport vesicles at the Golgi apparatus. *Current Opinion in Cell Biology* **47**, 16–23 (2017). URL <http://www.sciencedirect.com/science/article/pii/S0955067417300121>.
- [159] Blackburn, J. B., D’Souza, Z. & Lupashin, V. V. Maintaining order: COG complex controls Golgi trafficking, processing, and sorting. *FEBS Letters* **593**, 2466–2487 (2019). URL <https://febs.onlinelibrary.wiley.com/doi/abs/10.1002/1873-3468.13570>. \_eprint: <https://febs.onlinelibrary.wiley.com/doi/pdf/10.1002/1873-3468.13570>.
- [160] Kudlyk, T., Willett, R., Pokrovskaya, I. D. & Lupashin, V. COG6 Interacts with a Subset of the Golgi SNAREs and Is Important for the Golgi Complex Integrity. *Traffic* **14**, 194–204 (2013). URL <http://doi.wiley.com/10.1111/tra.12020>.
- [161] Shestakova, A., Suvorova, E., Pavliv, O., Khaidakova, G. & Lupashin, V. Interaction of the conserved oligomeric Golgi complex with t-SNARE Syntaxin5a/Sed5 enhances intra-Golgi SNARE complex stability. *The Journal of Cell Biology* **179**, 1179–1192 (2007). URL <http://jcb.rupress.org/content/179/6/1179>.
- [162] Willett, R. *et al.* COG complexes form spatial landmarks for distinct SNARE complexes. *Nature Communications* **4**, 1553–1553 (2013). URL <http://www.nature.com/articles/ncomms2535>.
- [163] Smith, R. D. *et al.* The COG Complex, Rab6 and COPI Define a Novel Golgi Retrograde Trafficking Pathway that is Exploited by SubAB Toxin. *Traffic* **10**, 1502–1517 (2009). URL <http://doi.wiley.com/10.1111/j.1600-0854.2009.00965.x>.
- [164] Willett, R. *et al.* COG lobe B sub-complex engages v-SNARE GS15 and functions via regulated interaction with lobe A sub-complex. *Scientific Reports* **6**, 29139–29139 (2016). URL <http://www.nature.com/articles/srep29139>.
- [165] Miller, V. J. & Ungar, D. Re'COG'nition at the Golgi. *Traffic* **13**, 891–897 (2012). URL <https://onlinelibrary.wiley.com/doi/abs/10.1111/j.1600-0854.2012.01338.x>.
- [166] Shestakova, A., Zolov, S. & Lupashin, V. COG Complex-Mediated Recycling of Golgi Glycosyltransferases is Essential for Normal Protein Glycosylation. *Traffic* **7**, 191–204 (2006). URL <https://onlinelibrary.wiley.com/doi/abs/10.1111/j.1600-0854.2005.00376.x>.
- [167] Pokrovskaya, I. D. *et al.* Conserved oligomeric Golgi complex specifically regulates the maintenance of Golgi glycosylation machinery. *Glycobiology* **21**, 1554–1569 (2011). URL <https://academic.oup.com/glycob/article/21/12/1554/1987839>. Publisher: Oxford Academic.
- [168] Reynders, E., Foulquier, F., Annaert, W. & Matthijs, G. How Golgi glycosylation meets and needs trafficking: the case of the COG complex. *Glycobiology* **21**, 853–863 (2011). URL <https://academic.oup.com/glycob/article/21/7/853/1988132>. Publisher: Oxford Academic.
- [169] Ong, Y. S., Tran, T. H. T., Gounko, N. V. & Hong, W. TMEM115 is an integral membrane protein of the Golgi complex involved in retrograde transport. *Journal of Cell Science* **127**, 2825–2839 (2014). URL <https://jcs.biologists.org/content/127/13/2825>. Publisher: The Company of Biologists Ltd Section: Research Article.

- [170] Climer, L. K., Pokrovskaya, I. D., Blackburn, J. B. & Lupashin, V. V. Membrane detachment is not essential for COG complex function. *Molecular Biology of the Cell* **29**, 964–974 (2018). URL <https://www.molbiolcell.org/doi/full/10.1091/mbc.E17-11-0694>. Publisher: American Society for Cell Biology (mbo).
- [171] Kodera, H. *et al.* Mutations in COG2 encoding a subunit of the conserved oligomeric golgi complex cause a congenital disorder of glycosylation. *Clinical Genetics* **87**, 455–460 (2015). URL <https://onlinelibrary.wiley.com/doi/abs/10.1111/cge.12417>. \_eprint: <https://onlinelibrary.wiley.com/doi/pdf/10.1111/cge.12417>.
- [172] Foulquier, F. *et al.* Conserved oligomeric Golgi complex subunit 1 deficiency reveals a previously uncharacterized congenital disorder of glycosylation type II. *Proceedings of the National Academy of Sciences* **103**, 3764–3769 (2006). URL <https://www.pnas.org/content/103/10/3764>.
- [173] Palmigiano, A. *et al.* MALDI-MS profiling of serum O-glycosylation and N-glycosylation in COG5-CDG. *Journal of Mass Spectrometry* **52**, 372–377 (2017). URL <https://onlinelibrary.wiley.com/doi/abs/10.1002/jms.3936>. \_eprint: <https://onlinelibrary.wiley.com/doi/pdf/10.1002/jms.3936>.
- [174] Abu Bakar, N., Lefever, D. J. & van Scherpenzeel, M. Clinical glycomics for the diagnosis of congenital disorders of glycosylation. *Journal of Inherited Metabolic Disease* **41**, 499–513 (2018). URL <https://doi.org/10.1007/s10545-018-0144-9>.
- [175] Foulquier, F. COG defects, birth and rise! *Genetic Glycosylation Diseases* **1792**, 896–902 (2009). URL <http://www.sciencedirect.com/science/article/pii/S0925443908002111>.
- [176] Morava, E. *et al.* A common mutation in the COG7 gene with a consistent phenotype including microcephaly, adducted thumbs, growth retardation, VSD and episodes of hyperthermia. *European Journal of Human Genetics* **15**, 638–645 (2007). URL <https://www.nature.com/articles/5201813>.
- [177] Ng, B. G. *et al.* Molecular and clinical characterization of a Moroccan Cog7 deficient patient. *Molecular Genetics and Metabolism* **91**, 201–204 (2007). URL <http://www.sciencedirect.com/science/article/pii/S109671920700073X>.
- [178] Kranz, C. *et al.* COG8 deficiency causes new congenital disorder of glycosylation type IIh. *Human Molecular Genetics* **16**, 731–741 (2007). URL <https://academic.oup.com/hmg/article/16/7/731/655711>.
- [179] Foulquier, F. *et al.* A new inborn error of glycosylation due to a Cog8 deficiency reveals a critical role for the Cog1–Cog8 interaction in COG complex formation. *Human Molecular Genetics* **16**, 717–730 (2007). URL <https://academic.oup.com/hmg/article/16/7/717/654283>.
- [180] Zeevaert, R. *et al.* Cerebrocostomandibular-like syndrome and a mutation in the conserved oligomeric Golgi complex, subunit 1. *Human Molecular Genetics* **18**, 517–524 (2009). URL <https://academic.oup.com/hmg/article/18/3/517/2527370>.
- [181] Ng, B. G. *et al.* Identification of the first COG–CDG patient of Indian origin. *Program and Abstracts for the 2011 Meeting of the Society for Inherited Metabolic Disorders* **102**, 364–367 (2011). URL <http://www.sciencedirect.com/science/article/pii/S1096719210005548>.
- [182] Miura, Y., Tay, S. K. H., Aw, M. M., Eklund, E. A. & Freeze, H. H. Clinical and Biochemical Characterization of a Patient with Congenital Disorder of Glycosylation (CDG) IIx. *The Journal of Pediatrics* **147**, 851–853 (2005). URL [https://www.jpeds.com/article/S0022-3476\(05\)00715-8/abstract](https://www.jpeds.com/article/S0022-3476(05)00715-8/abstract). Publisher: Elsevier.
- [183] Reynders, E. *et al.* Golgi function and dysfunction in the first COG4-deficient CDG type II patient. *Human Molecular Genetics* **18**, 3244–3256 (2009). URL <https://academic.oup.com/hmg/article/18/17/3244/2527327>.

## References

- [184] Ferreira, C. R. *et al.* A Recurrent De Novo Heterozygous COG4 Substitution Leads to Saul-Wilson Syndrome, Disrupted Vesicular Trafficking, and Altered Proteoglycan Glycosylation. *The American Journal of Human Genetics* **103**, 553–567 (2018). URL [https://www.cell.com/ajhg/abstract/S0002-9297\(18\)30314-8](https://www.cell.com/ajhg/abstract/S0002-9297(18)30314-8). Publisher: Elsevier.
- [185] Fung, C. W. *et al.* COG5-CDG with a Mild Neurohepatic Presentation. *JIMD reports* **3**, 67–70 (2012).
- [186] Paesold-Burda, P. *et al.* Deficiency in COG5 causes a moderate form of congenital disorders of glycosylation. *Human Molecular Genetics* **18**, 4350–4356 (2009).
- [187] Rymen, D. *et al.* COG5-CDG: expanding the clinical spectrum. *Orphanet Journal of Rare Diseases* **7**, 94 (2012).
- [188] Lübbehusen, J. *et al.* Fatal outcome due to deficiency of subunit 6 of the conserved oligomeric Golgi complex leading to a new type of congenital disorders of glycosylation. *Human Molecular Genetics* **19**, 3623–3633 (2010).
- [189] Huybrechts, S. *et al.* Deficiency of Subunit 6 of the Conserved Oligomeric Golgi Complex (COG6-CDG): Second Patient, Different Phenotype. *JIMD reports* **4**, 103–108 (2012).
- [190] Shaheen, R. *et al.* A novel syndrome of hypohidrosis and intellectual disability is linked to COG6 deficiency. *Journal of Medical Genetics* **50**, 431–436 (2013).
- [191] Zeevaert, R. *et al.* A new mutation in COG7 extends the spectrum of COG subunit deficiencies. *European Journal of Medical Genetics* **52**, 303–305 (2009). URL <http://www.sciencedirect.com/science/article/pii/S1769721209000743>.
- [192] Spaapen, L. J. M. *et al.* Clinical and biochemical presentation of siblings with COG-7 deficiency, a lethal multiple O- and N-glycosylation disorder. *Journal of Inherited Metabolic Disease* **28**, 707 (2005). URL <https://doi.org/10.1007/s10545-005-0015-z>. Publisher: John Wiley & Sons, Ltd.
- [193] Wu, X. *et al.* Mutation of the COG complex subunit gene COG7 causes a lethal congenital disorder. *Nature Medicine* **10**, 518–523 (2004). URL <https://www.nature.com/articles/nm1041>.
- [194] Xu, D., Joglekar, A. P., Williams, A. L. & Hay, J. C. Subunit structure of a mammalian ER/Golgi SNARE complex. *The Journal of biological chemistry* **275**, 39631–9 (2000). URL <http://www.ncbi.nlm.nih.gov/pubmed/11035026>.
- [195] Zhang, T. *et al.* Ykt6 forms a SNARE complex with syntaxin 5, GS28, and Bet1 and participates in a late stage in endoplasmic reticulum-Golgi transport. *The Journal of biological chemistry* **276**, 27480–7 (2001). URL <http://www.ncbi.nlm.nih.gov/pubmed/11323436>.
- [196] Dascher, C., Matteson, J. & Balch, W. E. Syntaxin 5 regulates endoplasmic reticulum to Golgi transport. *The Journal of biological chemistry* **269**, 29363–6 (1994). URL <http://www.ncbi.nlm.nih.gov/pubmed/7961911>.
- [197] Hay, J. C., Hirling, H. & Scheller, R. H. Mammalian vesicle trafficking proteins of the endoplasmic reticulum and Golgi apparatus. *The Journal of Biological Chemistry* **271**, 5671–5679 (1996).
- [198] Hay, J. C. *et al.* Localization, Dynamics, and Protein Interactions Reveal Distinct Roles for ER and Golgi SNAREs. *The Journal of Cell Biology* **141**, 1489–1502 (1998). URL <http://jcb.rupress.org/content/141/7/1489>.
- [199] Paek, I. *et al.* ERS-24, a Mammalian v-SNARE Implicated in Vesicle Traffic between the ER and the Golgi. *The Journal of Cell Biology* **137**, 1017–1028 (1997). URL <http://jcb.rupress.org/content/137/5/1017>.
- [200] Zhang, T. *et al.* The Mammalian Protein (rbet1) Homologous to Yeast Bet1p Is Primarily Associated with the Pre-Golgi Intermediate Compartment and Is Involved in Vesicular Transport from the Endoplasmic Reticulum to the Golgi Apparatus. *The Journal of Cell Biology* **139**, 1157–1168 (1997). URL <http://jcb.rupress.org/content/139/5/1157>.

- [201] Adolf, F., Rhiel, M., Reckmann, I. & Wieland, F. T. Sec24C/D-isoform–specific sorting of the preassembled ER–Golgi Q-SNARE complex. *Molecular Biology of the Cell* **27**, 2697–2707 (2016). URL <http://www.molbiolcell.org/content/27/17/2697.abstract>.
- [202] Malsam, J. & Söllner, T. H. Organization of SNAREs within the Golgi stack. *Cold Spring Harbor perspectives in biology* **3**, a005249–a005249 (2011). URL <http://www.ncbi.nlm.nih.gov/pubmed/21768609>.
- [203] Burri, L. *et al.* A SNARE required for retrograde transport to the endoplasmic reticulum. *Proceedings of the National Academy of Sciences* **100**, 9873–9877 (2003). URL <https://www.pnas.org/content/100/17/9873>. Publisher: National Academy of Sciences Section: Biological Sciences.
- [204] Xu, Y., Martin, S., James, D. E. & Hong, W. GS15 Forms a SNARE Complex with Syntaxin 5, GS28, and Ykt6 and Is Implicated in Traffic in the Early Cisternae of the Golgi Apparatus. *Molecular Biology of the Cell* **13**, 3493–3507 (2002). URL <https://www.molbiolcell.org/doi/10.1091/mcb.e02-01-0004>.
- [205] Volchuk, A. *et al.* Countercurrent Distribution of Two Distinct SNARE Complexes Mediating Transport within the Golgi Stack. *Molecular Biology of the Cell* **15**, 1506–1518 (2004). URL <https://www.molbiolcell.org/doi/10.1091/mbc.e03-08-0625>.
- [206] Tai, G. *et al.* Participation of the Syntaxin 5/Ykt6/GS28/GS15 SNARE Complex in Transport from the Early/Recycling Endosome to the Trans-Golgi Network. *Molecular Biology of the Cell* **15**, 4011–4022 (2004). URL <https://www.molbiolcell.org/doi/10.1091/mbc.e03-12-0876>.
- [207] Linders, P. *et al.* Congenital disorder of glycosylation caused by starting site-specific variant in syntaxin-5. *medRxiv* 2020.03.30.20044438 (2020). URL <http://medrxiv.org/content/early/2020/03/31/2020.03.30.20044438.abstract>.
- [208] Banfield, D. K., Lewis, M. J. & Pelham, H. R. B. A SNARE-like protein required for traffic through the Golgi complex. *Nature* **375**, 806–809 (1995). URL <https://www.nature.com/articles/375806a0>.
- [209] Parlati, F. *et al.* Topological restriction of SNARE-dependent membrane fusion. *Nature* **407**, 194–198 (2000). URL <https://www.nature.com/articles/35025076>.
- [210] Parlati, F. *et al.* Distinct SNARE complexes mediating membrane fusion in Golgi transport based on combinatorial specificity. *Proceedings of the National Academy of Sciences of the United States of America* **99**, 5424–9 (2002). URL <http://www.ncbi.nlm.nih.gov/pubmed/11959998>.
- [211] Araç, D. *et al.* Three-dimensional Structure of the rSly1 N-terminal Domain Reveals a Conformational Change Induced by Binding to Syntaxin 5. *Journal of Molecular Biology* **346**, 589–601 (2005). URL <http://linkinghub.elsevier.com/retrieve/pii/S0022283604015748>.
- [212] Bracher, A. & Weissenhorn, W. Structural basis for the Golgi membrane recruitment of Sly1p by Sed5p. *The EMBO journal* **21**, 6114–24 (2002). URL <http://www.ncbi.nlm.nih.gov/pubmed/12426383>.
- [213] Peng, R. & Gallwitz, D. Sly1 protein bound to Golgi syntaxin Sed5p allows assembly and contributes to specificity of SNARE fusion complexes. *Journal of Cell Biology* **157**, 645–655 (2002). URL <https://rupress.org/jcb/article/157/4/645/32625/Sly1-protein-bound-to-Golgi-syntaxin-Sed5p-allows>. Publisher: The Rockefeller University Press.
- [214] Yamaguchi, T. *et al.* Sly1 Binds to Golgi and ER Syntaxins via a Conserved N-Terminal Peptide Motif. *Developmental Cell* **2**, 295–305 (2002). URL [https://www.cell.com/developmental-cell/abstract/S1534-5807\(02\)00125-9](https://www.cell.com/developmental-cell/abstract/S1534-5807(02)00125-9). Publisher: Elsevier.

## References

- [215] Hui, N. *et al.* An isoform of the Golgi t-SNARE, syntaxin 5, with an endoplasmic reticulum retrieval signal. *Molecular biology of the cell* **8**, 1777–87 (1997). URL <http://www.ncbi.nlm.nih.gov/pubmed/9307973>.
- [216] Morelli, E. *et al.* Multiple functions of the SNARE protein Snap29 in autophagy, endocytic, and exocytic trafficking during epithelial formation in Drosophila. *Autophagy* **10**, 2251–2268 (2014).
- [217] Hsu, T. *et al.* CEDNIK: Phenotypic and Molecular Characterization of an Additional Patient and Review of the Literature. *Child Neurology Open* (2017). URL <https://journals.sagepub.com/doi/10.1177/2329048X17733214>. Publisher: SAGE PublicationsSage CA: Los Angeles, CA.
- [218] Ilaci, L. *et al.* Compound heterozygous mutations in SNAP29 is associated with Pelizaeus-Merzbacher-like disorder (PMLD). *Human Genetics* **138**, 1409–1417 (2019). URL <https://doi.org/10.1007/s00439-019-02077-7>.
- [219] Poojary, S., Shah, K. S., Bhalala, K. B. & Hegde, A. U. CEDNIK syndrome in an Indian patient with a novel mutation of the SNAP29 gene. *Pediatric Dermatology* **36**, 372–376 (2019). URL <https://onlinelibrary.wiley.com/doi/abs/10.1111/pde.13761>. \_eprint: <https://onlinelibrary.wiley.com/doi/pdf/10.1111/pde.13761>.
- [220] McDonald-McGinn, D. M. *et al.* Hemizygous mutations in SNAP29 unmask autosomal recessive conditions and contribute to atypical findings in patients with 22q11.2DS. *Journal of Medical Genetics* **50**, 80–90 (2013). URL <https://jmg.bmjjournals.org/content/50/2/80>. Publisher: BMJ Publishing Group Ltd Section: Genotype-phenotype correlations.
- [221] Zhang, J.-s. *et al.* [Genetic analysis of genitourinary malformations]. *Zhonghua Yi Xue Zi Zhi = Zhonghua Yixue Yichuanxue Zazhi = Chinese Journal of Medical Genetics* **26**, 134–138 (2009).
- [222] Sprecher, E. *et al.* A Mutation in SNAP29, Coding for a SNARE Protein Involved in Intracellular Trafficking, Causes a Novel Neurocutaneous Syndrome Characterized by Cerebral Dysgenesis, Neuropathy, Ichthyosis, and Palmoplantar Keratoderma. *The American Journal of Human Genetics* **77**, 242–251 (2005). URL <http://www.sciencedirect.com/science/article/pii/S0002929707629140>.
- [223] Fuchs-Telem, D. *et al.* CEDNIK syndrome results from loss-of-function mutations in SNAP29. *British Journal of Dermatology* **164**, 610–616 (2011). URL <https://onlinelibrary.wiley.com/doi/abs/10.1111/j.1365-2133.2010.10133.x>. \_eprint: <https://onlinelibrary.wiley.com/doi/pdf/10.1111/j.1365-2133.2010.10133.x>.
- [224] Praschberger, R. *et al.* Mutations in Membrin/GOSR2 Reveal Stringent Secretory Pathway Demands of Dendritic Growth and Synaptic Integrity. *Cell Reports* **21**, 97–109 (2017). URL <https://www.sciencedirect.com/science/article/pii/S2211124717312652?via%3Dihub>.
- [225] Praschberger, R. *et al.* Expanding the Phenotype and Genetic Defects Associated with the GOSR2 Gene. *Movement Disorders Clinical Practice* **2**, 271–273 (2015). URL <https://onlinelibrary.wiley.com/doi/full/10.1002/mdc3.12190>.
- [226] Corbett, M. *et al.* A Mutation in the Golgi Qb-SNARE Gene GOSR2 Causes Progressive Myoclonus Epilepsy with Early Ataxia. *The American Journal of Human Genetics* **88**, 657–663 (2011). URL <http://www.sciencedirect.com/science/article/pii/S0002929711001522>.
- [227] Bhide, G. P. & Colley, K. J. Sialylation of N-glycans: mechanism, cellular compartmentalization and function. *Histochemistry and Cell Biology* **147**, 149–174 (2017). URL <https://doi.org/10.1007/s00418-016-1520-x>.
- [228] Nilsson, T. *et al.* Kin recognition between medial Golgi enzymes in HeLa cells. *The EMBO journal* **13**, 562–574 (1994).

- [229] Nilsson, T., Rabouille, C., Hui, N., Watson, R. & Warren, G. The role of the membrane-spanning domain and stalk region of N-acetylglucosaminyltransferase I in retention, kin recognition and structural maintenance of the Golgi apparatus in HeLa cells. *Journal of Cell Science* **109** (Pt 7), 1975–1989 (1996).
- [230] Nilsson, T., Slusarewicz, P., Hoe, M. H. & Warren, G. Kin recognition. A model for the retention of Golgi enzymes. *FEBS letters* **330**, 1–4 (1993).
- [231] Chen, C., Ma, J., Lazic, A., Backovic, M. & Colley, K. J. Formation of Insoluble Oligomers Correlates with ST6Gal I Stable Localization in the Golgi. *Journal of Biological Chemistry* **275**, 13819–13826 (2000). URL <http://www.jbc.org/content/275/18/13819>. Publisher: American Society for Biochemistry and Molecular Biology.
- [232] Fenteany, F. H. & Colley, K. J. Multiple Signals Are Required for  $\alpha$ 2,6-Sialyltransferase (ST6Gal I) Oligomerization and Golgi Localization. *Journal of Biological Chemistry* **280**, 5423–5429 (2005). URL <http://www.jbc.org/content/280/7/5423>. Publisher: American Society for Biochemistry and Molecular Biology.
- [233] Opat, A. S., Houghton, F. & Gleeson, P. A. Medial Golgi but Not Late Golgi Glycosyltransferases Exist as High Molecular Weight Complexes ROLE OF LUMINAL DOMAIN IN COMPLEX FORMATION AND LOCALIZATION. *Journal of Biological Chemistry* **275**, 11836–11845 (2000). URL <http://www.jbc.org/content/275/16/11836>. Publisher: American Society for Biochemistry and Molecular Biology.
- [234] Hassinen, A. & Kellokumpu, S. Organizational Interplay of Golgi N-Glycosyltransferases Involves Organelle Microenvironment-Dependent Transitions between Enzyme Homo- and Heteromers. *Journal of Biological Chemistry* **289**, 26937–26948 (2014). URL <http://www.jbc.org/content/289/39/26937.abstract>.
- [235] Kellokumpu, S. Golgi pH, Ion and Redox Homeostasis: How Much Do They Really Matter? *Frontiers in Cell and Developmental Biology* **7** (2019). URL <https://www.frontiersin.org/articles/10.3389/fcell.2019.00093/full#B42>. Publisher: Frontiers.
- [236] Kokkonen, N. *et al.* Defective acidification of intracellular organelles results in aberrant secretion of cathepsin D in cancer cells. *The Journal of Biological Chemistry* **279**, 39982–39988 (2004).
- [237] Caplan, M. J. *et al.* Dependence on pH of polarized sorting of secreted proteins. *Nature* **329**, 632–635 (1987).
- [238] Marklová, E. & Albahri, Z. Screening and diagnosis of congenital disorders of glycosylation. *Clinica Chimica Acta* **385**, 6–20 (2007). URL <http://www.sciencedirect.com/science/article/pii/S0009898107003695>.
- [239] Morava, E. *et al.* Defective protein glycosylation in patients with cutis laxa syndrome. *European Journal of Human Genetics* **13**, 414–421 (2005). URL <https://www.nature.com/articles/5201361>. Number: 4 Publisher: Nature Publishing Group.
- [240] Rajab, A. *et al.* Geroderma osteodysplasticum hereditaria and wrinkly skin syndrome in 22 patients from Oman. *American Journal of Medical Genetics Part A* **146A**, 965–976 (2008). URL <https://onlinelibrary.wiley.com/doi/abs/10.1002/ajmg.a.32143>. \_eprint: <https://onlinelibrary.wiley.com/doi/pdf/10.1002/ajmg.a.32143>.
- [241] Rymen, D. *et al.* Key features and clinical variability of COG6-CDG. *Molecular Genetics and Metabolism* **116**, 163–170 (2015).
- [242] Paroutis, P., Touret, N. & Grinstein, S. The pH of the Secretory Pathway: Measurement, Determinants, and Regulation. *Physiology* **19** (2004).
- [243] Schapiro, F. B. & Grinstein, S. Determinants of the pH of the Golgi complex. *The Journal of biological chemistry* **275**, 21025–32 (2000). URL <http://www.ncbi.nlm.nih.gov/pubmed/10748071>.

## References

- [244] Vavassori, S. *et al.* A pH-Regulated Quality Control Cycle for Surveillance of Secretory Protein Assembly. *Molecular Cell* **50**, 783–792 (2013). URL [https://www.cell.com/molecular-cell/abstract/S1097-2765\(13\)00297-9](https://www.cell.com/molecular-cell/abstract/S1097-2765(13)00297-9). Publisher: Elsevier.
- [245] Sannino, S. *et al.* Progressive quality control of secretory proteins in the early secretory compartment by ERp44. *Journal of Cell Science* **127**, 4260–4269 (2014). URL <https://jcs.biologists.org/content/127/19/4260>. Publisher: The Company of Biologists Ltd Section: Research Article.
- [246] Watanabe, S., Harayama, M., Kanemura, S., Sitia, R. & Inaba, K. Structural basis of pH-dependent client binding by ERp44, a key regulator of protein secretion at the ER–Golgi interface. *Proceedings of the National Academy of Sciences* **114**, E3224–E3232 (2017). URL <https://www.pnas.org/content/114/16/E3224>. ISBN: 9781621426110 Publisher: National Academy of Sciences Section: PNAS Plus.
- [247] Shibuya, A., Margulis, N., Christiano, R., Walther, T. C. & Barlowe, C. The Erv41–Erv46 complex serves as a retrograde receptor to retrieve escaped ER proteins. *Journal of Cell Biology* **208**, 197–209 (2015). URL <https://doi.org/10.1083/jcb.201408024>.
- [248] Hassinen, A. *et al.* Functional Organization of Golgi N- and O-Glycosylation Pathways Involves pH-dependent Complex Formation That Is Impaired in Cancer Cells. *Journal of Biological Chemistry* **286**, 38329–38340 (2011). URL <http://www.jbc.org/content/286/44/38329.abstract>.
- [249] Johnson, D. E., Ostrowski, P., Jaumouillé, V. & Grinstein, S. The position of lysosomes within the cell determines their luminal pH. *The Journal of Cell Biology* **212**, 677 LP–692 (2016). URL <http://jcb.rupress.org/content/212/6/677.abstract>.
- [250] D'Amore, C. *et al.* Synthesis and Biological Characterization of a New Norbornide Derived Bodipy FL-Conjugated Fluorescent Probe for Cell Imaging. *Frontiers in Pharmacology* **9** (2018). URL <https://www.frontiersin.org/articles/10.3389/fphar.2018.01055/full>. Publisher: Frontiers.
- [251] Overly, C. C., Lee, K. D., Berthiaume, E. & Hollenbeck, P. J. Quantitative measurement of intraorganelle pH in the endosomal-lysosomal pathway in neurons by using ratiometric imaging with pyranine. *Proceedings of the National Academy of Sciences* **92**, 3156–3160 (1995). URL <https://www.pnas.org/content/92/8/3156>. Publisher: National Academy of Sciences Section: Research Article.
- [252] Liu, H. *et al.* Real-time monitoring of newly acidified organelles during autophagy enabled by reaction-based BODIPY dyes. *Communications Biology* **2**, 1–11 (2019). URL <https://www.nature.com/articles/s42003-019-0682-1>. Number: 1 Publisher: Nature Publishing Group.
- [253] Ma, L., Ouyang, Q., Werthmann, G. C., Thompson, H. M. & Morrow, E. M. Live-cell Microscopy and Fluorescence-based Measurement of Luminal pH in Intracellular Organelles. *Frontiers in Cell and Developmental Biology* **5**, 71–71 (2017). URL <https://www.frontiersin.org/article/10.3389/fcell.2017.00071>.
- [254] Kim, J. H. *et al.* Dynamic measurement of the pH of the Golgi complex in living cells using retrograde transport of the verotoxin receptor. *Journal of Cell Biology* **134**, 1387–1399 (1996). URL <https://doi.org/10.1083/jcb.134.6.1387>.
- [255] Kim, J. H. *et al.* Noninvasive measurement of the pH of the endoplasmic reticulum at rest and during calcium release. *Proceedings of the National Academy of Sciences* **95**, 2997–3002 (1998). URL <https://www.pnas.org/content/95/6/2997>. Publisher: National Academy of Sciences Section: Biological Sciences.
- [256] Wu, M. M. *et al.* Organelle pH studies using targeted avidin and fluorescein–biotin. *Chemistry & Biology* **7**, 197–209 (2000). URL [https://www.cell.com/cell-chemical-biology/abstract/S1074-5521\(00\)00088-0](https://www.cell.com/cell-chemical-biology/abstract/S1074-5521(00)00088-0). Publisher: Elsevier.

- [257] Miesenböck, G., De Angelis, D. A. & Rothman, J. E. Visualizing secretion and synaptic transmission with pH-sensitive green fluorescent proteins. *Nature* **394**, 192–5 (1998). URL <http://www.ncbi.nlm.nih.gov/pubmed/9671304>.
- [258] Mahon, M. J. pHluorin2: an enhanced, ratiometric, pH-sensitive green fluorescent protein. *Advances in Bioscience and Biotechnology* **2**, 132–137 (2011). URL <http://www.scirp.org/journal/abb/>.
- [259] Ward, W. W., Prentice, H. J., Roth, A. F., Cody, C. W. & Reeves, S. C. Spectral Perturbations of the Ae-quorea Green-Fluorescent Protein. *Photochemistry and Photobiology* **35**, 803–808 (1982). URL <https://onlinelibrary.wiley.com/doi/abs/10.1111/j.1751-1097.1982.tb02651.x>. \_eprint: <https://onlinelibrary.wiley.com/doi/pdf/10.1111/j.1751-1097.1982.tb02651.x>.
- [260] Wallrabe, H. & Periasamy, A. Imaging protein molecules using FRET and FLIM microscopy. *Current Opinion in Biotechnology* **16**, 19–27 (2005). URL <https://www.sciencedirect.com/science/article/pii/S0958166904001673>.
- [261] Jares-Erijman, E. A. & Jovin, T. M. FRET imaging. *Nature Biotechnology* **21**, 1387–1395 (2003). URL <https://www.nature.com/articles/nbt896>. Number: 11 Publisher: Nature Publishing Group.
- [262] Schmitt, F.-J. *et al.* eGFP-pHSens as a highly sensitive fluorophore for cellular pH determination by fluorescence lifetime imaging microscopy (FLIM). *Biochimica et Biophysica Acta (BBA) - Bioenergetics* **1837**, 1581–1593 (2014). URL <http://www.sciencedirect.com/science/article/pii/S0005272814001108>.
- [263] Lin, H.-J., Herman, P. & Lakowicz, J. R. Fluorescence lifetime-resolved pH imaging of living cells. *Cytometry Part A* **52A**, 77–89 (2003). URL <https://onlinelibrary.wiley.com/doi/abs/10.1002/cyto.a.10028>. \_eprint: <https://onlinelibrary.wiley.com/doi/pdf/10.1002/cyto.a.10028>.
- [264] Welch, L. G. & Munro, S. A tale of short tails, through thick and thin: investigating the sorting mechanisms of Golgi enzymes. *FEBS letters* **593**, 2452–2465 (2019).
- [265] Tie, H. C. *et al.* A novel imaging method for quantitative Golgi localization reveals differential intra-Golgi trafficking of secretory cargoes. *Molecular Biology of the Cell* **27**, 848–861 (2016). URL <http://www.molbiolcell.org/content/27/5/848.abstract>.
- [266] Boncompain, G. *et al.* Synchronization of secretory protein traffic in populations of cells. *Nature Methods* **9**, 493–493 (2012). URL <http://dx.doi.org/10.1038/nmeth.1928>.
- [267] Klausner, R. D., Donaldson, J. G. & Lippincott-Schwartz, J. Brefeldin A: insights into the control of membrane traffic and organelle structure. *Journal of Cell Biology* **116**, 1071–1080 (1992). URL <https://rupress.org/jcb/article/116/5/1071/14325/Brefeldin-A-insights-into-the-control-of-membrane>. Publisher: The Rockefeller University Press.
- [268] Verboogen, D. R. J., González Mancha, N., ter Beest, M. & van den Bogaart, G. Fluorescence Lifetime Imaging Microscopy reveals rerouting of SNARE trafficking driving dendritic cell activation. *eLife* **6** (2017). URL <https://elifesciences.org/articles/23525>.
- [269] Eisenberg-Lerner, A. *et al.* Golgi organization is regulated by proteasomal degradation. *Nature Communications* **11**, 409 (2020). URL <https://www.nature.com/articles/s41467-019-14038-9>. Number: 1 Publisher: Nature Publishing Group.
- [270] Baumann, J. *et al.* Golgi stress-induced transcriptional changes mediated by MAPK signaling and three ETS transcription factors regulate MCL1 splicing. *Molecular Biology of the Cell* **29**, 42–52 (2018). URL <https://www.molbiolcell.org/doi/10.1091/mbc.E17-06-0418>. Publisher: American Society for Cell Biology (mbc).
- [271] Oku, M. *et al.* Novel Cis-acting Element GASE Regulates Transcriptional Induction by the Golgi Stress Response. *Cell Structure and Function* **36**, 1–12 (2011).

## References

- [272] Taniguchi, M. *et al.* TFE3 Is a bHLH-ZIP-type Transcription Factor that Regulates the Mammalian Golgi Stress Response. *Cell Structure and Function* **40**, 13–30 (2015).
- [273] Reiling, J. H. *et al.* A CREB3–ARF4 signalling pathway mediates the response to Golgi stress and susceptibility to pathogens. *Nature Cell Biology* **15**, 1473–1485 (2013). URL <https://www.nature.com/articles/ncb2865>. Number: 12 Publisher: Nature Publishing Group.
- [274] Shiodio, J. I., Snyder, S. H. & Paul, B. D. Golgi stress response reprograms cysteine metabolism to confer cytoprotection in Huntington's disease. *Proceedings of the National Academy of Sciences* **115**, 780–785 (2018). URL <https://www.pnas.org/content/115/4/780>. Publisher: National Academy of Sciences Section: Biological Sciences.
- [275] Taniguchi, M. *et al.* MLX Is a Transcriptional Repressor of the Mammalian Golgi Stress Response. *Cell Structure and Function* **41**, 93–104 (2016).
- [276] Stransky, L., Cotter, K. & Forgac, M. The Function of V-ATPases in Cancer. *Physiological Reviews* **96**, 1071–1091 (2016). URL <https://doi.org/10.1152/physrev.00035.2015>.
- [277] Wolfe, D. M. *et al.* Autophagy failure in Alzheimer's disease and the role of defective lysosomal acidification. *European Journal of Neuroscience* **37**, 1949–1961 (2013). URL <https://onlinelibrary.wiley.com/doi/abs/10.1111/ejn.12169>. \_eprint: <https://onlinelibrary.wiley.com/doi/pdf/10.1111/ejn.12169>.
- [278] Koh, J.-Y., Kim, H. N., Hwang, J. J., Kim, Y.-H. & Park, S. E. Lysosomal dysfunction in proteinopathic neurodegenerative disorders: possible therapeutic roles of cAMP and zinc. *Molecular Brain* **12**, 18 (2019). URL <https://doi.org/10.1186/s13041-019-0439-2>.
- [279] Dehay, B. *et al.* Loss of P-type ATPase ATP13A2/PARK9 function induces general lysosomal deficiency and leads to Parkinson disease neurodegeneration. *Proceedings of the National Academy of Sciences* **109**, 9611–9616 (2012). URL <https://www.pnas.org/content/109/24/9611>. Publisher: National Academy of Sciences Section: Biological Sciences.
- [280] Jinn, S. *et al.* TMEM175 deficiency impairs lysosomal and mitochondrial function and increases synuclein aggregation. *Proceedings of the National Academy of Sciences* **114**, 2389–2394 (2017). URL <https://www.pnas.org/content/114/9/2389>. Publisher: National Academy of Sciences Section: Biological Sciences.
- [281] Fernandez-Mosquera, L. *et al.* Mitochondrial respiratory chain deficiency inhibits lysosomal hydrolysis. *Autophagy* **15**, 1572–1591 (2019). URL <https://doi.org/10.1080/15548627.2019.1586256>. Publisher: Taylor & Francis \_eprint: <https://doi.org/10.1080/15548627.2019.1586256>.
- [282] Bagh, M. B. *et al.* Misrouting of v-ATPase subunit V0a1 dysregulates lysosomal acidification in a neurodegenerative lysosomal storage disease model. *Nature Communications* **8**, 14612 (2017). URL <https://www.nature.com/articles/ncomms14612>. Number: 1 Publisher: Nature Publishing Group.
- [283] Falcón-Pérez, J. M., Nazarian, R., Sabatti, C. & Dell'Angelica, E. C. Distribution and dynamics of Lamp1-containing endocytic organelles in fibroblasts deficient in BLOC-3. *Journal of Cell Science* **118**, 5243–5255 (2005). URL <https://jcs.biologists.org/content/118/22/5243>. Publisher: The Company of Biologists Ltd Section: Research Article.
- [284] Warren, S. C. *et al.* Rapid Global Fitting of Large Fluorescence Lifetime Imaging Microscopy Datasets. *PLOS ONE* **8**, e70687 (2013). URL <https://journals.plos.org/plosone/article?id=10.1371/journal.pone.0070687>. Publisher: Public Library of Science.
- [285] Ritz, C., Baty, F., Streibig, J. C. & Gerhard, D. Dose-Response Analysis Using R. *PLOS ONE* **10**, e0146021 (2015). URL <https://journals.plos.org/plosone/article?id=10.1371/journal.pone.0146021>. Publisher: Public Library of Science.

- [286] Wickham, H. *ggplot2: Elegant Graphics for Data Analysis* (Springer-Verlag New York, 2016). URL <https://ggplot2.tidyverse.org>.
- [287] Chiu, C.-F. *et al.* ZFPL1, a novel ring finger protein required for cis-Golgi integrity and efficient ER-to-Golgi transport. *The EMBO journal* **27**, 934–47 (2008). URL <http://www.ncbi.nlm.nih.gov/pubmed/18323775>.
- [288] Linders, P., ter Beest, M. & van den Bogaart, G. Fluorescence lifetime imaging of pH along the secretory pathway. *bioRxiv* 2021.03.29.437519 (2021). URL <http://biorxiv.org/content/early/2021/03/29/2021.03.29.437519.abstract>.
- [289] Huss, M. & Wieczorek, H. Inhibitors of V-ATPases: old and new players. *Journal of Experimental Biology* **212**, 341 LP–346 (2009). URL <http://jeb.biologists.org/content/212/3/341.abstract>.
- [290] Ramachandran, N. *et al.* VMA21 deficiency prevents vacuolar ATPase assembly and causes autophagic vacuolar myopathy. *Acta Neuropathologica* **125**, 439–457 (2013). URL <http://link.springer.com/10.1007/s00401-012-1073-6>.
- [291] Maeda, Y., Ide, T., Koike, M., Uchiyama, Y. & Kinoshita, T. GPHR is a novel anion channel critical for acidification and functions of the Golgi apparatus. *Nature Cell Biology* **10**, 1135–1145 (2008). URL <https://www.nature.com/articles/ncb1773>.
- [292] Slaymaker, I. M. *et al.* Rationally engineered Cas9 nucleases with improved specificity. *Science* **351**, 84–88 (2016). URL <https://science.sciencemag.org/content/351/6268/84>. Publisher: American Association for the Advancement of Science Section: Report.
- [293] Putthenveedu, M. A. & Linstedt, A. D. Subcompartmentalizing the Golgi apparatus. *Current Opinion in Cell Biology* **17**, 369–375 (2005). URL <http://www.sciencedirect.com/science/article/pii/S0955067405000785>.
- [294] Barlowe, C. *et al.* COPII: A membrane coat formed by Sec proteins that drive vesicle budding from the endoplasmic reticulum. *Cell* **77**, 895–907 (1994). URL <http://www.sciencedirect.com/science/article/pii/0092867494901384>.
- [295] Bentley, M. *et al.* SNARE status regulates tether recruitment and function in homotypic COPII vesicle fusion. *The Journal of biological chemistry* **281**, 38825–33 (2006). URL <http://www.ncbi.nlm.nih.gov/pubmed/17038314>.
- [296] Newman, A. P., Shim, J. & Ferro-Novick, S. BET1, BOS1, and SEC22 are members of a group of interacting yeast genes required for transport from the endoplasmic reticulum to the Golgi complex. *Molecular and Cellular Biology* **10**, 3405–3414 (1990). URL <https://mcb.asm.org/content/10/7/3405>. Publisher: American Society for Microbiology Journals Section: Research Article.
- [297] Sacher, M., Stone, S. & Ferro-Novick, S. The Synaptobrevin-related Domains of Bos1p and Sec22p Bind to the Syntaxin-like Region of Sed5p \*. *Journal of Biological Chemistry* **272**, 17134–17138 (1997). URL [https://www.jbc.org/article/S0021-9258\(18\)39341-4/abstract](https://www.jbc.org/article/S0021-9258(18)39341-4/abstract). Publisher: Elsevier.
- [298] Dilcher, M. *et al.* Use1p is a yeast SNARE protein required for retrograde traffic to the ER. *The EMBO Journal* **22**, 3664–3674 (2003). URL <https://www.embopress.org/doi/full/10.1093/emboj/cdg339>. Publisher: John Wiley & Sons, Ltd.
- [299] Satoh, T., Nakamura, Y. & Satoh, A. K. The roles of Syx5 in Golgi morphology and Rhodopsin transport in Drosophila photoreceptors. *Biology Open* **5**, 1420–1430 (2016). URL <https://bio.biologists.org/content/5/10/1420>. Publisher: The Company of Biologists Ltd Section: Research Article.

## References

- [300] Suga, K., Hattori, H., Saito, A. & Akagawa, K. RNA interference-mediated silencing of the syntaxin 5 gene induces Golgi fragmentation but capable of transporting vesicles. *FEBS Letters* **579**, 4226–4234 (2005). URL <https://febs.onlinelibrary.wiley.com/doi/abs/10.1016/j.febslet.2005.06.053>.
- [301] Amessou, M. *et al.* Syntaxin 16 and syntaxin 5 are required for efficient retrograde transport of several exogenous and endogenous cargo proteins. *Journal of Cell Science* **120**, 1457–1468 (2007). URL <http://jcs.biologists.org/content/120/8/1457>.
- [302] Zhao, X. *et al.* Sec22 Regulates Endoplasmic Reticulum Morphology but Not Autophagy and Is Required for Eye Development in Drosophila. *Journal of Biological Chemistry* **290**, 7943–7951 (2015). URL [https://www.jbc.org/article/S0021-9258\(20\)64901-8/abstract](https://www.jbc.org/article/S0021-9258(20)64901-8/abstract). Publisher: Elsevier.
- [303] Renna, M. *et al.* Autophagic substrate clearance requires activity of the syntaxin-5 SNARE complex. *Journal of Cell Science* **124**, 469–482 (2011). URL <https://jcs.biologists.org/content/124/3/469>. Publisher: The Company of Biologists Ltd Section: Research Article.
- [304] Van Zyl, J. H. D., Den Haan, R. & Van Zyl, W. H. Overexpression of native *Saccharomyces cerevisiae* ER-to-Golgi SNARE genes increased heterologous cellulase secretion. *Applied Microbiology and Biotechnology* **100**, 505–518 (2016). URL <https://doi.org/10.1007/s00253-015-7022-2>.
- [305] Blomen, V. A. *et al.* Gene essentiality and synthetic lethality in haploid human cells. *Science* **350**, 1092–1096 (2015). URL <https://science/sciencemag.org/content/350/6264/1092>. Publisher: American Association for the Advancement of Science Section: Report.
- [306] Winzeler, E. A. *et al.* Functional Characterization of the *S. cerevisiae* Genome by Gene Deletion and Parallel Analysis. *Science* **285**, 901–906 (1999). URL <https://science.scienmag.org/content/285/5429/901>. Publisher: American Association for the Advancement of Science Section: Report.
- [307] Koscielny, G. *et al.* The International Mouse Phenotyping Consortium Web Portal, a unified point of access for knockout mice and related phenotyping data. *Nucleic Acids Research* **42**, D802–D809 (2014). URL <https://academic.oup.com/nar/article/42/D1/D802/1069801>.
- [308] Xu, H. *et al.* Syntaxin 5 Is Required for Cytokinesis and Spermatid Differentiation in Drosophila. *Developmental Biology* **251**, 294–306 (2002). URL <https://linkinghub.elsevier.com/retrieve/pii/S0012160602908304>.
- [309] Furukawa, N. & Mima, J. Multiple and distinct strategies of yeast SNAREs to confer the specificity of membrane fusion. *Scientific Reports* **4**, 4277 (2014). URL <https://www.nature.com/articles/srep04277>. Number: 1 Publisher: Nature Publishing Group.
- [310] Tsui, M. M., Tai, W. C. & Banfield, D. K. Selective Formation of Sed5p-containing SNARE Complexes Is Mediated by Combinatorial Binding Interactions. *Molecular Biology of the Cell* **12**, 521–538 (2001). URL <https://www.molbiolcell.org/doi/10.1091/mbc.12.3.521>. Publisher: American Society for Cell Biology (mbo).
- [311] Cosson, P. *et al.* Dynamic transport of SNARE proteins in the Golgi apparatus. *Proceedings of the National Academy of Sciences of the United States of America* **102**, 14647–52 (2005). URL <http://www.ncbi.nlm.nih.gov/pubmed/16199514>.
- [312] Nogueira, C. *et al.* SLY1 and Syntaxin 18 specify a distinct pathway for procollagen VII export from the endoplasmic reticulum. *eLife* **3** (2014). URL <https://elifesciences.org/articles/02784>.
- [313] Siddiqi, S. VLDL exits from the endoplasmic reticulum in a specialized vesicle, the VLDL transport vesicle, in rat primary hepatocytes. *Biochemical Journal* **413**, 333–342 (2008). URL <https://doi.org/10.1042/BJ20071469>.

- [314] Siddiqi, S., Mani, A. & Siddiqi, S. The identification of the SNARE complex required for the fusion of VLDL-transport vesicle with hepatic cis-Golgi. *Biochemical Journal* **429**, 391–401 (2010). URL <https://doi.org/10.1042/BJ20100336>.
- [315] Wagner, T., Dieckmann, M., Jaeger, S., Weggen, S. & Pietrzik, C. U. Stx5 is a novel interactor of VLDL-R to affect its intracellular trafficking and processing. *Experimental Cell Research* **319**, 1956–1972 (2013). URL <https://www.sciencedirect.com/science/article/pii/S0014482713002164>.
- [316] Siddiqi, S. A. *et al.* The Identification of a Novel Endoplasmic Reticulum to Golgi SNARE Complex Used by the Prechylomicron Transport Vesicle \*. *Journal of Biological Chemistry* **281**, 20974–20982 (2006). URL [https://www.jbc.org/article/S0021-9258\(18\)95226-9/abstract](https://www.jbc.org/article/S0021-9258(18)95226-9/abstract). Publisher: Elsevier.
- [317] Norlin, S., Parekh, V. S., Naredi, P. & Edlund, H. AsnA1/TRC40 Controls β-Cell Function and Endoplasmic Reticulum Homeostasis by Ensuring Retrograde Transport. *Diabetes* **65**, 110–119 (2016). URL <https://diabetes.diabetesjournals.org/content/65/1/110>. Publisher: American Diabetes Association Section: Islet Studies.
- [318] Schuldiner, M. *et al.* The GET Complex Mediates Insertion of Tail-Anchored Proteins into the ER Membrane. *Cell* **134**, 634–645 (2008). URL [https://www.cell.com/cell/abstract/S0092-8674\(08\)00777-0](https://www.cell.com/cell/abstract/S0092-8674(08)00777-0). Publisher: Elsevier.
- [319] Chen, L., Lau, M. S. Y. & Banfield, D. K. Multiple ER–Golgi SNARE transmembrane domains are dispensable for trafficking but required for SNARE recycling. *Molecular Biology of the Cell* **27**, 2633–2641 (2016). URL <http://www.molbiolcell.org/doi/10.1091/mbc.e16-05-0277>.
- [320] Sharpe, H. J., Stevens, T. J. & Munro, S. A Comprehensive Comparison of Transmembrane Domains Reveals Organelle-Specific Properties. *Cell* **142**, 158–169 (2010). URL <http://www.sciencedirect.com/science/article/pii/S0092867410006124>.
- [321] Watson, R. T. & Pessin, J. E. Transmembrane domain length determines intracellular membrane compartment localization of syntaxins 3, 4, and 5. *American Journal of Physiology-Cell Physiology* **281**, C215–C223 (2001). URL <https://www.physiology.org/doi/full/10.1152/ajpcell.2001.281.1.C215>.
- [322] Banfield, D. K., Lewis, M. J., Rabouille, C., Warren, G. & Pelham, H. R. Localization of Sed5, a putative vesicle targeting molecule, to the cis-Golgi network involves both its transmembrane and cytoplasmic domains. *Journal of Cell Biology* **127**, 357–371 (1994). URL <https://doi.org/10.1083/jcb.127.2.357>.
- [323] Kasai, K. & Akagawa, K. Roles of the cytoplasmic and transmembrane domains of syntaxins in intracellular localization and trafficking. *Journal of Cell Science* **114**, 3115–3124 (2001). URL <https://jcs.biologists.org/content/114/17/3115>. Publisher: The Company of Biologists Ltd Section: Research Article.
- [324] Suga, K., Saito, A., Tomiyama, T., Mori, H. & Akagawa, K. The Syntaxin 5 Isoforms Syx5 and Syx5L have Distinct Effects on the Processing of β-amyloid Precursor Protein. *The Journal of Biochemistry* **146**, 905–915 (2009). URL <http://dx.doi.org/10.1093/jb/mvp138>.
- [325] Mancias, J. D. & Goldberg, J. Structural basis of cargo membrane protein discrimination by the human COPII coat machinery. *The EMBO journal* **27**, 2918–28 (2008). URL <http://www.ncbi.nlm.nih.gov/pubmed/18843296>.
- [326] Geng, L. *et al.* Syntaxin 5 regulates the endoplasmic reticulum channel-release properties of polycystin-2. *Proceedings of the National Academy of Sciences of the United States of America* **105**, 15920–5 (2008). URL <http://www.ncbi.nlm.nih.gov/pubmed/18836075>.

## References

- [327] Lowe, M. Caspase-mediated cleavage of syntaxin 5 and giantin accompanies inhibition of secretory traffic during apoptosis. *Journal of Cell Science* **117**, 1139–1150 (2004). URL <http://jcs.biologists.org/cgi/doi/10.1242/jcs.00950>.
- [328] Huang, S., Tang, D. & Wang, Y. Monoubiquitination of Syntaxin 5 Regulates Golgi Membrane Dynamics during the Cell Cycle. *Developmental Cell* **38**, 73–85 (2016).
- [329] Weinberger, A., Kamena, F., Kama, R., Spang, A. & Gerst, J. E. Control of Golgi Morphology and Function by Sed5 t-SNARE Phosphorylation. *Molecular Biology of the Cell* **16**, 4918–4930 (2005). URL <https://www.molbiolcell.org/doi/10.1091/mbc.e05-02-0101>.
- [330] Dominguez, M. *et al.* gp25L/emp24/p24 protein family members of the cis-Golgi network bind both COP I and II coatomer. *The Journal of cell biology* **140**, 751–65 (1998). URL <http://www.ncbi.nlm.nih.gov/pubmed/9472029>.
- [331] Cho, J.-H., Noda, Y. & Yoda, K. Proteins in the early Golgi compartment of *Saccharomyces cerevisiae* immunoisolated by Sed5p. *FEBS Letters* **469**, 151–154 (2000). URL <https://febs.onlinelibrary.wiley.com/doi/abs/10.1016/S0014-5793%2800%2901268-0>. eprint: <https://febs.onlinelibrary.wiley.com/doi/pdf/10.1016/S0014-5793%2800%2901268-0>.
- [332] Miyazaki, K. *et al.* Contribution of the long form of syntaxin 5 to the organization of the endoplasmic reticulum. *Journal of Cell Science* **125**, 5658 LP–5666 (2012). URL <http://jcs.biologists.org/content/125/23/5658.abstract>.
- [333] Avci, D. *et al.* The intramembrane protease SPP impacts morphology of the endoplasmic reticulum by triggering degradation of morphogenic proteins. *Journal of Biological Chemistry* **294**, 2786–2800 (2019). URL <http://www.jbc.org/lookup/doi/10.1074/jbc.RA118.005642>.
- [334] Peng, R., Grabowski, R., Antoni, A. D. & Gallwitz, D. Specific interaction of the yeast cis-Golgi syntaxin Sed5p and the coat protein complex II component Sec24p of endoplasmic reticulum-derived transport vesicles. *Proceedings of the National Academy of Sciences* **96**, 3751–3756 (1999). URL <https://www.pnas.org/content/96/7/3751>. Publisher: National Academy of Sciences Section: Biological Sciences.
- [335] Mossessova, E., Bickford, L. C. & Goldberg, J. SNARE Selectivity of the COPII Coat. *Cell* **114**, 483–495 (2003). URL <http://www.sciencedirect.com/science/article/pii/S0092867403006081>.
- [336] Uchiyama, K. & Kondo, H. p97/p47-Mediated Biogenesis of Golgi and ER. *The Journal of Biochemistry* **137**, 115–119 (2005). URL <https://doi.org/10.1093/jb/mvi028>.
- [337] Rabouille, C. *et al.* Syntaxin 5 Is a Common Component of the NSF- and p97-Mediated Reassembly Pathways of Golgi Cisternae from Mitotic Golgi Fragments In Vitro. *Cell* **92**, 603–610 (1998). URL [https://www.cell.com/cell/abstract/S0092-8674\(00\)81128-9](https://www.cell.com/cell/abstract/S0092-8674(00)81128-9). Publisher: Elsevier.
- [338] Carr, C. M. & Rizo, J. At the junction of SNARE and SM protein function. *Current Opinion in Cell Biology* **22**, 488–495 (2010). URL <https://www.sciencedirect.com/science/article/pii/S095506741000058X>.
- [339] Li, Y., Gallwitz, D. & Peng, R. Structure-based Functional Analysis Reveals a Role for the SM Protein Sly1p in Retrograde Transport to the Endoplasmic Reticulum. *Molecular Biology of the Cell* **16**, 3951–3962 (2005). URL <https://www.molbiolcell.org/doi/10.1091/mbc.e05-02-0114>. Publisher: American Society for Cell Biology (mbo).
- [340] Dascher, C. & Balch, W. E. Mammalian Sly1 regulates syntaxin 5 function in endoplasmic reticulum to Golgi transport. *The Journal of biological chemistry* **271**, 15866–9 (1996). URL <http://www.ncbi.nlm.nih.gov/pubmed/8663406>.

- [341] Laufman, O., Kedan, A., Hong, W. & Lev, S. Direct interaction between the COG complex and the SM protein, Sly1, is required for Golgi SNARE pairing. *The EMBO journal* **28**, 2006–17 (2009). URL <http://www.ncbi.nlm.nih.gov/pubmed/19536132>.
- [342] Hou, N., Yang, Y., Scott, I. C. & Lou, X. The Sec domain protein Scfd1 facilitates trafficking of ECM components during chondrogenesis. *Developmental Biology* **421**, 8–15 (2017). URL <https://www.sciencedirect.com/science/article/pii/S001216061630272X>.
- [343] Peng, R. & Gallwitz, D. Multiple SNARE interactions of an SM protein: Sed5p/Sly1p binding is dispensable for transport. *The EMBO Journal* **23**, 3939–3949 (2004). URL <https://www.embopress.org/doi/full/10.1038/sj.emboj.7600410>. Publisher: John Wiley & Sons, Ltd.
- [344] Demircioglu, F. E., Burkhardt, P. & Fasshauer, D. The SM protein Sly1 accelerates assembly of the ER-Golgi SNARE complex. *Proceedings of the National Academy of Sciences* **111**, 13828–13833 (2014). URL <http://www.ncbi.nlm.nih.gov/pubmed/25189771>.
- [345] Kosodo, Y., Noda, Y., Adachi, H. & Yoda, K. Binding of Sly1 to Sed5 enhances formation of the yeast early Golgi SNARE complex. *Journal of Cell Science* **115**, 3683–3691 (2002). URL <https://jcs.biologists.org/content/115/18/3683>. Publisher: The Company of Biologists Ltd Section: Research Article.
- [346] Williams, A. L., Ehm, S., Jacobson, N. C., Xu, D. & Hay, J. C. rsly1 Binding to Syntaxin 5 Is Required for Endoplasmic Reticulum-to-Golgi Transport but Does Not Promote SNARE Motif Accessibility. *Molecular Biology of the Cell* **15**, 162–175 (2003). URL <https://www.molbiolcell.org/doi/10.1091/mbc.e03-07-0535>.
- [347] Lobingier, B. T., Nickerson, D. P., Lo, S.-Y. & Merz, A. J. SM proteins Sly1 and Vps33 co-assemble with Sec17 and SNARE complexes to oppose SNARE disassembly by Sec18. *eLife* **3**, e02272 (2014). URL <https://doi.org/10.7554/eLife.02272>. Publisher: eLife Sciences Publications, Ltd.
- [348] Braun, S. & Jentsch, S. SM-protein-controlled ER-associated degradation discriminates between different SNAREs. *EMBO reports* **8**, 1176–1182 (2007). URL <https://www.embopress.org/doi/full/10.1038/sj.embor.7401105>. Publisher: John Wiley & Sons, Ltd.
- [349] Joglekar, A. P. & Hay, J. C. Evidence for regulation of ER/Golgi SNARE complex formation by hsc70 chaperones. *European Journal of Cell Biology* **84**, 529–542 (2005). URL <https://www.sciencedirect.com/science/article/pii/S0171933505000208>.
- [350] Wang, T., Grabski, R., Sztul, E. & Hay, J. C. p115–SNARE Interactions: A Dynamic Cycle of p115 Binding Monomeric SNARE Motifs and Releasing Assembled Bundles. *Traffic* **16**, 148–171 (2015). URL <https://onlinelibrary.wiley.com/doi/abs/10.1111/tra.12242>. \_eprint: <https://onlinelibrary.wiley.com/doi/pdf/10.1111/tra.12242>.
- [351] Willett, R., Ungar, D. & Lupashin, V. The Golgi puppet master: COG complex at center stage of membrane trafficking interactions. *Histochemistry and Cell Biology* **140**, 271–283 (2013). URL <https://doi.org/10.1007/s00418-013-1117-6>.
- [352] Laufman, O., Freeze, H. H., Hong, W. & Lev, S. Deficiency of the Cog8 Subunit in Normal and CDG-Derived Cells Impairs the Assembly of the COG and Golgi SNARE Complexes. *Traffic* **14**, 1065–1077 (2013). URL <https://onlinelibrary.wiley.com/doi/abs/10.1111/tra.12093>. \_eprint: <https://onlinelibrary.wiley.com/doi/pdf/10.1111/tra.12093>.
- [353] Laufman, O., Hong, W. & Lev, S. The COG complex interacts with multiple Golgi SNAREs and enhances fusogenic assembly of SNARE complexes. *Journal of Cell Science* **126**, 1506–1516 (2013). URL <https://jcs.biologists.org/content/126/6/1506>.
- [354] Suvorova, E. S., Duden, R. & Lupashin, V. V. The Sec34/Sec35p complex, a Ypt1p effector required for retrograde intra-Golgi trafficking, interacts with Golgi SNAREs and COPI vesicle coat proteins. *Journal of Cell*

## References

- Biology* **157**, 631–643 (2002). URL <https://rupress.org/jcb/article/157/4/631/32620/The-Sec34-Sec35p-complex-a-Ypt1p-effector-required>. Publisher: The Rockefeller University Press.
- [355] Shorter, J., Beard, M. B., Seemann, J., Dirac-Svejstrup, A. B. & Warren, G. Sequential tethering of Golgins and catalysis of SNAREpin assembly by the vesicle-tethering protein p115. *Journal of Cell Biology* **157**, 45–62 (2002). URL <https://doi.org/10.1083/jcb.200112127>.
- [356] Yuan, H., Davis, S., Ferro-Novick, S. & Novick, P. Rewiring a Rab regulatory network reveals a possible inhibitory role for the vesicle tether, Uso1. *Proceedings of the National Academy of Sciences* **114**, E8637–E8645 (2017). URL <https://www.pnas.org/content/114/41/E8637>. Publisher: National Academy of Sciences Section: PNAS Plus.
- [357] Nelson, D. S. *et al.* The Membrane Transport Factor TAP/p115 Cycles between the Golgi and Earlier Secretory Compartments and Contains Distinct Domains Required for Its Localization and Function. *Journal of Cell Biology* **143**, 319–331 (1998). URL <https://doi.org/10.1083/jcb.143.2.319>.
- [358] Diao, A., Frost, L., Morohashi, Y. & Lowe, M. Coordination of golgin tethering and SNARE assembly: GM130 binds syntaxin 5 in a p115-regulated manner. *The Journal of biological chemistry* **283**, 6957–67 (2008). URL <http://www.ncbi.nlm.nih.gov/pubmed/18167358>.
- [359] Canton, J. & Kima, P. E. Targeting Host Syntaxin-5 Preferentially Blocks Leishmania Parasitophorous Vacuole Development in Infected Cells and Limits Experimental Leishmania Infections. *The American Journal of Pathology* **181**, 1348–1355 (2012). URL [https://ajp.amjpathol.org/article/S0002-9440\(12\)00523-8/abstract](https://ajp.amjpathol.org/article/S0002-9440(12)00523-8/abstract). Publisher: Elsevier.
- [360] Stechmann, B. *et al.* Inhibition of Retrograde Transport Protects Mice from Lethal Ricin Challenge. *Cell* **141**, 231–242 (2010). URL <http://www.sciencedirect.com/science/article/pii/S0092867410000784>.
- [361] Canton, J., Ndjamien, B., Hatsuzawa, K. & Kima, P. E. Disruption of the fusion of Leishmania parasitophorous vacuoles with ER vesicles results in the control of the infection. *Cellular Microbiology* **14**, 937–948 (2012). URL <https://onlinelibrary.wiley.com/doi/abs/10.1111/j.1462-5822.2012.01767.x>. \_eprint: <https://onlinelibrary.wiley.com/doi/pdf/10.1111/j.1462-5822.2012.01767.x>.
- [362] Cruz, L. *et al.* Potent Inhibition of Human Cytomegalovirus by Modulation of Cellular SNARE Syntaxin 5. *Journal of Virology* **91** (2017). URL <https://jvi.asm.org/content/91/1/e01637-16>. Publisher: American Society for Microbiology Journals Section: Structure and Assembly.
- [363] Nonnenmacher, M. E., Cintrat, J.-C., Gillet, D. & Weber, T. Syntaxin 5-Dependent Retrograde Transport to the trans-Golgi Network Is Required for Adeno-Associated Virus Transduction. *Journal of Virology* **89**, 1673 LP–1687 (2015). URL <http://jvi.asm.org/content/89/3/1673.abstract>.
- [364] SUGA, K., TOMIYAMA, T., MORI, H. & AKAGAWA, K. Syntaxin 5 interacts with presenilin holoproteins, but not with their N- or C-terminal fragments, and affects  $\beta$ -amyloid peptide production. *Biochemical Journal* **381**, 619–628 (2004). URL <https://doi.org/10.1042/BJ20040618>.
- [365] Suga, K., Saito, A., Tomiyama, T., Mori, H. & Akagawa, K. Syntaxin 5 interacts specifically with presenilin holoproteins and affects processing of  $\beta$ APP in neuronal cells. *Journal of Neurochemistry* **94**, 425–439 (2005). URL <https://onlinelibrary.wiley.com/doi/abs/10.1111/j.1471-4159.2005.03210.x>. \_eprint: <https://onlinelibrary.wiley.com/doi/pdf/10.1111/j.1471-4159.2005.03210.x>.
- [366] Suga, K., Saito, A., Mishima, T. & Akagawa, K. ER and Golgi stresses increase ER–Golgi SNARE Syntaxin5: Implications for organelle stress and  $\beta$ APP processing. *Neuroscience Letters* **604**, 30–35 (2015). URL <https://www.sciencedirect.com/science/article/pii/S0304394015300379>.

- [367] Thayanidhi, N. *et al.* Ⓣ-Synuclein Delays Endoplasmic Reticulum (ER)-to-Golgi Transport in Mammalian Cells by Antagonizing ER/Golgi SNAREs. *Molecular Biology of the Cell* **21**, 1850–1863 (2010). URL <https://www.molbiolcell.org/doi/10.1091/mbc.e09-09-0801>. Publisher: American Society for Cell Biology (mbo).
- [368] Canton, J. & Kima, P. E. Interactions of pathogen-containing compartments with the secretory pathway. *Cellular Microbiology* **14**, 1676–1686 (2012). URL <https://onlinelibrary.wiley.com/doi/abs/10.1111/cmi.12000>. \_eprint: <https://onlinelibrary.wiley.com/doi/pdf/10.1111/cmi.12000>.
- [369] Dickinson, M. E. *et al.* High-throughput discovery of novel developmental phenotypes. *Nature* **537**, 508–514 (2016). URL <https://www.nature.com/articles/nature19356>.
- [370] Gao, G. & Banfield, D. K. Multiple features within the syntaxin Sed5p mediate its Golgi localization. *Traf-fic* **21**, 274–296 (2020). URL <https://onlinelibrary.wiley.com/doi/abs/10.1111/tra.12720>.
- [371] Mallard, F. *et al.* Early/recycling endosomes-to-TGN transport involves two SNARE complexes and a Rab6 isoform. *The Journal of Cell Biology* **156**, 653–664 (2002). URL <http://jcb.rupress.org/content/156/4/653>.
- [372] Gleeson, P. A. *et al.* p230 is associated with vesicles budding from the trans-Golgi network. *Journal of Cell Science* **109**, 2811–2821 (1996). URL <https://jcs.biologists.org/content/109/12/2811>. Publisher: The Company of Biologists Ltd Section: Journal Articles.
- [373] Lippincott-Schwartz, J., Roberts, T. H. & Hirschberg, K. Secretory Protein Trafficking and Organelle Dynamics in Living Cells. *Annual Review of Cell and Developmental Biology* **16**, 557–589 (2000). URL <http://www.annualreviews.org/doi/10.1146/annurev.cellbio.16.1.557>.
- [374] Bindels, D. S. *et al.* mScarlet: a bright monomeric red fluorescent protein for cellular imaging. *Nature Methods* **14**, 53–56 (2017). URL <https://www.nature.com/articles/nmeth.4074>.
- [375] Griesbeck, O., Baird, G. S., Campbell, R. E., Zacharias, D. A. & Tsien, R. Y. Reducing the Environmental Sensitivity of Yellow Fluorescent Protein MECHANISM AND APPLICATIONS. *Journal of Biological Chemistry* **276**, 29188–29194 (2001). URL <http://www.jbc.org/content/276/31/29188>.
- [376] Antonin, W., Holroyd, C., Tikkanen, R., Höning, S. & Jahn, R. The R-SNARE Endobrevin/VAMP-8 Mediates Homotypic Fusion of Early Endosomes and Late Endosomes. *Molecular Biology of the Cell* **11**, 3289–3298 (2000). URL <https://www.molbiolcell.org/doi/10.1091/mbc.11.10.3289>.
- [377] Bajno, L. *et al.* Focal Exocytosis of Vamp3-Containing Vesicles at Sites of Phagosome Formation. *The Journal of Cell Biology* **149**, 697–706 (2000). URL <http://www.jcb.org/lookup/doi/10.1083/jcb.149.3.697>.
- [378] Manderson, A. P., Kay, J. G., Hammond, L. A., Brown, D. L. & Stow, J. L. Subcompartments of the macrophage recycling endosome direct the differential secretion of IL-6 and TNF. *The Journal of Cell Biology* **178**, 57–69 (2007). URL <http://www.jcb.org/lookup/doi/10.1083/jcb.200612131>.
- [379] Murray, R. Z. A Role for the Phagosome in Cytokine Secretion. *Science* **310**, 1492–1495 (2005). URL <http://www.sciencemag.org/cgi/doi/10.1126/science.1120225>.
- [380] Amberger, J. S., Bocchini, C. A., Schiettecatte, F., Scott, A. F. & Hamosh, A. OMIM.org: Online Mendelian Inheritance in Man (OMIM®), an online catalog of human genes and genetic disorders. *Nucleic Acids Research* **43**, D789–D798 (2015). URL <https://academic.oup.com/nar/article/43/D1/D789/2439148>.
- [381] Pedersen, A. G. & Nielsen, H. Neural network prediction of translation initiation sites in eukaryotes: perspectives for EST and genome analysis. *Proceedings. International Conference on Intelligent Systems for Molecular Biology* **5**, 226–233 (1997).

## References

- [382] Kochetov, A. V. Alternative translation start sites and hidden coding potential of eukaryotic mRNAs. *BioEssays* **30**, 683–691 (2008). URL <https://onlinelibrary.wiley.com/doi/abs/10.1002/bies.20771>.
- [383] Kozak, M. Regulation of translation via mRNA structure in prokaryotes and eukaryotes. *Gene* **361**, 13–37 (2005). URL <http://www.sciencedirect.com/science/article/pii/S0378111905004348>.
- [384] Jaiman, A. & Thattai, M. Algorithmic biosynthesis of eukaryotic glycans. *bioRxiv* 440792 (2018). URL <https://www.biorxiv.org/content/10.1101/440792v1>.
- [385] Ohtsubo, K. & Marth, J. D. Glycosylation in Cellular Mechanisms of Health and Disease. *Cell* **126**, 855–867 (2006). URL <http://www.sciencedirect.com/science/article/pii/S0092867406010865>.
- [386] Blackburn, J. B., Kudlyk, T., Pokrovskaya, I. & Lupashin, V. V. More than just sugars: Conserved oligomeric Golgi complex deficiency causes glycosylation-independent cellular defects. *Traffic* **19**, 463–480 (2018). URL <https://onlinelibrary.wiley.com/doi/full/10.1111/tra.12564>.
- [387] Hucthagowder, V. *et al.* Loss-of-function mutations in ATP6VOA2 impair vesicular trafficking, tropoelastin secretion and cell survival. *Human Molecular Genetics* **18**, 2149–2165 (2009). URL <https://academic.oup.com/hmg/article/18/12/2149/643863>.
- [388] Ashikov, A. *et al.* Integrating glycomics and genomics uncovers SLC10A7 as essential factor for bone mineralization by regulating post-Golgi protein transport and glycosylation. *Human Molecular Genetics* **27**, 3029–3045 (2018). URL <https://academic.oup.com/hmg/article/27/17/3029/5033379>.
- [389] Zhong, W. Golgi during Development. *Cold Spring Harbor Perspectives in Biology* **3** (2011). URL <https://www.ncbi.nlm.nih.gov/pmc/articles/PMC3181030/>.
- [390] Zhao, H. Membrane Trafficking in Osteoblasts and Osteoclasts: New Avenues for Understanding and Treating Skeletal Diseases. *Traffic* **13**, 1307–1314 (2012). URL <https://onlinelibrary.wiley.com/doi/abs/10.1111/j.1600-0854.2012.01395.x>.
- [391] Bogaert, A., Fernandez, E. & Gevaert, K. N-Terminal Proteoforms in Human Disease. *Trends in Biochemical Sciences* **45**, 308–320 (2020). URL <http://www.sciencedirect.com/science/article/pii/S0968000420300074>.
- [392] van Scherpenzeel, M., Steenbergen, G., Morava, E., Wevers, R. A. & Lefeber, D. J. High-resolution mass spectrometry glycoprofiling of intact transferrin for diagnosis and subtype identification in the congenital disorders of glycosylation. *Translational Research* **166**, 639–649.e1 (2015). URL <http://linkinghub.elsevier.com/retrieve/pii/S1931524415002534>.
- [393] Vissers, L. E. L. M. *et al.* A de novo paradigm for mental retardation. *Nature Genetics* **42**, 1109–1112 (2010). URL <https://www.nature.com/articles/ng.712>. Number: 12 Publisher: Nature Publishing Group.
- [394] Nikopoulos, K. *et al.* Next-Generation Sequencing of a 40 Mb Linkage Interval Reveals TSPAN12 Mutations in Patients with Familial Exudative Vitreoretinopathy. *The American Journal of Human Genetics* **86**, 240–247 (2010). URL <http://www.sciencedirect.com/science/article/pii/S0002929709006107>.
- [395] Jolanda, I., de Vries, M., Adema, G. J., Punt, C. J. A. & Figgdr, C. G. Phenotypical and Functional Characterization of Clinical-Grade Dendritic Cells. In Ludewig, B. & Hoffmann, M. W. (eds.) *Adoptive Immunotherapy: Methods and Protocols*, Methods in Molecular Medicine™, 113–125 (Humana Press, Totowa, NJ, 2005). URL <https://doi.org/10.1385/1-59259-862-5:113>.

- [396] Ran, F. A. *et al.* Genome engineering using the CRISPR-Cas9 system. *Nature Protocols* **8**, 2281–2308 (2013). URL <https://www.nature.com/articles/nprot.2013.143>.
- [397] Virtanen, P. *et al.* SciPy 1.0: fundamental algorithms for scientific computing in Python. *Nature Methods* **17**, 261–272 (2020). URL <https://doi.org/10.1038/s41592-019-0686-2>.
- [398] Schägger, H. Tricine–SDS-PAGE. *Nature Protocols* **1**, 16–22 (2006). URL <https://www.nature.com/articles/nprot.2006.4>.
- [399] Aridor, M. & Balch, W. E. Kinase Signaling Initiates Coat Complex II (COPII) Recruitment and Export from the Mammalian Endoplasmic Reticulum. *Journal of Biological Chemistry* **275**, 35673–35676 (2000). URL <http://www.jbc.org/content/275/46/35673>. Publisher: American Society for Biochemistry and Molecular Biology.
- [400] Nakagawa, H. *et al.* Sar1 translocation onto the ER-membrane for vesicle budding has different pathways for promotion and suppression of ER-to-Golgi transport mediated through H89-sensitive kinase and ER-resident G protein. *Molecular and Cellular Biochemistry* **366**, 175–182 (2012). URL <https://doi.org/10.1007/s11010-012-1295-x>.
- [401] Hipgrave Ederveen, A. L., de Haan, N., Baerenfaenger, M., Lefever, D. J. & Wuhrer, M. Dissecting Total Plasma and Protein-Specific Glycosylation Profiles in Congenital Disorders of Glycosylation. *International Journal of Molecular Sciences* **21**, 7635 (2020). URL <https://www.mdpi.com/1422-0067/21/20/7635>. Number: 20 Publisher: Multidisciplinary Digital Publishing Institute.
- [402] Witters, P. *et al.* D-galactose supplementation in individuals with PMM2-CDG: results of a multicenter, open label, prospective pilot clinical trial. *Orphanet Journal of Rare Diseases* **16**, 138 (2021). URL <https://doi.org/10.1186/s13023-020-01609-z>.
- [403] Wong, S. Y.-W. *et al.* Oral D-galactose supplementation in PGM1-CDG. *Genetics in Medicine* **19**, 1226–1235 (2017). URL <https://www.nature.com/articles/gim201741>. Number: 11 Publisher: Nature Publishing Group.
- [404] Voermans, N. C. *et al.* PGM1 deficiency: Substrate use during exercise and effect of treatment with galactose. *Neuromuscular Disorders* **27**, 370–376 (2017). URL [https://www.nmd-journal.com/article/S0960-8966\(16\)30251-6/abstract](https://www.nmd-journal.com/article/S0960-8966(16)30251-6/abstract). Publisher: Elsevier.
- [405] Mendell, J. R. *et al.* Single-Dose Gene-Replacement Therapy for Spinal Muscular Atrophy (2017). URL <https://www.nejm.org/doi/10.1056/NEJMoa1706198>. Archive Location: world Publisher: Massachusetts Medical Society.
- [406] Home. URL <https://noordzeeziekte.nl/>.
- [407] CDG Patient Groups. URL <http://www.apcdg.com/cdg-patient-groups.html>.
- [408] Argov, Z. & Yarom, R. “Rimmed vacuole myopathy” sparing the quadriceps: A unique disorder in iranian jews. *Journal of the Neurological Sciences* **64**, 33–43 (1984). URL [https://www.jns-journal.com/article/0022-510X\(84\)90053-4/abstract](https://www.jns-journal.com/article/0022-510X(84)90053-4/abstract). Publisher: Elsevier.
- [409] Broccolini, A., Gidaro, T., Morosetti, R., Sancricca, C. & Mirabella, M. Hereditary inclusion-body myopathy with sparing of the quadriceps: the many tiles of an incomplete puzzle. *Acta Myologica* **30**, 91–95 (2011). URL <https://www.ncbi.nlm.nih.gov/pmc/articles/PMC3235839/>.
- [410] Brasil, S. *et al.* CDG Therapies: From Bench to Bedside. *International Journal of Molecular Sciences* **19** (2018). URL <https://www.ncbi.nlm.nih.gov/pmc/articles/PMC5983582/>.
- [411] Voermans, N. C. *et al.* Clinical features, lectin staining, and a novel GNE frameshift mutation in hereditary inclusion body myopathy. *Clinical Neuropathology* **29**, 71–77 (2010).

## References

- [412] Willems, A. P., van Engelen, B. G. M. & Lefeber, D. J. Genetic defects in the hexosamine and sialic acid biosynthesis pathway. *Biochimica et Biophysica Acta (BBA) - General Subjects* **1860**, 1640–1654 (2016). URL <https://www.sciencedirect.com/science/article/pii/S0304416515003566>.
- [413] Luo, D. & Saltzman, W. M. Synthetic DNA delivery systems. *Nature Biotechnology* **18**, 33–37 (2000). URL [https://www.nature.com/articles/nbt0100\\_33](https://www.nature.com/articles/nbt0100_33). Number: 1 Publisher: Nature Publishing Group.
- [414] Lonez, C., Vandenbranden, M. & Ruysschaert, J.-M. Cationic liposomal lipids: From gene carriers to cell signaling. *Progress in Lipid Research* **47**, 340–347 (2008). URL <https://www.sciencedirect.com/science/article/pii/S0163782708000271>.
- [415] Luo, P. M. & Boyce, M. Directing Traffic: Regulation of COPI Transport by Post-translational Modifications. *Frontiers in Cell and Developmental Biology* **7** (2019). URL <https://www.frontiersin.org/articles/10.3389/fcell.2019.00190/full>.
- [416] Yamano, S., Dai, J. & Moursi, A. M. Comparison of Transfection Efficiency of Nonviral Gene Transfer Reagents. *Molecular Biotechnology* **46**, 287–300 (2010). URL <https://doi.org/10.1007/s12033-010-9302-5>.
- [417] Maurisse, R. *et al.* Comparative transfection of DNA into primary and transformed mammalian cells from different lineages. *BMC Biotechnology* **10**, 9 (2010). URL <https://doi.org/10.1186/1472-6750-10-9>.
- [418] Anderson, W. F. Human gene therapy. *Nature* **392**, 25–30 (1998).
- [419] Crystal, R. G. Transfer of Genes to Humans: Early Lessons and Obstacles to Success. *Science* **270**, 404–410 (1995). URL <https://science.sciencemag.org/content/270/5235/404>. Publisher: American Association for the Advancement of Science Section: Articles.
- [420] Tripathy, S. K., Black, H. B., Goldwasser, E. & Leiden, J. M. Immune responses to transgene-encoded proteins limit the stability of gene expression after injection of replication-defective adenovirus vectors. *Nature Medicine* **2**, 545–550 (1996). URL <https://www.nature.com/articles/nm0596-545>. Number: 5 Publisher: Nature Publishing Group.
- [421] Hsu, P. D., Lander, E. S. & Zhang, F. Development and Applications of CRISPR-Cas9 for Genome Engineering. *Cell* **157**, 1262–1278 (2014). URL [https://www.cell.com/cell/abstract/S0092-8674\(14\)00604-7](https://www.cell.com/cell/abstract/S0092-8674(14)00604-7). Publisher: Elsevier.
- [422] Cho, S. W., Kim, S., Kim, J. M. & Kim, J.-S. Targeted genome engineering in human cells with the Cas9 RNA-guided endonuclease. *Nature Biotechnology* **31**, 230–232 (2013). URL <https://www.nature.com/articles/nbt.2507>. Number: 3 Publisher: Nature Publishing Group.
- [423] Cong, L. *et al.* Multiplex Genome Engineering Using CRISPR/Cas Systems. *Science* **339**, 819–823 (2013). URL <https://science.sciencemag.org/content/339/6121/819>. Publisher: American Association for the Advancement of Science Section: Report.
- [424] Jinek, M. *et al.* A Programmable Dual-RNA-Guided DNA Endonuclease in Adaptive Bacterial Immunity. *Science* **337**, 816–821 (2012). URL <https://science.sciencemag.org/content/337/6096/816>. Publisher: American Association for the Advancement of Science Section: Research Article.
- [425] Agudelo, D. *et al.* Marker-free coselection for CRISPR-driven genome editing in human cells. *Nature Methods* **14**, 615–620 (2017). URL <http://www.nature.com/doifinder/10.1038/nmeth.4265>.
- [426] Ratz, M., Testa, I., Hell, S. W. & Jakobs, S. CRISPR/Cas9-mediated endogenous protein tagging for RESOLFT super-resolution microscopy of living human cells. *Scientific Reports* **5**, 9592 (2015). URL <https://www.nature.com/articles/srep09592>. Number: 1 Publisher: Nature Publishing Group.

- [427] Ali, R., Ramadurai, S., Barry, F. & Nasheuer, H. P. Optimizing fluorescent protein expression for quantitative fluorescence microscopy and spectroscopy using herpes simplex thymidine kinase promoter sequences. *FEBS Open Bio* **8**, 1043–1060 (2018). URL <https://doi.org/10.1002/2211-5463.12432>. \_eprint: <https://febs.onlinelibrary.wiley.com/doi/pdf/10.1002/2211-5463.12432>.
- [428] Klimanskaya, I., Chung, Y., Becker, S., Lu, S.-J. & Lanza, R. Human embryonic stem cell lines derived from single blastomeres. *Nature* **444**, 481–485 (2006). URL <https://www.nature.com/articles/nature05142>. Number: 7118 Publisher: Nature Publishing Group.
- [429] Takahashi, K. & Yamanaka, S. Induction of Pluripotent Stem Cells from Mouse Embryonic and Adult Fibroblast Cultures by Defined Factors. *Cell* **126**, 663–676 (2006). URL [https://www.cell.com/cell/abstract/S0092-8674\(06\)00976-7](https://www.cell.com/cell/abstract/S0092-8674(06)00976-7). Publisher: Elsevier.
- [430] Komor, A. C., Kim, Y. B., Packer, M. S., Zuris, J. A. & Liu, D. R. Programmable editing of a target base in genomic DNA without double-stranded DNA cleavage. *Nature* **533**, 420–424 (2016). URL <https://www.nature.com/articles/nature17946>. Number: 7603 Publisher: Nature Publishing Group.
- [431] Huang, T. P., Newby, G. A. & Liu, D. R. Precision genome editing using cytosine and adenine base editors in mammalian cells. *Nature Protocols* **16**, 1089–1128 (2021). URL <https://www.nature.com/articles/s41596-020-00450-9>. Number: 2 Publisher: Nature Publishing Group.
- [432] Anzalone, A. V. *et al.* Search-and-replace genome editing without double-strand breaks or donor DNA. *Nature* **576**, 149–157 (2019).
- [433] Cox, D. B. T., Platt, R. J. & Zhang, F. Therapeutic genome editing: prospects and challenges. *Nature Medicine* **21**, 121–131 (2015). URL <https://www.nature.com/articles/nm.3793>. Number: 2 Publisher: Nature Publishing Group.
- [434] Hilton, I. B. & Gersbach, C. A. Enabling functional genomics with genome engineering. *Genome Research* **25**, 1442–1455 (2015). URL <https://genome.cshlp.org/content/25/10/1442>. Company: Cold Spring Harbor Laboratory Press Distributor: Cold Spring Harbor Laboratory Press Institution: Cold Spring Harbor Laboratory Press Label: Cold Spring Harbor Laboratory Press Publisher: Cold Spring Harbor Lab.
- [435] Ihry, R. J. *et al.* p53 inhibits CRISPR–Cas9 engineering in human pluripotent stem cells. *Nature Medicine* **24**, 939–946 (2018). URL <https://www.nature.com/articles/s41591-018-0050-6>. Number: 7 Publisher: Nature Publishing Group.
- [436] Haapaniemi, E., Botla, S., Persson, J., Schmierer, B. & Taipale, J. CRISPR–Cas9 genome editing induces a p53-mediated DNA damage response. *Nature Medicine* **24**, 927–930 (2018). URL <https://www.nature.com/articles/s41591-018-0049-z>. Number: 7 Publisher: Nature Publishing Group.
- [437] St. Croix, C. M., Shand, S. H. & Watkins, S. C. Confocal microscopy: comparisons, applications, and problems. *BioTechniques* **39**, S2–S5 (2005). URL <https://www.future-science.com/doi/10.2144/000112089>. Publisher: Future Science.
- [438] Ladinsky, M. S., Mastronarde, D. N., McIntosh, J. R., Howell, K. E. & Staehelin, L. A. Golgi Structure in Three Dimensions: Functional Insights from the Normal Rat Kidney Cell. *Journal of Cell Biology* **144**, 1135–1149 (1999). URL <https://doi.org/10.1083/jcb.144.6.1135>.
- [439] Dickson, L. J., Liu, S. & Storrie, B. Rab6 is required for rapid, cisternal-specific, intra-Golgi cargo transport. *Scientific Reports* **10**, 16604 (2020). URL <https://www.nature.com/articles/s41598-020-73276-w>. Number: 1 Publisher: Nature Publishing Group.

## References

- [440] de Boer, P., Hoogenboom, J. P. & Giepmans, B. N. G. Correlated light and electron microscopy: ultrastructure lights up! *Nature Methods* **12**, 503–513 (2015). URL <https://www.nature.com/articles/nmeth.3400>. Number: 6 Publisher: Nature Publishing Group.
- [441] Joosten, B., Willemse, M., Fransen, J., Cambi, A. & van den Dries, K. Super-Resolution Correlative Light and Electron Microscopy (SR-CLEM) Reveals Novel Ultrastructural Insights Into Dendritic Cell Podosomes. *Frontiers in Immunology* **9** (2018). URL <https://www.frontiersin.org/articles/10.3389/fimmu.2018.01908/full>. Publisher: Frontiers.
- [442] Hoffman, D. P. *et al.* Correlative three-dimensional super-resolution and block-face electron microscopy of whole vitreously frozen cells. *Science* **367** (2020). URL <https://science.sciencemag.org/content/367/6475/eaaz5357>. Publisher: American Association for the Advancement of Science Section: Research Article.
- [443] Xu, C. S. *et al.* Enhanced FIB-SEM systems for large-volume 3D imaging. *eLife* **6**, e25916 (2017). URL <https://doi.org/10.7554/eLife.25916>. Publisher: eLife Sciences Publications, Ltd.
- [444] Chen, B.-C. *et al.* Lattice light-sheet microscopy: Imaging molecules to embryos at high spatiotemporal resolution. *Science* **346** (2014). URL <https://science.sciencemag.org/content/346/6208/1257998>. Publisher: American Association for the Advancement of Science Section: Research Article.
- [445] Hirvonen, L. M. *et al.* Lightsheet fluorescence lifetime imaging microscopy with wide-field time-correlated single photon counting. *Journal of Biophotonics* **13**, e201960099 (2020). URL <https://onlinelibrary.wiley.com/doi/abs/10.1002/jbio.201960099>. \_eprint: <https://onlinelibrary.wiley.com/doi/pdf/10.1002/jbio.201960099>.
- [446] Glick, B. S. & Luini, A. Models for Golgi traffic: a critical assessment. *Cold Spring Harbor perspectives in biology* **3**, a005215–a005215 (2011). URL <http://www.ncbi.nlm.nih.gov/pubmed/21875986>.
- [447] Pantazopoulou, A. & Glick, B. S. A Kinetic View of Membrane Traffic Pathways Can Transcend the Classical View of Golgi Compartments. *Frontiers in Cell and Developmental Biology* **7** (2019). URL <https://www.frontiersin.org/articles/10.3389/fcell.2019.00153/full>.
- [448] Harris, S. L. & Waters, M. G. Localization of a yeast early Golgi mannosyltransferase, Och1p, involves retrograde transport. *Journal of Cell Biology* **132**, 985–998 (1996). URL <https://doi.org/10.1083/jcb.132.6.985>.
- [449] Munro, S. What can yeast tell us about N-linked glycosylation in the Golgi apparatus? *FEBS Letters* **498**, 223–227 (2001). URL <https://febs.onlinelibrary.wiley.com/doi/abs/10.1016/S0014-5793%2801%2902488-7>. \_eprint: <https://febs.onlinelibrary.wiley.com/doi/pdf/10.1016/S0014-5793%2801%2902488-7>.
- [450] Mizuno-Yamasaki, E., Rivera-Molina, F. & Novick, P. GTPase Networks in Membrane Traffic. *Annual Review of Biochemistry* **81**, 637–659 (2012). URL <https://www.annualreviews.org/doi/10.1146/annurev-biochem-052810-093700>. Publisher: Annual Reviews.
- [451] Beznoussenko, G. V. *et al.* Transport of soluble proteins through the Golgi occurs by diffusion via continuities across cisternae. *eLife* **3**, 160–166 (2014). URL <http://www.ncbi.nlm.nih.gov/pubmed/24867214>.
- [452] McCaughey, J., Stevenson, N. L., Cross, S. & Stephens, D. J. ER-to-Golgi trafficking of procollagen in the absence of large carriers. *The Journal of cell biology* **jcb.201806035**–*jcb.201806035* (2018). URL <http://www.ncbi.nlm.nih.gov/pubmed/30587510>.